UNIVERSITÉ DE MONTRÉAL

MAGNETOTELLURIC PROSPECTING IN THE MATAGAMI MINING CAMP

TING-KUEI CHOU
DÉPARTEMENT DES GÉNIES CIVIL, GÉOLOGIQUE ET DES MINES
ÉCOLE POLYTECHNIQUE DE MONTRÉAL

MÉMOIRE PRÉSENTÉ EN VUE DE L'OBTENTION
DU DIPLÔME DE MAÎTRISE ÈS SCIENCES APPLIQUÉES
(GÉNIE MINÉRAL)
DÉCEMBRE 2010

UNIVERSITÉ DE MONTRÉAL

ÉCOLE POLYTECHNIQUE DE MONTRÉAL

Ce mémoire intitulé:

MAGNETOTELLURIC PROSPECTING IN THE MATAGAMI MINING CAMP

présenté par: CHOU Ting-Kuei

en vue de l'obtention du diplôme de : Maîtrise ès sciences appliquées

a été dûment accepté par le jury d'examen constitué de:

M. PASQUIER Philippe, Ph.D., président

M. CHOUTEAU Michel, Ph.D., directeur de recherche

M. CRAVEN Jim, M.Sc., membre

ACKNOWLEGEMENTS

I would like to thank my supervisor Prof. Michel Chouteau for his support, encouragement and guidance, as well as his availability and patience. I would also thank NRCan for supplying the financial support through the RAP program. A thank also goes to Michel Allard for his assistance and Xstrasta Zinc for supplying the MT data. I am grateful to Bernard Giroux and Abderrezak Bouchedda for their aids throughout my project. A big thank you to my dad, my mom and specially my sister for their support an encouragement. Finally, I want to thank my friends (Jeremie Lafac, Yasaman Khajehnouri, ...) for their moral support and entertainment.

RÉSUMÉ

Dans ce mémoire, un logiciel de modélisation 2D MT a été modifié afin d'y inclure une résistivité complexe variant en fonction de la fréquence suivant une équation Cole-Cole. Ce nouveau logiciel a été validé à l'aide de solutions analytiques et certains résultats publiés de modèles 2D incluant des effets de dispersion. Les réponses calculées de modèles présentant des effets de dispersion ont la possibilité d'être détectées mais seulement pour des corps situés à une profondeur inférieure à leurs dimensions. Les propriétés électriques (i.e. résistivité, chargeabilité, constante de temps) et les dimensions du corps influencent grandement les réponses MT et l'habilité d'être detectés par la méthode MT.

La possibilité d'imager des structures dans le camp de Matagami a été examinée par le moyen de modélisation et d'interprétation des sondages MT éxistants. La présence de distorsion et de bruit dans les données a été mise en évidence dans les sondages MT. Plusieurs méthodes ont été utilisées pour déterminer la dimension du sous-sol localisé sous la région sondée par la MT. Ces méthodes démontrent que la région se trouve entre 2D/3D et 3D. Des inversions 2D ont été effectuées pour les profils MT et les pseudo-profils (profils perpendiculaires aux profils MT). On en déduit que le milieu contient des structures 2D de toutes tailles, dimension et orientation dans un milieu 3D. Les résultats des inversions 2D ont été interpolés pour construire un modèle 3D. Une modélisation 3D MT a été faite pour vérifier la qualité des inversions 2D dans un cas 3D. Le résultat a été satisfaisant pour les données MT dont les réponses MT modélisées ressemblent fortement aux sondages. En ajustant les couches profondes et en ajoutant les corrections des effets statiques, il est possible de reproduire des modèles qui ajustent beaucoup mieux les données MT.

ABSTRACT

In this thesis, 2D MT modeling program was modified to include a varying complex resistivity with frequency by implementing the Cole-Cole equation in the forward code. The code was validated with analytical solutions and some existing results to MT models with resistivity dispersion. Bodies with induced polarization (IP) effects were found to be detectable but only for bodies at depths less than their geometrical dimensions. The electrical and inductive properties (i.e. chargeability (m), time constant (τ) ...) of the body greatly influence the outcome of the MT response and the ability to be detected by the MT.

The capability of mapping structures in the Matagami mining camp was investigated by modelling and by interpretation of a very large existing MT survey. Strong presence of distortion and noises were found in the magnetotelluric (MT) survey data at the Matagami southern flank region. Various methods were used to quantify the dimensionality of the surveyed region as 2D/3D and 3D. 2D inversion was done parrallel and perpendicular to the determined strike direction. We have found the MT surveyed area to contain 2D medium size structures of mixed size, orientation and shape in a 3D medium. The inversion results were then interpolated to build a 3D model. 3D forward response was done to verify the fit of the 3D model responses with the survey data. The 3D model responses resemble the survey data. By adjusting the 1D earth crust model and by adding a static shift correction, it is possible to produce responses that better fit the survey data.

CONDENSÉ

Une approche très différente de la stratégie classique de prospection des gisements de proche surface est nécessaire pour l'exploration des gisements à des profondeurs supérieures à 300 m (et jusqu'à 2500 m). La stratégie classique consiste à réaliser une étude électromagnétique aérienne (EM) suivie des mesures électriques (IP) aux sols. Ces sondages ont généralement une profondeur maximale de 250-300 m avec une extension possible de 500 m. Au-delà de cette profondeur une autre méthode doit être utilisée, consistant à explorer le milieu avec le sondage audiomagnétotellurique-magnétotellurique (AMT-MT). Cette méthode a une profondeur d'exploration théorique comprise entre 300 m et 3000 m dans la bande de fréquence 0.1-10,000 Hz et nécessite un environnement de hautes résistivités géologiques comme le Bouclier canadien. À la suite d'une première exploration, les anomalies de phase provoquées par les grandes cibles conductrices ont été localisées suivies forages afin de rencontrer/retrouver les cibles.

Théoriquement la méthode magnétotellurique permet d'avoir une très grande profondeur d'exploration de plusieurs centaines de kilomètre. Cette méthode permet de cartographier le sous-sol et d'imager les structures géologiques. Une étape essentielle à cette méthode est l'interprétation des données MT. Les gisements sont en effet de très petites cibles 3D situées à des profondeurs de plusieurs centaines de mètres. Leurs réponses sont fonction de l'orientation des capteurs; la topographie pourra en outre générer des effets connus comme des «distorsions» dues à l’effet galvanique. Celles-ci modifient et parfois masquent les réponses produites par les gisements. Beaucoup de techniques ont été développées afin de corriger ces distorsions jusqu'à un certain point. Une fois les corrections appliquées, les données sont généralement interprétées par une inversion 2D, qui est une approximation acceptable des corps minéralisés 3D. Dès ce moment, les corrections peuvent réduire ou éliminer les anomalies recherchées dans l'exploration, car certains corps conducteurs situés à des profondeurs intermédiaires peuvent provoquer des effets de distorsion galvanique semblables à des morts-terrains et à la topographie. Cette série de traitement ainsi que l'interprétation nécessitent une expertise et une solide expérience permettant de pouvoir sélectionner les cibles de forage.

Xstrata Zinc a déjà commencé le développement de la mine de Bracemac et de McLeod tandis que la mine de Persévérance s'approche vers la fin de sa production. Il apparaît donc essentiel de trouver des gisements supplémentaires pouvant contenir des minerais tels que le zinc dans la région de Matagami. Cette situation pousse la société Xstrata Zinc vers l'exploration de gisements en profondeur. Ainsi l'objectif de ce mémoire est de déterminer la capacité de détection MT pour les gisements en profondeur et les structures produisant des effets de la polarisation provoquée. Motivé par le besoin de trouver de nouvelles méthodes de recherche, la modélisation MT des gisements et des structures connus dans la région de Matagami a été faite. Le logiciel de modélisation MT 2D a été modifié pour introduire une résistivité complexe variant en fonction de la fréquence.

La méthode magnétotellurique est une technique qui utilise les champs électriques E et magnétique B mesurés dans des directions orthogonales à la surface du sol, afin de déterminer la distribution de résistivité du sous-sol. Ces champs sont des champs géomagnétiques d'origine naturelle. La profondeur du sondage peut atteindre plusieurs centaines de milliers de mètres, permettant de cartographier des structures profondes.

Également, les méthodes magnétotelluriques peuvent fournir des informations où la sismique rencontre un manque de résolution (i.e. en profondeur). Un émetteur de signal n'est pas nécessaire car les sources des champs magnétiques et électriques sont naturelles (i.e. champs terrestres). La méthode MT a également les avantages de l'utilisation d'équipements portatifs et de fournir une meilleure résolution que d'autres méthodes comme la gravimétrie ou la prospection magnétique. Leurs procédures d'interprétations ont été en constant développement, ce qui permet d'accélérer l'interprétation et l'utilisation de ces méthodes non destructives. Comme avec toutes les techniques d'exploration, la méthode MT a ses propres faiblesses. Les signaux MT sont par exemple irréguliers, sensibles au bruit industriel et aux corps conducteurs. Sa résolution est inférieure à la sismique, le traitement des données et l'interprétation sont complexes. De plus, le processus d'inversion s'appuie sur des modèles lisses.

Les traitements des données MT se déroulent en trois étapes. La première est constituée par la correction des effets de distorsion et l'analyse dimensionnelle de la région. La deuxième comprend le traitement des données MT (i.e. Inversion 1D, 2D et/ou 3D) tandis que la troisième est l'analyse des résultats et la confrontation avec la géologie.

Il existe plusieurs méthodes qui peuvent être utilisées pour déterminer la dimensionnalité géo-électrique de la structure géologique. Bahr (1991) propose une méthode pour déterminer la dimension sans avoir de corrélation avec les propriétés physiques. Q-Bahr (Marti et al. 2005) utilise les critères d'origine Bahr en tenant compte de l'erreur produite par le bruit. Ce changement permet ainsi une meilleure détermination de la dimension géo-électrique. En outre, les invariants WAL (Weaver et al, 2000) offrent de meilleures informations sur le type de dimension que son homologue Bahr, mais ceci est cependant moins robuste que la méthode Q-Bahr. Les invariants WAL apportent également une réelle interprétation physique. Enfin il y'a la technique du tenseur de phase qui fournit une bonne représentation graphique de la dimension. Aussi, la direction des structures régionales n'est théoriquement pas affectée par des distorsions galvaniques. Les traitements des données MT se font avec les logiciels d'inversion 1D, 2D et/ou 3D, selon les possibilités. De plus, il existe de nombreux logiciels disponibles et utilisables gratuitement. L'analyse finale consiste à confronter les résultats MT et la géologie.

La méthode MT utilise les propriétés magnéto-électriques comme la conductivité, la résistivité et la permittivité pour déterminer la réponse MT (c'est-à-dire la résistivité apparente et la phase). Treize trous de forage situés dans le camping minier de Matagami ont été obtenus par Xstrata Zinc. De nombreuses propriétés physiques ont été mesurées (i.e. la susceptibilité magnétique, la résistance de pointe, la radioactivité naturelle, la densité, le potentiel spontané, la température, etc.). Les analyses des propriétés électriques de sept forages qui contiennent des renseignements pertinents pouvant utilisés pour notre modélisation ont été effectuées. Le forage des puits et les analyses des carottes ont été effectués par la Commission géologique du Canada (CGC), la Société IFG et le Quantec Logging Services (QLS).

Pour estimer la valeur de résistivité globale pour chaque type de roche, nous avons utilisé la moyenne géométrique définie dans les équations 4.4 et 4.5. Les résultats se trouvent dans le tableau 4.4. Durant notre analyse des forages provenant du dépôt Orchan Ouest, nous avons constaté une relation entre la valeur de résistivité et la profondeur à laquelle les échantillons ont été prélevés pour le gabbro et les différents types de roche basaltique. De l'observation, nous avons remarqué que la résistivité des deux types de roches a tendance à augmenter avec la profondeur. Afin de montrer qu'une relation pourrait existe entrer les deux variables, la résistivité et la profondeur, une analyse de régression linéaire a été faite. Une bande de confiance à 95% a également été calculée. On trouve que la résistivité du gabbro varie fortement avec la profondeur et l'intervalle de confiance de 95% est alors très large. Statistiquement, nous ne pouvons confirmer aucune corrélation entre la résistivité du gabbro et la profondeur, mais une tendance montrant l'augmentation de la résistivité avec la profondeur semble pourvoir être observée. Une forte corrélation a été observée pour le type de roche basaltique et une enquête plus approfondie avec la régression linéaire et les bandes de confiance de 95% montrent qu'il existe une corrélation positive entre la résistivité et la profondeur. Dans la figure 4.5, deux points sont isolés des autres. Les paramètres de régression se trouvent dans le tableau 4.6. Ainsi, on observe une forte corrélation entre la résistivité du basalte et de la profondeur à laquelle il se trouve. De même, nous avons trouvé deux résistivités distinctes pour le basalte (tableau 4.2). Cela permettrait d'améliorer les modèles de la région de Matagami et ainsi générer des réponses MT plus proches de celles figurant dans le sondage MT ainsi qu'une interprétation plus précise des résultats d'inversion.

Une partie de cette thèse a pour objectif de rendre compte de l'étude de la capacité de détection MT des corps minéralisés et VMS avec la polarisation provoquée (PP). Il a été porté à notre attention par les sociétés d'exploration que les anomalies PP et les données MT semblent être corrélées dans la région de Matagami. En effet, M. Allard suggère qu'il pourrait exister une certaine corrélation entre l'inversion des données PP et l'inversion des données MT, obtenues à l'aide du logiciel d'inversion IP de l'UBC (University of Brittish Columbia) et de l'invariant de phase à 1 Hz. Des gisements étudiés à différentes profondeurs dans le Bouclier canadien ont été modélisés. Il s'agit des gisements de Raglan, de Bracemac et de McLeod avec les structures qui contrôlent la minéralisation comme le Key Tuffite avec les effets PP.

Dans un projet préliminaire, Boulanger et Chouteau (2007) ont réalisé en collaboration avec Xstrata Zinc la modélisation MT 3D des gisements typiques de Matagami, Raglan et des camps miniers de Rouyn-Noranda. La méthode utilisée a été la magnétotellurique et les résultats du projet sont les suivants: (1) un élément isolé du corps conducteur massif peut être détecté à une profondeur d'environ la taille moyenne de ce dernier. Par exemple, un corps mesurant 100 x 100 x 100 m peut être détecté à une profondeur d'environ 100-150 m. (2) Un corps massif peut être plus détectable lorsqu'il est entouré de la matière disséminée (la minéralisation combinée avec des zones de roches altérées). (3) La capacité de détection de la MT est limitée à 100-150m pour les gisements de Raglan type et à 300m pour ceux de type VMS.

L'étude dans la détection MT des corps minéralisés et VMS avec la polarisation provoquée (PP), a été faite par la modélisation MT 2D. Les corps conducteurs tels que les gisements de sulfures génèrent l'effet de polarisation provoquée (PP) qui dépend de la fréquence (Hartman et Mutmansky, 2002). La résistivité d'un corps sous sa forme complexe varie avec la fréquence. Ces changements peuvent être calculés avec l'équation de Cole-Cole à condition que certains paramètres soient connus. Dans l'exploration minière, les structures d'intérêt, telles que les sulfures massifs, peuvent être conductrices et situées à une profondeur de plusieurs centaines de mètres et cependant ne pas être détectées. Ces corps conducteurs peuvent influencer les réponses MT à une fréquence où la limite statique DC est atteinte. Cette influence peut être déterminée en comparant les profils de résistivité à deux fréquences où la limite DC est atteinte. En outre sans l'effet PP, les parties réelles et imaginaires du champ électrique sont presque identiques, alors qu'avec l'effet PP, les parties réelles et imaginaires des champs sont différentes (Gasperikova et Morrison, 2001). Ces effets peuvent être utilisés comme un outil dans la détection de corps conducteurs tels que les sulfures massifs dans l'exploration minière. L'aspect principal de cette étude est d'estimer la capacité de détection des corps conducteurs ou des structures présentant l'effet PP.

Des modèles 3D ont été créés afin de détecter les gisements conducteurs massifs à Matagami, Raglan et base VMS (sulfures massifs volcanogènes). Ces derniers montrent que les corps de dimensions et de résistivité typiques de ceux que l'on trouve dans la région ne peuvent pas être détectés par la méthode MT pour des profondeurs de l’ordre de quelques centaines de mètres de profondeur (Chouteau, Boulanger et Allard, 2008). Le tableau 5.1 montre la profondeur de détection pour chaque type de corps cité dans la figure 5-3, en supposant qu’un changement de 12,5% sur la résistivité et une variation de 10% pour la phase sont nécessaires pour être significatifs. Ces mêmes modèles sont recréés en 2D avec des corps dont le sommet se situe à des profondeurs de 30m, 60m, 100m, 150m, 200m et 300m. Comme le modèle de polarisation provoquée est en 2D, nous choisissons de positionner les corps minéralisés le long des directions Y et Z. Le modèle que Gasperikova et Morrison (2001) ont utilisé a été utilisé pour valider le code de modélisation 2D comprenant les effets PP.

Dans le domaine quasi-statique, la réponse MT d’un corps conducteur sans effet PP est continue. Cependant cette propriété n’est plus valable lorsque le corps conducteur subit une dispersion provoquée. La modélisation MT 2D démontre que l'effet de l’ajout de la polarisation provoquée à un corps conducteur profond n’augmente pas la capacité de la méthode MT à détecter le corps. Ceci s’explique par la faible contribution de l’effet PP d'un corps conducteur aux données MT (voir section 5.1.1). De plus, si le corps conducteur produit une importante réponse inductive MT, l’effet PP ne sera pas détectable. Par contre, l’effet de la polarisation provoquée permet d’améliorer la détection et la localisation de gisements et des corps conducteurs qui se trouvent près de la surface. Ainsi, l’effet PP est significatif lorsque la dimension du corps est supérieure ou égale à sa profondeur.

Afin de confronter la démarche utilisant l’effet PP expliquée plus haut aux données de terrains, trois gisements connus ont été choisis comme cibles d'essais. Les gisements de Bracemac, McLeod, Orchan et Bell Allard ont été modélisés. Ces gisements contiennent en effet de sulfures massifs riches en minerai et se trouvent sur des zones d'altération. Ces mêmes zones d'altération et les amas de sulfures massifs s’y trouvant pourraient avoir certaines propriétés de dispersion. Ainsi, l'impact des corps polarisables sur les réponses MT et sur la capacité à détecter les zones d'altération seront examinées. La modélisation PP a montré que l’effet PP d'un corps conducteur sera uniquement détectable dans le cas où la taille du corps est égale ou supérieur à sa profondeur. En outre, si le corps est très conducteur et/ou très gros, les réponses inductives masqueront l'effet IP. Cela permet d’expliquer pourquoi les modèles de Bell Allard, Bracemac et McLeod, dans le cas où les structures contrôlant la minéralisation avec les propriétés PP, ne peuvent être détectées par la méthode MT.

La deuxième partie de cette thèse vise à caractériser la géologie et les structures à partir de l’analyse des sondages magnétotelluriques. Les sondages MT ont été effectués sur le flanc sud de Matagami. Des sondages gravimétriques et magnétiques ont également été effectués dans cette région. Le Titan-24 a été utilisé afin de recueillir les données MT pour Xstrata Zinc. Des données ont été acquises sur plus de 1297 stations et 22 profiles. En traitant les données MT à partir des inversions 2D, les structures sous-terraines peuvent être cartographiées. Toujours avec les résultats des inversions 2D, il est possible de construire un modèle 3D grâce à des interpolations. Ensuite, une modélisation 3D MT a été faite pour vérifier la qualité des inversions 2D dans un cas 3D.

Tout d'abord, la dimension géologique a été déterminée en appliquant les méthodes de Bahr, Groom et Bailey, de la tenseur impédance ainsi que d'autres méthodes qui seront discutées dans le chapitre 3. La méthode de Bahr décrit la dimensionnalité comme étant une composition 3D/1D2D, 3D/2D et 3D. L'invariant WAL nous indique que les structures sous-jacentes de la région sont de type 3D. Les méthodes de Q-Bahr classent également la dimensionnalité comme étant le plus probablement de type 3D ou alors 3D/2D. Le logiciel fourni par Torquil Smith (Smith, 1995) a été utilisé pour déterminer la direction principale des structures régionales. Par la suite, les données ont été traitées en utilisant le code d'inversion 2D de Macie utilisé dans le logiciel Winglink (Rodi et Mackie, 1998). L’inversion MT 2D Mackie utilise la méthode de régularisation de Tikhonov non linéaire associée aux gradients conjugués. Suivit de cela, les résultats des inversions 2D ont été combinés en utilisant UBC meshtool3d (Shekhtman, UBC, 2007) afin de pourvoir visualiser les structures sous-terraines de la région en 3D. Cela permet d'identifier les structures principales, les similitudes et les changements entre les profils (coupes 2D). Les inversions ont compris entre 200 et 1000 itérations par profile et se sont arrêtées lorsqu'elles ne convergeaient plus ou avaient atteint l’erreur rms minimale définie.

Les résultats des inversions MT 2D ont été validés avec la modélisation MT 3D. Le logiciel UBC meshtool3d (Shekhtman, UBC, 2007) a été utilisé pour combiner les résultats d'inversion 2D en un même modèle 3D. Trois modèles 3D ont été créés, correspondant aux trois différentes mesures prises au cours du processus d'inversion MT 2D. Ensuite, les réponses MT ont été calculées à partir de ces modèles 3D et comparées avec les sondages du Titan 24. À partir de ces résultats, on constate que les courbes de résistivité pour des fréquences inférieures à 3 Hz et supérieure de 50 Hz s'ajustent bien aux résultats si l'effet du décalage statique est inclus, tandis qu'entre 3 Hz et 50 Hz, les réponses du modèle 3D n'ajustent pas bien aux données MT. Le maximum des réponses MT 3D se localise entre 3 Hz et 10 Hz alors que les données de sondage MT montrent que les points maximum se localisent entre 10 Hz et 50 Hz. Considérant que le code de modélisation MT 3D est limité par le maillage et que les conditions frontières sont mal connues, les modèles peuvent être considérés comme une représentation géologique réaliste/relativement réaliste/raisonnable de la région. Une inversion 3D complète doit donc être effectuée afin de vérifier le résultat.

L'analyse des données de sondage MT provenant du flanc sud de la région de Matagami a permis de montrer une forte présence de distorsions et de bruits dans les données . Nous avons aussi observé que la région de Matagami, là où le sondage MT a été pris, peut être interprétée comme une superposition de trois couches distinctes. La première couche peut être associée à des morts-terrains, moyennement résistante. L'épaisseur des morts-terrains et de la couche varient de 0 m à 300m. La deuxième couche peut être associée aux gabbros et basaltes. Le gabbro et le basalte peuvent atteindre environ 1 à 1,5 km de profondeur et 2 km dans certaines régions. Finalement, la troisième couche est associée à la rhyolite. Les profils MT font environ 5 km de longueur ; ainsi, au-delà de 5 km de profondeur, la résolution de l'inversion 2D se trouve diminuée. On propose le modèle 1D produit par Tournerie et Chouteau (1998) pour modéliser les régions plus profondes que 5 km. Dans les figures 6-15 et 6-16, les structures verticales se trouvent à partir d'une profondeur d'environ 1.5 km. Ces structures pourraient correspondre à des digues similaires à celles qui se trouvent dans la région de Matagami. Ces digues pourraient être reliées aux roches ignées, volcaniques extrusives ou intrusives. Elles pourraient être extrusives si du magma chaud circule à la surface sous forme de lave ou intrusive si le magma n'a jamais pu faire surface. Respectivement, ce magma pourrait avoir fourni du basalte ou du gabbro, deux types de roche dominante dans la région de Matagami.

Les résultats des analyses MT ont été comparés avec la topographie, l'épaisseur du mort-terrain, les anomalies magnétiques et gravimétriques et les anomalies PP; de fortes corrélations avec les modèles 3D MT ont été observées. Les structures discriminées par la MT sont bien corrélées avec la topographie. L'épaisseur du mort-terrain est reliée aux structures ayant une résistivité de magnitude inférieure ou égale à 10^3 $\Omega\cdot$m ; de fait seule le produit conductivité-épaisseur est bien déterminé ($\sigma t \sim 0.3$ Siemens). De même, cette corrélation a été observée pour le levé gravimétrique. La comparaison entre les anomalies magnétiques et les résultats MT n'a pu mettre en évidence de fortes corrélations. Des structures verticales semblent être mises en évidence par le traitement des données MT à des profondeurs supérieures à 1.5 km. Ces structures géoélectriques pourraient être reliées aux dykes de même orientation mis en évidence par les anomalies magnétiques.

Les anomalies PP (figure 6-19) sont reliées aux structures de haute résistivité. En effet, l'interprétation des modèles 3D produits par l'inversion 2D et par la résistivité apparente et l'invariant de phase le confirment. Ces structures du socle pourraient contenir une faible dissémination en sulfures qui, couplée avec la forte résistivité des formations, générent ainsi les anomalies de PP. Ces anomalies PP peuvent également être causées par l'altération des minéraux situés dans la région. Ainsi, nous recommandons que certains forages soient effectués dans ces zones de haute résistivité, particulièrement là où se trouvent les anomalies PP (figure 6-19) afin de mieux discriminer la source de ces anomalies.

En conclusion, les objectifs de cette thèse étaient de mettre au point des techniques de prospection des corps minéralisés et de structures avec des effets IP avec la méthode MT, et de discriminer les différentes structures géologiques de la région de Matagami à partir des sondages MT. Motivés par le besoin de trouver de nouvelles façons de détecter les gisements à grande profondeur, des modèles possédant des propriétés qui représentent les gisements et les roches

encaissantes connus dans le camp minier de Matagami, ont été crées. Occam 2D, un programme de modélisation 2D MT, a été modifié afin d'inclure la résistivité complexe variant avec la fréquence. Le modèle de Cole-Cole a été utilisée pour générer l'effet de la dispersion (ou effet de polarisation provoquée). En outre, la modification du programme a été validée en comparant les résultats de modélisation avec les solutions analytiques.

L'effet de polarisation provoquée (PP) ne permet pas de mieux détecter ou localiser les gisements par la méthode MT, à moins que les gisements ne se trouvent à une profondeur plus faible que leur taille. Les propriétés PP du corps influencent énormément la réponse MT. Ayant une plus grande chargeabilité (m) et un constant de temps (τ), la polarisation provoquée (PP) produit un effet plus prononcé sur la réponse MT.

L'analyse des données de sondage MT provenant du flanc sud de la région de Matagami, a permis de mieux comprendre les structures géologiques et de faire des liens entre la MT d'une part, et la topographie, l'épaisseur du mort-terrain, les anomalies magnétiques et gravimétriques et les anomalies PP d'autre part. Le traitement des sondages MT a été fait à partir des inversions 2D. Les résultats des inversions 2D ont été ensuite interpolés afin de construire un modèle 3D. Une modélisation 3D MT a été menée à bien pour vérifier la qualité des inversions 2D dans un cas 3D. Les résultats ont été satisfaisants pour les données MT dont les réponses MT modélisées ressemblent fortement aux sondages observés. De plus, de fortes corrélations ont été remarquées avec la topographie, l'épaisseur du mort-terrain, les anomalies gravimétriques et magnétiques et les anomalies PP.

En recommandation, l'inversion 3D MT est fortement recommandée pour à fin de comparaison avec nos modèles 3D. Un objectif à plus long terme serait d'inclure la correction d'effet statique dans un code d'inversion MT 3D. La minimisation du temps de calcul est également une autre possibilité à explorer. Finalement un code d'inversion MT, 2D ou 3D, qui intègre des distributions de résistivité complexe peut aider à mieux représenter la réponse électrique des structures géologiques.

TABLE OF CONTENTS

LIST OF TABLES

LIST OF FIGURES

LIST OF ACRONYMS AND ABBREVIATIONS

i	Imaginary numbers
c	Decay spectrum flatting factor
m	Intrinsic Chargeability
AMT-MT	Audiomagnetotelluric-Magnetotelluric
EM	Electromagnetic
IP	Induced polarization
MT	Magnetotelluric
PT	Phase tensor
T	Tipper
TDEM	Time domain electromagnetic
TE	Transverse electric
TM	Transverse magnetic
UTM	Universal Transverse Mercator
g	Groom and Bailey distortion gain value
ϕ_t	Groom and Bailey distortion twist value
ϕ_c	Groom and Bailey distortion shear value
ϕ_s	Groom and Bailey distortion anisotropy value
$g_{1,2}$	Smith distortion gain parameters
$\phi_{1,2}$	Smith distortion angle parameters
κ	Swift skew
μ	Phase difference in MT tensor
η	Regional skew or phase sensitive skew
Σ	Relation with 2D Dimensionality

$I_{1,2,3,4,5,6,7}$	WAL invariant parameters
$\Theta_{Distortion}$	WAL distortion angle (deg.)
θ_{Strike}	Regional strike direction (deg.)
M	Magnetotelluric tensor matrix
R	Rotational matrix
R^T	Tranpose of the rotational matrix
S	Singular matrix
Φ	Phase tensor matrix
B	Magnetic field (Tesla)
E	Electric field (mV/km))
ε_O	Electric permittivity of free space (F/m)
μ_O	Magnetic permeability of free space (H/m)
J_f	Free current density (A/m^2)
Σ	Conductivity (S/m)
ρ	Resistivity (Ω·m)
ρ_{DC}	DC resistivity (Ω·m)
ρ_{IP}	Induced polarization resistivity (Ω·m)
δ	Skin depth (m)
ω	Angular frequency (radians/s)
τ	Time constant (s)
Z	Impedance (Ω)

LIST OF APPENDICES

INTRODUCTION

A very different approach to traditional prospecting of near-surface bodies is needed for the exploration of ore bodies at depths in excess of 300 m (and up to 2500 m). A traditional strategy consists in carrying out airborne electromagnetic (EM) surveys followed by ground EM/electrical (IP) surveys. Those surveys have usually a maximum depth of investigation of 250-300 m with a possible extension of up to 500 m using large loop Time-Domain EM methods. Beyond that depth another strategy has to be used, which consists of exploring with audiomagnetotelluric-magnetotelluric (AMT-MT) soundings. The method has a theoretical exploration depth of 300 m to >3000 m for the frequency range 0.1-10,000 Hz in the resistive geological environment of the Canadian Shield. Following a first exploration, phase anomalies caused by large conductive targets are located and boreholes drilled to intersect the targets. Downhole 3-component time domain electromagnetics (TDEM) surveys are then performed to extend the range of investigation to 100-150 m around the hole to detect any missed targets and to orient the location of the next borehole to be drilled. A critical step with this strategy is interpreting the MT data. The ore bodies are very small 3D targets at the investigated depths. The responses will depend on the orientation of the sensors; topography and variable overburden conditions will in addition generate effects known as “galvanic distortions” that alter and sometimes mask the expected target responses.

Some techniques were developed to correct those distortions up to a certain point. Once done the corrected data is usually interpreted using 2D inversion which is an acceptable approximation of the 3D ore bodies if they are elongated in one direction. Already up to this point the corrections done might have reduced or eliminated the anomalies searched for in exploration because some conductive bodies at intermediate depths can cause galvanic distortion effects similar to overburden and topography. This series of processing and interpretation requires strong expertise and experience from the interpreter (geophysicist) requested to select targets for drilling. Interpretation also requires simultaneously taking into account numerous MT parameters for each sounding with typical MT surveys including 100 to 600 sounding sites. This thesis aims to see if inductive bodies with induced polarization (IP) effects increase the detection capabilities and attempts to shed more light on phase anomalies that have been found to correlate with chargeability anomalies.

CHAPTER 1 RESEARCH OBJECTIVES

1.1 Matagami background

Matagami is located directly west of Chibougamau on the north side of the Abitibi greenstone belt and it is part of the Superior Province of the Canadian Shield. It is in the province of Quebec, within the UTM zone 18U (NAD 83) and part of the James Bay Corridor district. It is accessible by air and ground transportations. Zinc and copper are the principle ores mined at Matagami. The ore bodies lie above structures controlling the mineralization such as faults and marker layer (i.e. such as exhalites for volcanogenic massive sulfides,VMS, and Key Tuffite for massive sulfides) and surrounded by dominant basalt and rhyolite. The general structures, along with the Key Tuffite horizon, are aligned between N 45° W and N 60° W with a dip of 30° to 55° SW (Jenny, 1961). Another study demonstrated the principal regional structure as an anticline plunging toward the west direction with dip ranging between 40° and 60° south (Gwilym, 1975).

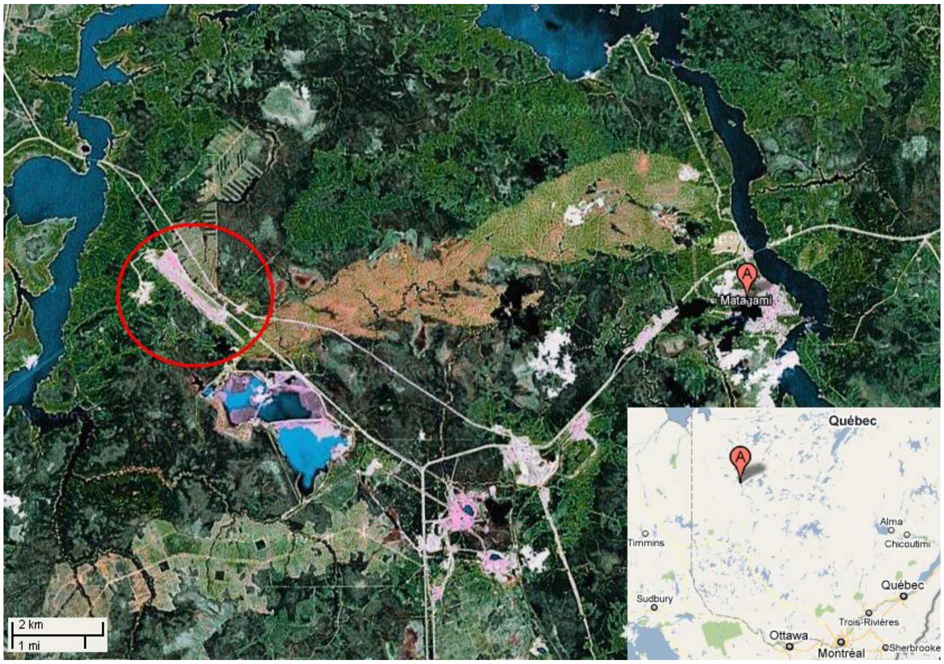

Figure 1-1 : Satellite picture showing the location of Matagami city with respect to the Capital of Canada, Ottawa and larger cities such as Montreal and Quebec. The Matagami airport is circled in red while the red tag A denotes Matagami city. Image provided by Google Maps Inc.

In a study using the seismic reflection method to assess its usefulness in mapping the lithology showed that the base where the mineralization lies has a dip of S45W with a strike of N130W over a distance of 20km (Adam et al., 1998). This was done with the seismic method in the south flank of the Galinée anticline. Resolving the Key Tuffite through the seismic method was impossible, therefore they used the seismic methods to image the base of the Wabassee Group, which is where the Key Tuffite are usually deposited. Another seismic study was done over the Bell Allard mine (Calvert and Li, 1999). This study showed that the massive sulfide deposits seem to be located at a depth of 900 m and 1150 m which coincides with the results provided by the drilling and the mining activities. The geological structures have a dip of around 50^o facing southern direction.

1.2 Motivation of this Thesis Work

Xstrata Zinc has already begun the construction of the Bracemac-McLeod Mine while the Perseverance Mine is near the end of its life. It is critical to find additional ore bodies that could contain ores such as zinc in the Matagami region. This situation pushes the company toward the exploration of deep sulfide orebodies.

In a preliminary project (Boulanger and Chouteau, 2007) done in collaboration with Xstrata (formerly Falconbridge), typical bodies from Matagami, Raglan and Rouyn-Noranda mining camps were defined and modeled using 3D numerical modeling software. The method used was the magnetotelluric and the results of the project were: (1) an isolated conductive massive body can be detected at a depth of about the average size of the body. For example, a body 100 x 100 x 100 m can be detected at a depth of about 100-150 m, (2) it was also shown that MT is sensitive to small resistivity variations and that alteration around the massive bodies makes them detectable to a larger depth, (3) the detection capability of the MT reaches as little as 100-150m for Raglan type ore bodies and 300m for VMS type.

Part of this thesis aims toward studying the MT detection capability of ore bodies and VMS with induced polarization (IP) effects. It was brought to our attention by exploration companies prospecting in the Abitibi sub-province that deep IP and MT data seem to be correlated. Correlation was noted between the chargeability magnitude obtained from IP surveys and the low-frequency impedance phase from coincident MT surveys (figure 1-2). M. Allard suggests that there could be some correlation between the IP MT inversion done using the IP inversion software from UBC and the phase invariant at 1 Hz. We will model the massive ore bodies prospected for at various depths in the Canadian Shield. We will also model the Raglan, the Bracemac and the Mcleoid mine with structures controlling the mineralization such as the Key Tuffite with IP effect.

Gravity, magnetic and magnetotelluric surveys were done in the Southern flank region of Matagami. The second part of this thesis aims toward uncovering the geological features and structures by means of interpreting magnetotelluric soundings. The Titan-24 survey MT data collected for Xstrata Zinc will be used. First we will determine the geological dimensionality and the strike direction. Secondly, we will treat the data through 2D inversion. The results generated by the 2D inversion will be used to created 3D models that will be used to compare with the survey data through 3D forward response.

This thesis is divided in 7 chapters. Chapter 1 explains the goals of this thesis. Chapter 2 provides a general understanding of the magnetotelluric method. Chapter 3 discusses different methods for characterizing the geoelectric dimensionality of a MT survey. Chapter 4 determines the resistivity of different rock types by means of borehole analysis. Chapter 5 studies the MT sensitivity in detecting disseminated mineralization associated with alteration zones at depths and the mechanism for the relationship between those phase anomalies and inductive properties. Chapter 6 contains all the data treatments (i.e. the dimensionality, the strike angle and the 2D inversion) for the Titan 24 survey data and discussions about any findings regarding the geological features and structures. Finally chapter 7 validates the results from the 2D inversion by interpolating 2D inversion models into a 3D model, and compares the MT response of this 3D model with the survey data.

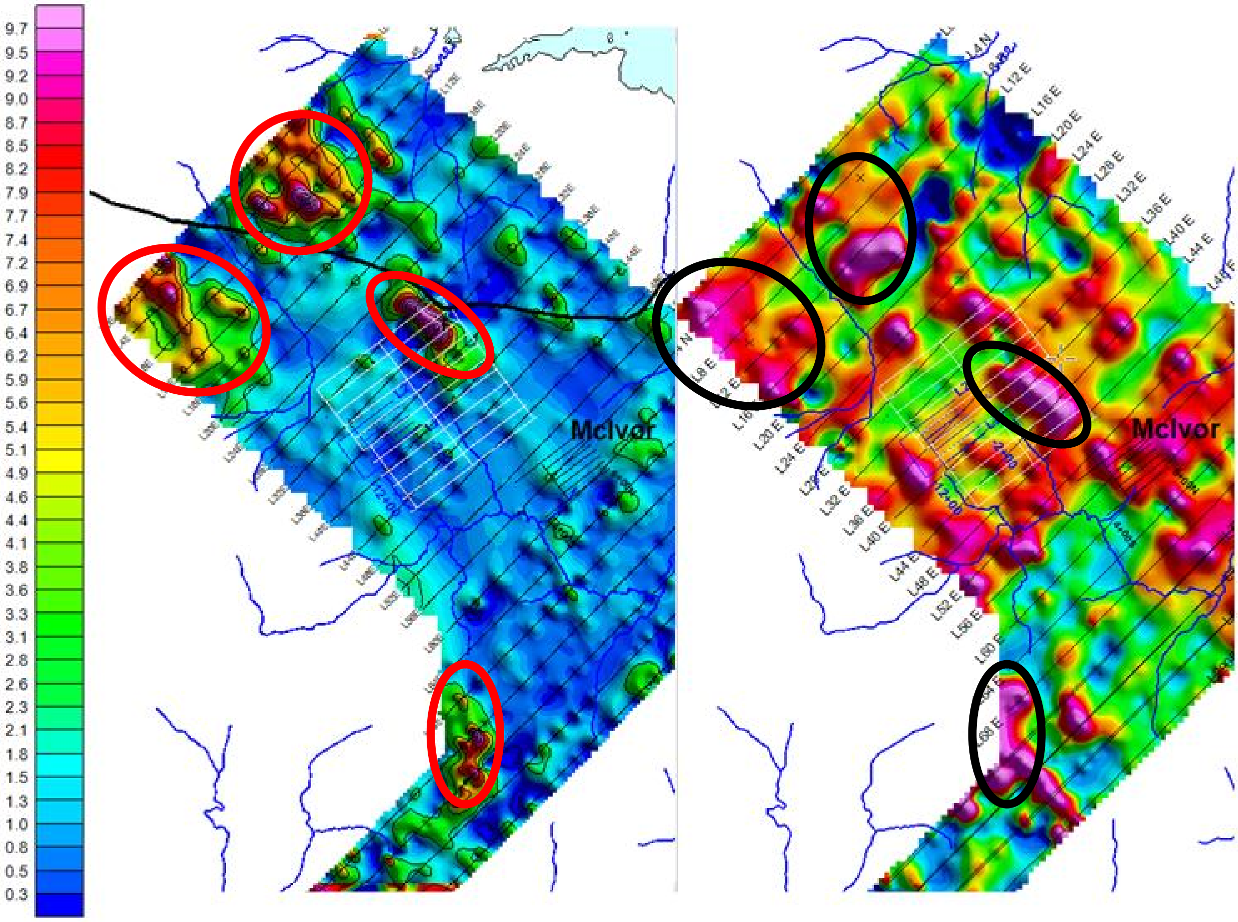

Figure 1-2 : Left: IP measured with the Titan-24. Result of the UBC inversion at 100m depth view. Right: Phase invariant at 1 Hz. Note the correlated regions circled in both maps. Picture provided by M. Allard, senior geophysicist of Xstrata Zinc.

CHAPTER 2 MAGNETOTELLURIC METHOD

The magnetotelluric method is a technique that utilizes the naturally occurring electric E and magnetic B fields in order to determine the resistivity distribution of the subsurface. The fields are measured in orthogonal directions at the earth's surface. The sounding depth can reach several hundred thousand meters and is thus very versatile for mapping deep structures.

The magnetotelluric method can provide information in area where seismic method is unavailable. A signal transmitter is not required as the source of the magnetic and electric fields are produced by the planet Earth. The MT method also has the advantages of using portable equipment and providing a better resolution than other methods (i.e. gravititational or magnetic methods). Their interpretations procedures have been in constant development allowing faster interpretation and can be accessed almost anywhere while leaving little impact on the environment. As with any other exploration techniques, the MT method has its own difficulties. Naturally occurring signals are irregular and they are sensitive to industrial noise and conductors. Its resolution is less than the seismic method, the data processing and interpretation are complex and the inversion process relies on smooth models.

There are several dominant power sources that generate the time-varying EM fields. Micropulsations provided from the interaction between the solar winds and the earth's magnetic fields create frequencies lower than 10 Hz (10^{-1} s and more). Another dominant power source is the atmospheric discharge of electricity such as the lightning, which occurs as many as 16 million times per year (National Weather Service, 2007). Thunderstorms produce EM fields in the frequency band [1 Hz – 50 KHz] which can be transmitted at huge distances. Since a constant-flow of power is important, it is favorable to record MT data during times when thunderstorms are the most active and during periods when sunspots are the most abundant. An increase in solar activity (more sunspots) produces more and greater solar wind by ejecting ionized particles from the surface of the sun away into space. Figure 2-1 shows the historical count of sunspots per year as well as future predictions.

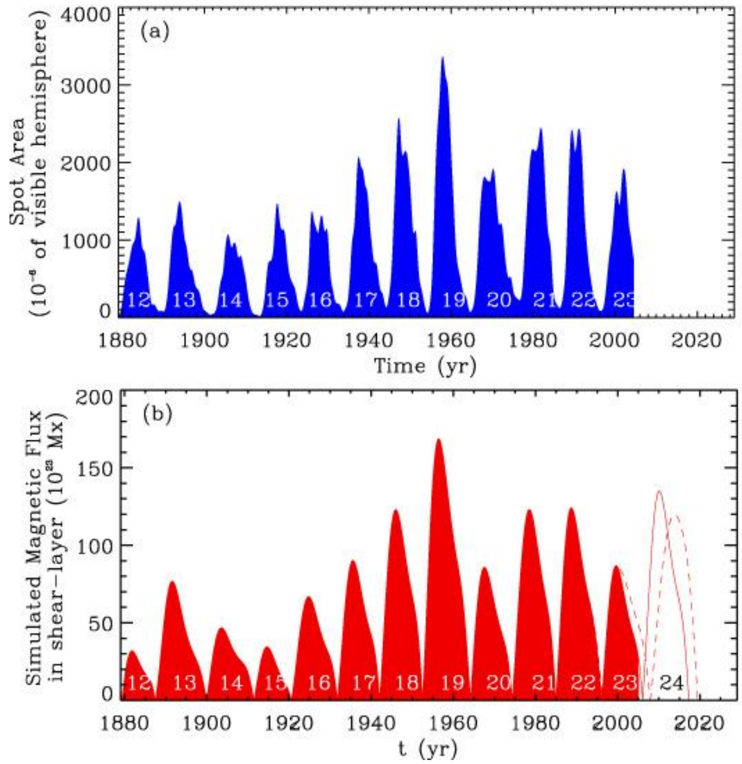

Figure 2-1 : Sunspot predictions by Mausumi Dikpati, Peter Gilman, and Giuliana de Toma, NCAR.

2.1 Theory (Homogeneous half-space)

The magnetotelluric method is based upon Maxwell's equations of electromagnetic theory. In a linear medium, the classical electrodynamic equations take the following form. Note that SI units (and not CGS) are used.

Faraday's law
$$\nabla \times E = -\frac{\partial B}{\partial t} \tag{2.1}$$

Gauss's law
$$\nabla \cdot E = \frac{1}{\varepsilon}\rho \tag{2.2}$$

Ampere's law
$$\nabla \times B = \mu\left(\sigma \cdot J + \varepsilon \frac{\partial E}{\partial t}\right) \tag{2.3}$$

$$\nabla \cdot B = 0 \tag{2.4}$$

Equation 2.1 dictates that a changing magnetic field induces an electric field.

Equation 2.2 dictates that the electric flux through any closed surface is proportional to the enclosed electric charge.

Equation 2.3 dictates that a changing electric field induces a magnetic field.

Equation 2.4 dictates that there are no point sources for the magnetic field B.

In materials that are subject to electric and magnetic polarizations, the interior of the polarized matter will be free of bound charge and current. The ampere law equation (equation 2.3) can be rewritten as follows in terms of free charges (ρ_f) and free currents (J_f). Gauss's law for matter and Ampere's law for matter, respectively, are given below:

$$\nabla \cdot D = \rho_f \tag{2.5}$$

$$\nabla \times H = J_f + \frac{\partial D}{\partial t} \tag{2.6}$$

Aside from Maxell's equations, we have Ohm's law (equation 2.7) and two relationships that will be useful in a linear isotropic medium (equation 2.8 and 2.9).

$$B = \mu H \tag{2.7}$$

$$D = \varepsilon E \tag{2.8}$$

$$B = C_0 e^{-ikz} + C_1 e^{ikz} \tag{2.9}$$

The conductivity, σ (S/m), the permeability, μ (H/m), and the permittivity, ε (F/m), are the intrinsic properties of the materials throughout the medium.

2.1.1 E-field and H-field formulation in a uniform half-space

The earth is modeled as a uniform half-space. Taking the curl of Ampere's law (equation 2.3) gives equation 2.10. This new equation describes the characteristic of a diffusive wave in a conductive medium.

$$\nabla \times (\nabla \times B) = \mu\left(\sigma \frac{\partial B}{\partial t} + \varepsilon \frac{\partial^2 B}{\partial^2 t} \right) \tag{2.10}$$

Equation 2.10 can be simplified down with angular frequency and imaginary number. This gives equation 2.11 called the Helmholtz equation.

$$\nabla^2 B = \left(i\sigma\mu\omega - \varepsilon\mu\omega^2\right)B = \left(k^2 - \kappa^2\right)B \tag{2.11}$$

In a homogeneous medium, the quasi-static assumption makes the constant k dominate over κ (as σ >>εϖ) at low frequencies (long periods). This leads to equation 2.12 and equation 2.13 that are derived, respectively for the E-field and B-field, by taking into account the non-existence of charge and current in a homogeneous half-space 1D medium. These two equations are known as the diffusion equations for EM fields.

$$\left(\nabla^2 - k^2\right)B = 0 \tag{2.12}$$

$$\left(\nabla^2 - k^2\right)E = 0 \tag{2.13}$$

The diffusion equations are the sought-out solutions of the EM fields from Maxwell's equations and they are the key to understanding the MT method. These show that MT measurements rely on a source of energy that exponentially dissipates throughout a medium (the earth). Solutions to equations 2.12 and 2.15 have the following exponential form:

$$B = C_0 e^{-ikz} + C_1 e^{ikz} \tag{2.14}$$

$$E_x = C_2 e^{-ikz} + C_3 e^{ikz} \tag{2.15}$$

C_1, C_2, C_3 & C_4 are constants. The first term describes the downward-traveling waves and the second term describes the forward-traveling waves. By applying the curl to equation 2.6 and going through the same process as above, the magnetic field in a medium containing no electric or magnetic sources is written as follows:

$$H_y = \frac{k}{\omega\mu}\left(C_4 e^{-ikz} - C_5 e^{ikz}\right) \tag{2.16}$$

2.1.2 Skin Depth

The penetration depth (δ ~ meters) of the fields at which they have fallen off to e^{-1} of their original values at the surface is defined by the inverse of the real part of the value k from the Helmholtz equation (equation 2.11). The skin depth is defined as follows (equation 2.18) and is approximated into equation 2.19:

$$k^2 = i\sigma\mu\omega = \sigma\mu\omega \cdot e^{-i\frac{\pi}{2}} \tag{2.17}$$

$$\delta = \frac{1}{k} = \sqrt{\frac{2}{\sigma\mu\omega}} \tag{2.18}$$

$$\delta \approx 503\sqrt{\rho \cdot \mathrm{T}} \tag{2.19}$$

Where ρ represents the resistivity (Ω·m) and T represents the period seconds. As long as the recording time (period) is sufficiently long, any depth can be measured by the magnetotelluric method.

2.1.3 Apparent Resistivity and Phase

The electrical impedance (Z ~ Ω) can be defined as the ratio of the electric to the magnetic fields (equation 2.20), while the apparent resistivity (ρ ~ Ω ·m) can be defined as the scaled magnitude to the square of the impedance (equation 2.21):

$$Z_{xy}(\varpi) = \frac{E_x(\omega)}{H_y(\omega)} = \frac{\omega\mu}{k} \tag{2.20}$$

$$\rho_{app,xy}(\varpi) = \frac{1}{\varpi\mu_o}\left|\frac{E_x(\omega)}{H_y(\omega)}\right|^2 \tag{2.21}$$

For a homogenous uniform half-space, the phase is simply the argument of the impedance Z_{xy}.

$$\varphi_{xy}(\varpi) = \arg(Z) = \arg\left(\sqrt{\frac{\omega}{\sigma\mu}} \cdot e^{i\frac{\pi}{4}}\right) = 45^o \tag{2.22}$$

Because the E-field and the H-field are perpendicular to each other, the angle should therefore be 45^o.

2.2 MT Dimensionality

In section 2.1, the MT method was described thoroughly. In this section, the 1D, 2D and 3D model's magnetic tensor will be described and their apparent resistivity and phase will be calculated analytically.

2.2.1 Impedance & Magnetotelluric Tensors and Transfer Function

The impedance tensor relates the orthogonal electric (E) and magnetic (H) field components to each other's.

$$\begin{pmatrix} E_x \\ E_y \end{pmatrix} = \begin{pmatrix} Z_{xx} & Z_{xy} \\ Z_{yx} & Z_{yy} \end{pmatrix} \begin{pmatrix} H_x \\ H_y \end{pmatrix} \tag{2.23}$$

The MT tensor relates the same thing but utilizes the B-field instead of the H-field to describes this relationship ($Z = \mu_o M$ and $B = \mu_o H$). The impedance or the MT tensors are both dependent on the angular frequency $\omega = 2\pi$ f.

$$\begin{pmatrix} E_x \\ E_y \end{pmatrix} = \begin{pmatrix} M_{xx} & M_{xy} \\ M_{yx} & M_{yy} \end{pmatrix} \begin{pmatrix} B_x \\ B_y \end{pmatrix} \tag{2.24}$$

The apparent resistivity and the impedance phase are then calculated using the following formulas, respectively:

$$\rho_{app}(\varpi) = \frac{\mu_o}{\varpi}|M(\omega)|^2 \tag{2.25}$$

$$\varphi(\varpi) = arcTan\left(\frac{\mathrm{Im}(M(\omega))}{\mathrm{Re}(M(\omega))}\right) \tag{2.26}$$

The transfer function is the tipper vector and it is defined as the relation between the vertical and the two horizontal components of the magnetic field.

$$B_x(\varpi) = \begin{bmatrix} T_x(\varpi) & T_y(\varpi) \end{bmatrix} \cdot \begin{bmatrix} B_x(\varpi) \\ B_y(\varpi) \end{bmatrix} \tag{2.27}$$

The tipper, T, is a dimensionless magnitude of the complex vector and is decomposed into two real vectors, called induction vectors/arrows. These vectors are in the xy plane and represent the projection of the vertical magnetic field in this xy plane. They indicate the lateral variations in the conductivity. The induction arrows can be calculated using the following equations:

$$M_{real} = \sqrt{\mathrm{Re}(T_x)^2 + \mathrm{Re}(T_y)^2} \tag{2.28}$$

$$M_{imaginary} = \sqrt{\mathrm{Im}(T_x)^2 + \mathrm{Im}(T_y)^2} \tag{2.29}$$

$$\theta_{real} = arcTan\left(\frac{\mathrm{Re}(T_y)}{\mathrm{Re}(T_x)}\right) \tag{2.30}$$

$$\theta_{imaginary} = arcTan\left(\frac{\mathrm{Im}(T_y)}{\mathrm{Im}(T_x)}\right) \tag{2.31}$$

2.2.2 The 1D Case

In the case where the conductivity varies only with depth, the MT transfer function remains the same throughout any depth and any orientation. In fact, because the incidences of these EM fields are considered to be perpendicular to the surface and do not change direction with depth, the tipper components are zero. The MT tensor becomes a non-diagonal vector with its two components equal to the modulus but with opposite signs:

$$M_{1D}(\omega)=\begin{pmatrix} 0 & M_{xy}(\omega) \\ M_{yx}(\omega) & 0 \end{pmatrix} \tag{2.32}$$

$$M_{xy}=-M_{yx} \tag{2.33}$$

The apparent resistivity and phase are:

$$\rho_{app}(\varpi)=\rho_{xy}(\varpi)=\rho_{yx}(\varpi)=\frac{\mu_o}{\varpi}\left|M_{xy}(\omega)\right|^2=\frac{\mu_o}{\varpi}\left|M_{yx}(\omega)\right|^2 \tag{2.34}$$

$$\varphi_{xy}(\varpi)=arcTan\left(\frac{\operatorname{Im}(M_{xy}(\omega))}{\operatorname{Re}(M_{xy}(\omega))}\right) \tag{2.35}$$

2.2.3 The 2-D Case

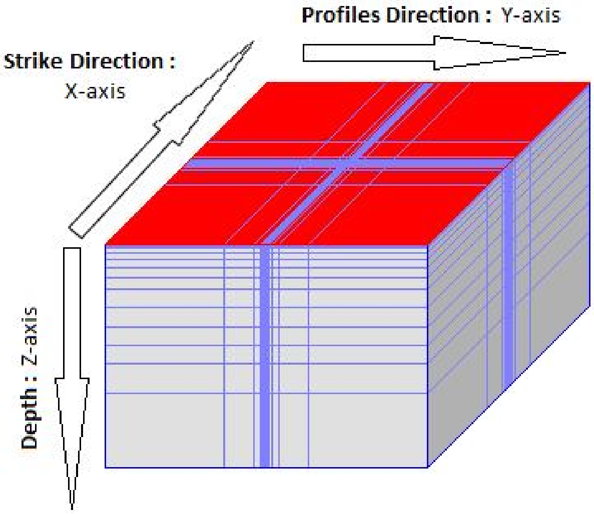

Figure 2-2 : 3D Earth model.

In a 2D Earth model, the conductivity varies along the y-z directions while it remains constant for the x-direction. The x-direction is known as the geoelectrical strike direction, while the y-direction is usually aligned along the measured profile direction. The variation in the conductivity along the y-z direction will induce a vertical magnetic field B_z. Since the conductivity varies along the y-direction, the tipper becomes non-zero and varies along the profile direction (y-direction) in relation to the horizontal component of the magnetic field (H_z / H_y). The tipper is given by:

$$\vec{T}_{2D} = \left(0, T_y\right) = \left(0, \frac{B_z}{B_y}\right) \tag{2.36}$$

In 2D models, we have the xy and yx modes. The xy mode is the transverse electric TE (E_x, B_y, B_z) and its currents are parallel to the strike direction. The yx mode is the transverse magnetic (B_x, E_y, E_z) and its currents are perpendicular to the strike direction.

The MT tensor in 2D models is again a non-diagonal matrix and is written as follows:

$$M_{2D}(\omega) = \begin{pmatrix} 0 & M_{xy}(\omega) \\ M_{yx}(\omega) & 0 \end{pmatrix} = \begin{pmatrix} 0 & M_{TE}(\omega) \\ M_{TM}(\omega) & 0 \end{pmatrix} \tag{2.37}$$

The direction is usually not known beforehand. Consequently the measurements are usually taken as perpendicular as possible to the guessed strike direction. After completing the sounding, the MT data are rotated to its determined geoelectrical strike angle. The rotated MT tensor and tipper are computed using the following equations:

$$M_{rot} = R_\theta M R_\theta^T \tag{2.38}$$

$$T_{rot} = R_\theta T \tag{2.39}$$

$$R_\theta = \begin{pmatrix} Cos(\theta) & Sin(\theta) \\ -Sin(\theta) & Cos(\theta) \end{pmatrix} \tag{2.40}$$

The rotation angle (strike angle) can be found by using numerous techniques that will be explained in chapter 3.

2.2.4 The 3-D Case

In a 3D Earth model, the conductivity varies along the x, y, z axis. There will be no strike direction and the MT tensor retains all four components (M_{xx}, M_{xy}, M_{yx} and M_{yy}). Thus the MT tensor and tipper are expressed in equations 2.24 and 2.27 as there is no rotation that will make the MT tensor non-zero on the diagonal.

2.3 Distortion Effect

The distortion effect can be caused by local bodies and/or heterogeneities where their sizes are much smaller than the skin depths. In turn, the regionally induced currents flowing through those bodies results in distortions of the MT data.

Two types of distortion exist:

1. The inductive distortion is created by a current distribution of small amplitude and decays with the time period. It seems that under certain conditions (i.e. $\sigma >> \omega\varepsilon$), the inductive distortion can be ignored (Berdichevsky and Dimitriev, 1976).

2. The galvanic distortion is created by the accumulation of charge on the surface of shallow conductive bodies. The accumulation of charge produces an anomalous EM-field. The magnetic field is weak and can be ignored but the electric field is of the same order of magnitude as the regional part and it is frequency independent (Bahr, 1988).

This anomalous E-field can be express as a 2x2 non-dimensional time-independent matrix:

$$C = \begin{pmatrix} C_1 & C_2 \\ C_3 & C_4 \end{pmatrix} \tag{2.41}$$

The measured MT tensor can be computed as follow:

$$M_{measured} = C \cdot M_{Regional} \tag{2.42}$$

Adding the strike rotation matrix, $M_{Measured}$ becomes:

$$M_{measured} = R_\theta C M_{\mathrm{Re}gional} R_\theta^T \tag{2.43}$$

Groom and Bailey (Groom and Bailey, 1989) proposed a method that involves the combination of four effects to describe the distortion effect: The gain (g), the twist (ϕ_t), the shear (ϕ_e) and the anisotropy (ϕ_s). The latter three, the twist, the shear and the anisotropy effects, can also be define by their tangents t, e and s respectively.

$$C = g\begin{pmatrix} (1+\phi_S)(1-\phi_t\phi_e) & (1-\phi_S)(\phi_e-\phi_t) \\ (1+\phi_S)(\phi_e+\phi_t) & (1-\phi_S)(1+\phi_t\phi_e) \end{pmatrix} \tag{2.44}$$

Smith (1994) proposed a similar methodology to describe the distortion. Similar to Groom's and Bailey's method, four parameters were used: two gain parameters, g_1 and g_2, and two distortion angles, ϕ_1 and ϕ_2.

$$C = \begin{pmatrix} g_1 Cos(\phi_1) & -g_2 Sin(\phi_2) \\ g_1 Sin(\phi_1) & g_2 Cos(\phi_2) \end{pmatrix} \tag{2.45}$$

We can bridge the Groom-Bailey and Smith parameters using the following equations:

$$g_{1,2} = g(1 \pm s) \tag{2.46}$$

$$\phi_{1,2} = \phi_t \pm \phi_e \tag{2.47}$$

CHAPTER 3 GEOELECTRIC DIMENSIONALITY

Magnetotelluric data have been collected in a manner where the sounding MT profile is not perfectly aligned perpendicular to the regional strike direction. Sometime the regional dimensionality of the region is poorly known and quantified. It is important to determine the regional dimensionality and the regional strike in order to properly analyze the MT data.

In this chapter, different methods for characterizing the geoelectric dimensionality of a MT survey are discussed. We introduce methods that allow finding the dimensionality of the survey region and the recovery of the regional tensor. Most methods are based upon the rotational invariant to determine the regional structure dimensionality.

3.1 Introduction to Tensor Rotation

Starting with a pre-introduction, a MT tensor undergoing a rotation of θ can be defined as the following:

$$M_{Rot} = R_\theta \cdot M \cdot R_\theta^T \tag{3.1}$$

For a clockwise rotation the impedance tensors are formulated in the following way:

$$M'_{xx} = M_{xx} \cdot Cos^2(\theta) + M_{yy} \cdot Sin^2(\theta) + \left(M_{xy} + M_{yx}\right) \cdot Sin(\theta) \cdot Cos(\theta) \tag{3.2}$$

$$M'_{yy} = M_{xx} \cdot Sin^2(\theta) + M_{yy} \cdot Cos^2(\theta) - \left(M_{xx} + M_{yy}\right) \cdot Sin(\theta) \cdot Cos(\theta) \tag{3.3}$$

$$M'_{xy} = M_{xy} \cdot Cos^2(\theta) + M_{yx} \cdot Sin^2(\theta) + \left(- M_{xx} + M_{yy}\right) \cdot Sin(\theta) \cdot Cos(\theta) \tag{3.4}$$

$$M'_{yx} = M_{yx} \cdot Cos^2(\theta) - M_{xy} \cdot Sin^2(\theta) + \left(- M_{xx} + M_{yy}\right) \cdot Sin(\theta) \cdot Cos(\theta) \tag{3.5}$$

If the geological structure is 2D, the stations must be rotated to the strike direction (geoelectric structure). The strike angle can be determined using several advanced techniques that correct for galvanic distortion effects developed by Groom and Bailey, (Groom and Bailey, 1989), Smith, (Smith, 1994), and McNeice and Jones, (McNeice and Jones, 2001). Supposedly if a perfect 2D

MT tensor is readily available then the strike direction is determined by setting equations 3.2 and 3.3 to zero. But solving for those equations can be quite tedious when the MT tensor matrix is not diagonalizable. In Vozoff (Vozoff, 1972), an approximation based on the maximization and minimization of the non-diagonal components of the MT tensor is used.

$$\left|M'_{xy}(\theta)\right|^2 + \left|M'_{yx}(\theta)\right|^2 = Maximum \tag{3.6}$$

$$\left|M'_{xx}(\theta)\right|^2 + \left|M'_{yy}(\theta)\right|^2 = Minimum \tag{3.7}$$

$$\theta_{Swift\_Angle} = 0.25 \cdot aTan\left(\frac{2 \cdot \mathrm{Re}(D_1 \cdot S_2)}{|D_1|^2 + |S_2|^2}\right) \tag{3.8}$$

Equation 3.8 is the swift angle (Swift, 1967), where $D_1 = M_{xx} - M_{yy}$ and $D_1 = M_{xy} + M_{yx}$.

3.2 Bahr Parameters

Bahr uses four rotational real-valued invariant parameters in order to classify the geoelectrical dimensionality and distortion type (Bahr, 1991). These parameters were derived from the impedance tensor (Z = μ_oM). Once derived, the parameters are then compared to Bahr's criteria in order to determine the geoelectrical dimensionality as seen in (table 3.1).

$$\kappa = \frac{|S_1|}{|D_2|} \tag{3.9}$$

$$\mu = \frac{([D_1, S_2] + [S_1, D_2])^{\frac{1}{2}}}{|D_2|} \tag{3.10}$$

$$\eta = \frac{([D_1, S_2] - [S_1, D_2])^{\frac{1}{2}}}{|D_2|} \tag{3.11}$$

$$\Sigma = \frac{D_1^2 + S_2^2}{D_2^2} \tag{3.12}$$

$$[A,B] = \mathrm{Re}(A)\,\mathrm{Im}(B) - \mathrm{Re}(B)\,\mathrm{Im}(A) \tag{3.13}$$

$$S_1 = Z_{xx} + Z_{yy} \tag{3.14}$$

$$S_2 = Z_{xy} + Z_{yx} \tag{3.15}$$

$$D_1 = Z_{xx} - Z_{yy} \tag{3.16}$$

$$D_2 = Z_{xy} - Z_{yx} \tag{3.17}$$

$$\tan(2\theta) = \frac{[S_1, S_2] - [D_1, D_2]}{[S_1, D_2] + [S_1, D_2]} \tag{3.18}$$

Dimensionality	κ	μ	Σ	η	Q
1D	< 0.1	-	< 0.1	-	-
2D	< 0.1	-	> 0.1	-	-
3D/2D Larsen	> 0.1	0	-	-	-
3D/1D Bahr	> 0.1	≠ 0	-	< 0.05	-
3D	> 0.1	≠ 0	-	> 0.30	-

Table 3.1 : Dimensionality criteria for the Bahr technique.

η : Regional skew or phase sensitive skew. It is normalized to unity.

κ : Swift skew

μ :Measure of phase difference in MT tensor. It is normalized to unity.

Σ : Relation with 2D dimensionality

3.3 Bahr-Q method

In Table 3.1, a gap can be found between 3D/2D and 3D. The geoelectric dimensionality is undefined when $0.05 < \eta < 0.3$, therefore there are conditions which Bahr can not define. According to Ledo and colleagues, (Ledo et al., 2002), $\eta > 0.3$ is a sufficient condition to define a 3D dimensionality. In the case where $0.05 < \eta < 0.3$, one might misinterpret the Bahr treatment and assume the region to be a continuous 3D/2D. According to Marti et al. (2005), the Bahr method threshold values possess no mathematical or physical connection. By implementing WAL invariants set, which we will see in section 3.4, the Bahr method is improved.

Case	**Dimensionality**	**κ**	**μ**	**Σ**	**η**	**Q**
1	1D	< 0.06	< 0.34	< 0.01	< 0.12	-
2a	2D	< 0.06	< 0.34	> 0.01	> 0.12	< 0.1
2b					< 0.12	-
2c					> 0.12	< 0.1
3a	3D/2D	> 0.06	< 0.34	> 0.01	< 0.12	> 0.1
3b	3D/1D2D				Any	< 0.1
4	3D/2D	> 0.06	> 0.34	> 0.01	< 0.12	-
					> 0.12	< 0.1
5	3D	-	-		> 0.12	> 0.1

Table 3.2 : Dimensionality criteria for the Bahr-Q technique.

3.4 WAL rotational invariant parameters

The WAL invariant is a new formulation of the rotational invariant parameters of the MT tensor (Weaver et al., 2000). But this method is limited to good quality data (i.e. low noise and distortion), and to the condition that the regional dimensionality corresponds closely to a 2D subsurface (Marti et al. 2004). In cases that deviate from the above mentioned criteria, for example distorted data and complex subterranean structures, alternative methods are required for analysis (i.e. Bahr, Torquil Smith, etc...). The WAL invariants are defined so that they are non-dimensional, have good graphical representations, and contain physical interpretation. The WAL invariant decomposes the MT tensor into complex numbers. The following equation defines the MT tensor matrix with its components.

$$M = \begin{pmatrix} M_{xx} & M_{xy} \\ M_{yx} & M_{yy} \end{pmatrix} = \begin{pmatrix} u_1 + u_3 & u_2 + u_4 \\ u_2 - u_4 & u_1 - u_3 \end{pmatrix} + i \begin{pmatrix} v_1 + v_3 & v_2 + v_4 \\ v_2 - v_4 & v_1 - v_3 \end{pmatrix} \tag{3.19}$$

$$I_1 = \sqrt{u_1^2 + u_4^2} \tag{3.20}$$

$$I_2 = \sqrt{v_1^2 + v_4^2} \tag{3.21}$$

$$I_3 = \frac{\sqrt{u_2^2 + u_3^2}}{I_1} \tag{3.22}$$

$$I_4 = \frac{\sqrt{v_2^2 + v_3^2}}{I_2} \tag{3.23}$$

$$I_6 = \frac{u_4 v_1 - u_1 v_4}{I_1 I_2} \tag{3.24}$$

$$I_7 = \frac{d_{41} - d_{14}}{Q} \tag{3.25}$$

$$d = \frac{u_i v_j - u_j v_i}{I_1 I_2} \quad (i, j = 1 - 4) \tag{3.26}$$

$$Q = \sqrt{(d_{12} - d_{34})^2 + (d_{13} - d_{24})^2} \tag{3.27}$$

Case	I1	i2	i3	i4	i5	i6	i7	Q	u4	v4
1D	-	-	0	0	0	0	-	-	-	-
2D	-	-	≠ 0	≠ 0	= 0	= 0	= 0	= 0	≠ 0	≠ 0
3D/2Dtwist	-	-	≠ 0	≠ 0	≠ 0	= 0	= 0	-	-	-
3D/1D or 3D/2D	-	-	≠ 0	≠ 0	≠ 0	= 0	-	= 0	-	-
3D/1D or 3D/2D	-	-	≠ 0	≠ 0	= 0	= 0	= 0	= 0	= 0	= 0
3D/2Dtwist	-	-	≠ 0	≠ 0	≠ 0	≠ 0	= 0	-	-	-
3D	-	-	-	-	-	-	≠ 0	-	-	-

Table 3.3 : Dimensionality criteria for the WAL invariant technique.

Once the invariants are calculated, the geoelectrical dimensionality and the galvanic distortion effects can be examined through WAL criteria (table 3.3). Four different outcomes of galvanic and dimensionality assessments can be obtained, with the fifth as the determination of a 3D medium:

1. A twist in the electric field caused a galvanic distortion over a 2D medium .

2. Equal phase polarization in both E-field and B-field over 1D or 2D medium. The latter strike direction cannot be determined.

3. Special case: A diagonal MT tensor over 1D or 2D medium.

4. General galvanic distortion over 2D medium.

5. MT tensor corresponding to a 3D medium.

In the third outcome, when the galvanic distortion is over a 2D medium and $u_4 = v_4 = 0$, the strike direction can be obtained using equation 3.29 when the distorted diagonal tensor is recovered.

$$\theta_{STRIKE} = 0.5 \cdot aTan\left(\frac{u_2}{u_3}\right) = 0.5 \cdot aTan\left(\frac{v_2}{v_3}\right) \tag{3.28}$$

For the first and the fourth outcomes, the strike angle and the distortion parameters can be computed using the follow formulas.

$$\theta_{STRIKE} = 0.5 \cdot aTan\left(\frac{d_{12} - d_{34}}{d_{13} + d_{24}}\right) \tag{3.29}$$

$$\theta_{Distortion\_1} = aTan\left(\frac{\mathrm{Re}(M'_{yy})}{\mathrm{Re}(M'_{xy})}\right) = aTan\left(\frac{\mathrm{Im}(M'_{yy})}{\mathrm{Im}(M'_{xy})}\right) \tag{3.30}$$

$$\theta_{Distortion\_2} = aTan\left(\frac{\mathrm{Re}(M'_{xx})}{\mathrm{Re}(M'_{yx})}\right) = aTan\left(\frac{\mathrm{Im}(M'_{xx})}{\mathrm{Im}(M'_{yx})}\right) \tag{3.31}$$

The downside of the WAL invariant method is that the invariant values of the sounding data are rarely zero due to the presence of noise. Weaver et al. take this problem into account and suggest that any value equal-to-or-less than 0.1 can be treated as zero (Weaver et al., 2000). This method was tested with a synthetic model of 2% noise and it was consistent.

3.5 MT phase tensor

The phase tensor is another method capable of obtaining information on the geoelectrical dimensionality for distortion free MT data (Caldwell et al. 2004). Because it is not affected by galvanic distortion nor influenced by the conductive structure in the medium, the MT phase tensor is essential in both its usefulness and its robustness. Taking the complex tensor $M = X + iY$, the phase tensor is expressed as:

$$\Phi = X^{-1}Y = \begin{bmatrix} \Phi_{11} & \Phi_{12} \\ \Phi_{21} & \Phi_{22} \end{bmatrix} = \frac{1}{\det(X)} \begin{bmatrix} X_{22}Y_{11} - X_{12}Y_{21} & X_{22}Y_{12} - X_{12}Y_{22} \\ X_{11}Y_{21} - X_{21}Y_{11} & X_{11}Y_{22} - X_{21}Y_{12} \end{bmatrix} \tag{3.32}$$

where $\det(X) = X_{11}X_{22} - X_{12}X_{21}$.

The phase tensor can then be represented through Singular Value Decomposition (SVD) as the product of three matrices: The rotational matrix “R”, the transpose of the rotation matrix “R^T” and the singular matrix “S”.

$$\Phi = R^T \cdot S \cdot R = \begin{bmatrix} Cos(\varphi) & Sin(\varphi) \\ -Sin(\varphi) & Cos(\varphi) \end{bmatrix}^T \cdot \begin{bmatrix} \Phi_{\max} & 0 \\ 0 & \Phi_{\min} \end{bmatrix} \cdot \begin{bmatrix} Cos(\varphi) & Sin(\varphi) \\ -Sin(\varphi) & Cos(\varphi) \end{bmatrix} \tag{3.33}$$

where:

$$\varphi = \alpha_P - \beta_P \tag{3.34}$$

$$\alpha_P = 0.5 \cdot aTan\left(\frac{\Phi_{12} + \Phi_{21}}{\Phi_{11} - \Phi_{22}}\right) \tag{3.35}$$

$$\beta_P = 0.5 \cdot aTan\left(\frac{\Phi_{12} - \Phi_{21}}{\Phi_{11} + \Phi_{22}}\right) \tag{3.36}$$

$$\Phi_{Max} = \left(\Phi_1^2 + \Phi_3^2\right)^{0.5} + \sqrt{\Phi_1^2 + \Phi_3^2 - \det(\Phi)} \tag{3.37}$$

$$\Phi_{Min} = \left(\Phi_1^2 + \Phi_3^2\right)^{0.5} - \sqrt{\Phi_1^2 + \Phi_3^2 - \det(\Phi)} \tag{3.38}$$

$$\Phi_1 = \frac{\Phi_{11} + \Phi_{22}}{2} \tag{3.39}$$

$$\Phi_3 = \frac{\Phi_{12} - \Phi_{21}}{2} \tag{3.40}$$

$$\det(\Phi) = \left(\Phi_{11}\Phi_{22} - \Phi_{12}\Phi_{21}\right) \tag{3.41}$$

$$\Delta\Phi = \sqrt{\left(\Phi_{11} - \Phi_{22}\right)^2 + \left(\Phi_{12} + \Phi_{21}\right)^2} \tag{3.42}$$

$$\lambda = \frac{\Delta\Phi}{\sqrt{\left(\Phi_{11} + \Phi_{22}\right)^2 + \left(\Phi_{12} - \Phi_{21}\right)^2}} \tag{3.43}$$

. Φ_{Max}, Φ_{Max} and $\alpha_P - \beta_P$ are used to graphical represent the phase tensor.

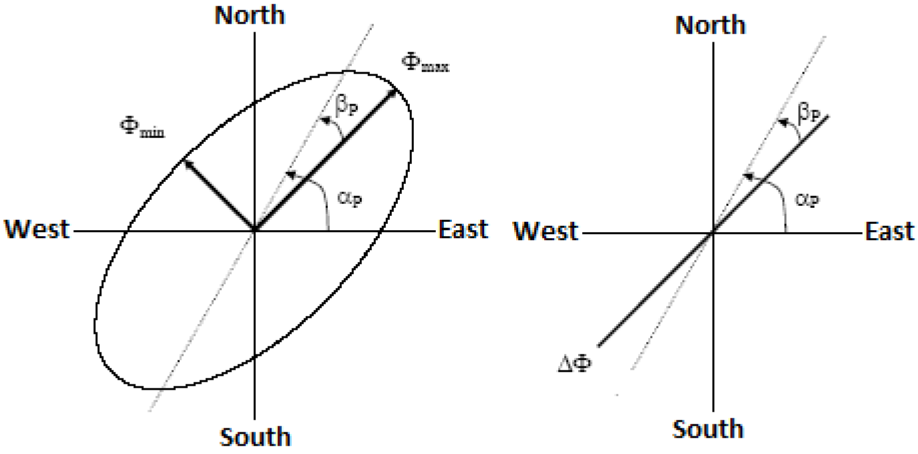

Figure 3-1: Graphical representation of the phase tensor.

Table 3.3 contains all the criteria required for 1D, 2D and 3D cases. In a 1D medium, the graphical representation of the phase tensor is a circle. In 2D, the graphical representation becomes an ellipse with its main axis of length Φ_{Max} and Φ_{Max}. Because β_P is zero in 2D, the strike direction is directly aligned along one of the two axes.

The only condition for being a 3D medium is for $\beta_P > 0$. Like Bahr-Q, the WAL invariant and any other methods, the phase tensor invariant method is not immune to noise contained in MT data. Therefore the PT components and invariants are usually non-zero values. By setting a threshold values for β_P and λ, tolerance for the 2D approximation can be made without diverging far from the real model while working within an acceptable amount of ambiguity.

3.6 Summary

There are several methods that can be used to determine the geoelectrical dimensionality of the geological structure. Bahr (1991) provided a method to determine the dimensionality at its simplest case of 1D, 2D and 3D without having any correlation with the physical properties. Q-Bahr (Marti et al. 2005) was made to adjust the original Bahr criteria in order to take into account the error produced by noise thus allowing a better determination of the geoelectrical dimensionality. The WAL invariants (Weaver et al., 2000) offer better detail on the type of dimensionality than its Bahr counterpart but not as robust as the Q-Bahr method. The WAL invariants also provide real physical interpretation. Lastly there is the phase tensor technique which provides a good graphical representation of the dimensionality, the strike direction and in theory, it is unaffected by galvanic distortions.

Having all these methods does not guarantee an easy determination of the geoelectric dimensionality. Both Bahr methods (Bahr and Q-Bahr) and the WAL invariants are easily affected by galvanic distortions and require correction. The phase tensor is only accurate in determining the dimensionality of MT data that is free from distortion.

To conclude, there are three steps to take into account when determining the dimensionality of the regional structure:

1. The noise errors need to be taken into account and the galvanic distortions need to be corrected;
2. To allow certain elasticity on the criteria limits, as real data rarely matches with theoretical models;
3. To utilize several methods in order to have a broader analysis and to come up with a general conclusion on the regional geoelectrical dimensionality.

CHAPTER 4 BOREHOLE ANALYSIS

4.1 Introduction

The magnetotelluric method utilizes the electrical properties such as conductivity, resistivity and permitivity to determine the MT response (i.e. apparent resistivity and phase). Well-logging data of 13 boreholes located in the Matagami mining campsite were obtained from Xstrata Zinc. Many physical properties were measured such as magnetic susceptibility, point resistance, natural gamma, density, spontaneous potential, temperature, etc. We proceed in analyzing the electrical properties from 13 boreholes but only seven boreholes contain pertinent information that can be used for our modeling purpose. Borehole drilling and analyses were done by the Geological Survey of Canada (GSC), the IFG Corporation and the Quantec Logging Services (QLS).

Borehole #	Ores Deposits	Depth ~ meters	Company	Date
BAS-95-41	Bell Allard South	1038.45	GSC Survey	1996
DJV-03-76	Near Perseverance	440	Quantec Survey	unknown
DJV-03-77	Near Perseverance	690.5	Quantec Survey	unknown
OR-90-14	Orchan West	1442.31	GSC Survey	≈ April 1996
OR-90-14	Orchan West	1442.31	IFG Survey	35034
OR-90-15g	Orchan West	1411.83	IFG Survey	35034
OR-90-16a	Orchan West	1412.14	IFG Survey	35034
OR-90-25	Orchan West	954.94	IFG Survey	35034

Table 4.1 : Borehole descriptions. Note: OR-90-14 was logged by the GSC and IFG

Part of our goal in this project is to create 2D models of subsurface structure of the Matagami mining campsite in order to measure the MT response. Out of the seven boreholes, we utilize only five of them that are from the Orchan mining campsite. The targeted location includes past producers such as the Bell Allard mines, the Isle Dieu mine, the Lac Mattagami mine and the Orchan mine. The model also includes the known deposits located beneath the Orchan West. We utilized 4 Orchan West boreholes to determine the general lithology of the surrounding area. The resistivities of the lithology are estimated from logging done through different companies such as Quantec Survey, GSC or IFG Survey. Details on how the resistivity logging is done can be found in the Geophysical Survey Logistics Report (Coulson et al., 2003).

4.2 Borehole analysis

4.2.1 Boreholes details

For each of the 4 boreholes located at Orchan West, we plot the resistivity of each rock type as a function of depth. While the boreholes are located relatively close to each other (within a kilometer radius), the lithology varies greatly between boreholes. We will be using 7 different types of rock in our modeling, which includes Wabassee basalt, gabbro, Dumagami Rhyolite, Watson Lake Rhyolite, lower basalt, Key Tuffite and massive sulfides. We eliminated thin layers of dyke, quartz, lava, etc. that are not part of the 7 different rock types and replaced them with one of the rock types that best represents their resistivity (Figure 4-1 Left). This new 1D lithology represents the offshoot lithology of those 4 boreholes. Sulfides and ore bodies will be added above the Key Tuffite. This lithology corresponds well to the one given by Xstrata Zinc (figure 4-1 Right) and the seismic data (figure 4-2).

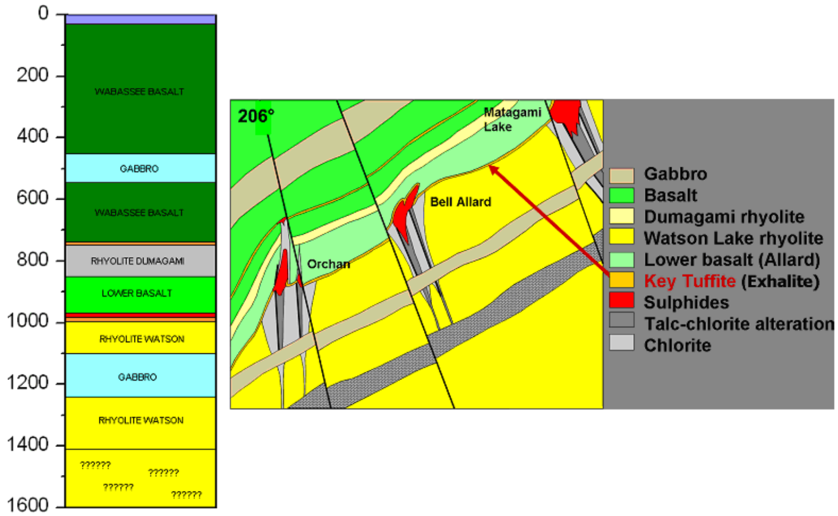

Figure 4-1 : Left: The simplified version of the geological lithology found in the Orchan West boreholes. Right: A model created by Xstrata representing the Orchan mine, Bell Allard and Matagami Lake. Image provided by Michel Allard, senior geophysicist of Xstrata Zinc.

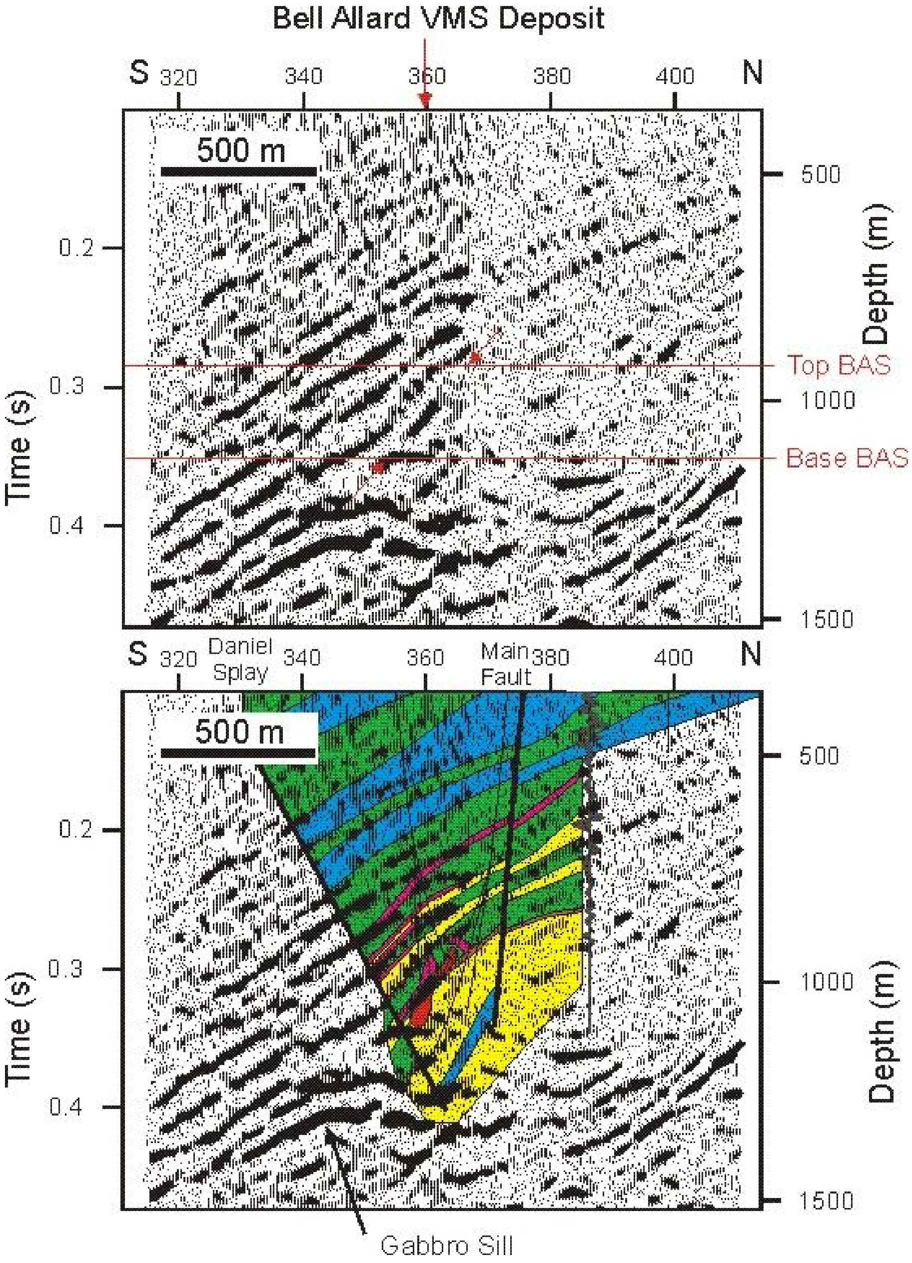

Figure 4-2 : Seismic reflection data (top) of the Bell Allard VMS deposit with the borehole's synthetics seismogram superimposed (bottom). Regions between the horizontal lines (red) mark the location of sulfide found from drill core. **Color coding:** Red: Sulfide, Green: Basalt, Blue: Gabbro, Brown: Key Tuffite, Yellow: Rhyolite. Image provide by Andrew J. Calvert from Simon Fraser University (Calvert and Li, 1999).

4.2.2 Resistivity analysis

By carefully analyzing the resistivity logs, we vigilantly chose the best resistivity value for each of the rock types. The values of the resistivity shown in table 4.2 are calculated by computing the mean and the variance of the resistivity for each rock type at each borehole. We combine the experimental results from the same type of layer for all the boreholes through a process of calculating the new error and the new mean value (equation 4.1 and 4.2).

$$\frac{1}{\sigma_T^2} = \sum_{i=1}^{M} \frac{1}{\sigma_i^2} \tag{4.1}$$

$$\overline{x}_T = \sigma_T^2 \sum_{i=1}^{M} \frac{\overline{x}_i}{\sigma_i^2} \tag{4.2}$$

Rock type	Resistivity	Error	New Resistivity	#	Start	End
	(Ω · m)	(Ω · m)	(Ω · m)		(m)	(m)
Conductive Key Tuffite	533.79	787	534	33	-	-
Resistance Key Tuffite *	34 905.04	0.0025	35 000*	126	-	-
Upper Basalt	12 081.84	0.0003	12 000	1676	0	225
Intermediate Basalt	39 928.83	0.0058	40 000	2293	225	+
Gabbro	31 122.42	0.0025	31 000	3333	75	+
Dumagami Rhyolite *	35 218.61*	0.0006	35 000*	850	-	-
Watson Lake Rhyolite	20 771.86	0.008	21 000	1141	-	-
Sulfides**	--	--	0.1	--	-	-

Table 4.2 : Electrical properties for each rock type. *The Dumagami Rhyolite and the more resistive tuffite have similar resistance. We can regroup them together as a single rock type with a single averaged resistivity value. **The value of the massive sulfide is taken from a progress report (Chouteau and Boulanger, 2007). This value of resistivity for the massive sulfide will be used in our 2D modeling.

The resisitivity of the surface layer (overburden) has been estimated to be approximately 100 Ω·m and its thickness is on the order of a few meters. The resisitivity contrast between the overburden and the second layer is on the order of 100. A good 2D model of the Blake River Group region located at Abitibi region was created with an overburden 50 m thick and 100 Ω·m (Tournerie and Chouteau, 1998). The resistivity decreases enormously with large depths, ranging from 10^6 Ω·m for structures located at the surface, to 1 Ω·m for those located at depths of 100 km and beyond.

Type	Mean	Std. Dev.	Max	Mini
Linear	534	788	2280	0.39
Logarithmic	1.46	1.34	3.36	-0.41
Log to Linear	29	22	2280	0.39
Difference	505	766	0	0
Linear for Rho < 4	1.69	0.75	3.55	0.39

Table 4.3 : Statistical Analysis for the conductive Key Tuffite.

Next, we notice that the conductive Key Tuffite has a resistivity smaller than its error bar. A closer look at the repartition of the resistivity logs for the Key Tuffite showed us that the data posses a skew of 1.1298 which was calculated using equation 4.3. Over 62% of the data are located between the bins [0,200]. Over 98% of the data located in this bin have a resistivity value lying between 0 Ω·m and 40 Ω·m. Over this interval, 69% of the data are located between 0 Ω·m and 4 Ω·m. This means that over 42% of the resistivity logs for this conducting Key Tuffite have a value between 0 Ω·m and 4 Ω·m.

$$Skew = \frac{n}{(n-1)\cdot(n-2)} \sum_{i=1}^{M} \left(\frac{(x_i - \bar{x})}{\sigma_i} \right)^3 \qquad (4.3)$$

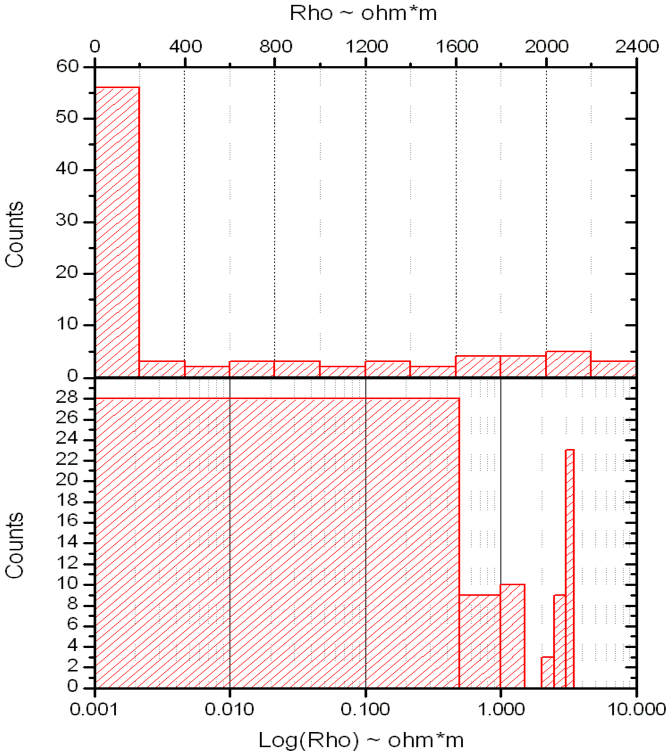

Figure 4-3 : Conductive Key Tuffite histograms.
Top: Linear resistivity. Bottom: Log resistivity.

In table 4.4, we listed a series of possible resistivity values that best represent the Key Tuffite. The resistivity value obtained by calculating the mean for all Key Tuffite resistivity equal to or less than 4 Ω·m, is 1.68 Ω·m. The resistivity obtained by calculating the geometric mean is 29 Ω·m and the linear mean is 533 Ω·m. According to these borehole analyses, the resistivity of Key Tuffite varies from region to region. We suggest that the resistivity value shall be chosen depending on the location of the Key Tuffite and the properties of the surrounding lithology.The boreholes contain a variable quantity of different rock types, and each rock type possesses a range of resistivity values. To estimate the global resistivity value for each rock type we used the geometric mean defined in equations 4.4 and 4.5.

$$\log(\bar{x}_T) = \frac{1}{M}\sum_{i=1}^{M} Log(x_i) \qquad (4.4)$$

Rock type	Resistivity (Ω · m)	Log - Resistivity (Ω · m)	# Sample
Conductive Key tuff	534	29	90
Resistance Key tuff	34 900	30 580	99
Basalt	12 080	16 000	4438
Gabbro	31 100	24 630	3448
Rhyolite	-	14 900	1521
Dumagami Rhyolite	35 220	24 860	3343
Watson Lake Rhyolite	20 770	11 370	132
Mafic Dyke	-	24 630	1145

Table 4.4 : Electrical properties for different rock types found at the Matagami region.

4.2.3 Relationship between rock resistivity and depth

While analyzing the resisitivty of each individual rock type located in the proximity of the Orchan West deposit, we found a relationship between the resistivity value and the depth at which the sample was located for the gabbro and basalt rock types. From observation, we noticed that the resistivity of both rock types tends to increase with depth. In order to show that a relationship might exists between the two variables, resistivity and depth, a linear regression analysis was done. An upper and a lower 95% confidence limit were also calculated. These confidence bands enclose the true best-fit linear regression line, leaving a 5% chance that the true value resides outside those boundaries.

Linear Function: y = A + B x		
Rock Type	A	B
Gabbro	9 391 ± 5 280	31 ± 10
Basalt	11 563 ± 3 991	24 ± 6.56
Basalt with Masking	8 772 ± 2 492	35 ± 4

Table 4.5 : Parameter values and errors for a linear regression line.

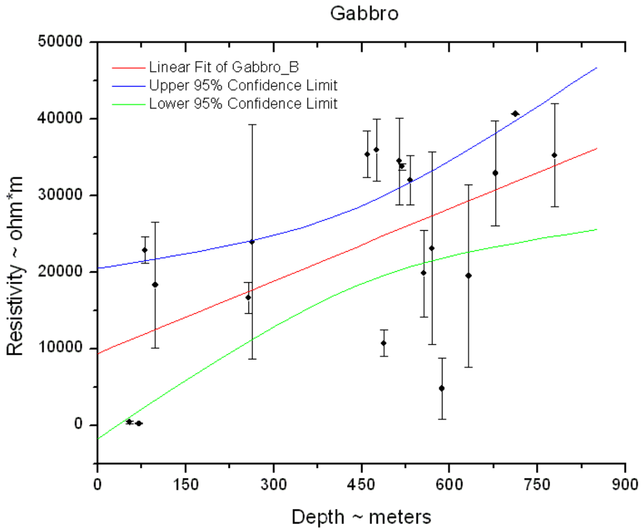

Figure 4-4 : Linear regression and 95% confidence interval for gabbro rock type.

The resistivity of the gabbro varies greatly with depth and the 95% confidence interval is very broad. Statistically, we cannot confirm any correlation between the resistivity value of the gabbro and the depth, but a small trend of increasing resistivity with depth can be observed. A strong correlation was observed for the basalt rock type and further investigation with the linear regression and 95% confidence bands show us that there is a positive correlation between the resistivity and depth. In figure 4.5, there are two data points that are isolated from the others. By removing those 2 points, we shrink the gap between the confidence estimates of the bands while at the same time smoothing the curved bands (figure 4.5 Bottom). The regression parameters can be found in table 4.6.

In conclusion, there's a strong relationship between the resistivity of basalt and the depth at which it is located. We have found 2 distinct values for basalt (table 4.2). This discovery could improve models of the Matagami regions thus generating MT modeling responses that are closer to those found in the MT survey and enabling a more accurate interpretation of the inversion results.

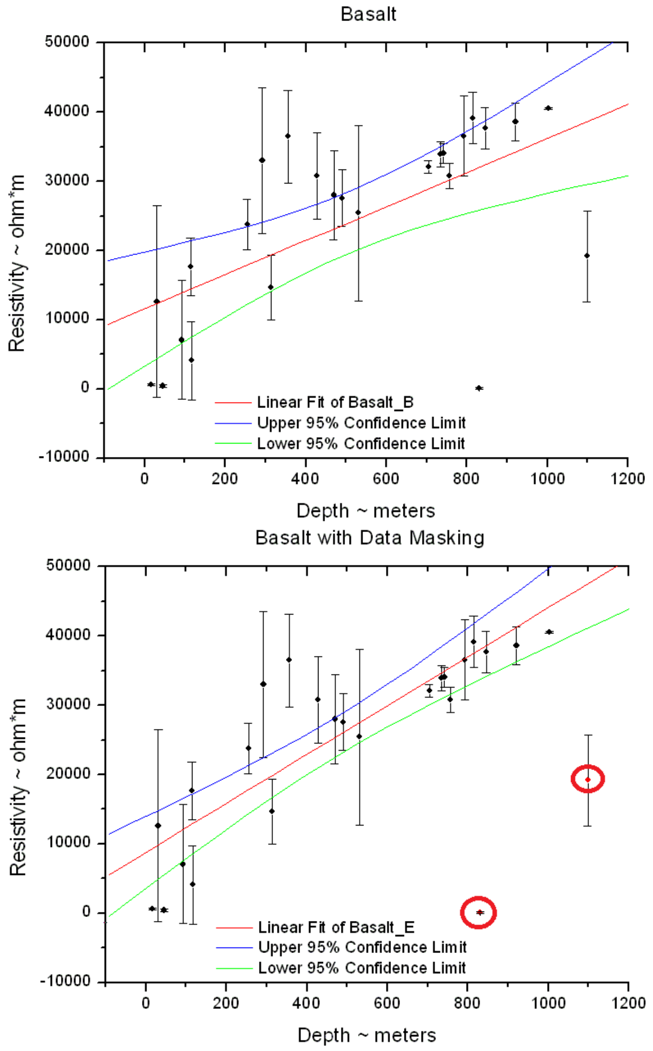

Figure 4-5. Linear regression and 95% confidence interval for basalt rock type. Top: Without masking. Bottom: With masking; the removed data points are circled in red.

CHAPTER 5 INDUCED POLARIZATION 2D MODEL

The standard technique to model the MT response of subsurface structures is to create a model with real isotropic resistivity values assigned to the geological structures. Conductive bodies such as sulfide deposits, generate an induced polarization (IP) response that is frequency-dependent (Hartman and Mutmansky, 2002). The resistivity of a polarizable body varies with frequency and is complex. These changes can be calculated with the Cole-Cole equation provided that certain parameters are known.

$$\rho_{IP} = \rho_{DC}\left[1 - m\frac{(i\omega\tau)^C}{\left(1 + (i\omega\tau)^C\right)}\right] \tag{5.1}$$

where:

i is the imaginary number.

ω is the angular frequency.

ρ_{IP} is the IP resistivity.

ρ_{DC} is the DC resistivity.

m is the chargeability, known as the positive dispersion amplitude.

c is the decay spectrum flatting factor.

τ is the main time constant.

In mining exploration, structures of interest, such as the massive sulfides, can be conductive and occur at a depth of several hundred meters and go undetected. Conductive bodies have been found to influence MT responses at a frequency where the static DC limit is reached and this influence can be determined by comparing the resistivity profiles at two frequencies where the dc limit is reached. Furthermore, the real and imaginary parts of the electric field are near identical without any IP effect and with the IP introduced, the real and imaginary parts are different (Gasperikova and Morrison, 2001). Such effects can be used as a tool in detecting inductive bodies such as massive sulfide in mining exploration. The major aspect of this chapter is to estimate the detection capability of inductive bodies or structures exhibiting the induced polarization effect. The detection capability is defined as when there is a significant change in the MT response in the quasi-static realm.

5.1 MT 2D Modeling with IP

Occam 2D MT v3.0 inversion code was used to compute the MT response of a 2D model with IP effects (DeGrootHedlin and Constable, 1990). The Occam inversion code implements the Wannamaker code for the 2D forward calculation (Wannamaker, 1987). We modified the forward code to incorporate resistivity with complex values and frequency dependence. To test the validity of the code some tests were done. First we compute the MT response of a homogenous medium with resistivity linearly varying with frequency excluding any complex resistivity values (equation 5.2). The apparent resistivity varies with frequency and corresponds to the expected values while the phase stays at a constant 45 degrees (equation 5.3).

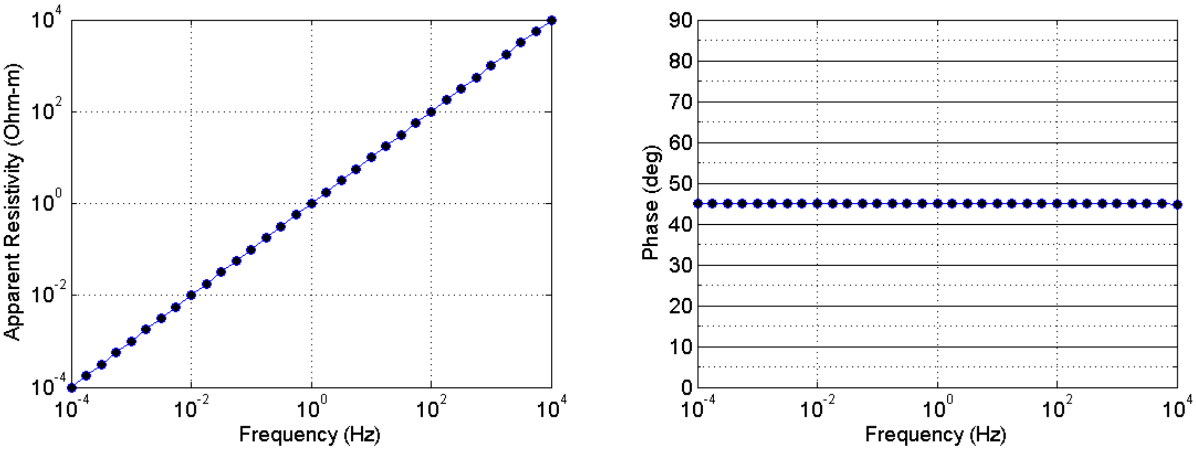

Figure 5-1 : MT response for a homogenous model with varying real resistivity.

$$\rho(freq.) = frequency \quad \Omega \cdot m \tag{5.2}$$

$$Z = \frac{E}{B} = \sqrt{\varpi \mu_o \rho}\sqrt{i} \Rightarrow \arg(z) = 45^o \tag{5.3}$$

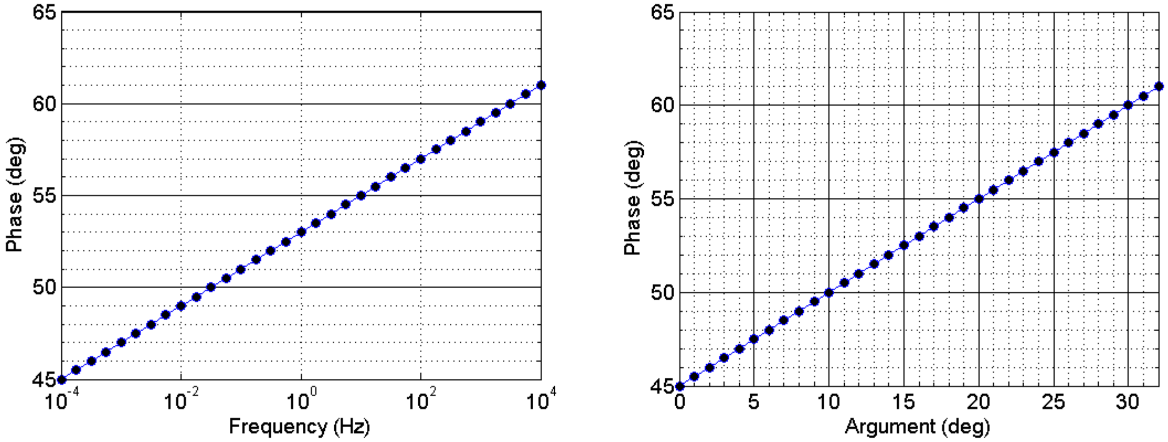

Figure 5-2 : MT response for a homogenous model with varying complex resistivity. Left: MT modeling response. Right: Analytic response.

We then added a complex resistivity with a real and complex part (equation 5.4). The real part was set at 100 Ω·m while the complex part (ρ_c) varies with frequency so that the argument of the complex resistivity increases by 1 degree for every new computed frequency (equation 5.5 and 5.6). There is a total of 33 frequencies and *nFreq* represents the numbering order of each frequency. We noticed that an increase of 1 degree in the argument of the complex resistivity results in an increase of the apparent MT phase by 0.5 degrees. We tested it analytically and found it to be the case. Therefore, the modifications made to the Occam code are validated.

$$Z = \frac{E}{B} = \sqrt{\varpi\mu_o}\sqrt{i(\rho_R + \rho_C)} \Rightarrow \arg(z) = \arctan\left(\frac{Z_{COMPLEX}}{Z_{REAL}}\right) \tag{5.4}$$

$$Z = \frac{E}{B} = \sqrt{\varpi\mu_o}\sqrt{i(100 + \rho_C)} \tag{5.5}$$

$$\rho_{IP} = 100 + i \cdot 100 \cdot \tan\left(\frac{\pi(nFreq - 1)}{180}\right) \quad \Omega \cdot m \tag{5.6}$$

5.1.1 Model Study

3D models previously created in order to detect deep conductive massive ore bodies at Matagami, Raglan and basic VMS (Volcanogenic Massive Sulfides) show that bodies with the same dimensions and resistivity as found in the region cannot be detected past a few hundred meters in depth (Chouteau, Boulanger et Allard, 2008). Table 5.1 shows the detection depth for each type of bodies shown in figure 5-3, assuming that a 12.5% change in resistivity and a 10% change in phase is needed to be significant.

Models	Depth of detection
Matagami	200m
VMS-1	350m
VMS-2	350m
Raglan-Ni	100-150m

Table 5.1 : Depth detection for 3D models.

Model	Y (m)	Z (m)	Rho (Ω·m)	Rho Bedrock (Ω·m)
-	-	-	-	-
Block	100	100	10	100
Matagami	300	200	0.1	40 000
Raglan1	100	100	0.1	100
Raglan2	100	100	0.1	40 000
VMS-1	100	100	1 000	40 000
-	-	-	-	-
	Y_1 ~ m	**Z_1 ~ m**	**Rho$_1$ ~ Ω·m**	**Rho Bedrock ~ Ω·m**
VMS-2	350	500	1 000	40 000
	Y_2 ~ m	**Z_2 ~ m**	**Rho$_2$ ~ Ω·m**	
	150	300	0.1	

Table 5.2 : 2D inductive models properties.

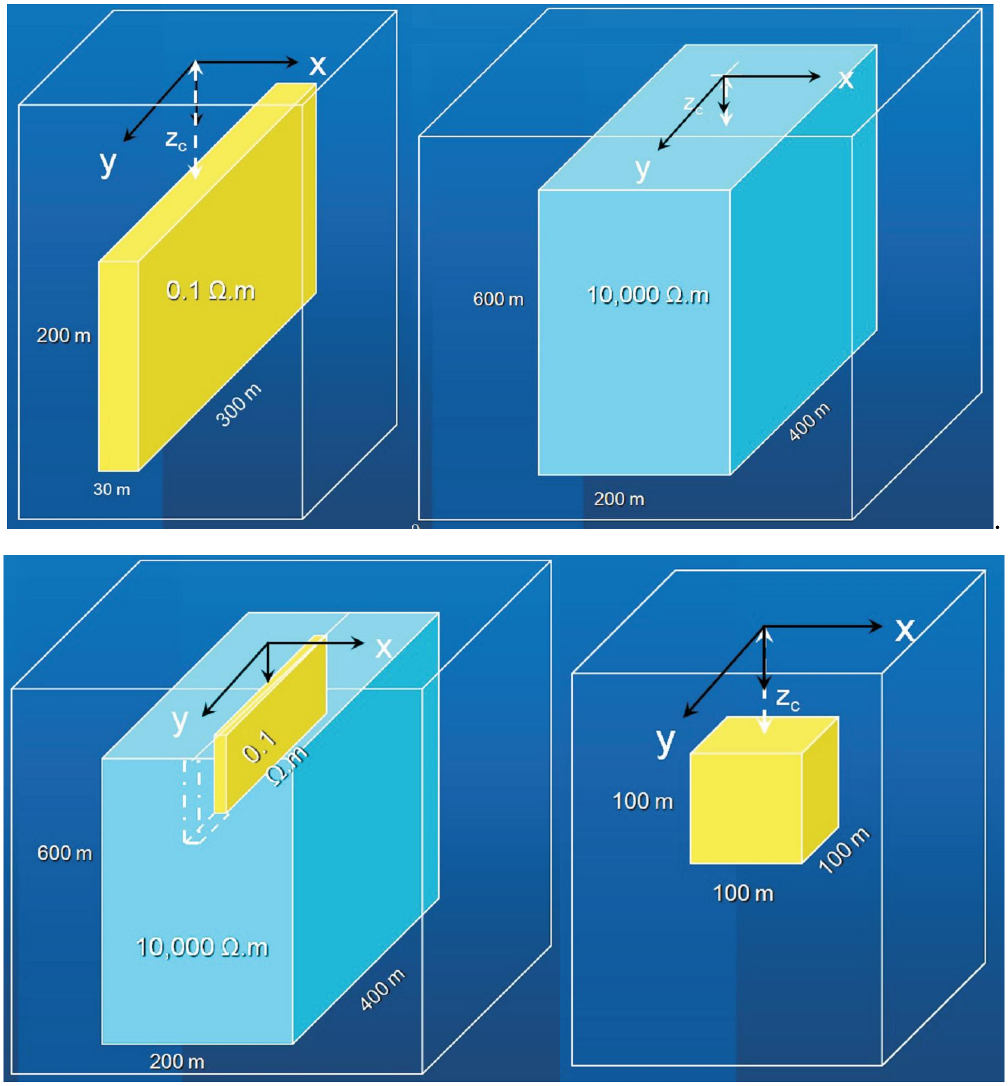

Figure 5-3 : Top left: Matagami. Top right: VMS-1. Bottom left: VMS-2 with alteration zone. Bottom right: Raglan (Pictures taken from Chouteau, Boulanger and Allard, 2008).

The same models are recreated under 2D conditions with conductive VMS bodies at depths of 30m, 60m, 100m, 150m, 200m and 300m from the surface to the top of the bodies. The body in VMS-1 represents a disseminated mass produced by sulphide dissemination and rock alteration, while the body located in VMS-2 contains a massive sulfide body enclosed in the disseminated mass. Since the induced polarization model is in 2D, we choose the dimension of the ore bodies to be along the Y and Z direction. Slight modifications were made to VMS-2 model; the ore body was moved from the top to the middle of the alteration zone. VMS-1 size was reduced in order to compare with the Raglan model and we have also recreated the exact 100 m x 100 m model that Gasperikova and Morrison (2001) used and we compared with their work in order to validate our code.

To explore the IP effects, five different combinations of parameters were used in the Cole-Cole equation and can be seen in table 5.3. The massive sulfide Cole-Cole parameters values can be found in table 5.4. The time constant of the massive sulfide increases with increasing chargeability. A time constant of greater than 10s is correlated with a chargeability of 0.5 or higher (Reynold, 1997).

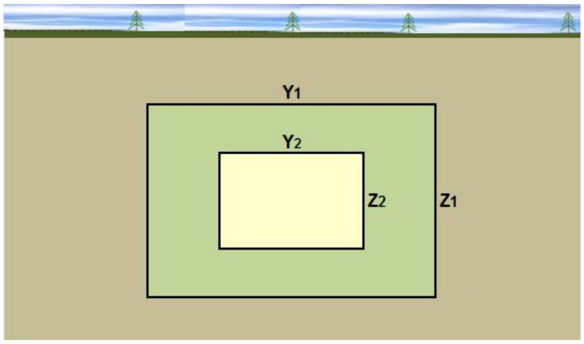

Figure 5-4 : VMS-2 model.

Massive Sulfide ore bodies		
	Range	
M	0.05	1
C	0.25	0.3
T	0.001s	125.8925s

Table 5.3 : Sulfide Properties.

-	code	m	t ~ s.	c
a	MT2Dna	0.00	0.6	0.3
b	MT2Dnb	0.25	0.6	0.3
c	MT2Dnc	0.50	0.6	0.3
d	MT2Dnd	0.75	0.6	0.3
e	MT2Dne	0.95	0.6	0.3
-	code	m	t ~ s.	c
ia	MT2Dia	0.00	126	0.3
ib	MT2Dib	0.25	126	0.3
ic	MT2Dic	0.50	126	0.3
id	MT2Did	0.75	126	0.3
ie	MT2Die	0.95	126	0.3

Table 5.4 : Parameters for 2D inductive modeling.

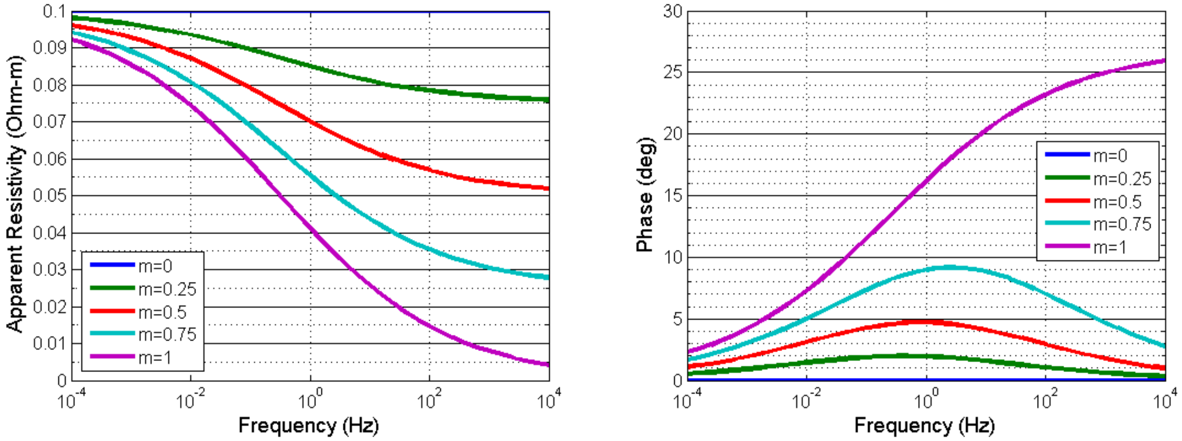

Figure 5-5 : The norm (App. resistivity) and argument (phase) of a complex resisitivity following the Cole-Cole equation (m = [0, 1], t = 0.6s and c = 0.3).

We first determine the apparent resisitvity and phase of the ore bodies through Cole-Cole equation when the chargeability is at its maximum (m = 1) with t = 0.6 s and c = 0.3 (figure 5-5). As seen earlier, we have found that in a homogeneous medium the apparent MT phase increases by 0.5 degree for every increase of 1 degree in the argument of the complex resistivity. A phase change of 10% in a MT survey is required for detection. With the Cole-Cole parameters stated in equation 5.1, the complex resistivity yields a minimum of 2.5 degrees at 10^{-4} Hz and a maximum of 26 degrees at 10^{4} Hz, which in return contributes a maximum of 13 degrees for a MT survey at a frequency of 10^{4} Hz (figure 5-5). To yield a 10 degrees change in the MT response, which corresponds to an argument of 20 degrees for the complex resistivity, the chargeability has to be equal to 1 and the time constant has to be at least 49.64 seconds (figure 5-6). By increasing the time constant to its maximum allowed value of 126s, it appears to have a minimal effect on the response. As the time constant (t) increases, the phase plateau's to a maximum. In our modelling, the time constant computed by the logmean t=0.6s and the maximum value t=126s for the massive sulfide will be used and compared. As stated earlier, a time constant greater than 10s generally appears when the chargeability (m) is equal or greater than 0.5; therefore, we cannot have a time constant of 126s for a massive sulfide with chargeability less then 0.5.

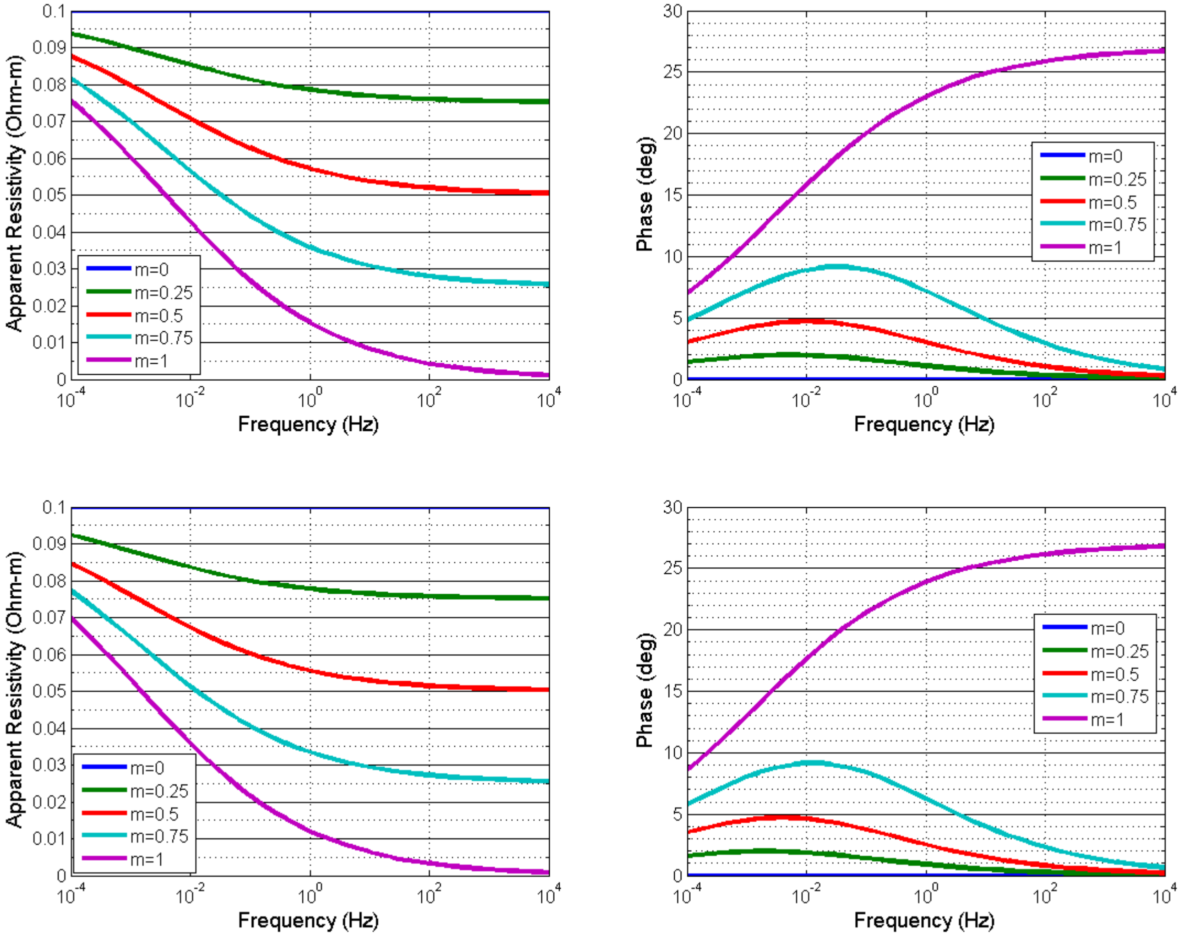

Figure 5-6 : The norm (App. resistivity) and argument (phase) of a complex resisitivity following the Cole-Cole equation. Top: t = 49.64s and c = 0.3. Bottom: t = 126s and c = 0.3. The Cole-Cole expression for the latter parameters is shown in equation 10.1.

$$\rho_{IP} = 0.1\left[1-(1)\frac{\left(i(2\pi f)(126)\right)^{0.3}}{\left(1+\left(i(2\pi f)(126)\right)^{0.3}\right)}\right] \tag{10.1}$$

5.1.2 IP Response Analysis

We have computed the MT response for the six different 2D models that represent the Matagami, Raglan and VMS. For each response, we computed the percent difference of the apparent resistivity and phase at two frequencies located in the region of quasi-static (at 0.1 Hz and 0.01 Hz) in TM mode. The profiles of apparent resistivity and phase at 0.01 Hz and 0.1 Hz are vertically shifted to coincide on the right and left ends of the profiles. The percent difference is the difference between the apparent resistivity and phase at 0.01 Hz and 0.1 Hz normalized respectively by the apparent resistivity and phase at 0.01 Hz. The background resistivity is either 100 Ω·m or 40 000 Ω·m, that yield respectively a skin depth of 15.9 km and 318 km at 0.1Hz. Depending on the model, the quasi-static is closely reached at frequencies below 0.1Hz.

Model	**Resistivity Max % Percent difference (0.01Hz - 0.1Hz)**					
Depth	30	60	100	150	200	300
Block	17	5	1.9	0.83	0.3	0.2
Matagami	nil	nil	nil	Nil	nil	nil
Raglan-1	nil	nil	nil	Nil	nil	nil
Raglan-2	nil	nil	nil	Nil	nil	nil
VMS-1	8.5	1.8	0.67	0.31	0.13	0.094
VMS-2	30	14.7	4.2	1.7	0.92	0.4
Model	**Max Phase difference (0.01Hz - 0.1Hz)**					
Depth	**30**	**60**	**100**	**150**	**200**	**300**
Block	0.11°	0.016°	-0.005°	-0.005°	-0.008°	-0.008°
Matagami	nil	nil	nil	Nil	nil	nil
Raglan-1	nil	nil	nil	Nil	nil	nil
Raglan-2	nil	nil	nil	Nil	nil	nil
VMS-1	0.05°	0.01°	0.002°	0.001°	0.001°	0.001°
VMS-2	0.85°	0.15°	0.03°	-0.01°	-0.01°	-0.01°

Table 5.5 : Observed apparent resisitivty % difference and phase difference between 0.01 Hz and 0.1 Hz for MT response with a time constant of 0.6 s.

Modelling with a time constant (t) of 0.6s shows that there is a significant effect on the MT response when the resistivity is of complex form. Furthermore, beyond 60m the IP effect is no longer considered significant for any of the models, as the IP effect quickly diminishes with increasing depth. The complex resistivity has a bigger effect on the apparent resisitivity then the phase. For the majority of the models, there is no significant change between the real and complex part of the impedance at a depth of 60m and beyond (see appendix A and B). With the time constant (t) set at 126s, the percent difference for the block model increases by an additional 4% for the apparent resistivity while the phase changes from 1.8% to -4%. A negative percent difference signifies that the apparent resistivity or phase at 0.1 Hz is of higher magnitude then when it is at 0.01 Hz. Having a longer time constant does not necessary increase the detection depth or affect the data. Based on the six models results, the inductive bodies or complex resistivity have a huge impact in the MT response when the bodies are located near the surface. But the IP effect diminishes greatly with increasing depth. In other words, the magnitude of the change added by the inductive body depends on the physical size of the body and its depth to the surface. The effect is enhanced if the electrical properties such as the chargeability, the time constant and the value of the decay spectrum flatting factor are set for optimum change.

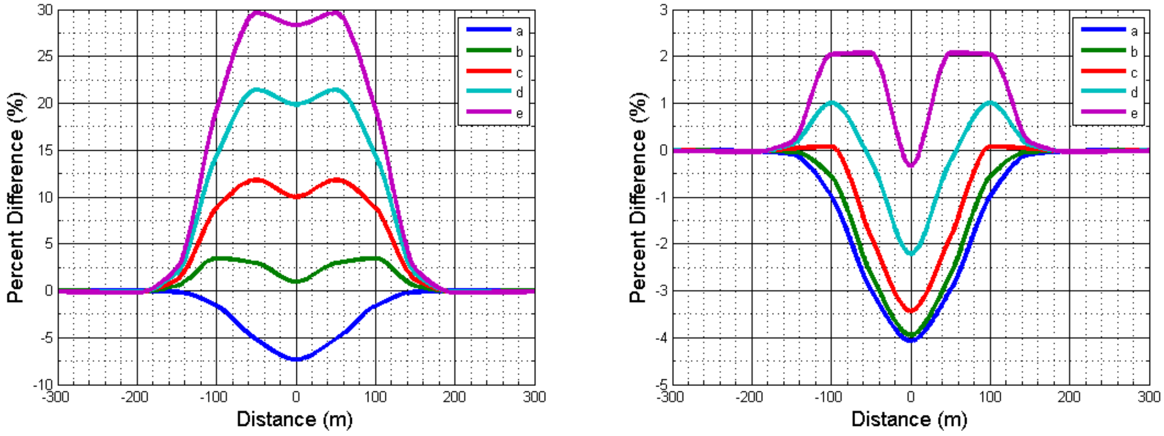

Figure 5-7 : Observed apparent resisitivty and phase percent difference between 0.01 Hz and 0.1 Hz for the MT response utilizing the Matagami model with a time constant (t) of 0.6s and at depth of 30m. Information regarding the legend can be found in table 5.4 (a, b, c, d and e).

For the Matagami, Raglan-1 and Raglan-2 models, there is minimal difference between the complex free resistivity 2D MT response and the complex resisitivity 2D MT response. The size of the body as well as the contrast between the background resistivity and the body is infuencial enough to dominate the IP effect. Due to these factors the contribution of varying complex resistivity with frequency is minimal, and consequently IP effects cannot be measured in a significant way. One added factor to this is that if a body is highly detectable by MT method, the IP effects cannot be observed.

Model	**Resistivity Max % Percent difference (0.01Hz - 0.1Hz)**					
Depth	30	60	100	150	200	300
Block	21	5.1	1.85	0.8	0.275	0.17
Matagami	Nil	nil	nil	nil	nil	nil
Raglan-1	Nil	nil	nil	nil	nil	nil
Raglan-2	Nil	nil	nil	nil	nil	nil
VMS-1	8.3	1.62	0.6	0.28	0.116	0.083
VMS-2	48	16.5	3.8	1.5	0.8	0.34
Model	**Max Phase difference (0.01Hz - 0.1Hz)**					
Depth	**30**	**60**	**100**	**150**	**200**	**300**
Block	-1.62°	-0.54°	-0.25°	0.14°	-0.082°	-0.067°
Matagami	Nil	nil	nil	nil	nil	nil
Raglan-1	Nil	nil	nil	nil	nil	nil
Raglan-2	Nil	nil	nil	nil	nil	nil
VMS-1	-0.5°	-0.13°	-0.044°	-0.022°	-0.01°	-0.008°
VMS-2	-8°	-2.2°	-0.49°	-0.2°	-0.12°	-0.064°

Table 5.6 : Observed apparent resisitivty % difference and phase difference between 0.01 Hz and 0.1 Hz for MT response with time constant of 126s. The highest percent difference occurs at the station located at the center top of the ore bodies. This is true for all models except the VMS-2, where the highest percent difference occurs at the side (figure 5-7).

5.2 Mining Camp Models

To evaluate actual application of the MT 2D modeling with IP effect approach, three well-known ore bodies were selected as test targets. Cross-sections of the ore bodies Bracemac, McLeod, Orchan and Bell Allard are modeled. They contain rich massive sulfide deposits that lie within alteration zones and alteration pipes that are larger then the massive sulfide alone. At a depth of several hundred meters the massive bodies could be undetectable while the alteration zone could remain detectable. We will model the alteration zone by a weak decrease of resistivity (factor of 10^2 to 10^4) with regards to the host rock. This alteration zone and the massive sulfide bodies could have dispersive properties. We will evaluate the impact of polarizable bodies on the MT responses and on the capability to detect alteration zones.

5.2.1 Model Study

Based on the cross-section images provided by Xstrata Zinc, we created 2D models that represent the ore bodies of Bracemac, the McLeod and the Bell Allard located at the Matagami mining camp. The MT response will be computed for Key Tuffite with resistivity of 1 k Ω·m, 533.79 Ω·m and 29.02 Ω·m. The massive sulfide will have a resistivity of 1 Ω·m or 0.1 Ω·m. Bell Allard has an overburden of 80m thick while Bracemac and McLeod have a 30m thick overburden. The resisitivity is 200 Ω·m for the overburden, 35 kΩ·m to 40 kΩ·m for the rhyolite, 35 k Ω·m for the gabbro and 25 kΩ·m to 30k Ω·m for the basalt.

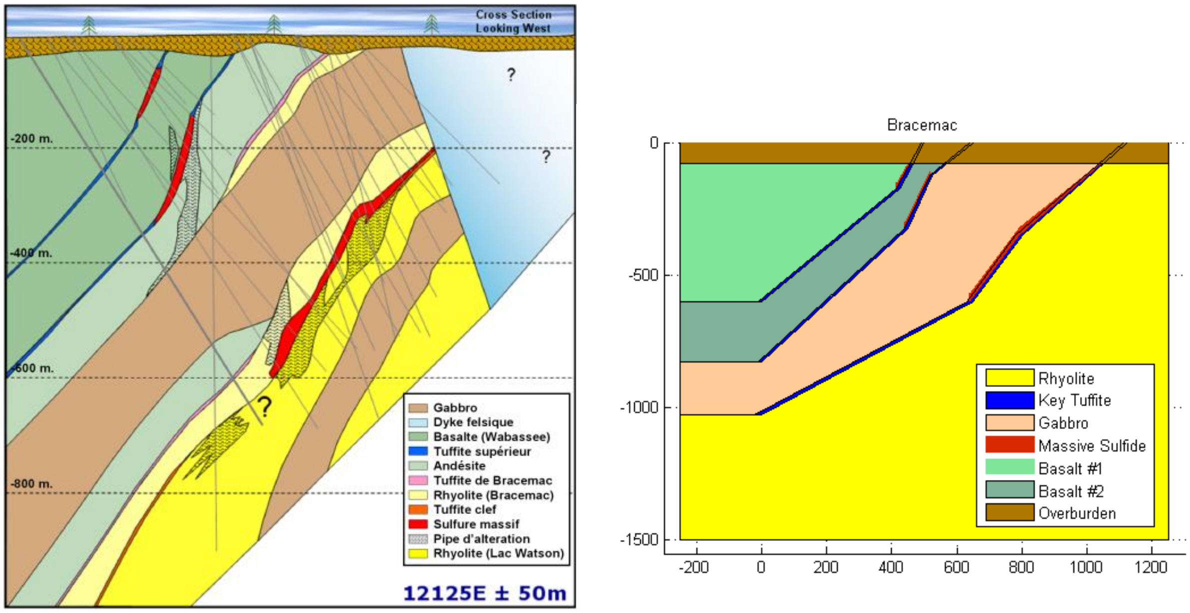

Figure 5-8 : Left: Image provided by Xstrata for Bracemac ore bodies. Right: Actual model used in calculating 2D MT forward response.

The Key Tuffite has a thickness of 10m, while the massive sulfide has variable thickness, length and orientation. The 2D model of Bracemac contains three massive sulfides deposit of size (thickness x length) 15m x 50 m, 20m x 75m and 25m x 295m with an approximate dip of 50 degrees angle. The McLeod model possesses two massive sulfides deposits of size 20m x 105m and 15m x 55m. The Bell Allard model contains a single 150m x 300m massive sulfide at a depth ranging from 900m to 1050m.

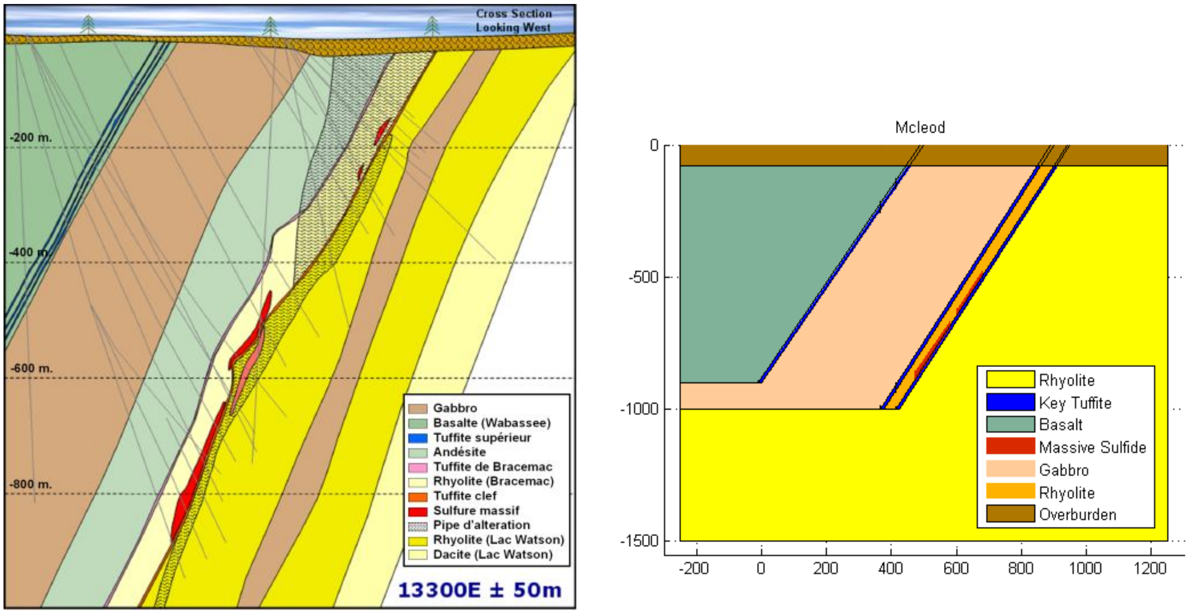

Figure 5-9 : Left: Image provided by Xstrata for McLeod mining camp. Right: Actual model used in calculating 2D MT forward response.

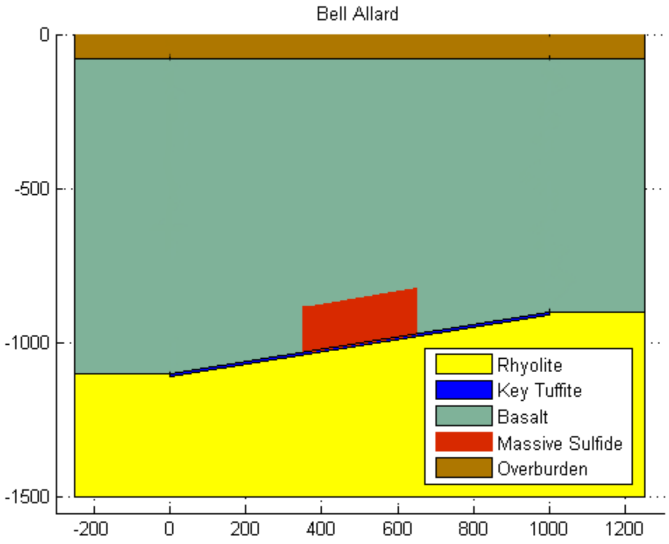

Figure 5-10 : Bell Allard mining camp 2D model used in the 2D MT forward response.

5.2.2 IP Response Analysis

The 2D MT response is computed for each individual model and repeated for various electrical properties. We follow the same steps as shown in section 5.2.2 by calculating the percent difference of the response in the quasi-static realm of frequency in order to detect any change in the MT response with conductive structures. The apparent resisitivty and phase percent differences are computed at a frequency of 0.1 Hz and 0.01 Hz. The results are shown in appendix C, D and E. The blue lines represent the percent difference for a MT response without IP effects. The quasi-static can be considered reached as the percent difference between the profile at 0.1 Hz and 0.01Hz for apparent resisitivty and phase is very small. Table 5.7 shows the percent difference between 0.01 Hz and 0.1 Hz when complex resistivity is added. The change in apparent resisitivity and phase is minimal for different electrical properties for all three models. No change can be observed between the real and complex components of the impedance for the IP free model and the IP inherent model. They are nearly indistinguishable.

Key Tuffite = 1 kΩ·m & massive sulfide = 1 Ω·m		
Model	**Apparent Resistivity**	**Phase**
BellAllard	0.045 %	0.012 %
Bracemac	0.6 %	0.18 %
McLeod	0.045 %	0.0025 %
Key Tuffite = 534 Ω·m & massive sulfide = 0.1 Ω·m		
Model	**Apparent Resistivity**	**Phase**
BellAllard	0.034 %	0.0085 %
Bracemac	0.5 %	0.14 %
McLeod	0.0045%	0.00135 %
Key Tuffite = 29 Ω·m & massive sulfide = 0.1 Ω·m		
Model	**Apparent Resistivity**	**Phase**
BellAllard	0.015 %	0.0018 %
Bracemac	0.23 %	0.14 %
McLeod	~ 10^{-4} %	~ 10^{-4} %

Table 5.7 : Percent difference for various Key Tuffite and massive sulfide electrical properties. Degrees differences are $10^{-2\,\circ}$ magnitude or less.

5.3 Conclusion

IP modelling has shown that a conductive body does increase the detectability in the quasic-static regime but only when the body size is comparable to its depth. If the conductive body is highly detectable with the MT method, then any IP effect will be difficult to measure. The reason is due to the fact that any influence produced by the conductive body will be dominated by the strong MT response produced by the strong contrast between the background and body resistivity. This is in agreement with the Matagami and Raglan models.

At depth where the conductive bodies cannot be detected throught traditional MT method, the added IP effect to the body does not increase its detectability or allow it to be detected. A possible explanation is that even though we reach the quasi-static regime where the MT response is independent of frequency, the contribution of a conductive body with frequency dependent resisitivity is very small (see section 5.1.1). At the quasi-static limit, the MT response will be almost identical to a conductive free body. Therefore we cannot detect ore bodies with IP effects when the size of the body is smaller than its depth.

Therefore models representing Matagami mining camp (i.e. Bell Allard, Bracemac and McLeod), the ore bodies and the structures controlling the mineralization with conductive properties cannot be detected through the MT method with or without IP effects.

CHAPTER 6 MATAGAMI TITAN 24 ANALYSIS

6.1 Introduction

The goal of this chapter is to analyze the MT survey of the southern flank of Matagami mining camp in terms of subsurface structures. MT survey of the Matagami lower West flank, obtained by the Titan-24 instrument, was treated using the Mackie 2D smooth inversion code (Winglink). Prior to the 2D inversion process, the subsurface dimensionality of the surveyed region and the regional strike were determined. The 2D inversion results were taken as a 2D slice of the 3D regional structure. These 2D slices were then combined using UBC meshtool3d (Shekhtman, UBC, 2007) to recreate the 3D model of the regional structure. This allows for the identification of any major structures and similarities between profiles (2D slices).

6.2 Survey in Matagami Area

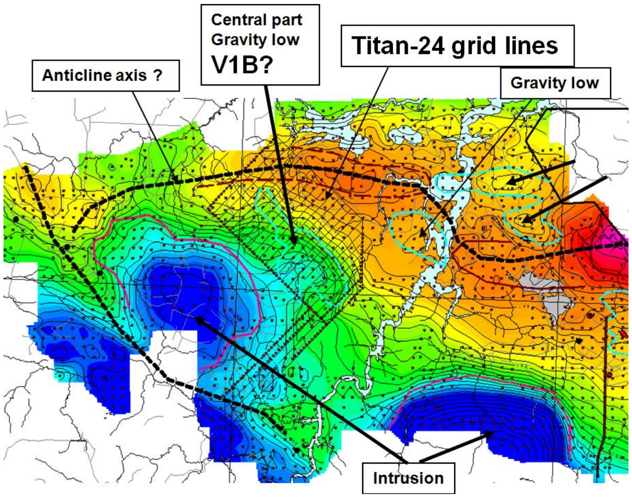

Figure 6-1 : The MT survey zone plotted over the gravity Bouguer anomaly (Provided by Michel Allard, chief geophysicist of Xstrata Zinc).

The MT survey, done using a Titan 24 system, was conducted by Quantec Geoscience. The survey took place on the Southern flank region of the Matagami Mining Camp during the month of July and August 2007. There are a total of 1297 stations and 22 profiles line which are broken down as follows: 16 profiles with 50 stations, 2 profiles with 48 stations, 3 profiles with 100 stations and 1 with 101 stations. The MT data were acquired through frequencies of 0.1Hz to 10kHz. In our WinGlink database file, we referenced the survey area in the UTM zone #18 with the WGS 1984 as the datum.

6.3 Dimensionality Analysis

The Bahr, Q-Bahr, WAL invariant and MT tensor methods discussed in chapter 3, were utilized to determine the dimensionality for the Titan 24 MT Matagami data. The dimensionality for Bahr methods resides between 3D/1D2D, 3D/2D and 3D. The WAL invariant determined the underlying structures of the region are of 3D type. The Q-Bahr methods also classify the dimensionality directly as 3D but the possibility of a 3D/2D dimensionality cannot be ruled out.

Parameters	**Mean**	**Std**	**Skew**	**Kurt**
K: Swift Skew	0.16	0.00146	30459.6	2799650.32
μ: ΔPhase	0.25	0.002	-360.39	22 601.36
η: Phase Skew	0.2	0.00169	-626.83	32 080.56
Σ: 2D Dim.	0.04	0.00089	1 443 007.77	418 388 410.84
Parameters	**Model 1**	**Parameters**	**Model 3**	**Model 4**
I_1	759 937 644.29	21 357 617.16	3437.92	154 552.26
I_2	237 455 761.17	4 981 399.27	8396.75	398 582.94
I_3	0.51	0.0026	-68259.5	15 436 644.96
I_4	0.41	0.00305	9356.83	4 397 879.01
I_5	0.5	0.00446	-76902.51	8 769 330.26
I_6	-0.1	0.00316	1427.42	43 228.86
I_7	-0.32	0.00915	-3218.07	150 207.38
U_4	748 467 548.86	21 127 942.34	3173.1	139 657.37
V_4	225 986 156.06	5 090 416.49	1920.14	60 109.14

Table 6.1 : Dimensionality analysis results for the Matagami MT survey.

Given that none of the given methods provide a unique answer (i.e. 3D/1D2D, 3D/2D or 3D) we can assume that the regional sub-terrainean structures are very complex. This is backed by calculating the Latorraca Skew value for all the stations that show significant 3D effect in the region (figure 6-4). Consequently, it is important to verify the dimensionality through 2D inversion with 3D modeling and 3D inversion in order to properly assess and analyze the MT data.

6.4 Regional Strike

Under the assumption of 3D/1D2D or 3D/2D regional structures, the direction of the regional strike needs to be determined. Utilizing the Torquil Smith method seen in chapter 3, the direction for the strike was found to be approximately N40W for all stations. The software used to determine the direction of the regional strike is Torquil Smith's personal Fortran code (Smith, 1996). Tsmith code allows the determination of the best regional strike for a grouping of stations in a profile (up to 60 stations during a test).

Profile #	Strike Direction North-West	Chi-Square	Profile #	Strike Direction North-West	Chi-Square
0	-40	64.4	**44**	-40	97.72
4	-34	100.5	**48**	-42	112.7
8	-16	114.6	**52**	-44	59.51
12	-22	129.6	**56**	-44	134.1
16	-34	104.3	**60**	-40	140.3
20	-48	101.1	**64**	-36	97.31
24	-40	72.3	**68**	-46	155.9
28	-19	122.4	**72**	-48	99.68
32	-26	110.6	**76**	-44	123.2
36	-26	103	**80**	-47	118.9
40	-52	177	**84**	-34	154.1

Table 6.2 : Strike orientation computed using Torquil Smith code for the survey profiles.

Using Tsmith code, the regional strike was determined in 2 ways. First, it was used on each individual profile with its respective stations. For example, the strike angle for profile L00E was calculated by finding the best strike direction for its 50 MT stations for all recorded frequencies. The second method was to create pseudo-profiles, 50 of them, that are perpendicular to the original MT survey profiles where each pseudo-profile regroups 16 stations, 1 from each profile.

For example, the strike angle for pseudo-profile #1 was calculated by finding the best strike direction for all first MT stations from the 16 MT profiles. Pseudo-profile #2 regroups the entire second MT stations from the 16 MT profiles and forth.

Pseudo-Profile #	Strike Direction North-West	Chi-Square	Pseudo-Profile #	Strike Direction North-West	Chi-Square
1	-43	95.01	26	-47	94.6
2	-44	79.41	27	-44	177.6
3	-49	91.93	28	-44	97.43
4	-46	98.82	29	-40	71.78
5	-42	122.9	30	-46	132.5
6	-42	101.9	31	-37	63.41
7	-44	84.6	32	-30	61.46
8	-64	91.69	33	-28	72.09
9	-50	105.4	34	-26	102.7
10	-32	102.7	35	-26	68.71
11	-44	123.4	36	-31	87.23
12	-39	123.2	37	-24	74.21
13	-40	123.5	38	-28	105.6
14	-37	122.1	39	-28	91.1
15	-42	122	40	-28	110.5
16	-62	106.2	41	-24	74.36
17	-68	112.9	42	-26	115.6
18	-52	110.4	43	-22	122.4
19	-70	110.4	44	-34	105.1
20	-22	104.8	45	-26	136.6
21	-58	97.21	46	-18	95.13
22	-60	110.7	47	-18	132.2
23	-42	108	48	-26	117.3
24	-36	99.68	49	-30	96.21
25	-44	79.57	50	-28	107.5

Table 6.3 : Strike orientation computed using Torquil Smith code using the pseudo-profiles.

The best regional strike for each station is shown graphically by figures 6-2 and 6-3. The best regional strike computed by averaging the best angle of all profiles, all pseudo profiles and all stations can be seen in table 6.4. Since the profiles are oriented at N44°E and to avoid having to interpolate stations, we have choosen our strike angle to be N46°W.

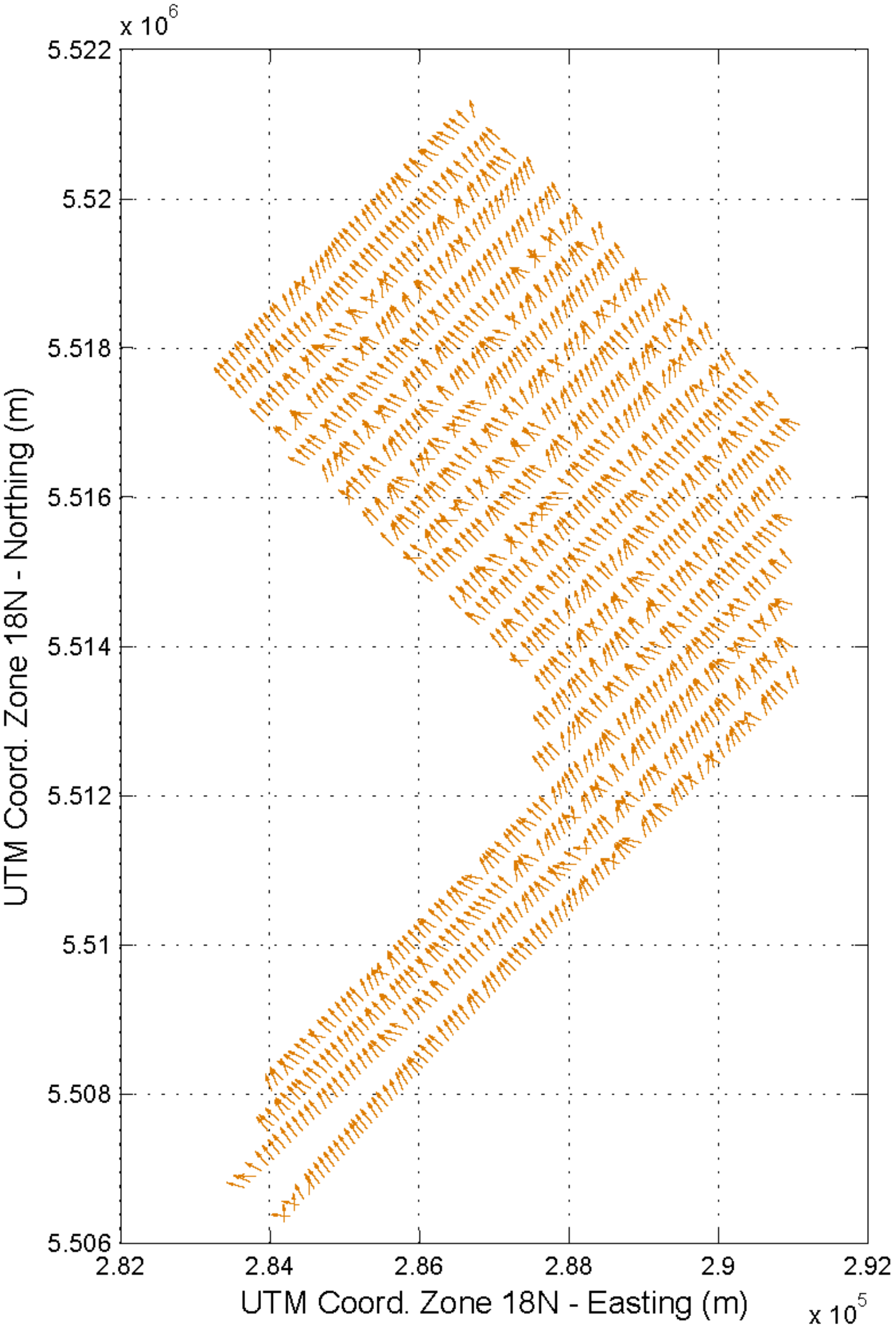

Figure 6-2 : Arrows showing the "best" strike direction computed for each site for all frequencies

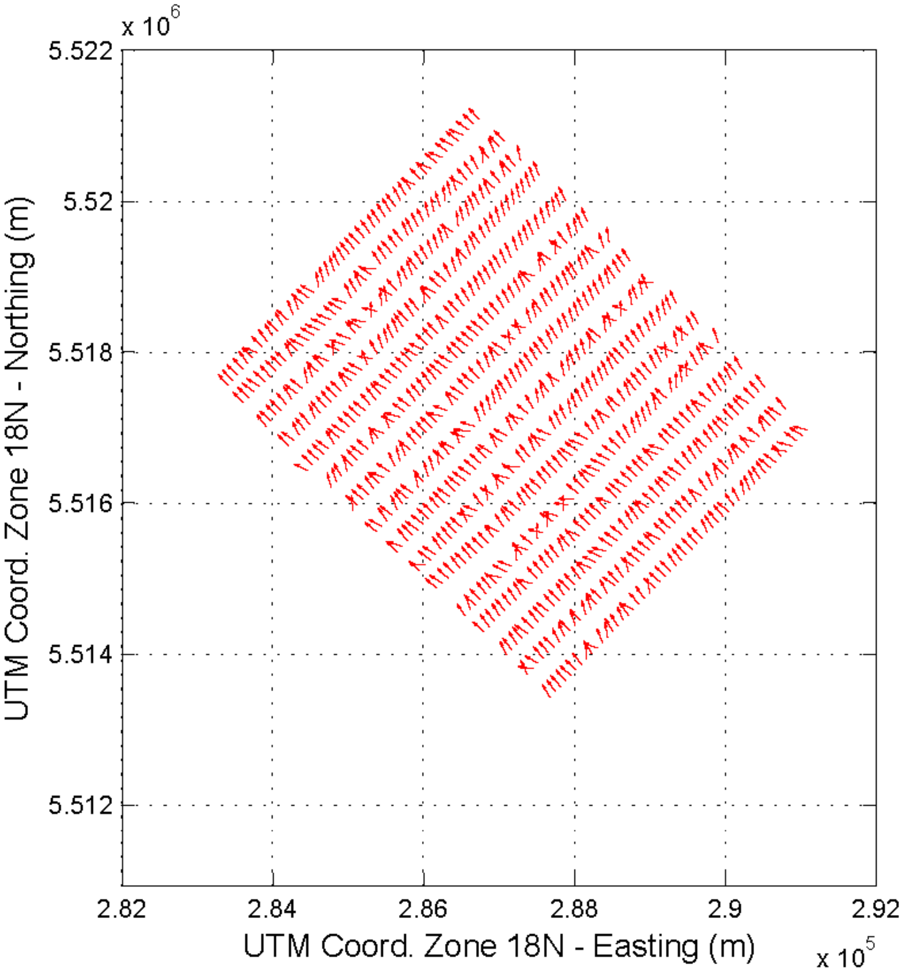

Figure 6-3 : Arrows showing the "best" strike direction computed for each site for all frequencies for the pseudo-profiles.

About	Average Angle
22 original profiles	-37.36 N
50 orthogonal profiles	-38.62 N
1297 Stations of original profiles	-40.84 N
800 Stations of orthogonal profiles	-39.46 N
Angle of MT profiles	44 N
Angle perpendicular to MT profiles	-46 N

Table 6.4 : Various computed strike angles.

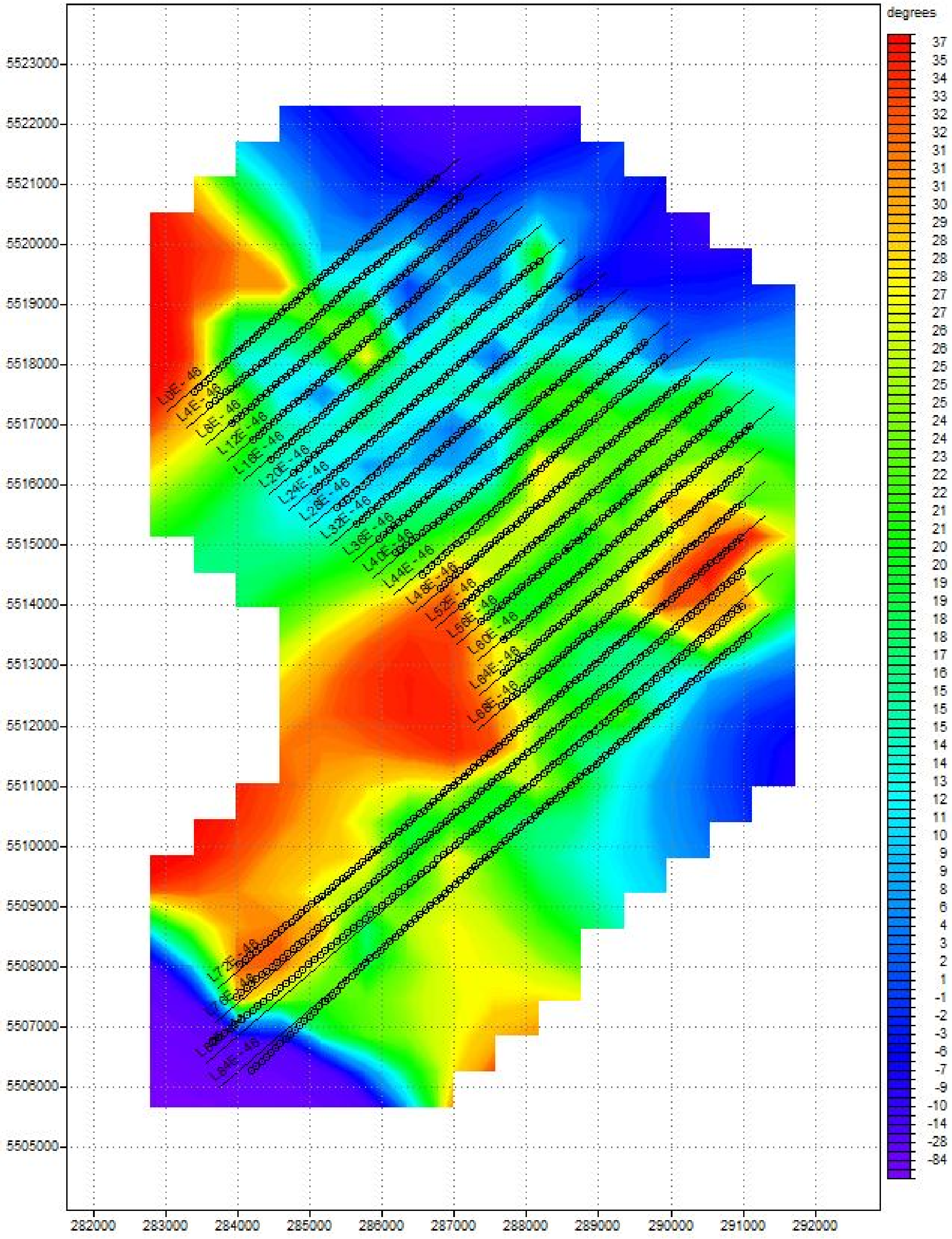

Figure 6-4 : Latorraca Skew Angle at 0.16 Hz. Area where the angle is greater than 20 degrees shows significant 3D effect (Green, yellow and red).

6.5 2D Inversion

The models were inverted using Winglink software. Winglink 2D MT inversion uses Mackie 2D smooth inversion code (Rodi and Mackie, 1998). Using Tikhonov regularization method combined with nonlinear conjugate gradients, this routine finds regularized solutions to the two-dimensional inverse problem for the MT data (Winglink manual, 2008). The inversions ran for 500 to 1000 iterations per profiles and stopped when they could no longer converge to a lower rms value. A variety of different settings were used to do the 2D inversions and out of all the trials, 3 were found to be good candidates.

> **Setting 1.** The first setting was set as follows: Both TE & TM modes and phase were set at 5% error. The interval of frequency was from 0.1 Hz to 10 000 Hz. The initial model contained a homogenous medium of 40 000 Ω·m with a fixed 1D model starting below 5 000m. The number of iterations varies between profiles and the number of iterations was limited to 500. Static shift was added and an other 100 iterations were done for all profiles. The 1D model was produced by Tournerie and Chouteau (2007) and details of it can be seen in table 7.1.
>
> **Setting 2.** The second setting was set as follows: The TM resistivity and TM & TE phase were set with 5% error while the TE resistivity was set at 50% error. 200 iterations were done for frequencies between 0.1 Hz to 10 000 Hz with static shift. The inversion started with a homogeneous model of 40 000 Ω·m without the 1D model.
>
> **Setting 3.** The third setting was set as follows: TE resistivity and TE & TM phase are set to 5% error throughout the inversions. The TM resistivity was first set at 50% error with 50 iterations. Afterward, the TM resisitivity error was reduced to 5%, the static shift was added and 50 more iterations were done. The inversion started with a homogenous model of 40 000 Ω·m with frequency ranging from 0.1Hz to 1 000 Hz.

6.5.1 TM inversions

According to Wannamaker (1999), two-dimensional modeling and inversion should concentrate on the transverse magnetic (TM) because of its low sensitivity to the effects of finite strike. In addition, the TM mode is more immune to probable 3-D effects in the area than is the transverse electric (TE) mode. Inversions done with the TM mode are better in differentiating any lateral contacts than TE mode (Wannamaker et al., 1991).However, TM mode inversion performed solely using profile data would only reveal resistivity structures crossing the profiles but not the ones parallel. In order to detect resistivity changes caused by 3D structures in the NW-SE direction (orthogonal to the profile orientation), one needs to perform TM inversion (resistivity in the NW-SE direction) along profiles orthogonal to the survey lines. For this reason 2D inversions of TM mode were done for the profiles and the pseudo-profiles. The pseudo-files are composed of 800 stations divided evenly among 50 pseudo profiles (16 stations per pseudo-profiles and 400 m spacing between stations). The pseudo-profiles were constructed by regrouping the stations by their numbers. The survey profiles consist of 50 stations per profiles, thus we were able to produced 50 pseudo-profiles. The first pseudo-profile contains all stations #1 from the first 16 survey profiles (L0E to L60E), the second pseudo-profile contains all stations #2 from the first 16 survey profiles and so forth.

We first run a series of inversions in TM mode only with 5% error in the resistivity and 2.5% in phase for the survey profiles and pseudo profiles. From hereforth when the word profile is use alone, it means the Titan 24 survey profiles while when the word pseudo-profile is used, it represents the profiles that are perpendicular to the survey profiles. This is to compare the inversion results from two different directions and to see if they recover similar structures. We used 3 types of data; the original uncorrected MT data, the original data with static shift correction type 1 and the original data with static shift correction type 2.

The static shift correction consists of vertically shifting all the data points so that the apparent resistivity at the highest frequency of each station is the same for TE and TM mode. This value is calculated by averaging all the values at this particular frequency. Type 1 consists of a standard mean while type 2 consists of a logmean averaging system. For our inversions, our highest frequency is 1 kHz. The apparent resistivity values at this frequency are 4 051 Ω·m and 1 122 Ω·m, for standard mean and logmean, respectively. A high misfit can be observed for pseudo profiles 43 and 44, (Figure 6-5: right).

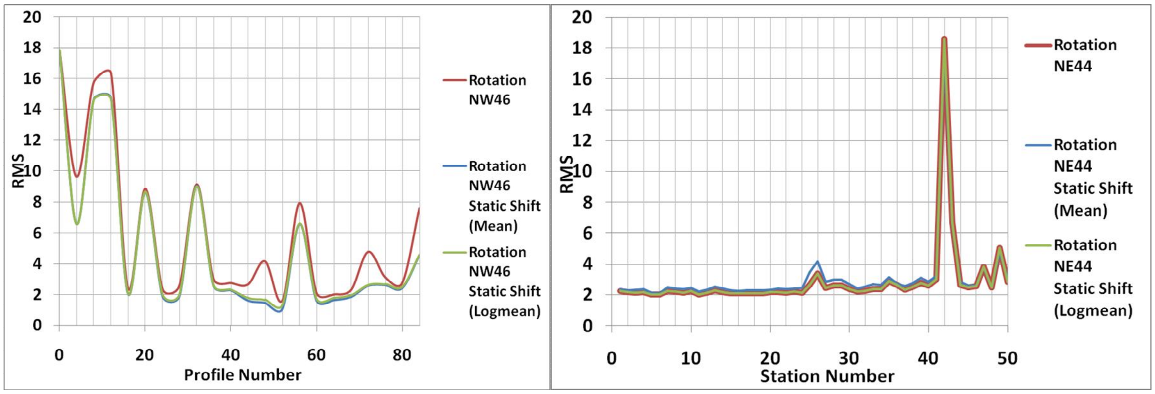

Figure 6-5 : RMS values for the profile (left) and the pseudo-profiles (right) inversion in TM mode. Each data type undergoes a few hundred iterations in TM mode.

The inversions done with profiles and pseudo-profiles generate coherent results. As seen in figures 6-6, at a depth of 100m, a zone of high resistivity is located across profiles L0E to L18E. A zone of lower resistivity can be found across profiles L28E to L80E. The area appears to contain localized 2D regions. Similar results were observed at a depth of 250m. At a depth of 500m, we observe a change in the subterrean structures and it appears to be 3D as no clear structures or strikes can be seen. Nevertheless, inverted resistivity models obtained along the MT survey profiles and the pseudo-profiles yield consistent results. This tells us that the inversions done along either direction (parallel or perpendicular to the strike) will produce similar results.

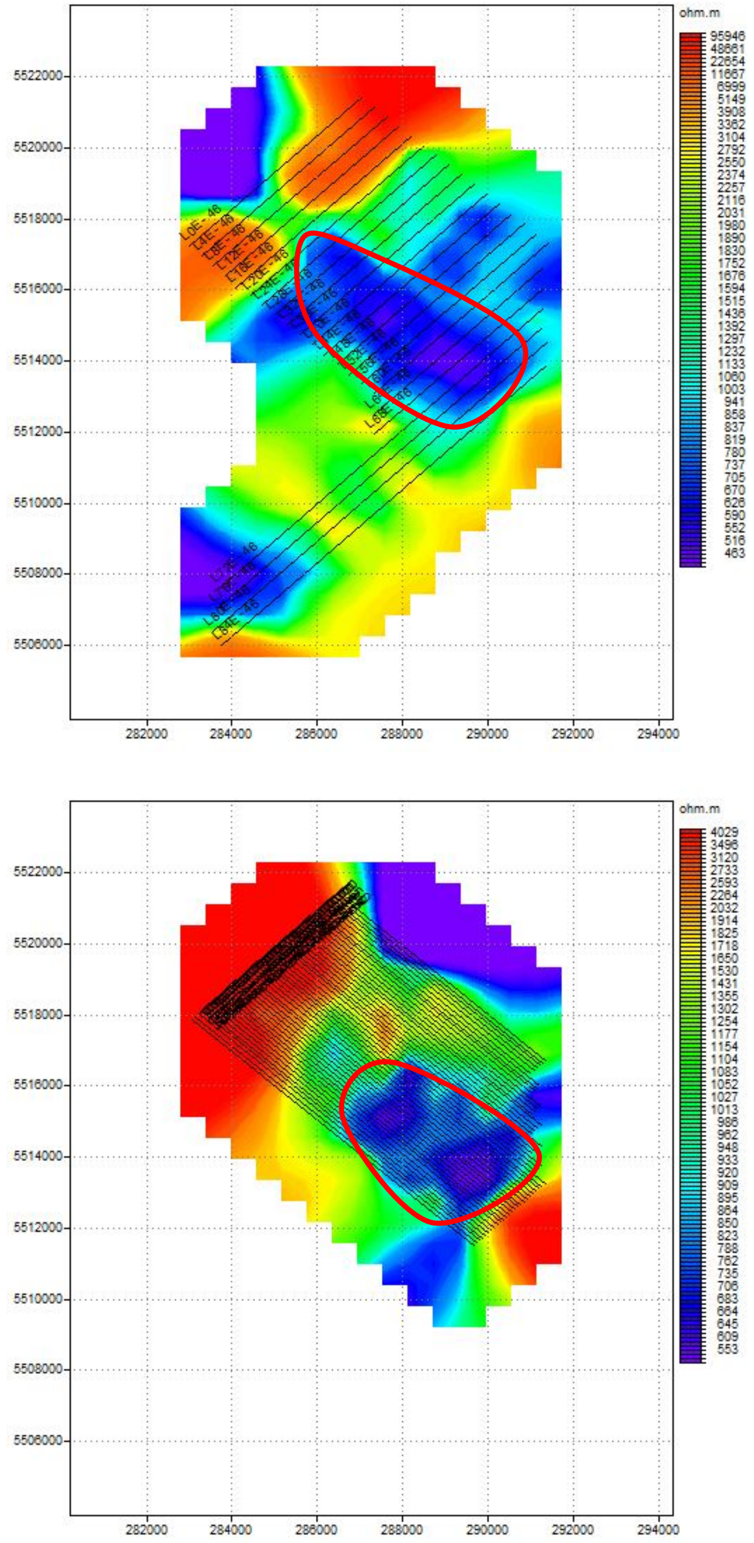

Figure 6-6 : Depth = 100m - TM mode inversion (Top to Bottom). Inversions run with survey profiles and pseudo-profiles.

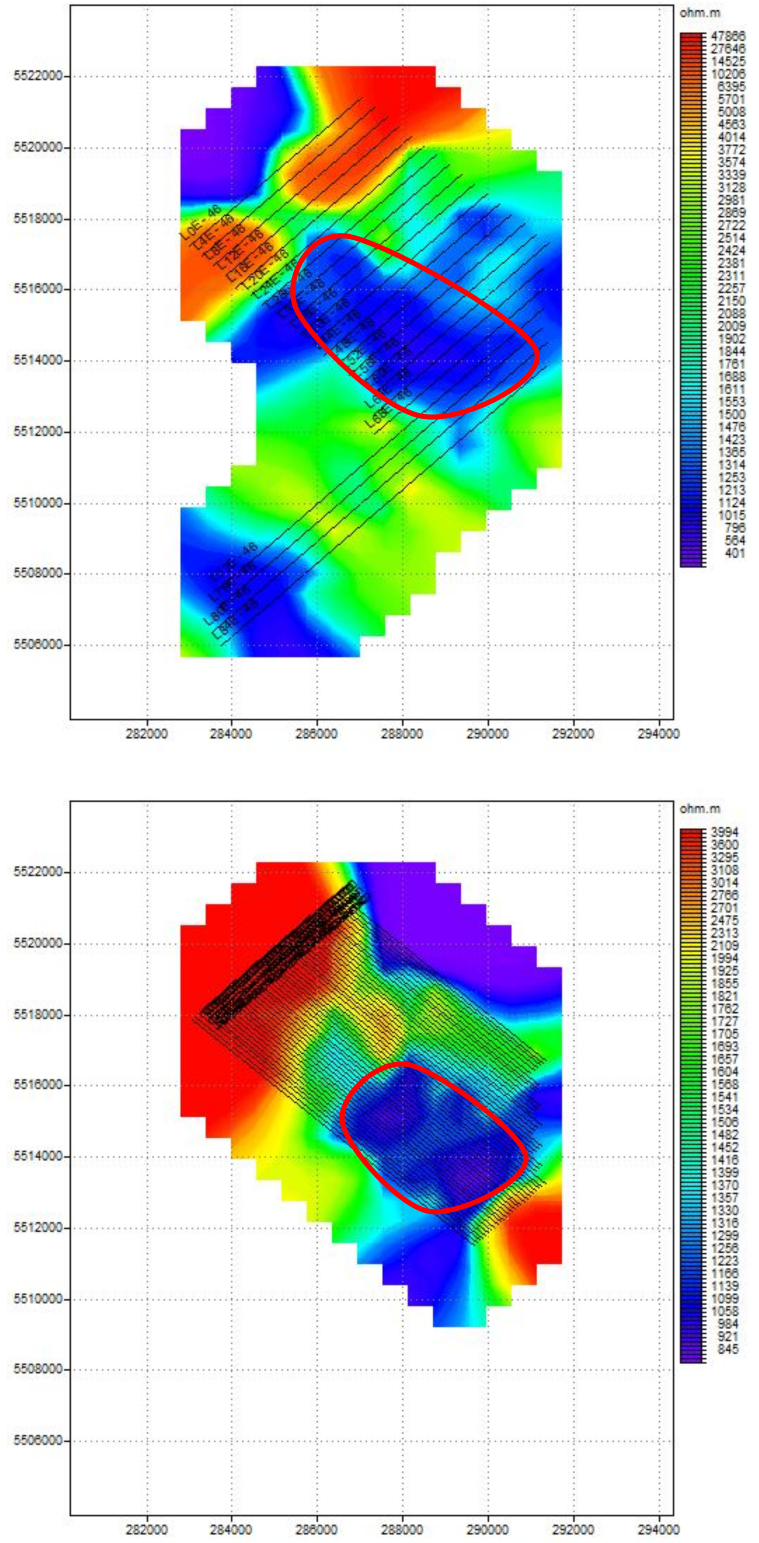

Figure 6-7 : Depth = 250m - TM mode inversion (Top to Bottom). Inversions run with survey profiles and pseudo-profiles.

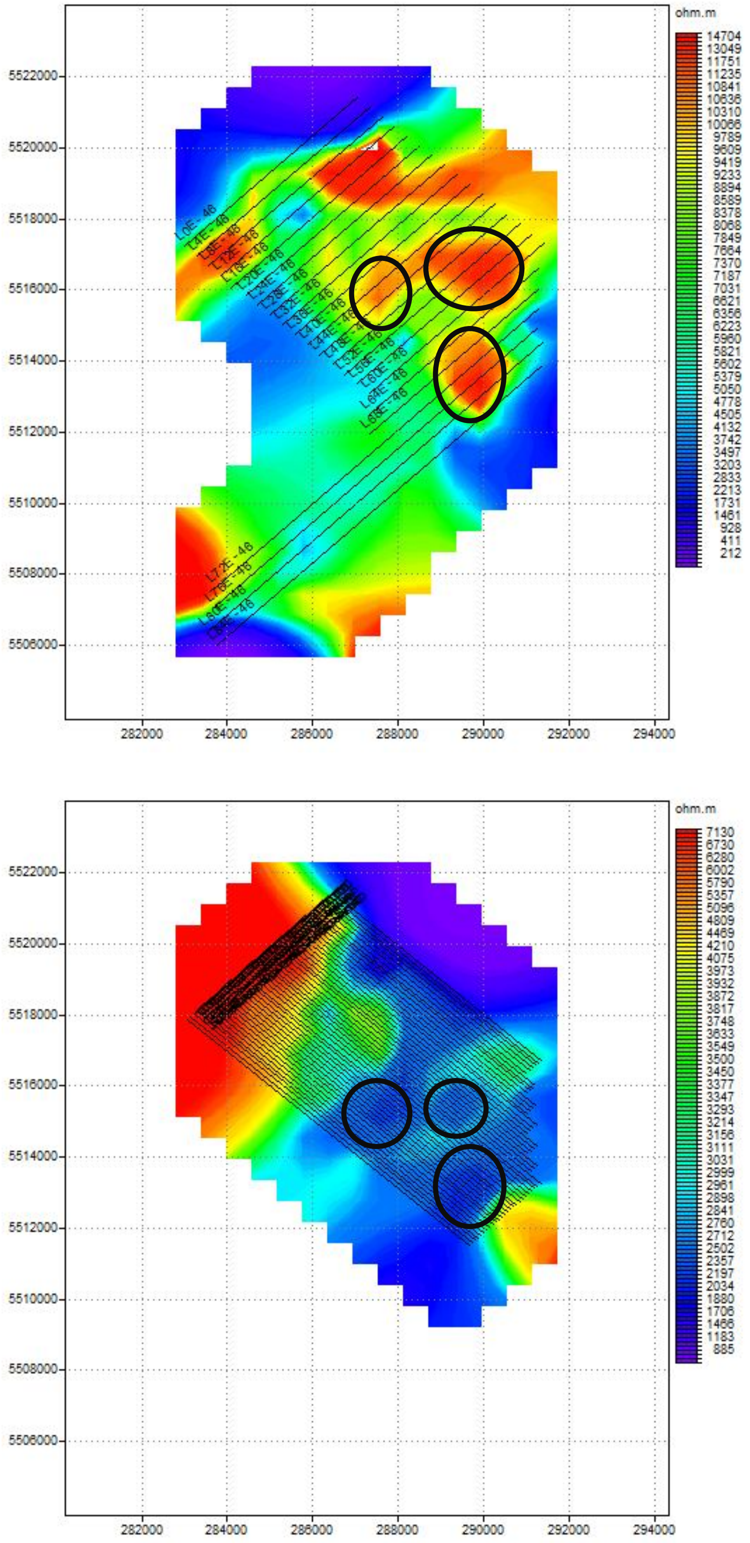

Figure 6-8 : Depth = 500m - TM mode inversion (Top to Bottom).
Inversions run with survey profiles and pseudo-profiles.

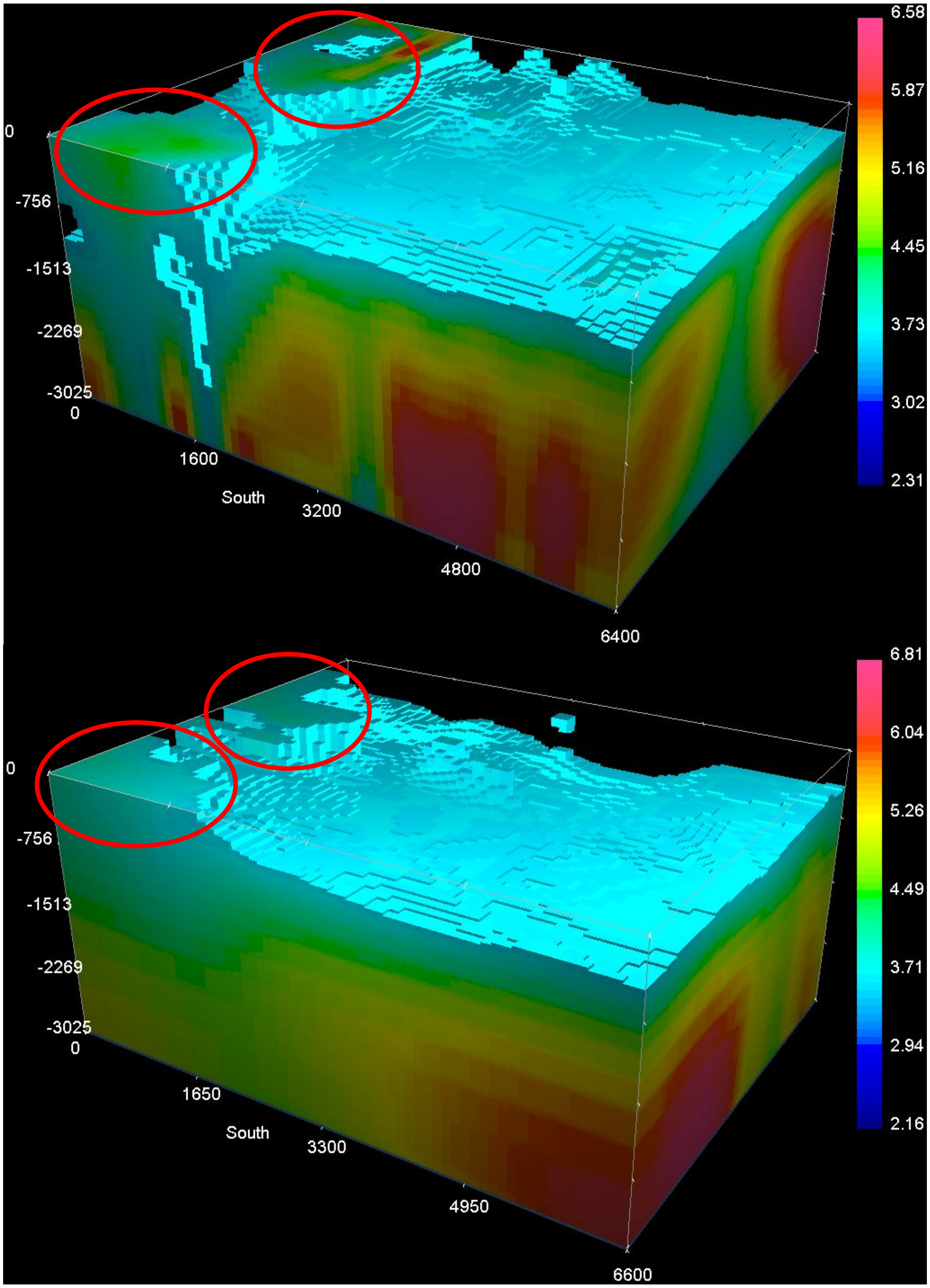

Figure 6-9 : 2D inversion (TM mode) results interpolated into 3D models with a minimum cut off of 4 kΩ·m. Top: Survey profiles. Bottom: Pseudo-profiles. Of particular interest, high resistivity zones in west side of the MT survey zone.

6.5.2 TE & TM Inversion Analysis

All 3 inversion procedures yield similar rms values as those found in the previous section. Regardless of which inversion procedure we used, most of the profiles converge to a specific rms value. The adjustment is better since the highest rms obtained here is 5.75 while in previous stations the highest rms value for TM inversions is 17.86. There are several factors such as inversion mesh size and different inversion steps that can produce different results and quality.

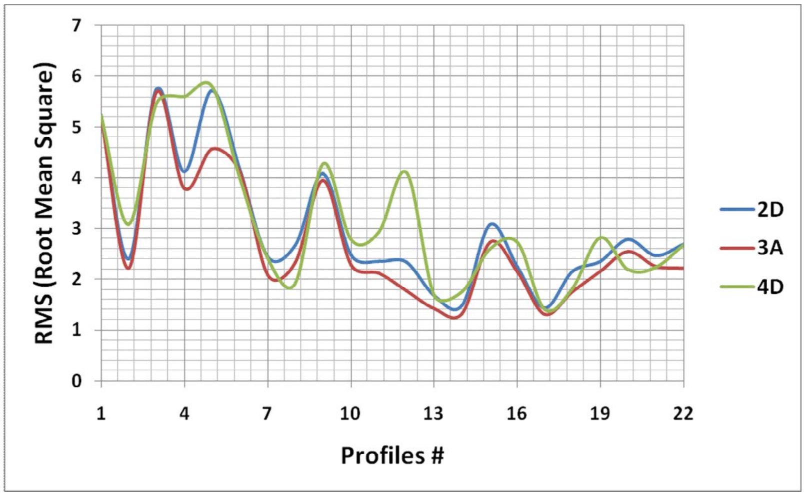

Figure 6-10 : RMS values for the profile in TE and TM modes.

There is a good correlation between the 3 different types of inversions. Profiles located on the left (starting with L0E….) are located in a region with a more resistant overburden, while the region becomes more conductive toward the South (Profile L60E). This can be observed in figures 6-11, for setting 1. The resistivity map for setting 2 and 3 can be found in appendix 6. At the depth of 500 m, the resistivity in the range of 10 kΩ·m is observed for all 3 models (see figure 6-13 and appendix Fig. 31). The medium seems to be homogenous and it corresponds well with the resistivity found in boreholes for upper basalt. At the depth of 1 km, 1.5 km and 2 km, the models retain similar shape (see figures 6-13, 6-14 and appendix fig. 32 to 34). At a depth of 1 500 m some resistant structures are noted. Distinct vertical structures are found in all 3 settings. They generated structures that appear to overlap over one another. At a depth of 2 000 m, continuation of resistive structures can be seen in figures 6-14 and in appendix fig. 34.

The three different inversion procedures produced a 3D model with 3 distinct non-uniform layers. The first layer has a resistivity of ranging 1 kΩ·m to 10 kΩ·m and it can be associated as the overburden with altered bedrock. The second layer has a resistivity ranging from 10 kΩ·m to 100 kΩ·m and it can be associated with the upper gabbro. The upper gabbro reaches down to about 1 km to 1.5 km deep and in some parts down to 2 km deep. The third layer begins right after the upper gabbro and possesses resistivity greater than 100 kΩ·m. Since the MT survey profiles are about 5 km in legnth, beyond the depth of 5 000 m the resolution is greatly decreased, therefore we introduced the 1D model produced by Tournerie and Chouteau (1998) and indicated in table 7.1 of chapter 7.

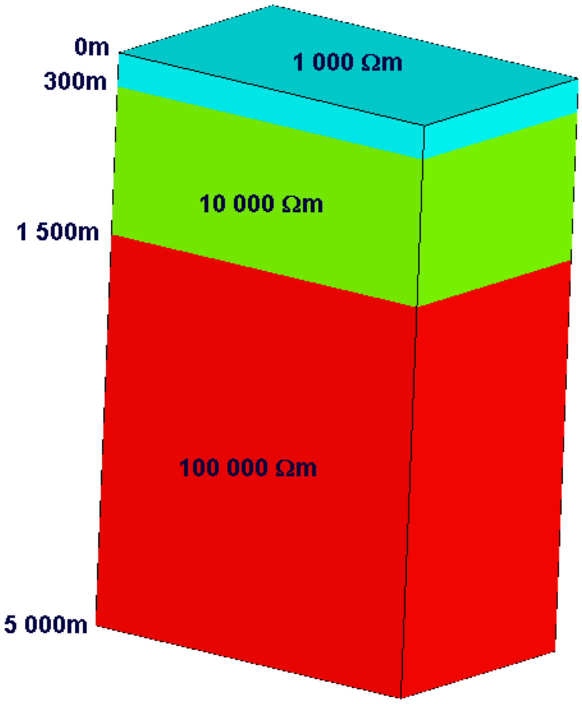

Figure 6-11. Simple representation of the 3D models. The actual layers are non-uniform and have curvature and structures of various sizes and dimensions.

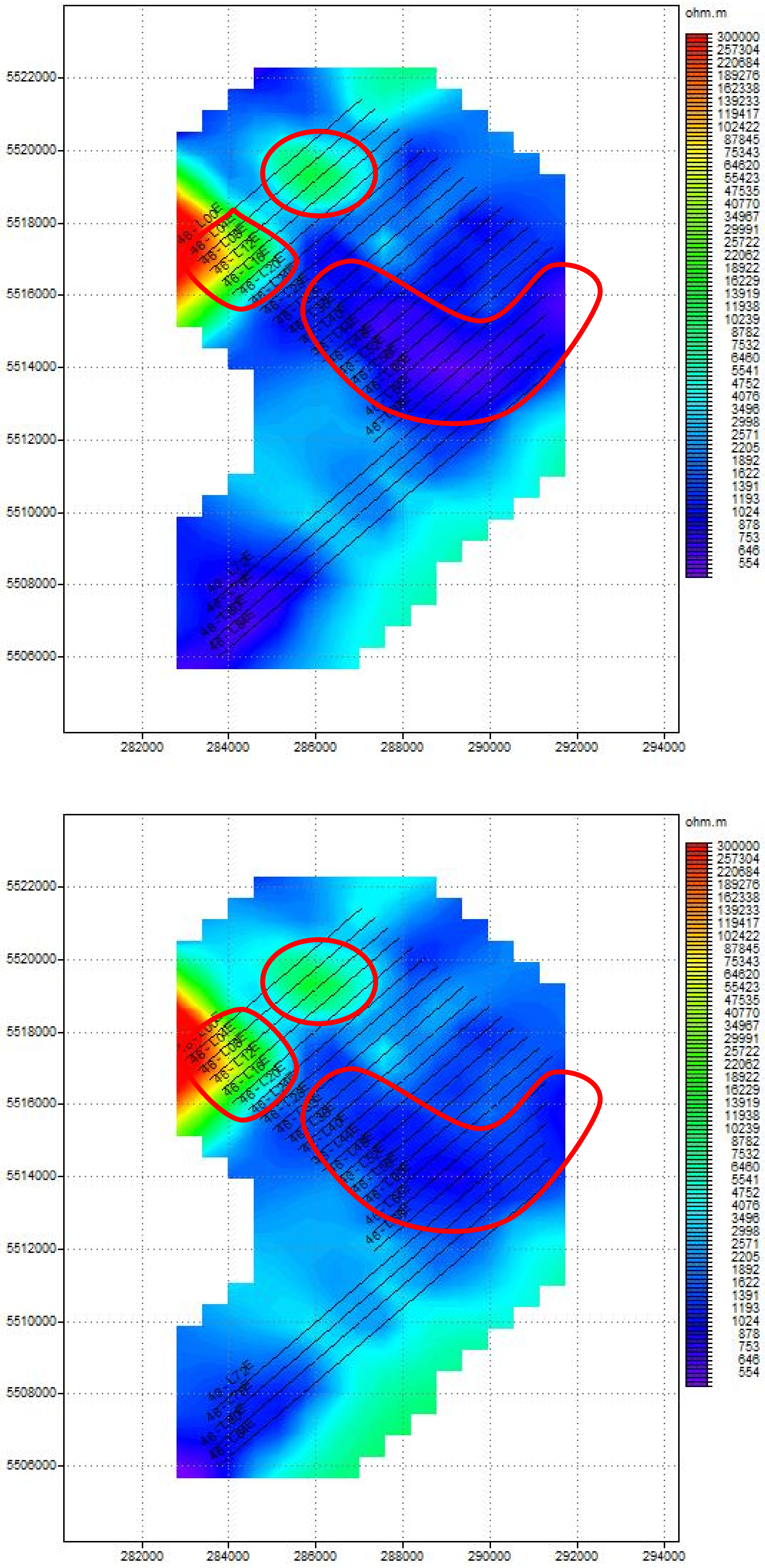

Figure 6-12 : Inversion resistivity maps for setting 1 at depths of 100m and 250m (top-bottom).

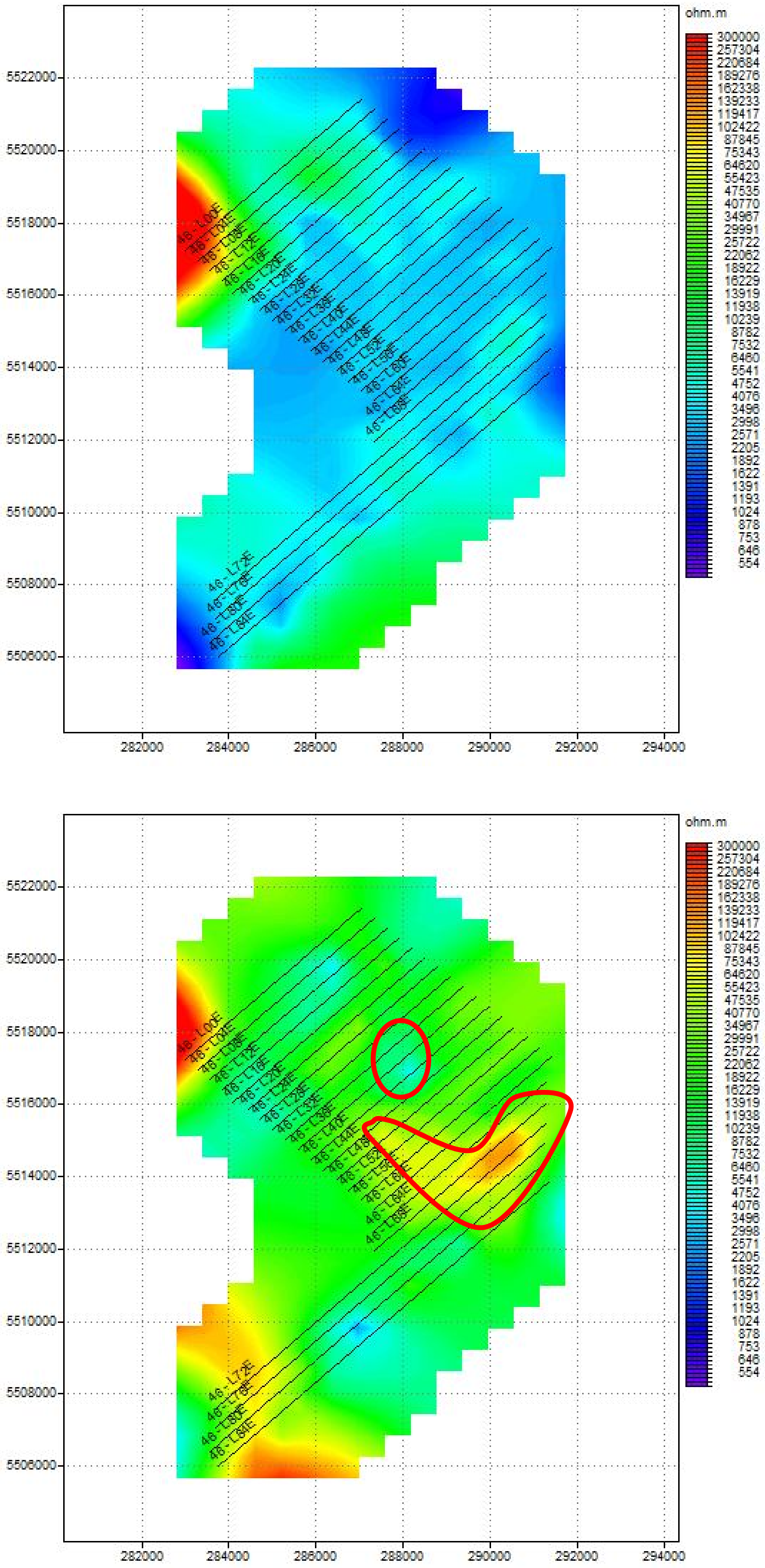

Figure 6-13 : Inversion resistivity maps for setting 1 at depths of 500m and 1000m (top-bottom).

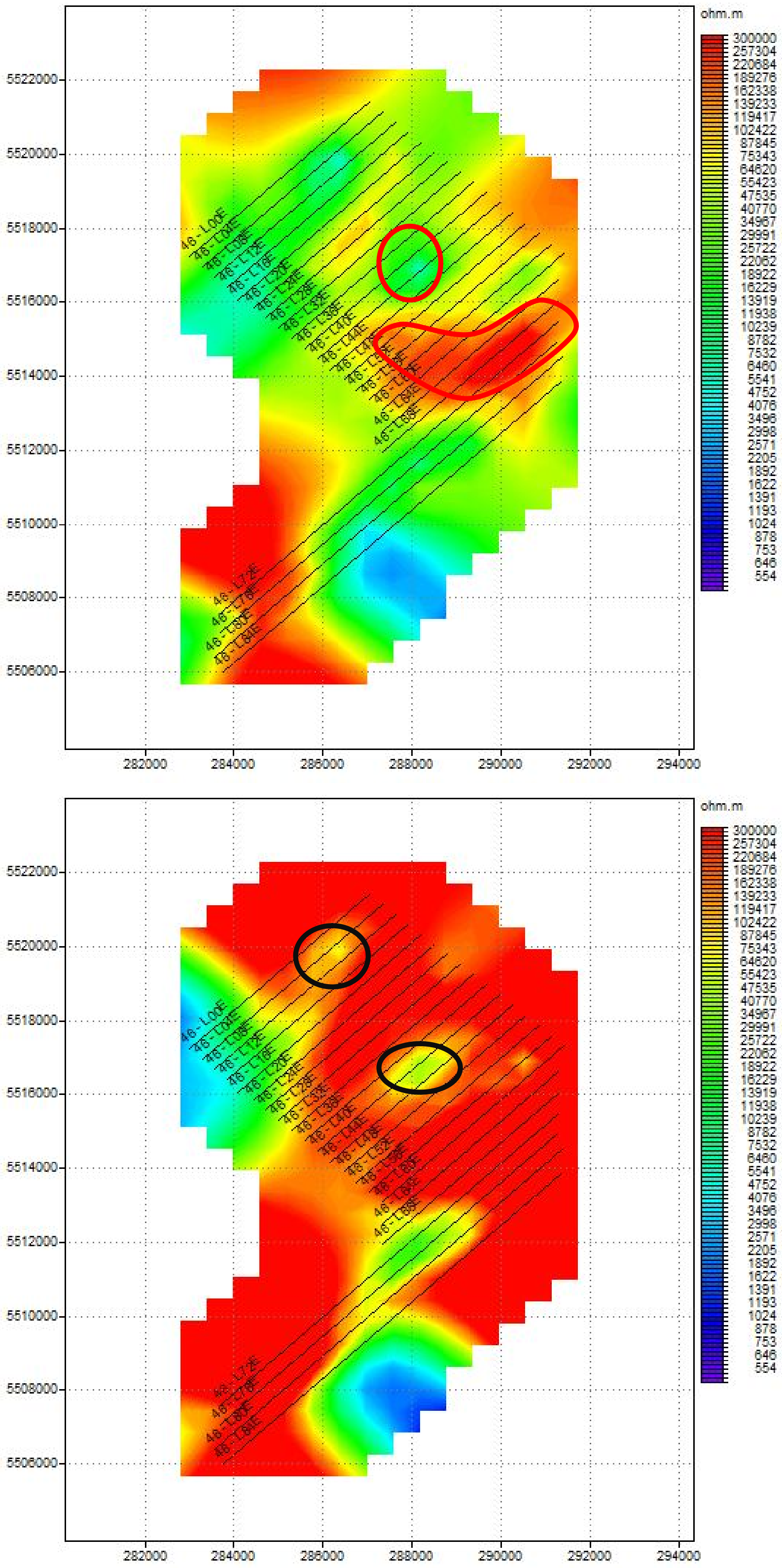

Figure 6-14 : Inversion resistivity maps for setting 1 at depths of 1500m and 2000m (top-bottom).

All 3 settings generated models that have very similar geological features for the first kilometer. Three structures of high resisitivity (greater than 4 kΩ·m) are observed. They are located in the West side of the MT survey and they are encircled in red in figures 6-15, 6-16 and 6-17. The remaining area corresponds well to the inital model of three distinct layers. At a depth of 2 km and beyond, vertical structures can be found in all 3 models. The same geological features are observed for interpolated 2D inversion results with TM mode only (figure 6-9).

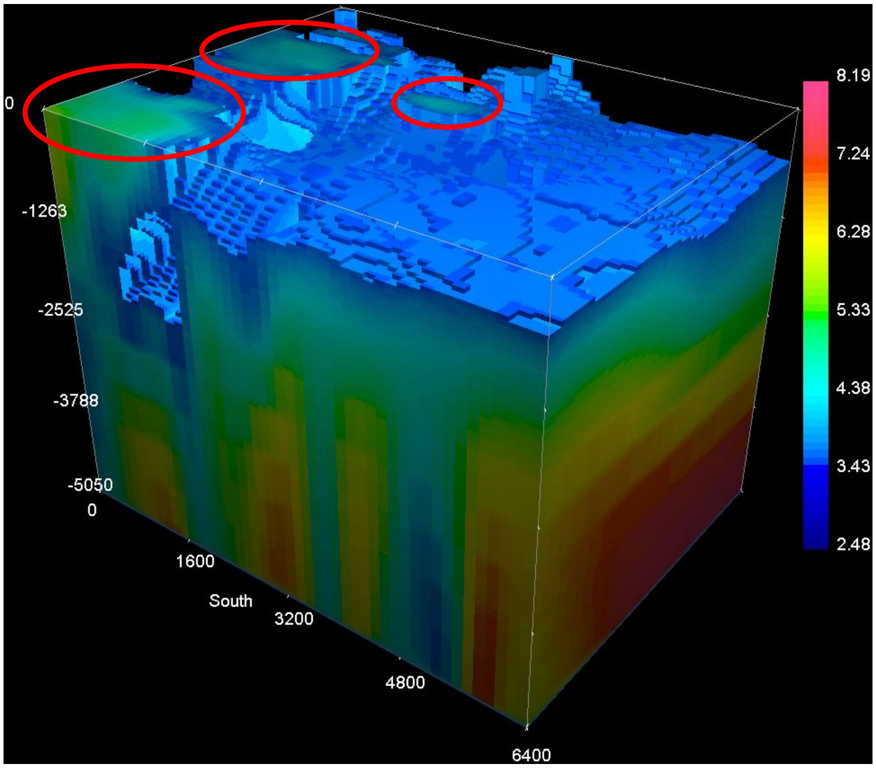

Figure 6-15 : 2D inversion (setting 1) results interpolated into 3D models with a minimum cut off of 4 KΩ·m.

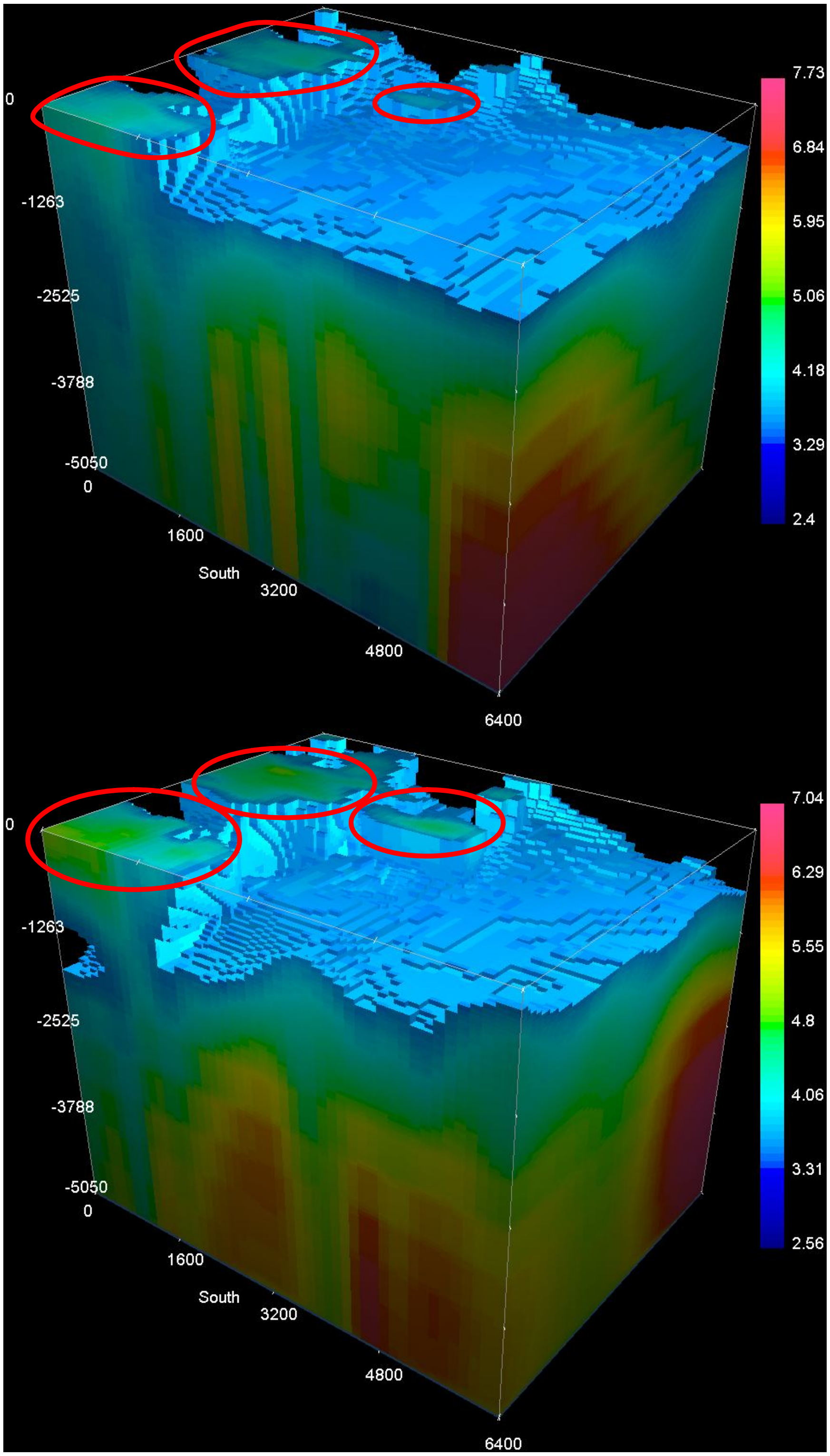

Figure 6-16 : 2D inversion results interpolated into 3D models with a minimum cut off of 4 kΩ·m. Top: Setting 2. Bottom: Setting 3.

6.5.3 Static-Shift Corrections

In previous section, strong static-shift correction was done during the 2D inversion process. In this section, the data have being corrected for static-shift prior to 2D inversions. Static-shift correction was done on the magnetotelluric data by normalising the impedances at high frequency. Normalising was done by finding the geometric mean of Zxy and Zyx at that particular frequency. For Titan 24 data, the geometric mean is 1122 Ω·m for the xy and yx impedances at frequency of 1 kHz. 2D inversions were done for the TM mode, the TE-TM mode, the survey profiles and the pseudo profiles.

Inversions done for survey profiles and pseudo-profiles show results that are similar to those observed in the previous section. They contain a thin layer of low resistivity, followed by a resistivity layer of the order of 10^3-10^4 Ω·m that reaches down to 1.5 km deep. We noticed that at the west side of the model, the high resisitivity structures seen in previous section are missing. In addition, two limited shallow resistivity zones are identified (circled in red in figure 6-17 and 6-18). The effects are more pronounced for the 2D inversions done with the survey profiles. Footprints of these zones can be found in the 2D inversions done with the pseudo-profiles. We know that static shifts can be a severe problem in MT soundings. If they are not properly corrected, they could lead to misleading interpretation, therefore we argue the validity of these inversion results.

To validate this, 3D inversion needs to be done on the Titan 24 MT soundings and this is due to two important reasons: the first reason is that 3D inversion includes the extra Z_{XX} and Z_{YY} impedances thus providing more adequate information on geometry of subsurface structure. The second reason is that 2D models produced through 2D MT inversion for 3D MT data, are an approximate representation of the 3D region, 2D inversion requires a TE and TM mode and the strike direction. The strike direction is obtained by estimating and correcting for noise and distortions effects. The estimated strike is used to estimate TE and TM resistivities for the 2D inversion. If the strike direction isn't properly determined, the 2D inversion models could be wrongly misinterpreted, whereas 3D MT inversion doesn't have this problem.

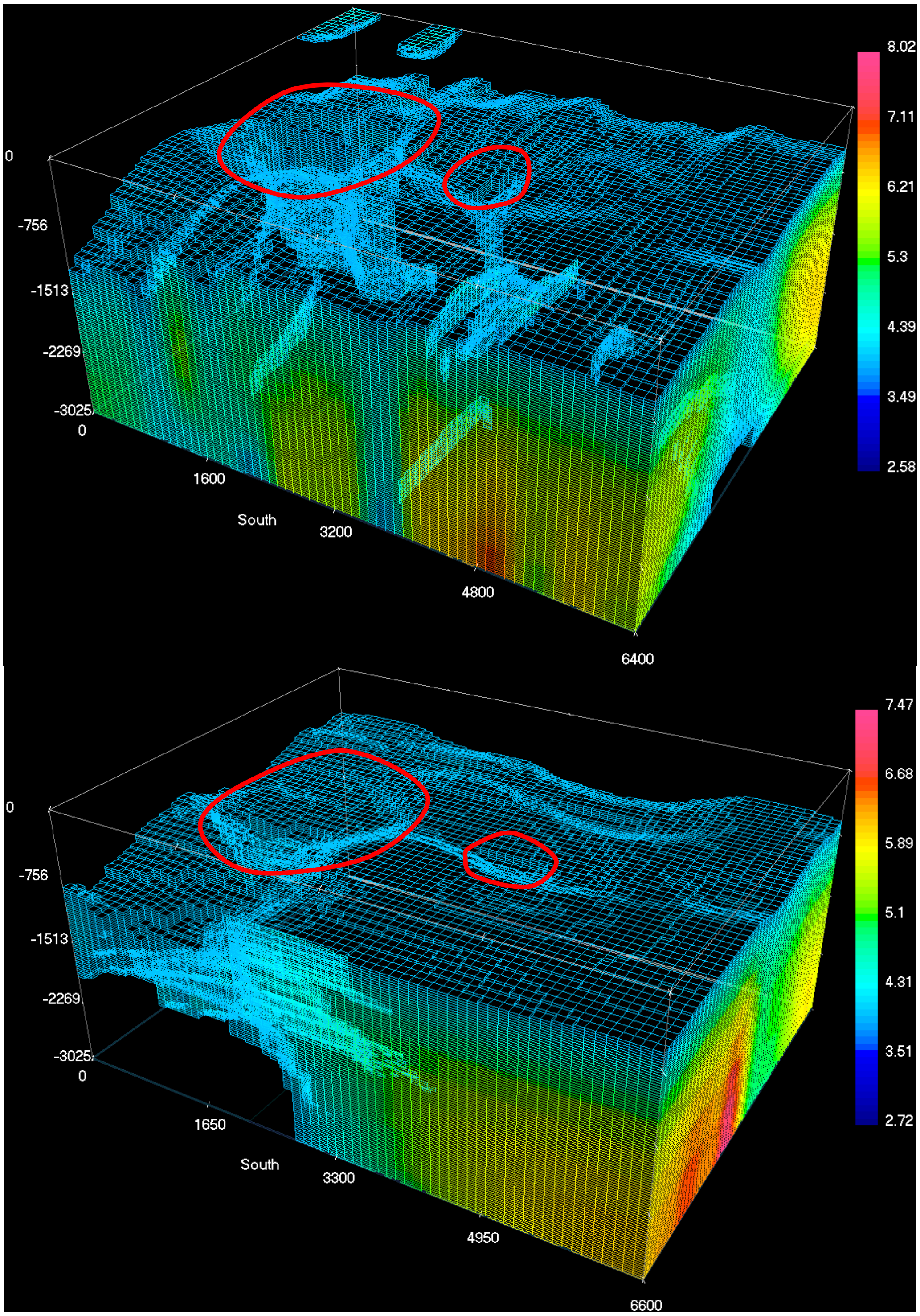

Figure 6-17 : 2D inversion results (TM+TE mode) interpolated into 3D models with a minimum cut-off of 4 kΩ·m. Top: Survey profiles. Bottom: Pseudo profiles.

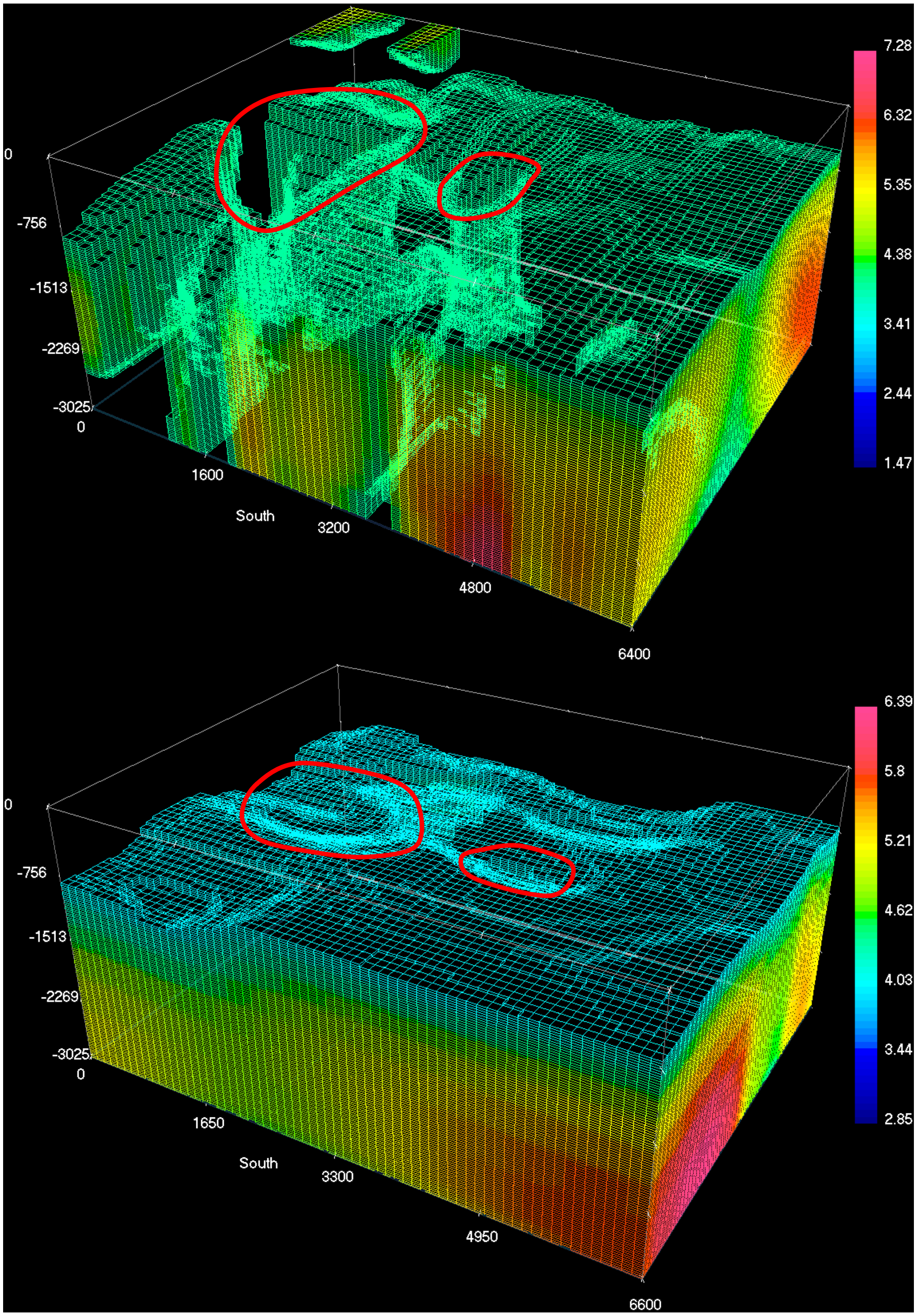

Figure 6-18 : 2D inversion results (TM mode) interpolated into 3D models with a minimum cut-off of 4 kΩ·m. Top: Survey profiles. Bottom: Pseudo profiles.

6.5.4 Correlation between IP, Resistivity and Phase

Correlation was noted between the chargeability magnitude obtained from IP surveys and the low-frequency impedance phase from coincident MT surveys (figure 1-2). Part of this thesis aims in interpreting the IP anomalies found in UBC inversion (figure 6-19, circled in yellow).

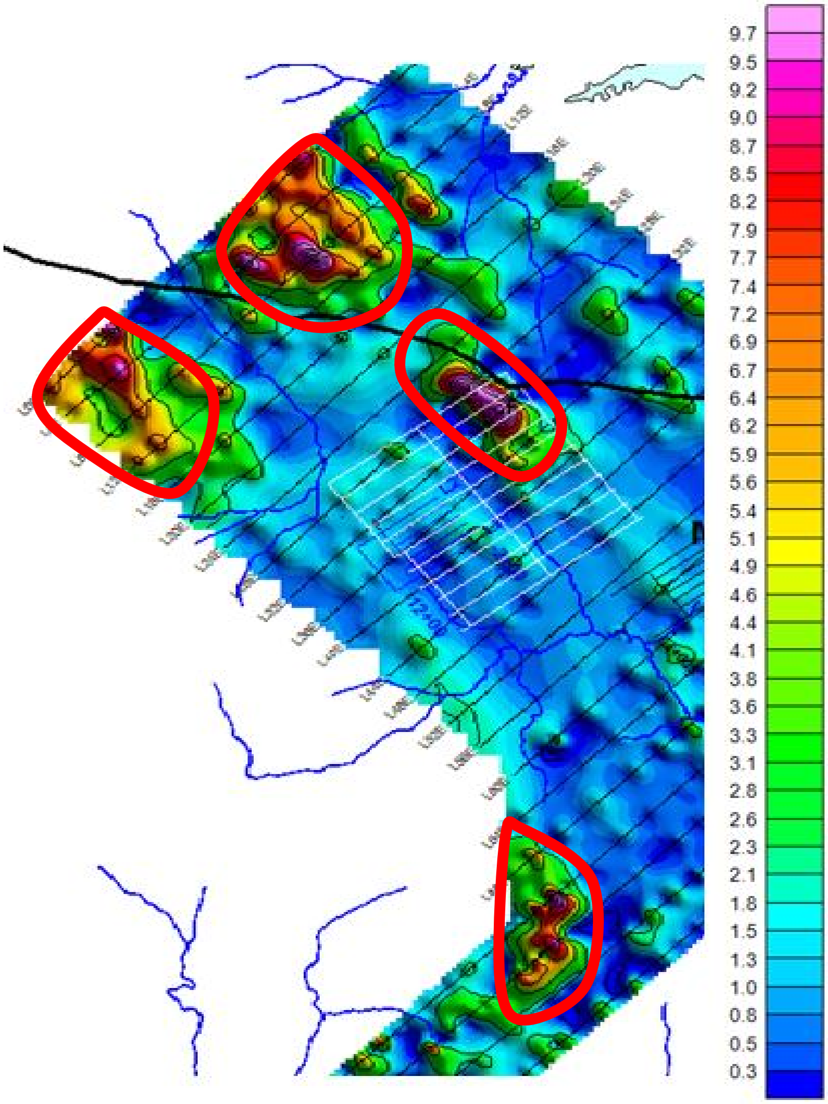

Figure 6-19 : IP measured with the Titan-24. Result of the UBC inversion at 100m depth view.. Picture provided by M. Allard, senior geophysicist with Xstrata Zinc.

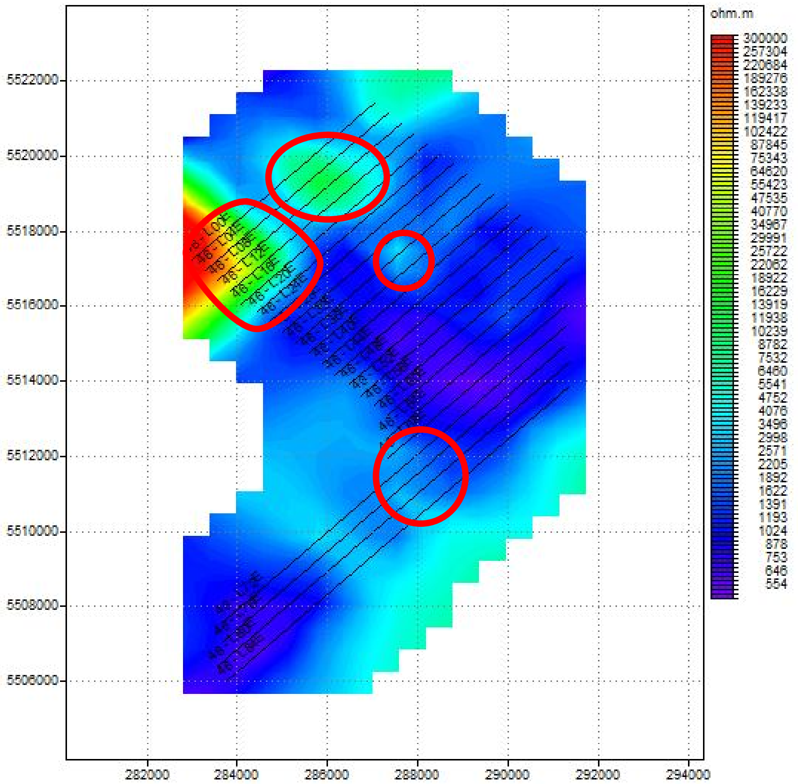

Figure 6-20 : 2D Resistivity map at depth of 100m for setting 1.

Strong correlations are found between the IP anomalies and the resistivity maps at depth of 100m. The location of the anomalies coincides with the high resistivity regions we found in our 2D inversions. Furthermore, they are located in the same region as where the limited shallow resistivity zones are identified in the 2D inversion of static-shift corrected MT data (section 6.5.3). The IP anomalies seem to indicate the presence of large resistive structures, like those found in 2D inversion (section 6.5.2). Looking at the invariant resistivity and phase map at depth of 100m, further confirm that these IP anomalies are located at sites of high resistivity materials. The reason for the IP anomalies is thought to be related to the sulphide dissemination within the bedrock. High resistivity of the bedrock enhances the weak IP response from the subsurface at sites where the glacial cover is thin while it decreases the IP response in places where the non-polarizable overburden is thick.

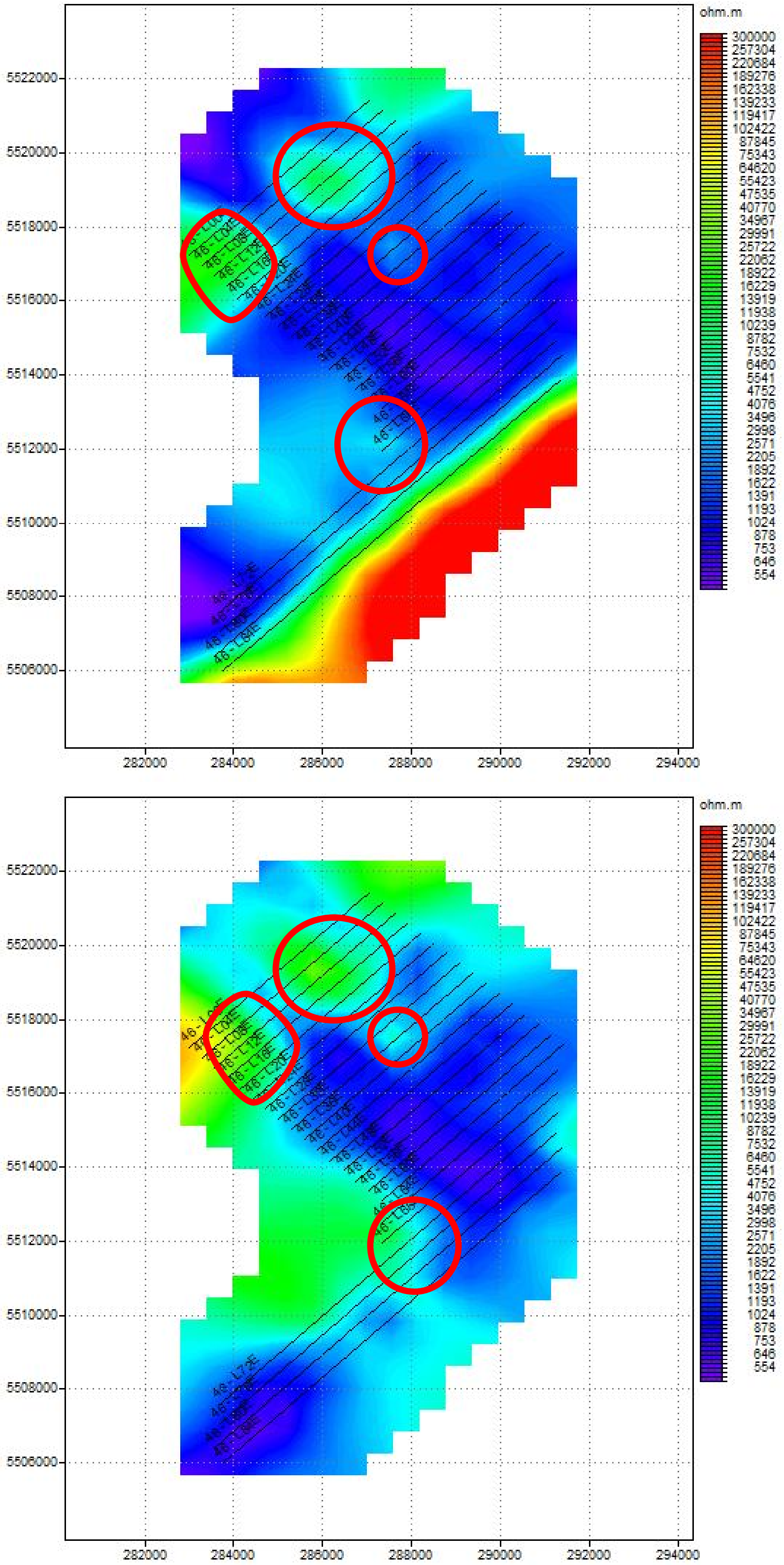

Figure 6-21 : 2D Resistivity maps at depth of 100m. Top: Setting 2. Bottom: Setting 3.

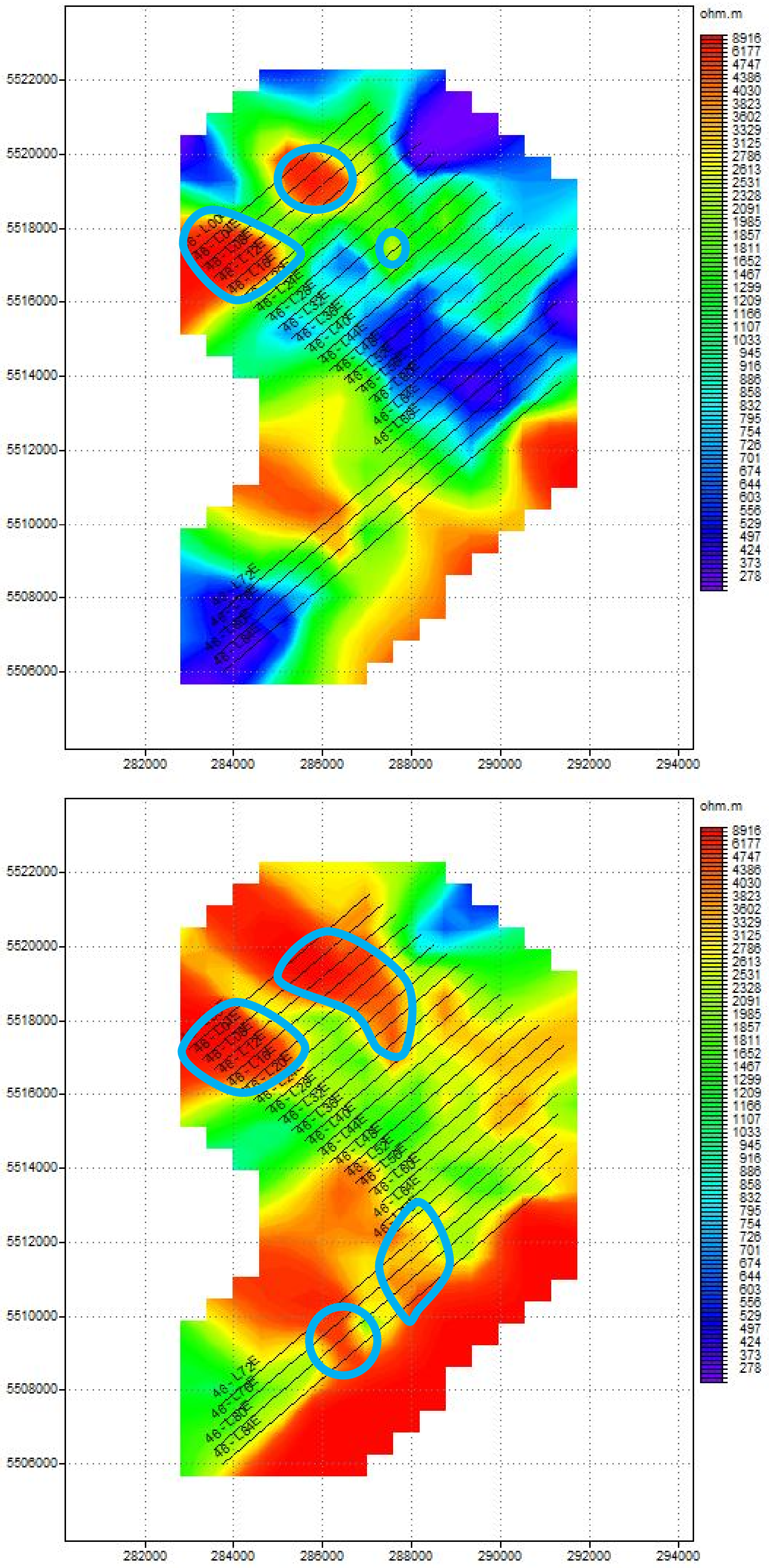

Figure 6-22 : 2D Invariant resistivity maps at frequency of 1 kHz and 1 Hz (top and bottom).

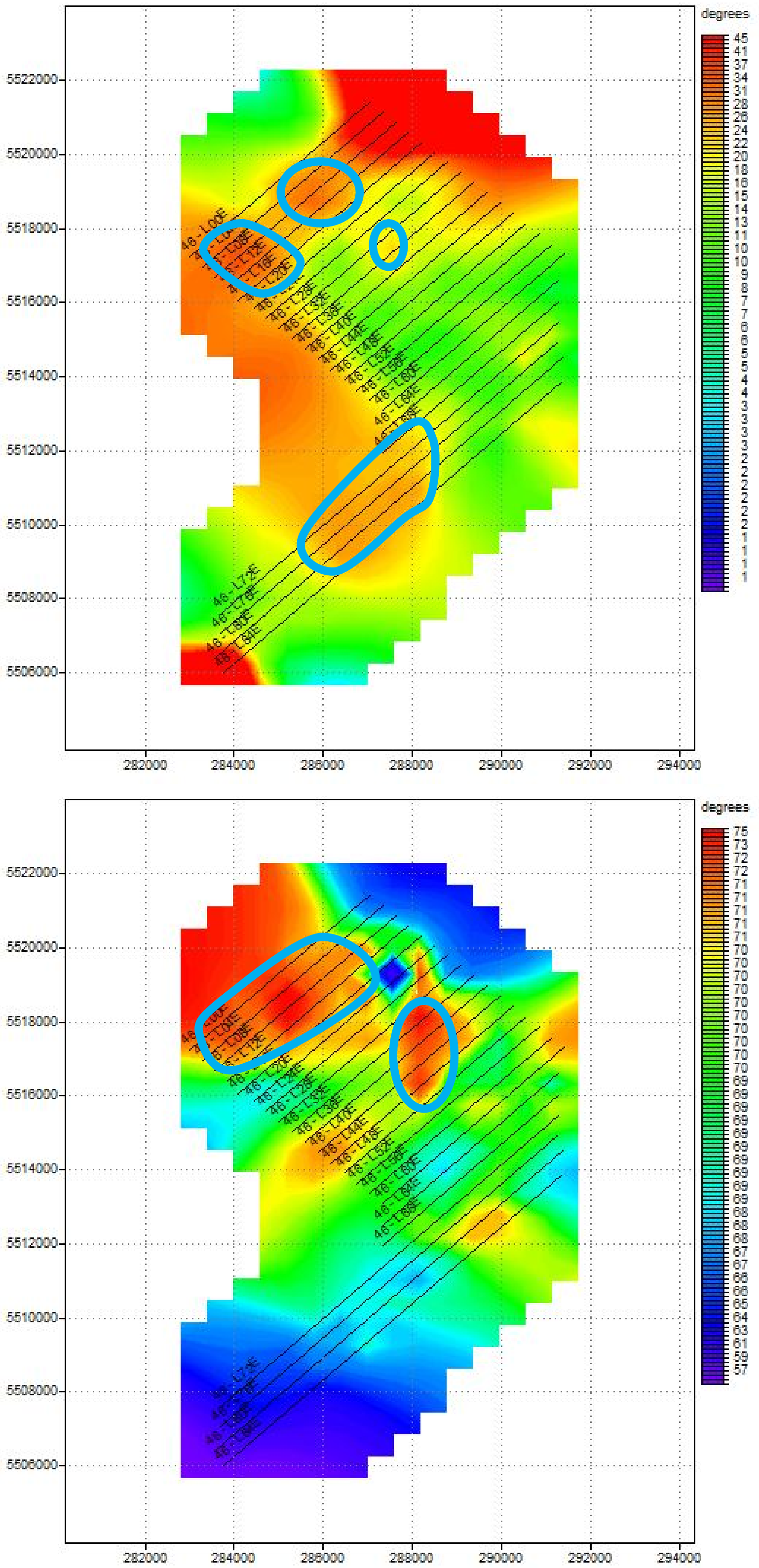

Figure 6-23 : 2D Invariant Phase maps at frequency of 1 kHz and 1 Hz (top and bottom).

6.5.1 MT Correlation with the Geology and Gravity/Magnetic Methods

A MT survey was done in the southern flank of the Matagami mining camp. Because the stratigraphy ressembles to those found in sectors of productivity, Xstrata Zinc was hoping to find ore bodies in the southern flank region. The assumption was that the rocks located beneath the surface ressemble to those hosting mines located in the southern flank region. In figure 6-24, geology of the MT survey area consists mainly of basalt, granite and gabbro intrusions, and rhyolite patches. There was no correlation between the MT results and the rock type. The MT was not able to distinguishe those rock types due to the similarity in their resistivity values.

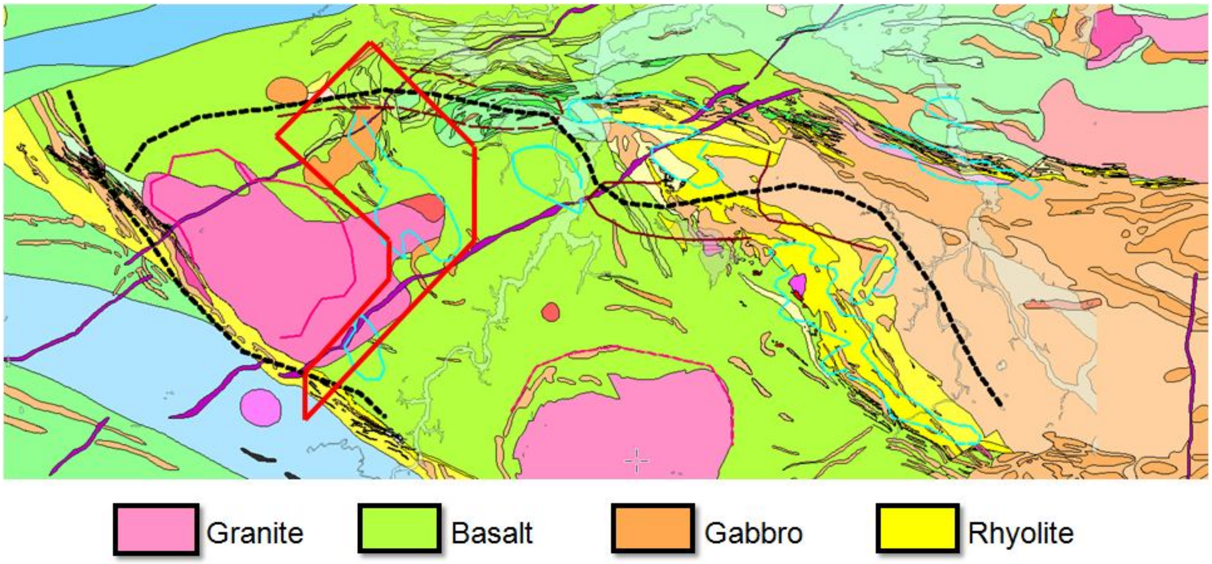

Figure 6-24 : Matagami geological map. MT Survey region is confined within the red line.

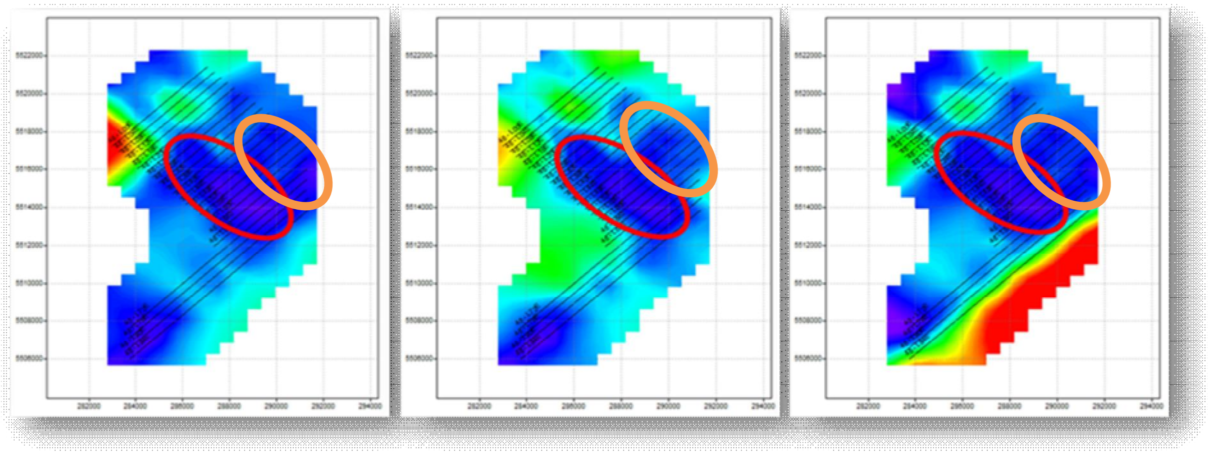

Figure 6-25 : Left to Right: Resistivity maps for 3D model 1, 2 and 3 at a depth of 100 m.

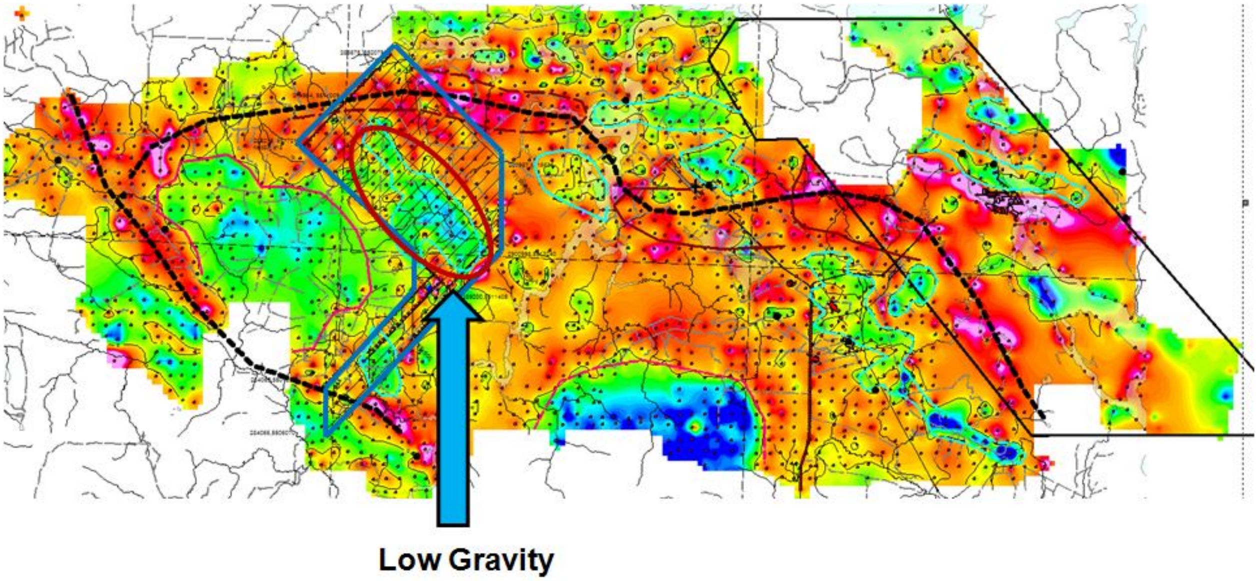

Figure 6-26 : Gravity map of the Matagami southern flank region. MT Survey region is confined within the blue line. Low gravity found in the MT survey region is delimited by a red circle.

Correlation was found between the gravity map and our 3D models. Regions of lower resistivity values, indicated by the red ellipsoids of figure 6-25, correspond to the region of gravity low anomaly in figure 6-26. The gravity low anomaly can be related to the thickening of the overburden layer shown in figure 6-27 left (indicated by the dark line). The overburden thickness map was interpreted from Megatem time domanin EM data and log data from a few available boreholes. With appropriate analysis of the MT data the overburden can be mapped more efectively than by gravity method. Furthermore, the topography shows two hills located on the NorthWest of the MT survey with a valley in between (figure 6-27 left: red arrow point the valley that is located between the two hills in red and purple). The MT models feature resistivity highs related to the topography high causing resistive bedrock to outcrop.

Strong correlations can be deduced between the thickness of the overburden (figure 6-27 right) and the 3D MT models (figure 6-28). Correlation such as area where the overburden is thin, the MT shows structures of higher resistivty are located closer to the surface. For area where the overburden is thicker, the MT shows a lower resistivity value for the first few hundred meters.

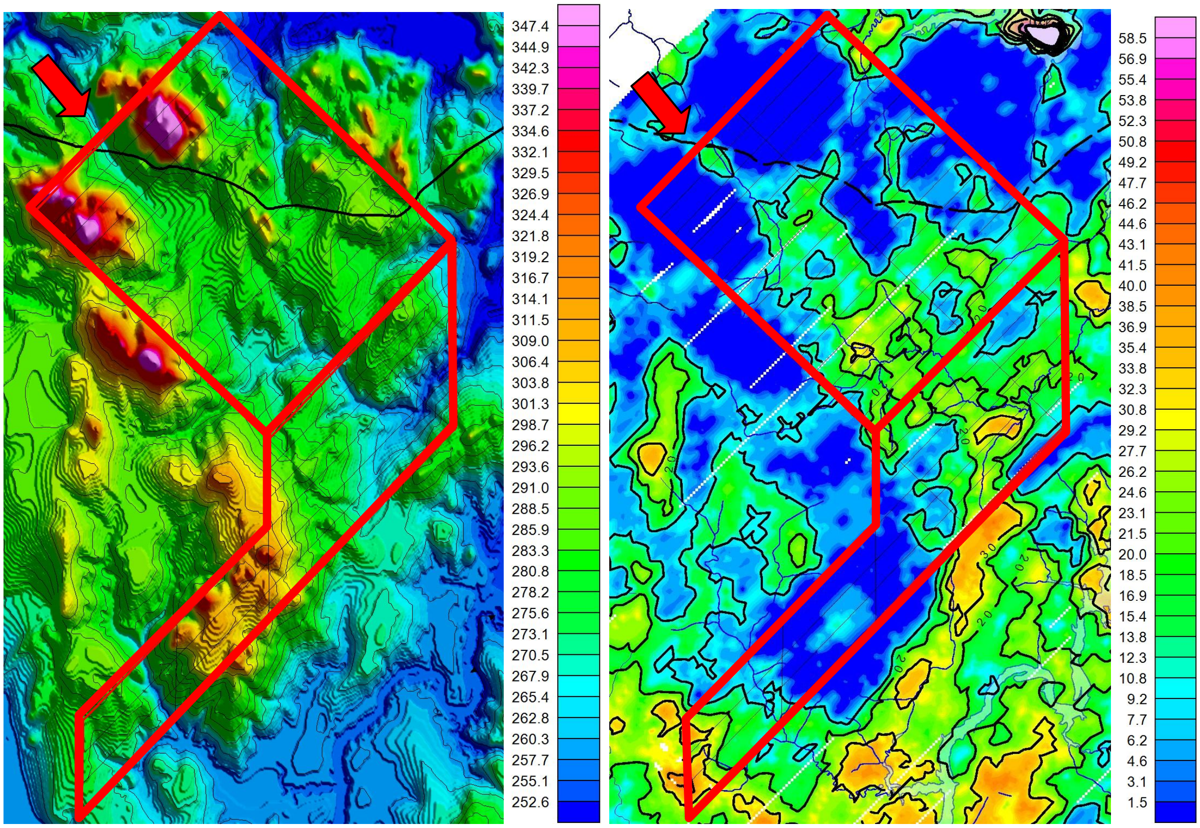

Figure 6-27 : Left: Map showing the topography located in the MT survey area. Right: Map showing the overburden thickness. The MT survey area is delimited in red. The 3D MT models correspond to region bounded by the red rectangle.

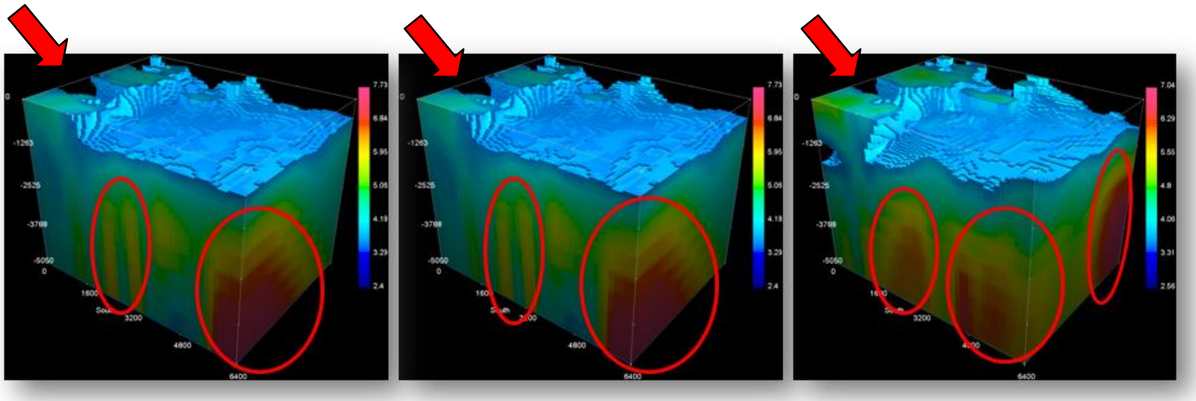

Figure 6-28 : 3D models produced through interpolating 2D inversion results. Left to Right: 3D model 1, 2 and 3. Resistivity cut off at 4 kΩ·m.

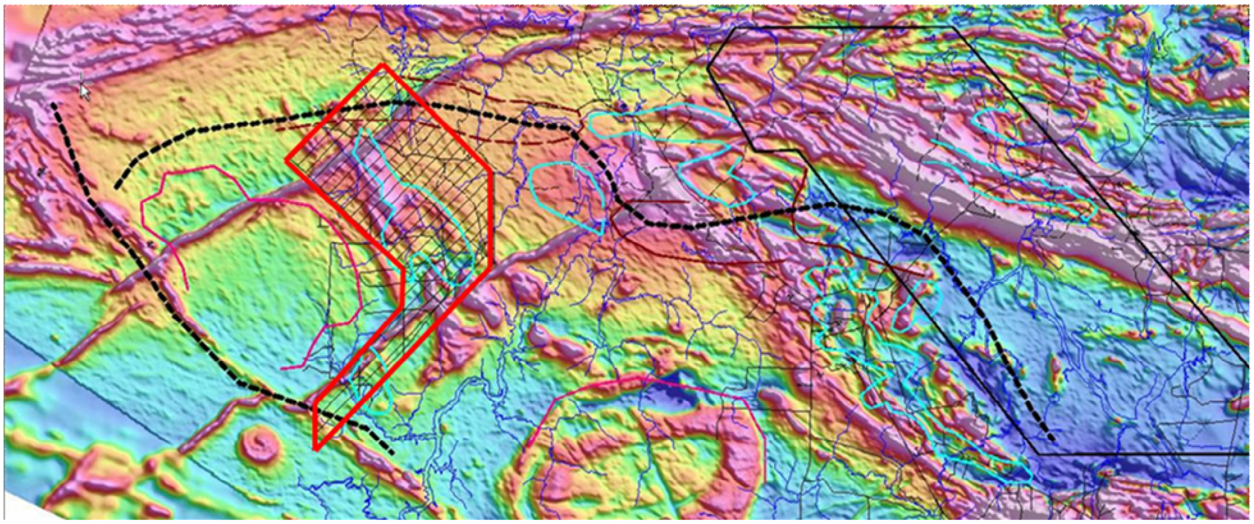

Figure 6-29 : Magnetic map of the Matagami region. MT Survey region is confined within the red line.

In figure 6-28 (circled in red), structures of very high resistivity can be observed at a depth of approximately 1.8 km and beyond. The resistivity is at an ordered of $10^5\Omega\cdot m$ or greater. Vertical structures of lesser resistivity are located in between these high resistivity structures and this can be better observed in figure 6-15 and 6-16. They could be related to structures imaged by magnetic anomalies as dikes and magmatic intrusions (seen in figure 6-29: purple color signifies high magnetic signature). As for the high resistivity level at depth, it could be related to the deep bedrock of rhyolite composition found in the boreholes located in the current and past Matagami mining camp (i.e. Orchan, Bracemac, Mcleoid and Bell Allard).

CHAPTER 7 3D MODELING

In this chapter we validate our 2D inversion results. UBC meshtool3d (Shekhtman, UBC, 2007) was used to combine the independent 2D inversion models into a 3D model. Three 3D models are created corresponding to the three different steps taken during the 2D inversion process. This allows us to visualize the regional geological structures in 3D. They showed consistency and have similar features for the first few hundred meters. A single light smoothing was done on the 3D model to avoid sudden abrupt changes in the resistivity. The MT response was then computed from these 3D models and compared with the Titan 24 survey data.

Winglink 3D forward-modeling code developed by Randy Mackie (Mackie et al, 1994) was used to calculate the MT response. This forward finite difference modeling code computes the magnetic and electric fields at the surface of a 3D resistivity model illuminated by EM plane waves. The fields computed by the forward modeling code are automatically converted to MT impedances for pre-positioned sounding stations. These can in turn be used to compare with the Titan 24 MT survey data and a conclusion can be drawn about how well the 3D models agree with the MT survey data.

7.1 3D Model Properties

The properties and the characteristics of the 3D models are defined in chapter 6.5. Resistivity from the 2D inversions was retained for depths from 0m to 5 000 m. From 5000m to 150 km a 1D model was used to recreate the earth’s crust at depths of 5 km and beyond. Properties of this 1D model can be found in table 7.1.

The 3D models are composed of 45 144 cells (x: 57, y: 24, z: 33). Cells are 100 m long and 400 m wide. The cell height depends on the depth and can be seen in table 7.2. Each model possesses a boundary condition in order to prevent a sharp contrast at the boundary of the 3D model region. The boundary condition was obtained by extending the resistivity that delimits the region of interest far enough so that the dimensionality of the region becomes 2D. This resulted in an extension of 106 km on each side.

Depth	Resistivity (Ω·m)	Start (m)	End (m)
Depth 1	10 000	5 000	15 000
Depth 2	1 000	15 000	30 000
Depth 3	100	30 000	80 000
Depth 4	10	80 000	100 000
Depth 5	1	100 000	150 000

Table 7.1 : Properties of the 1D model.

Size #	Cell height (meters)	Start (m)	End (m)
1	50	0	2 000
2	500	2 000	2 500
3	1 000	2 500	3 500
4	1 500	3 500	5 000
5	5 000	5 000	15 000
6	7 500	15 000	30 000
7	12 500	30 000	80 000
8	20 000	80 000	100 000
9	50 000	100 000	150 000

Table 7.2 : Variation of the 3D model cell heights with depth.

It is important to note that the 3D model created through the combination of 2D inversion models contains 475 104 cells (x: 48, y: 98, z: 101) not counting the addition of the 1D deep earth crust model. Importing into Winglink 3D model was possible, but since Winglink is limited to 32 bit memory, the computation grid was too large and the forward computation could not be done. Furthermore, the size of the computation grid is dependent on the number of stations, distinct frequencies and the modes (TE and TM). The real relation between the computation grid and the system memory is unknown. Two working examples given by the Winglink manual show that the following models work: (20x20x20, 3 freq) and (35x35x35, 3 freq). Based on these examples, the 3D models created through the combination of 2D inversion models have been mapped into a coarser meshing. This process was done by averaging out the resistivity of the cells that share the same cell in the new coarser mesh.

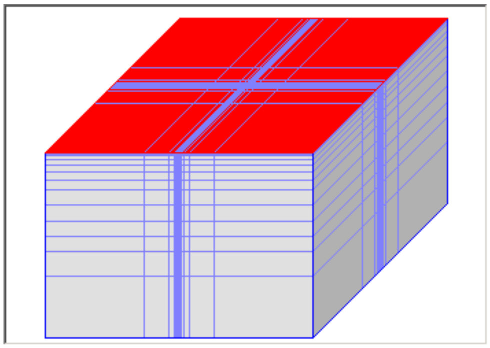

Figure 7-1 : A perspective view of the 3D modeling mesh with the boundary condition. The center crossed by the two thick bold lines contains the 3D model.

7.2 3D Modeling Settings

The models were inverted using Winglink smooth inversion. Once the inversions achieved satisfying results, UBC meshtool3d was used to interpolate the 2D inversion models to a 3D model. A variety of different settings were used to do the inversion, out of all the trials, three were found to be good candidates.

1. The frequency calculated during the forward process is between 0.1 Hz to 1 000 Hz with four frequencies per decade for a total of 20 frequencies. Part of the 3D response parameters was the minimum error set at 10^{-8}, the relaxation set at 200, the number of air layers set at 10 and the convergence factor set to 8 by default.
2. The stations are positioned in a distinct pattern to avoid any bias while maximizing the surface coverage and minimizing the quantity of stations needed for the forward computation. This can be observed in figure 7-2. Stations numbering consists of the profile number followed by the station number. For example, 01-25 means that it belongs to the first profile and represents the station number 25. The positions of the stations on the 3D forward computation are not perfectly above the Titan 24 survey stations. Therefore a direct comparison is difficult. To deal with this problem, a comparison of the forward response with the 3 closest survey stations is done.

3. The process of mapping the original fine 3D model to the more coarse mesh was done by averaging out the resistivity of the cells that share the same cell in the new coarser mesh.

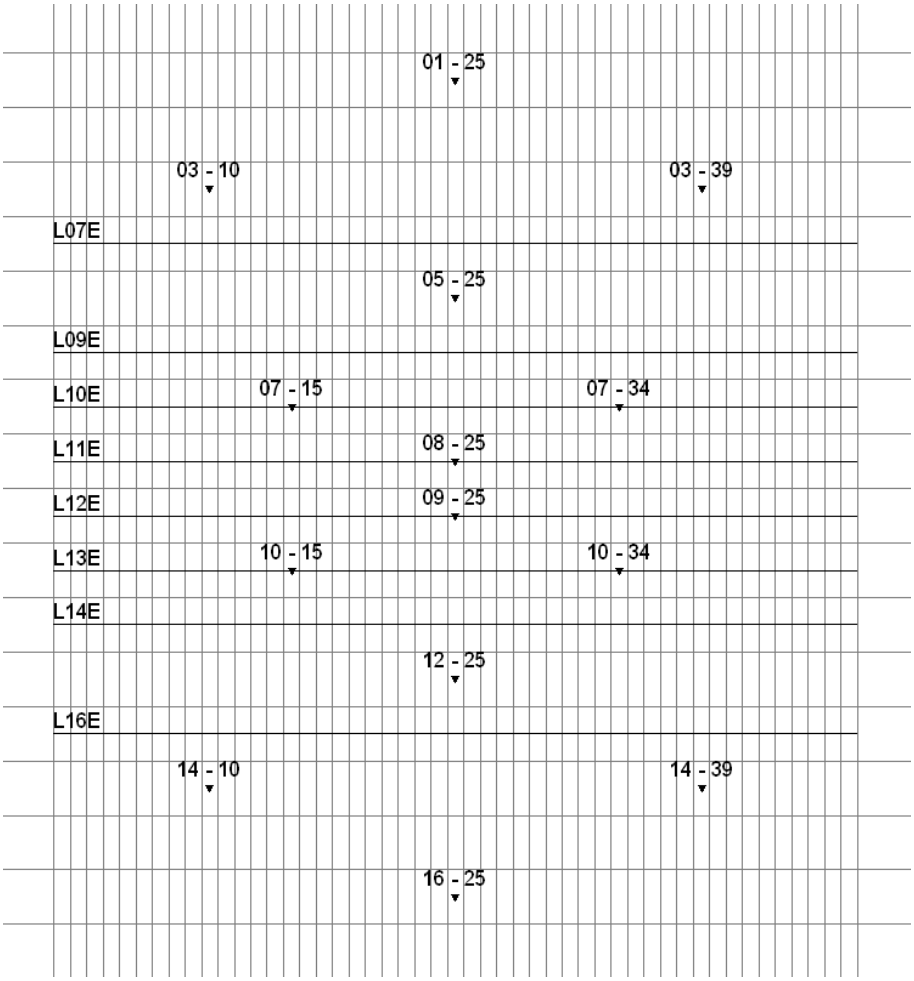

Figure 7-2 : 3D modeling sites and their locations with respect to the MT survey profiles. The profiles are named in order from 1 to 16. Profile L01E represents the Titan 24 profile L00E, profile L02E represents L04E, profile L10E represents L36E, etc.

7.3 Modeling Results

The MT responses generated by the 3D models are shown in Figure 7-3 and 7-4. The fit with the observed data is found to be satisfactory. The 3D models generated through the compilation of 2D slices obtained by 2D inversions of the MT Titan 24 data have similar characteristics and closely yield the same results. The apparent resistivity curves show shapes similar to the observed MT Titan 24 data. The 1D deep layer model taken from Chouteau et al. (2008) and defined in table 7.1, was able to produce an MT response with shapes similar to those found in the MT survey. Distortion effects are noticed at every response with their prominence varying from station to station. As shown earlier, the lack of proper information beyond the 3D model region has a great impact on the forward response, especialy in stations located near the boundary. By approximating the outer region as 2D, the MT responses are biased toward the condition we set. Lacking the ability to correct any topographic effect and static shift adjustment, the results are similar to those measured in the field but not perfect.

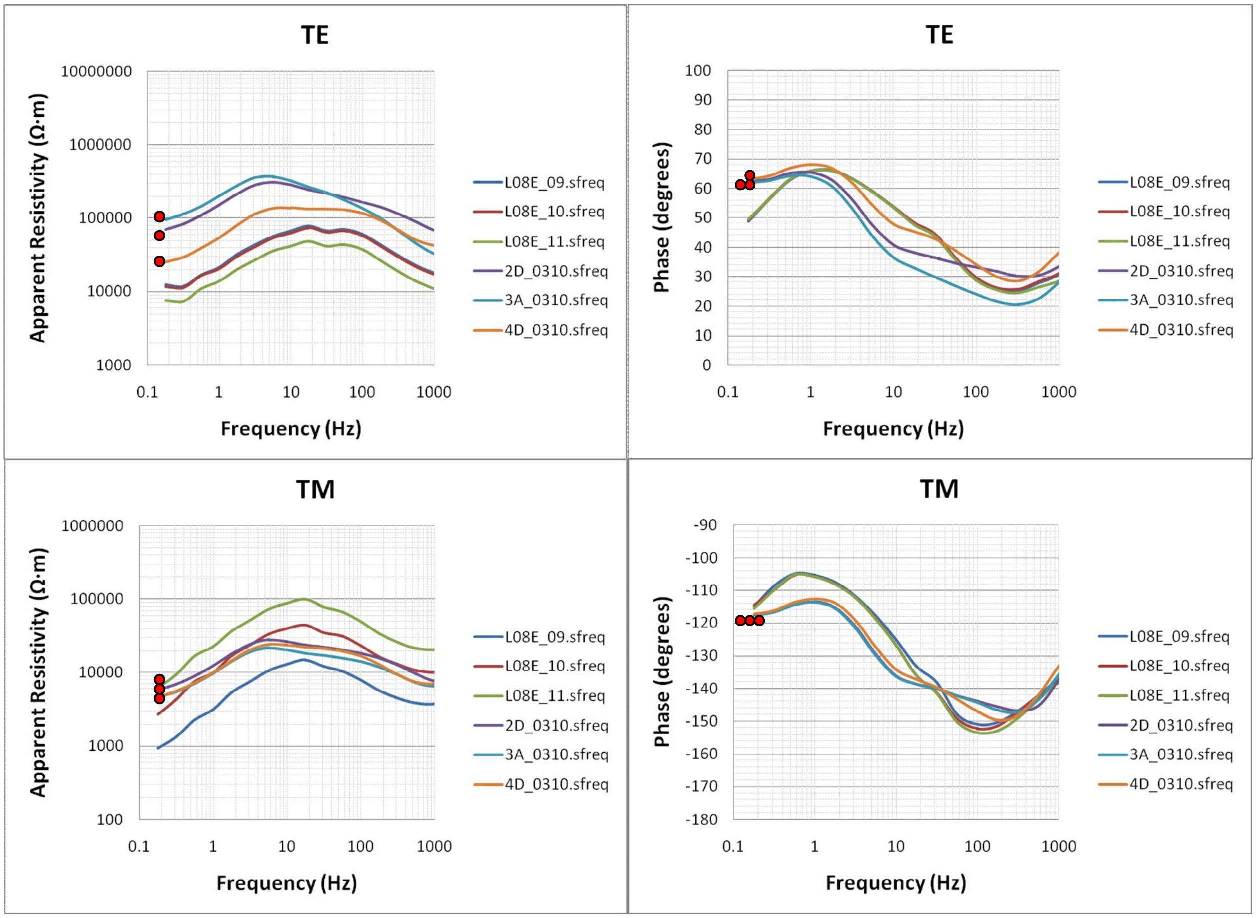

Figure 7-3 : Comparison of the 3D modeling responses produced by the three 3D models with the MT stations 09, 10 and 11 of MT survey profile L08E. Synthetic data is denoted by a red dot on the left side.

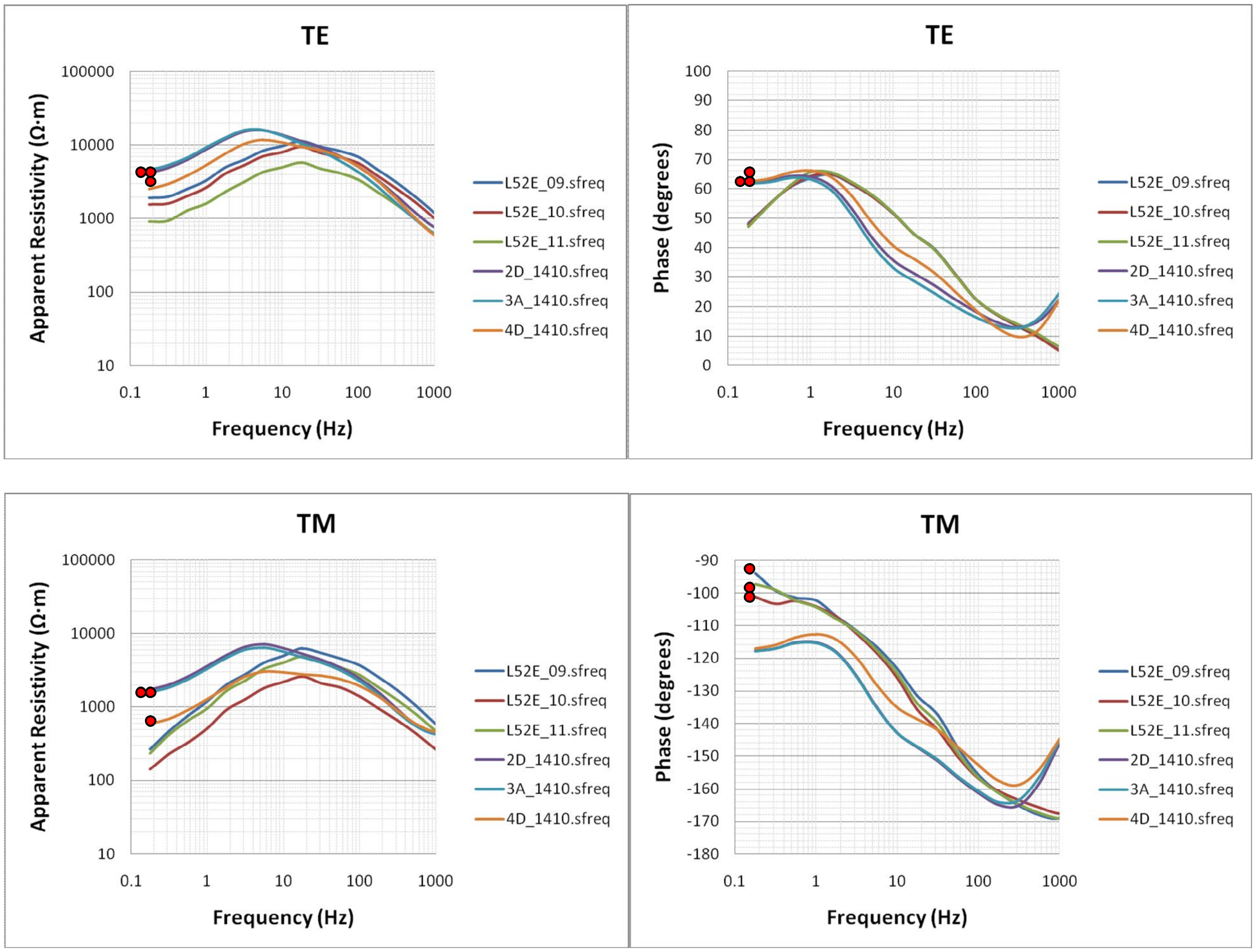

Figure 7-4 : Comparison of the 3D modeling responses produced by the three 3D models with the MT stations 09, 10 and 11 of MT survey profile L52E.

From these results, we notice that the resistivity responses for frequencies above 30 Hz fit the results very well, if the effect of static shift is included. Below 30 Hz discrepancy between modelled and observed data increases. The 3D model responses show a peak resistivity about 3-5 Hz for TE and TM resistivity curves while it is about 10-20 Hz for the observed data. This could be explained by the poor model boundary conditions since the 3D MT response fit the data very well at high frequencies (small skin depths). Also modifications to the 3D resistivity model at large depths (>15 km) could improve data fit for frequency below 10 Hz. More response comparisons can be found in the appendix (fig. 37 to 50). Considering that the 3D MT forward code limits the model mesh size, the boundary conditions are poorly known, and that only the impedance tensor has been used, the model can be considered as a reasonable geological representation of the region. A full 3D inversion has to be done in order to verify the result.

CONCLUSION AND DISCUSSION

The objectives of this thesis was to determine the MT detection capability of ore bodies and structures with IP effects, and to determine the geological subterranean features and structures bellow the Titan 24 MT soundings. Motivated by the need to find new ways to detect ore bodies at great depths, we created models that represent known Matagami ore bodies and host rocks. We first modified a 2D MT modeling program to include the varying complex resistivity with frequency by implementing the Cole-Cole frequency-dependant resistivity in the forward code. Along the way, we derived analytical solutions to ensure the validity of our code modification. We found that an ore body with induced polarization (IP) does provide a better chance of detecting or locating shallow ore bodies. The electrical properties of the body also influence the outcome of the MT response. Having a higher chargeability (m) and the right time constant (τ), the induced polarization (IP) will produced a more pronounced effect on the MT response. Having higher values allows us to assess the detectability of conductive body but it may not be a good approximation to the real world model as the effects might not be as pronounced as we had hoped.

We also analyzed the MT survey data at the Matagami southern flank region. We found that there is a strong presence of distortions and noises in the data itself. We observed that in general, the MT survey region can be interpreted as 3 distinct layers. The first layer can be associated with overburden of various size and shape. The thickness of the overburden varies from 0m to 300m. The second layer can be associated with the gabbro and the basalt. The gabbro and the basalt reach down to about 1 km to 1.5 km deep and in some parts down to 2 km deep. The third layer is associated with the rhyolite. Since the MT survey profiles are about 5 km in length, beyond the depth of 5 000 m the resolution of 2D inversion is greatly decreased, therefore we suggest the 1D model produced by Tournerie and Chouteau (1998). In figure 6-15 and 6-16, vertical structures are found along the south axis. These structures could correspond to the dikes seen in the region of Matagami. The dikes could be related to the extrusive or intrusive igneous volcanic rock. It could be extrusive if the hot magma flows to the surface as lava or intrusive if the magma never reaches the surface. Respectively, it could be basalt or gabbro, two of the dominant rock types found in Matagami and borehole loggings.

We also found that the IP anomalies (figure 6-19) are caused by geological structures of high resistivity. Interpretation of the models produced by 2D inversion and by the apparent invariant resistivity and phase further confirms it. 2D inversion was also done on static-shift corrected MT data and two distinct anomalies are found and coincide with the location of the IP anomalies. 3D inversions need to be done in order to validate our 3D models that were produced through interpolating results from parallel 2D inversion. The IP anomalies could be related to the high resistivity structures found in TE-TM inversions. These structures could contain dissiminated grain like materials of high resistivity and with high porosity thus generating the IP anomalies. The IP anomalies could also be caused by the alteration of the minerals located in the region. We recommend that some boreholes logging are done in areas where IP anomalies are found (figure 6-19) in order to better discreminate the source of these anomalies.

Future work involves obtaining a true 3D inversion model by using one of the available 3D MT inversion codes. This allows us to compare our interpolated 2D inversion models with 3D inversion results. We have the Weerachai Siripunvaraporn full 3D MT inversion program (WSINV3DMT) that seeks the smoothest minimum structure models that fit the data (Siripunvaraporn et al., 2005). If possible, we look forward to using other 3D inversion methods such as the 3D inversion of MT data using the integral equations method and a receiver footprint (Gribenko et al. 2010) that is more efficient and cuts computational costs. A more long-term future goal would be to develop or modify an existing 3D MT inversion code with a static shift correction. As computational hardwares (i.e. CPU, memory …) become more widely and cheaply available, minimizing the computational cost while increasing the speed through cloud computing or parallel computing will generate finer 3D inversion models. Currently, 3D inversion uses non-linear conjugate gradient method to solve for inverse MT problems. Direct matrix solvers could be used to solve for the MT inverse problem requiring less computational time. Developing an MT inversion code that integrates varying complex resistivities might be of interest even thought we have shown that the induced polarization does not provide a significant contribution to the MT response when the conductive body is located at depths beyond detection. But for cases where the conductive or the disseminate bodies are found, the MT inversion code with IP effect can be use to determine various properties such as chargeability.

REFERENCES

Adam, E., Milkereit, B. and Mareschal, M. (1998). Seismic Reflection and Borehole Geophysical Investigations in the Matagami Mining Camp, *Canadian Journal of Earth Sciences*, 35, 686-695.

Bahr, K., (1988), Interpretation of the magnetotelluric impedance tensor: regional induction and local telluric distortion, *Journal of Geophysics*, 62, 119–127.

Bahr, K., (1991) Geological noise in magnetotelluric data: A classification of distortion types, *Physics of the Earth and Planet ary Interiors*, 66, 24–38.

Berdichevsky, M.N., Dimitriev, V.I., (1976). Basic principles of interpretation of magnetotelluric sounding curves, *Geolelectric and Geothermal Studies*, 165– 221.

Caldwell, T.G., Bibby, H.M. and Brown, C., (2004), The magnetotelluric phase tensor, *Geophysical Journal International*, 158, 457-469.

Calvert, A. J. and Li, Y. (1999). Seismic Reflection Imaging over a Massive Sulfide Deposit at the Matagami Mining Camp, Quebec, *Geophysics*, 64, 24-32.

Chouteau, M. and Boulanger, O. (2007). Detection of Deep Conductive Massive Orebodies by Magnetotelluric Surveys: A Feasability Study on Xstrata Orebodies, Progress Report LGAP-2007-05.

Coulson, S., Stewart, B. and Gerrie, V. (2003). Geophysical Survey Logistics Report, QLS Inc.

deGroot-Hedlin, C. and S.C. Constable, (1990), Occam's inversion to generate smooth, two-dimensional models from magnetotelluric data, *Geophysics*, 55, 1613-1624.

Dikpati, M., Gilman, P. and Toma, G., (2006), The National Center for Atmospheric Research, http://www.ucar.edu/news/releases/2006/sunspot.shtml

Gasperikova, E. and Frank Morrison, H., (2001), Mapping of induced polarization using natural fields, *Geophysics*, 86 (1), 137-147.

Gribenko, A., Marie Green, A., Cuma, M. and Zhdanov, M.S., (2010) Efficient 3D inversion of MT data using integral equations method and the receiver footprint approach: application to the large-scale inversion of the EarthScope MT data, *SEG Denver 2010 Annual Meeting*, 644-649.

Groom, R.W. and Bailey, R.C., (1989), Decomposition of Magnetotelluric Impedance Tensors in the Presence of Local Three-Dimensional Galvanic Distortion, *Journal of Geophysical Research*, 96, 1913-1925.

Gwilym Roberts, R. (1975). The Geological Setting of the Mattagami Lake Mine, Quebec: A Volcanogenic Massive Sulfide Deposit, *Economic Geology*, 70, 115-129.

Hartman, H.L. and Mutmansky, J.M., (2002), Introductory Mining Engineer, John Wiley and Sons, 2nd Edition, 57.

Jenny, C.P., (1961), Geology and Ore Deposits of the Mattagami Area, Quebec, *Economic Geology*, 56, 740-757.

Ledo, J., P. Queralt, A. Marti and A.G. Jones, (2002), Two dimensional interpretation of 3-D magnetotelluric data: an example of limitations and resolution. *Geophysical Journal International*, 150, 127-139.

Mackie, R. L., Smith, J. T. and Madden, T. R., (1994), 3D electromagneticmodeling using finite differences equations: The magnetotelluric example, Radio Science, 29, 923–935.

Marti, A., Queralt, P. and Roca, E, (2004), Geoelectrical dimensionality in complex geologic areas: Application to the Spanish Betic Chain. *Geophysical Journal Internationa1*, 57, 964 – 974.

McNeice, G.W. and Jones, A.G., (2001), Multisite, multifrequency tensor decomposition of magnetotelluric data, *Geophysics*, 66, 158-173.

National Weather Service (2007). "Lightning Safety". National Weather Service. Retrieved September 21, 2007. http://www.lightningsafety.noaa.gov/science.htm

Reynolds, J.M., (1997), An introduction to Applied and Environmental Geophysics, *John Wiley & Sons*, West Sussex, England.

Rodi, W. and Mackie, R.L., (1998), Nonlinear Conjugate Gradients Algorithm for 2-D Magnetotelluric Inversion, Geophysics, 66, 174-187.

Shekhtman, R., 2007, MeshTools3D software, UBC Geophysical Inversion Facility, Vancouver, B.C., Canada.

Siripunvaraporn, W., Egbert, G., Lenbury, Y., Uyeshima M., (2005), Three-dimensional magnetotelluric inversion: data-space method, *Physics of The Earth and Planetary Interior*, 150, 3-14.

Smith, J.T., (1995), Understanding telluric distortion matrices, *Geophysical Journal International*, 122 , 219-226.

Smith, J.T., (1996), Estimating galvanic-distortion magnetic fields in magnetotellurics, *Geophysical Journal International*, 130 , 65–72.

Swift, C.M., (1967), A magnetotelluric investigation of electrical conductivity anomaly in the southwestern United States, *PhD Thesis, Massachusetts Institute of Technology*, Cambridge, MA.

Tournerie, B. and Chouteau, M. (1998). Deep Conductivity Structure in Abitibi, Canada, using Long Dipole Magnetotelluric Measurements, *Geophysical Research Letters*, 25, 2317-2320.

Tournerie, B. and Chouteau, M. (2002). Analysis of Magnetotelluric data along the Lithoprobe Seismic line 21 in the Blake River Group, Abitibi, Canada, *Earth Planets Space*, 54, 575-589.

Vozoff, K., (1972), The magnetotelluric method in the exploration of sedimentary basins, *Geophysics*, 37, 98-141.

Wannamaker, P.E., (1989), PW2DIS User Documentation - Finite element program for solution of magnetotelluric responses and sensitivities for two-dimensional earth resistivity structure: Earth Science Laboratory, University of Utah Research Institute, Salt Lake City, Utah, ESL-89043-TR.

Wannamaker, P.E., (1999), Affordable magnetotelluric: Interpretation in natural environments, in Three-dimensional electromagnetics, ed. by Oristaglio and B. Spies, Geophys. Devel. Ser., 7, Soc. Explor. Geophys., Tulsa, 349-374.

Wannamaker, P.E., Wright, P.M., Zhou, Z.-X., Li, X. B., and Zhao J.-X., (1991), Magnetotelluric transect of Long Valley Caldera: Resistivity cross section, structural implications, and the limits of a two-dimensional analysis, Geophysics, 56, 926-940.

Weaver, J.T., Agarwal, A.K. and F.E.M. Lilley, (2000), Characterization of the magnetotelluric tensor in terms of its invariants, *Geophysical Journal International*, 141, 321-336.

Winglink, (2008), A guide to Winglink, Geosystem SRL.

APPENDICES

APPENDIX A – 2D MT MODELING (T=0.6S)

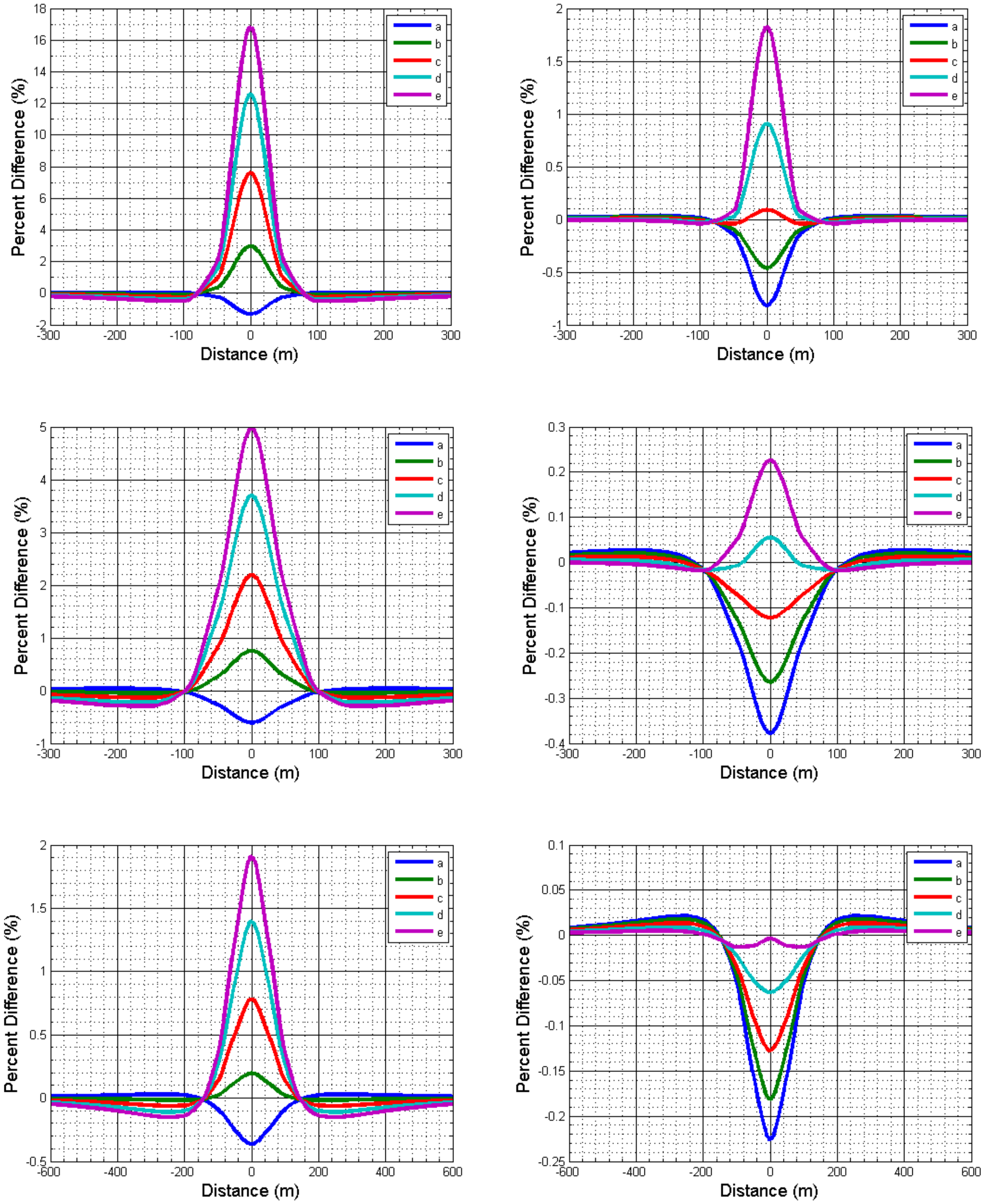

Fig. 1: (Left to Right) Apparent resistivity and phase percent difference between 0.01 and 0.1 Hz. (Top to Bottom) Block at depths of 30, 60 and 100m.

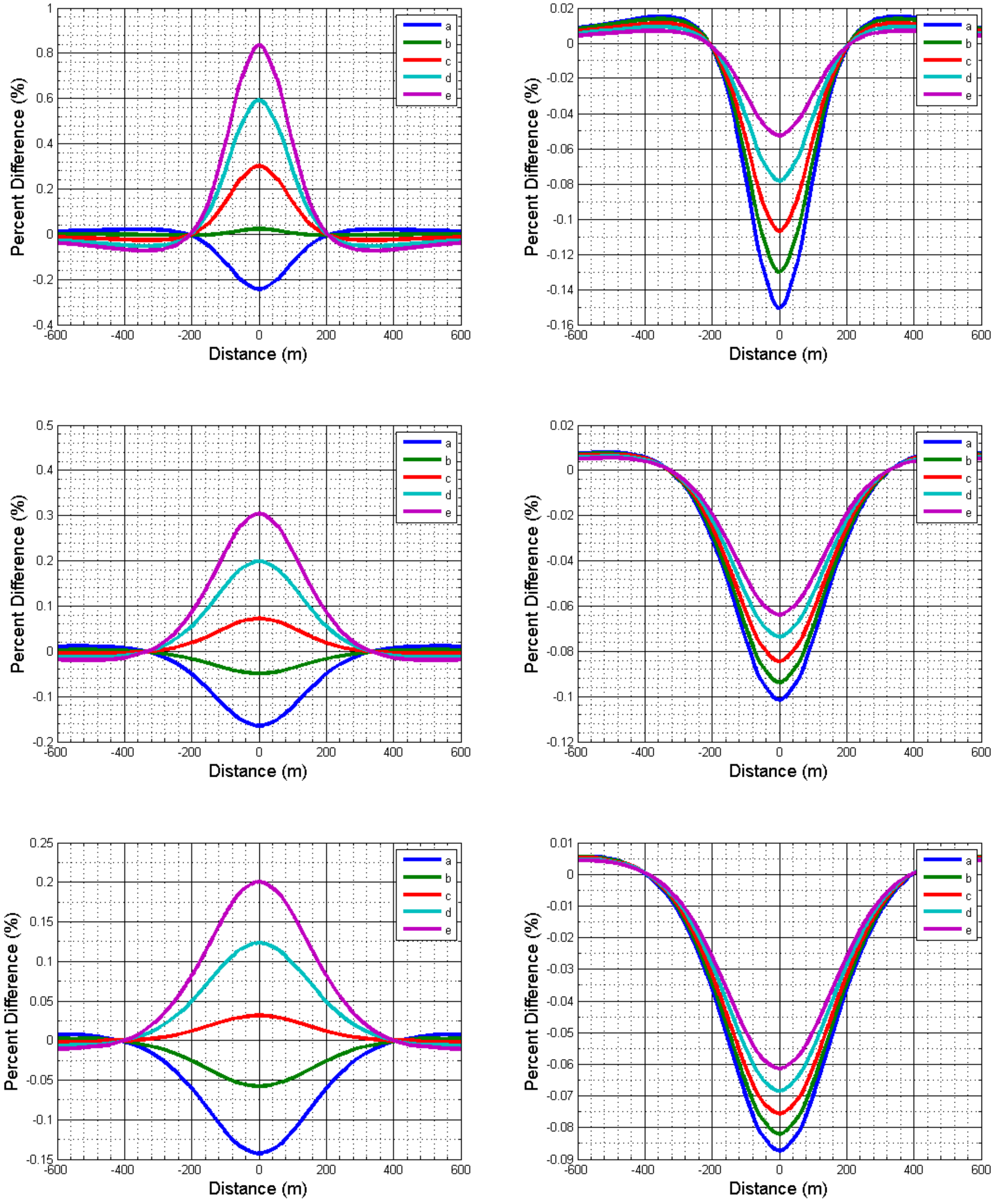

Fig. 2: (Left to Right) Apparent resistivity and phase percent difference between 0.01 Hz and 0.1 Hz. (Top to Bottom) Block at depths of 150m, 200m and 300m.

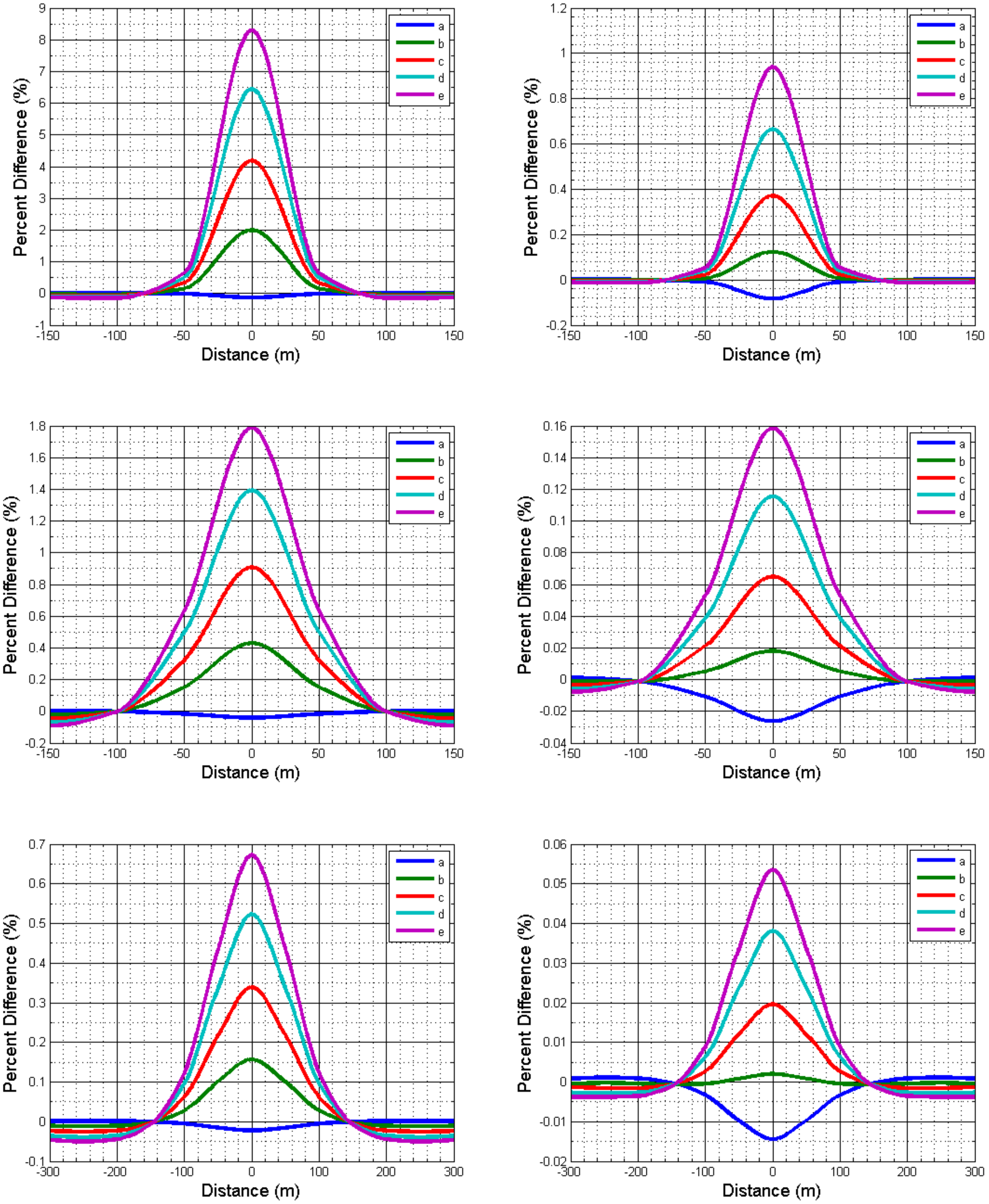

Fig. 3: (Left to Right) Apparent resistivity and phase percent difference between 0.01 Hz and 0.1 Hz . (Top to Bottom) VMS-1 at depths of 30m, 60m and 100m.

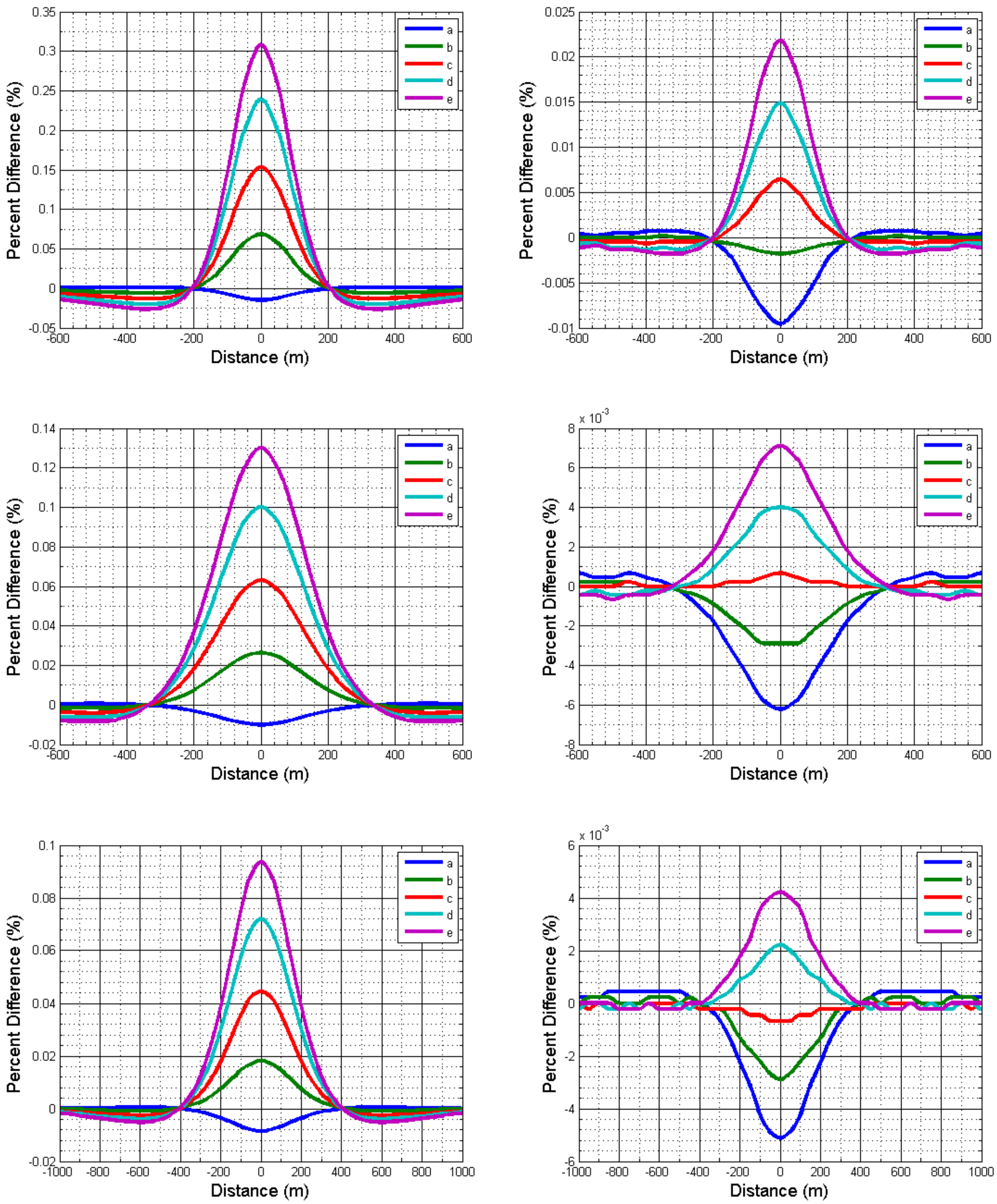

Fig. 4: (Left to Right) Apparent resistivity and phase percent difference between 0.01 Hz and 0.1 Hz . (Top to Bottom) VMS-1 at depths of 150m, 200m and 300m.

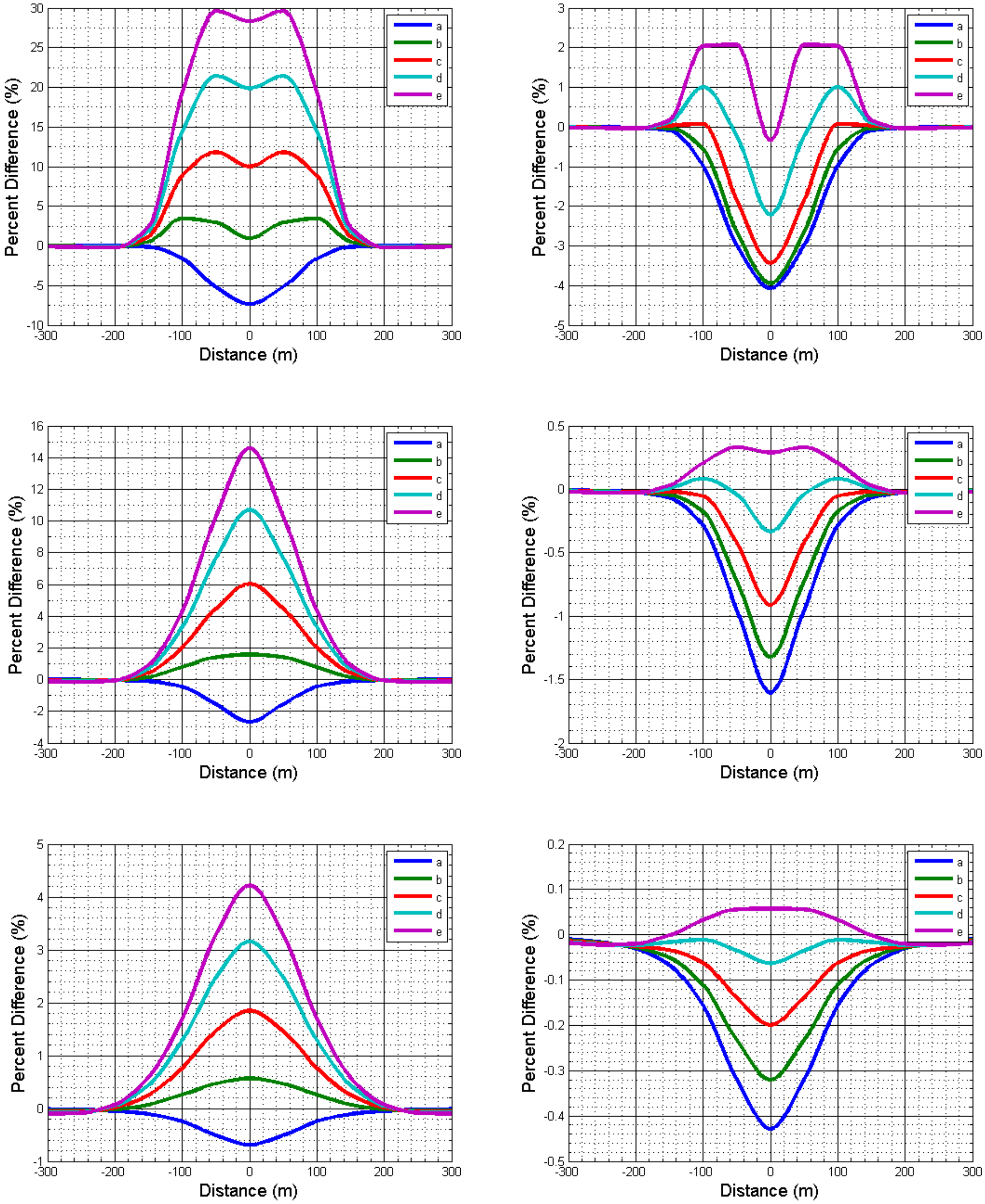

Fig. 5: (Left to Right) Apparent resistivity and phase percent difference between 0.01 Hz and 0.1 Hz . (Top to Bottom) VMS-2 at depths of 30m, 60m and 100m.

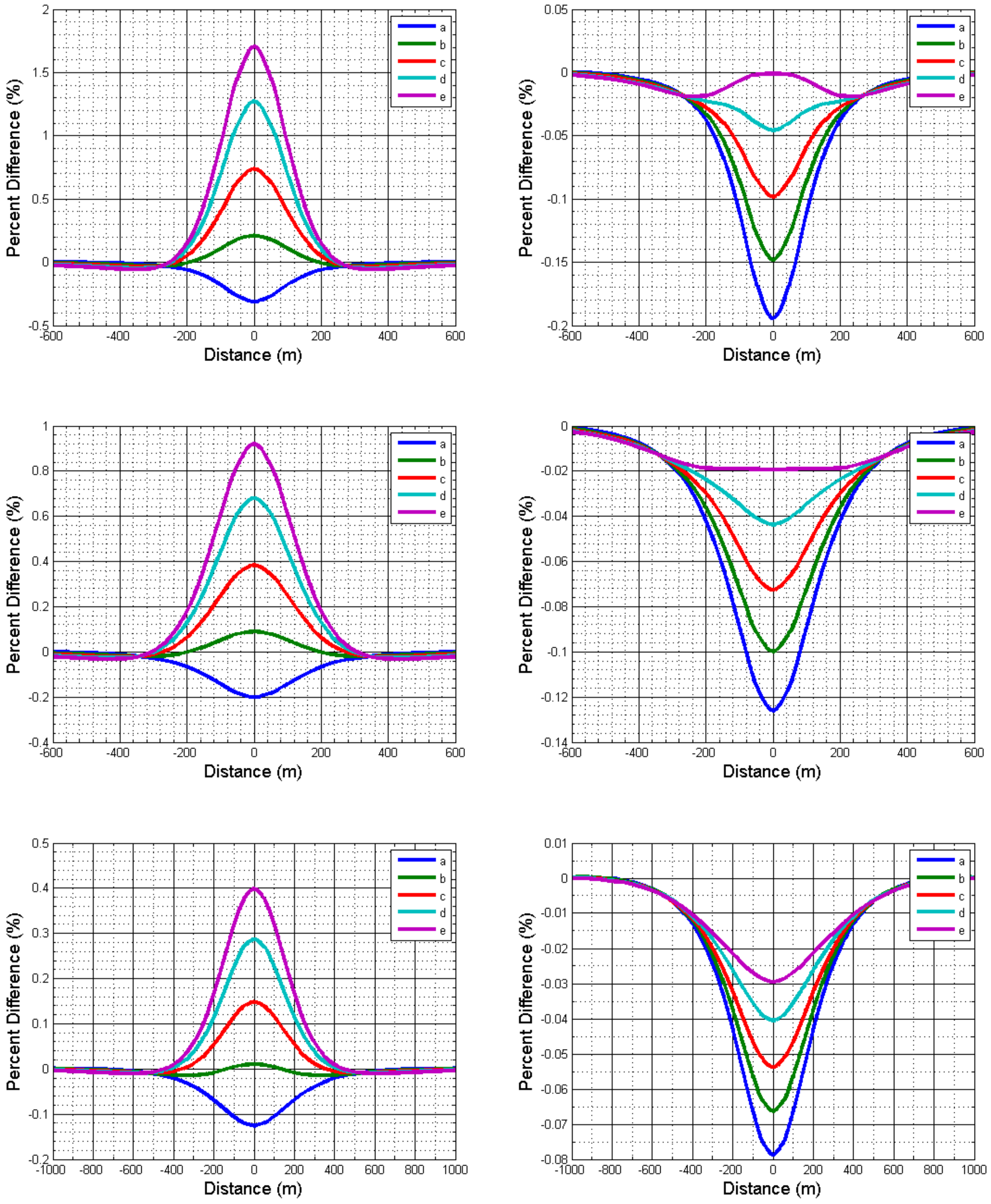

Fig. 6: (Left to Right) Apparent resistivity and phase percent difference between 0.01 Hz and 0.1 Hz . (Top to Bottom) VMS-2 at depths of 150m, 200m and 300m.

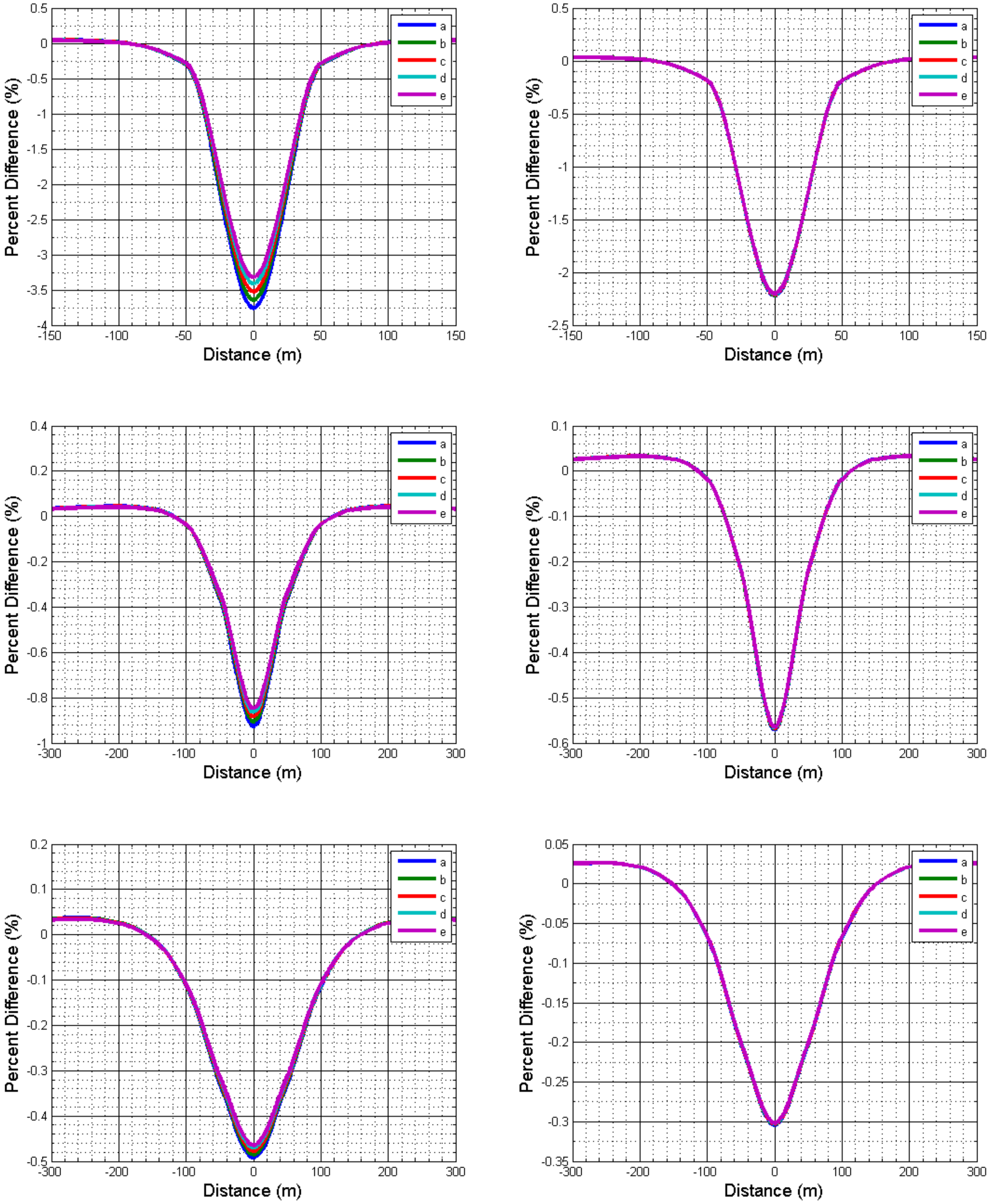

Fig. 7: (Left to Right) Apparent resistivity and phase percent difference between 0.01 Hz and 0.1 Hz . (Top to Bottom) Raglan-1 at depths of 30m, 60m and 100m.

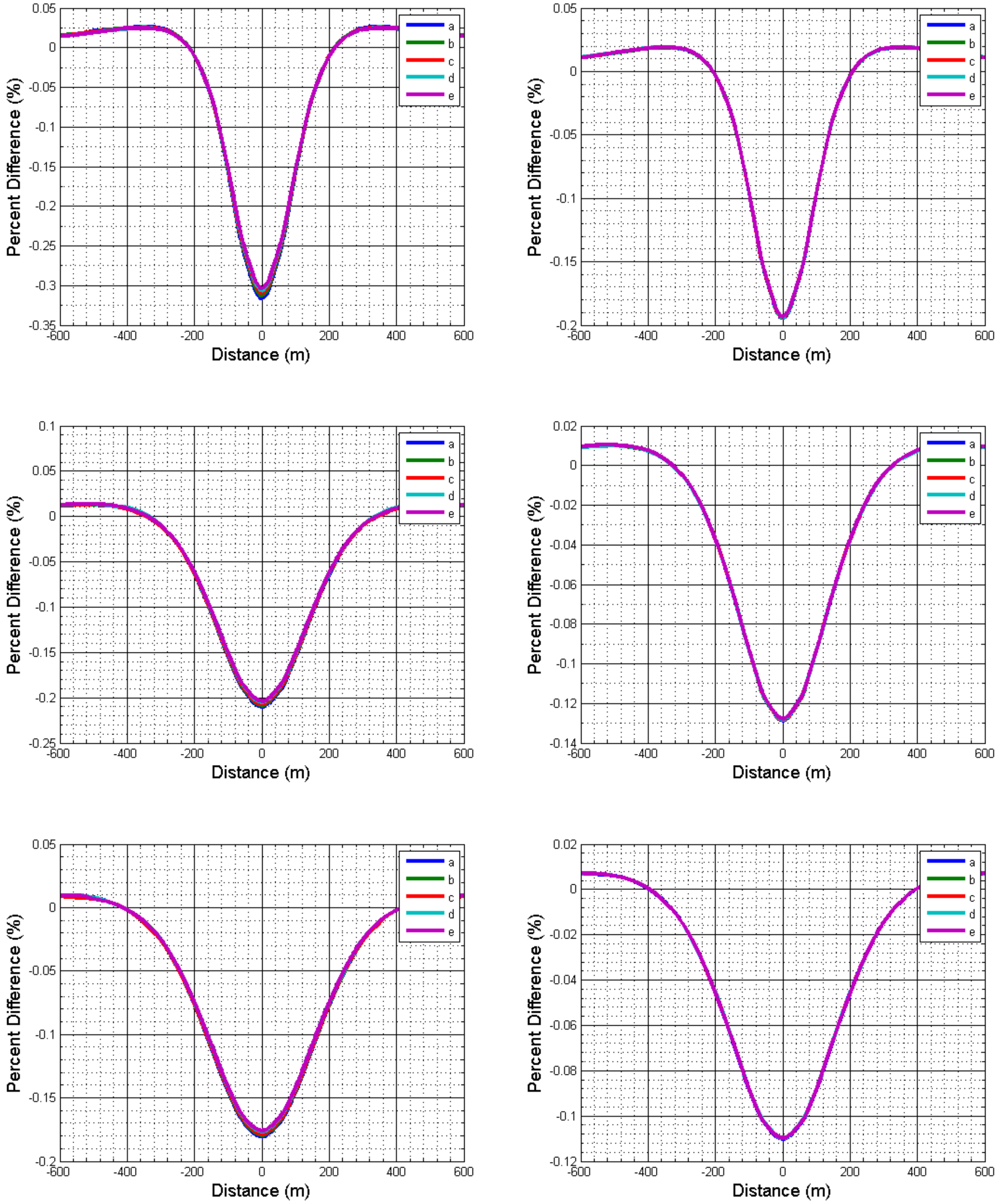

Fig. 8: (Left to Right) Apparent resistivity and phase percent difference between 0.01 Hz and 0.1 Hz . (Top to Bottom) Raglan-1 model response at depths of 150m, 200m and 300m.

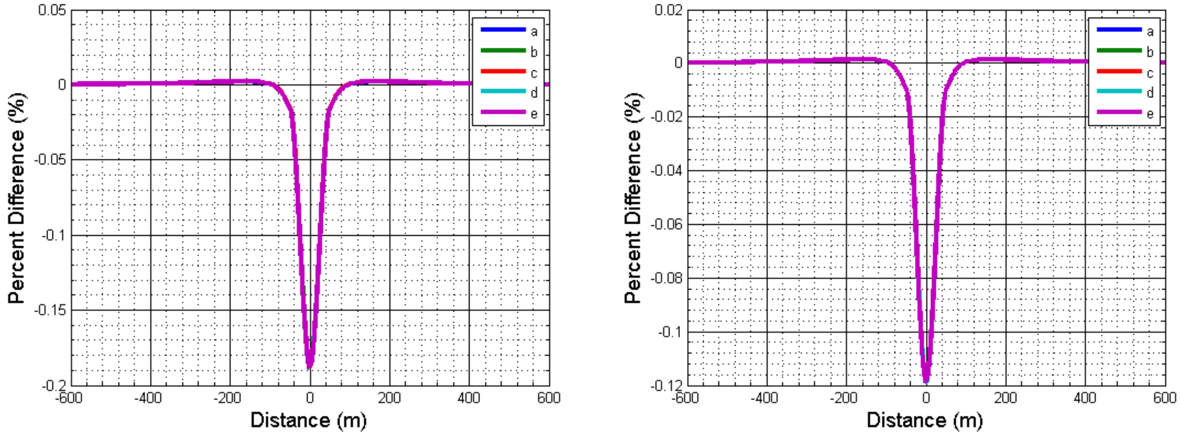

Fig. 9: (Left to Right) Apparent resistivity and phase percent difference between 0.01 Hz and 0.1 Hz. Raglan-2 model response at depth of 30m.

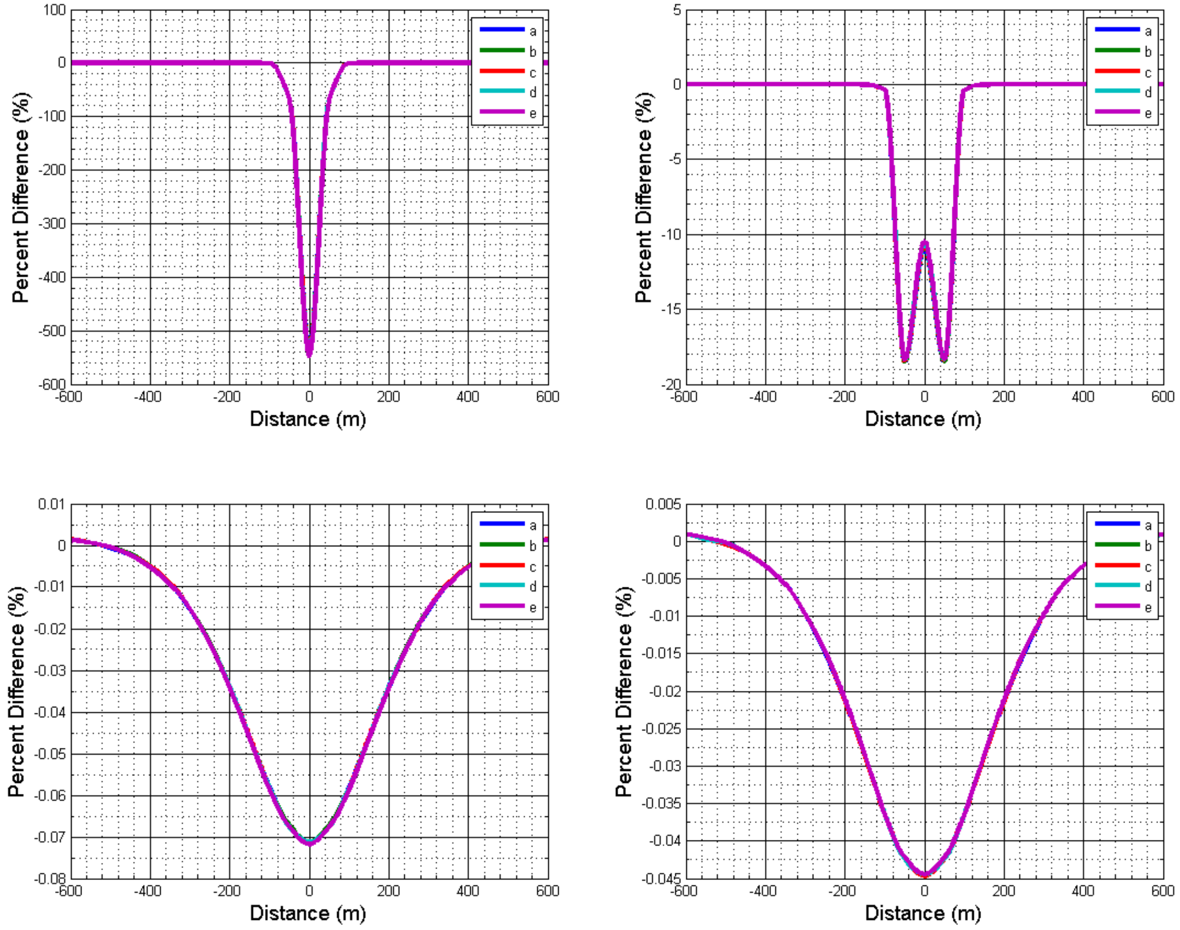

Fig. 10: (Left to Right) Apparent resistivity and phase percent difference between 0.01 Hz and 0.1 Hz . (Top to Bottom) Matagami model at depths of 30m and 300m.

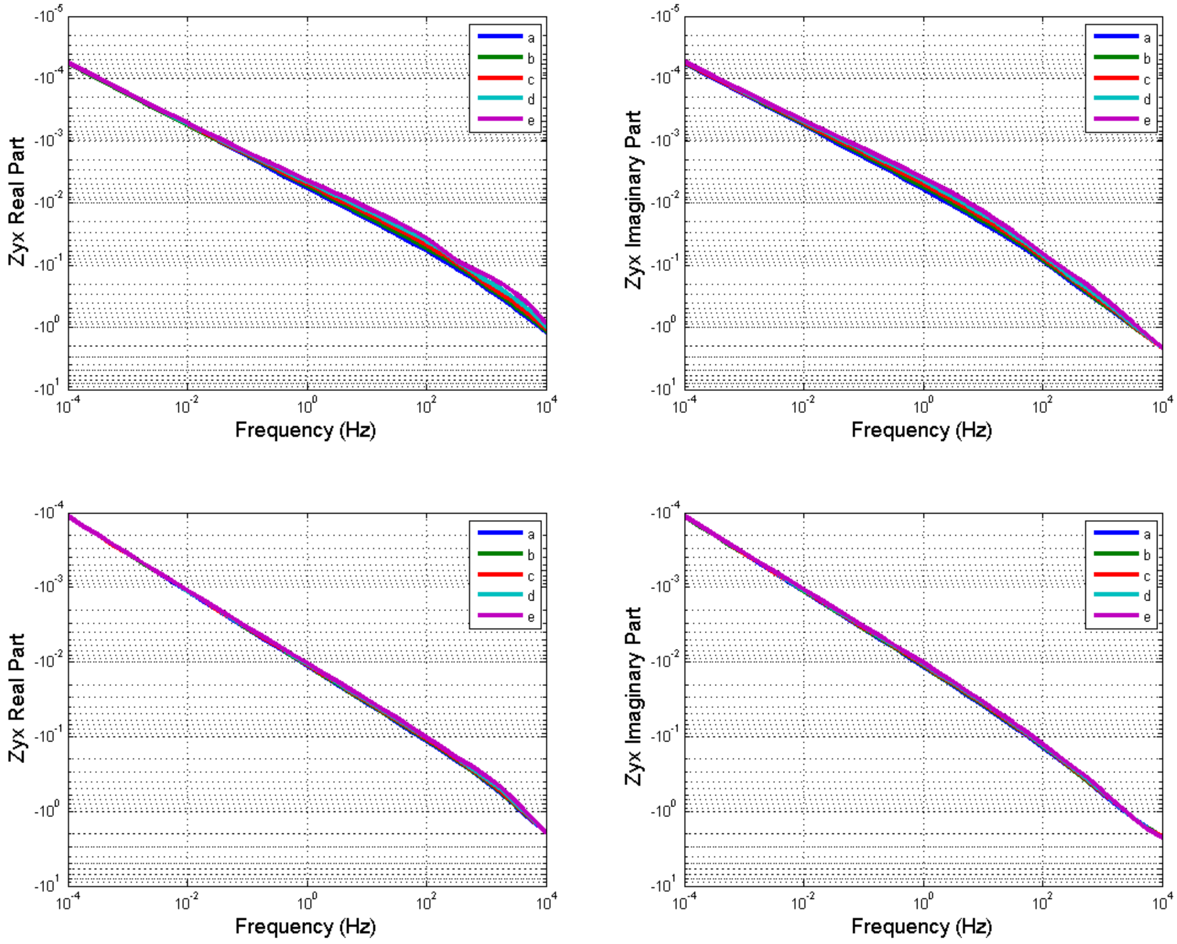

Fig. 11: (Left to Right) Apparent resistivity and phase percent difference between 0.01 Hz and 0.1 Hz . (Top to Bottom) Block at depths of 30m and 60m.

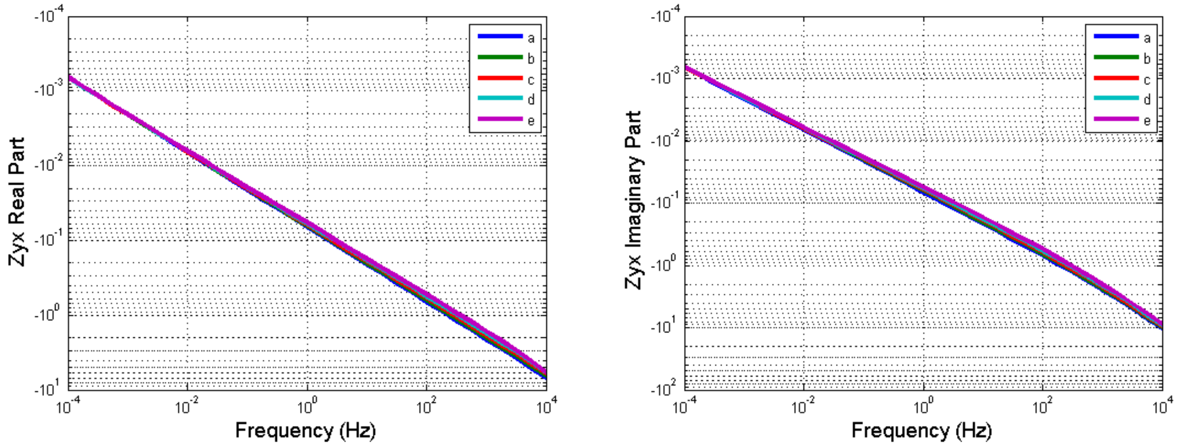

Fig. 12: (Left to Right) Apparent resistivity and phase percent difference between 0.01 Hz and 0.1 Hz . (Top to Bottom) VMS at depths of 30m.

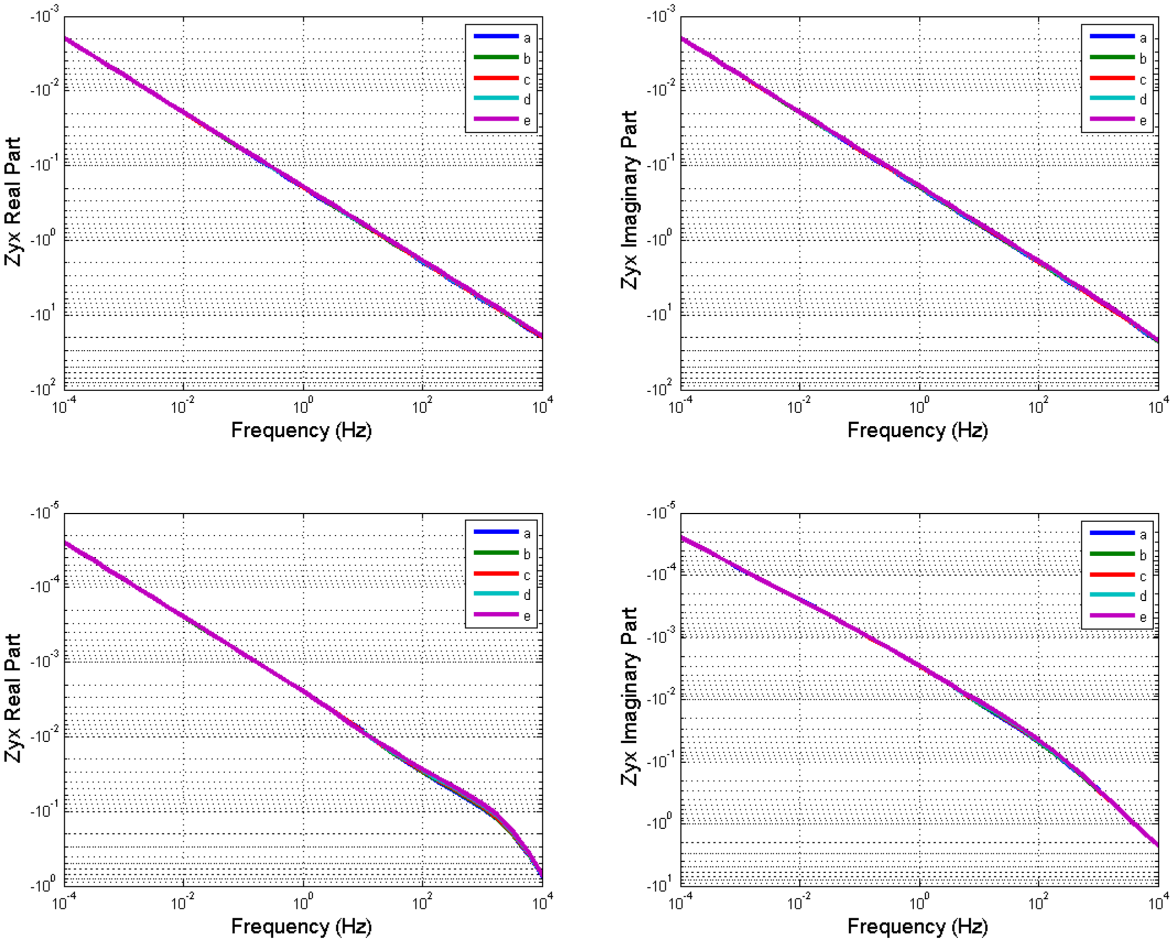

Fig. 13: Real and complex part of the TM impedences for the middle stations for ore bodies located at depth of 30m. Top: VMS-1 model. Bottom: Raglan-1 model.

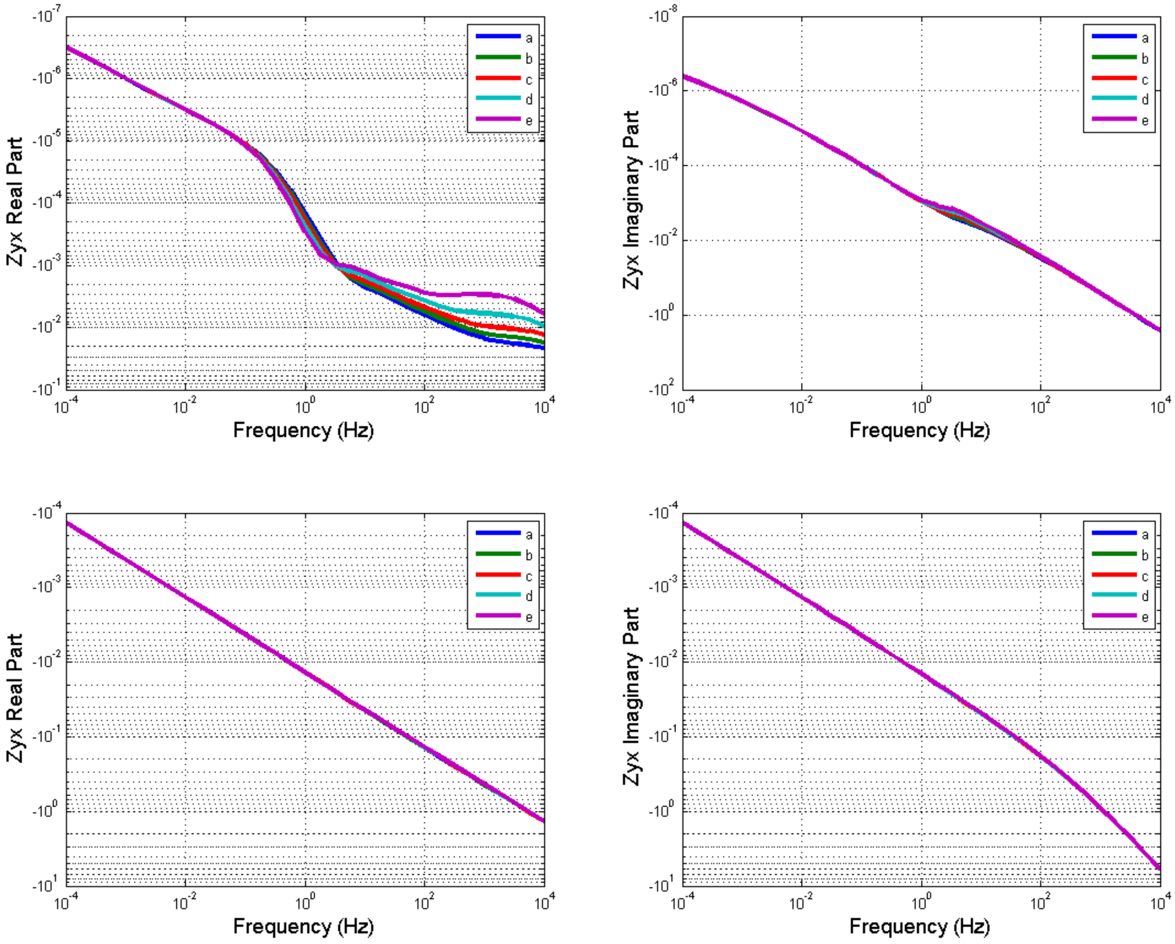

Fig. 14: Real and complex part of the TM impedences for the middle stations for ore bodies located at depths of 30m and 60m. Matagami model.

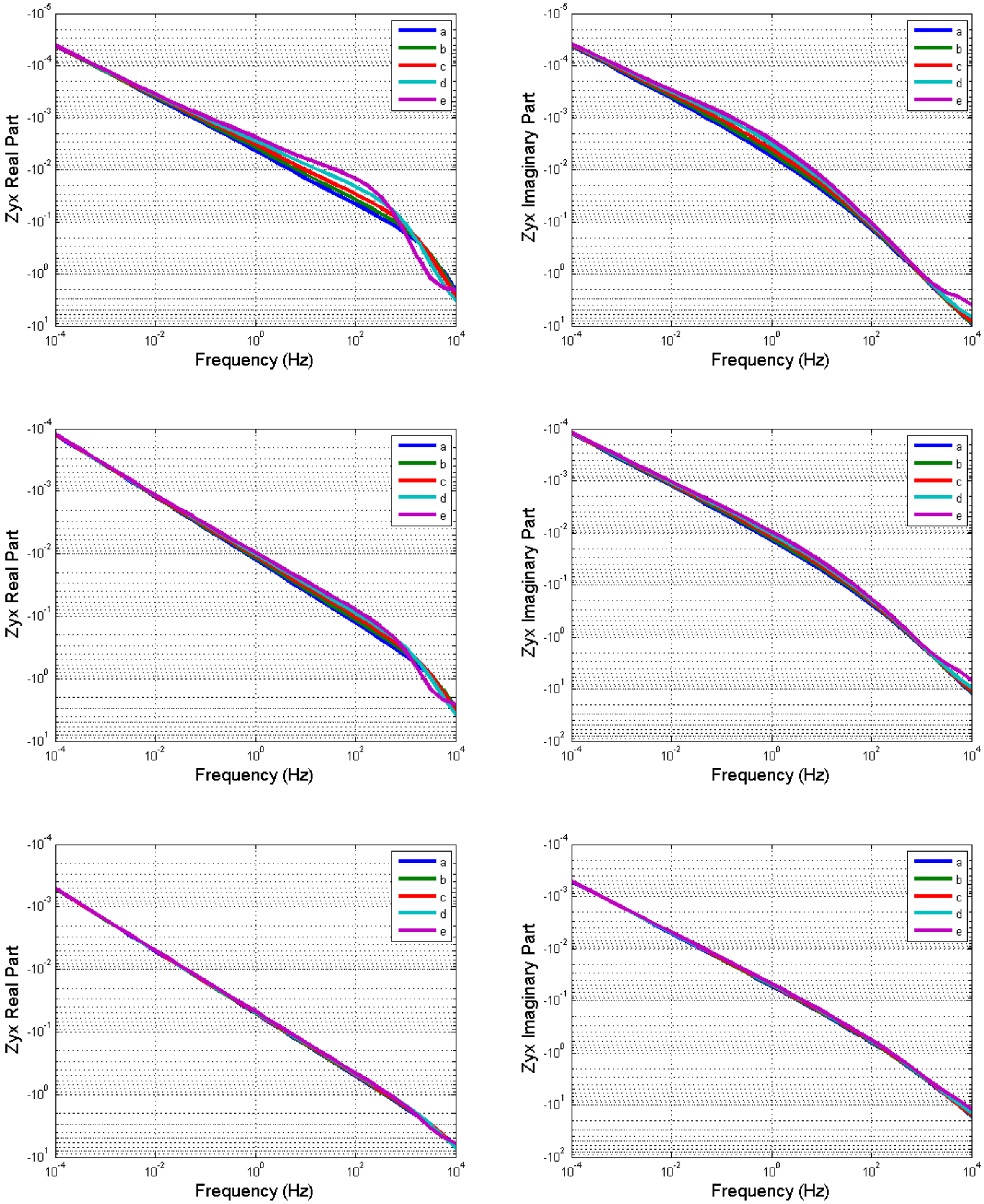

Fig. 15: (Top to Bottom) Real and complex part of the TM impedences for the middle stations for ore bodies located at depths of 30m, 60m and 100m. VMS-2 model.

APPENDIX B – 2D MT MODELING (T=126S)

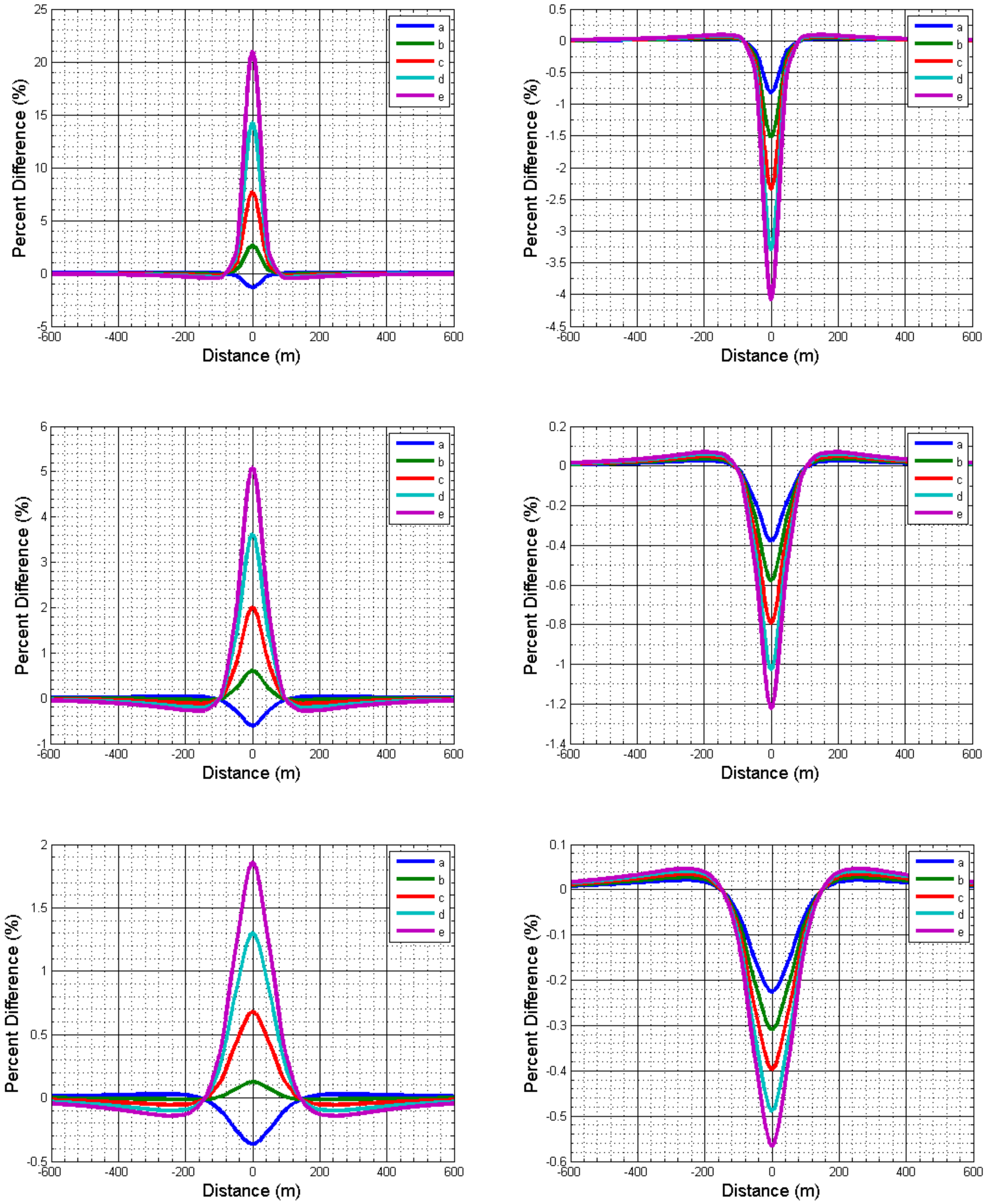

Fig. 16: (Left to Right) Apparent resistivity and phase percent difference between 0.01 Hz and 0.1 Hz. (Top to Bottom) Block model responses at depths of 30m, 60m, 100m.

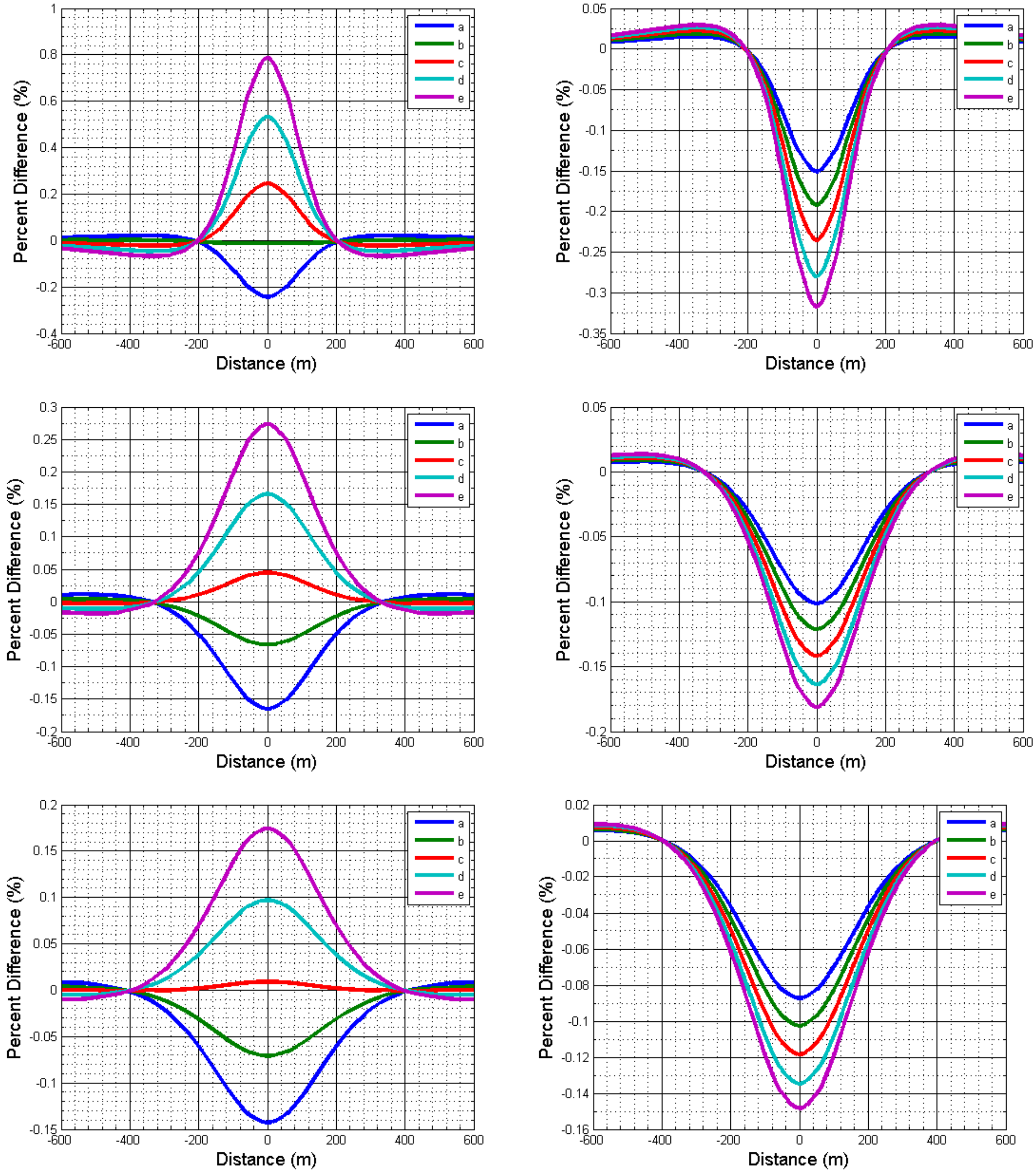

Fig. 17: (Left to Right) Apparent resistivity and phase percent difference between 0.01 Hz and 0.1 Hz. (Top to Bottom). Block model responses at depths of 150m, 200m and 300m.

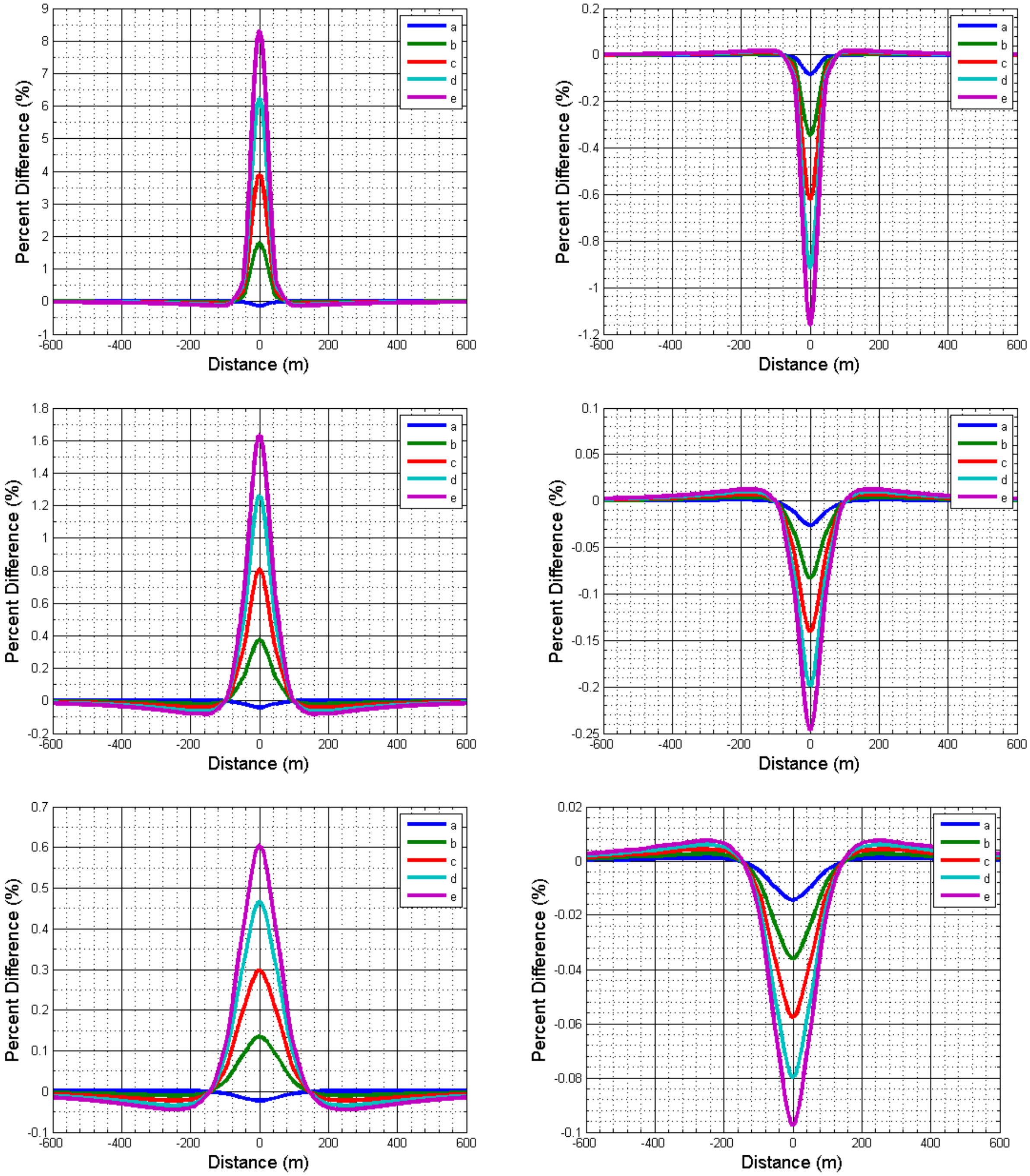

Fig. 18: (Left to Right) Apparent resistivity and phase percent difference between 0.01 Hz and 0.1 Hz. (Top to Bottom) VMS-1 model responses at depths of 30m, 60m and 100m.

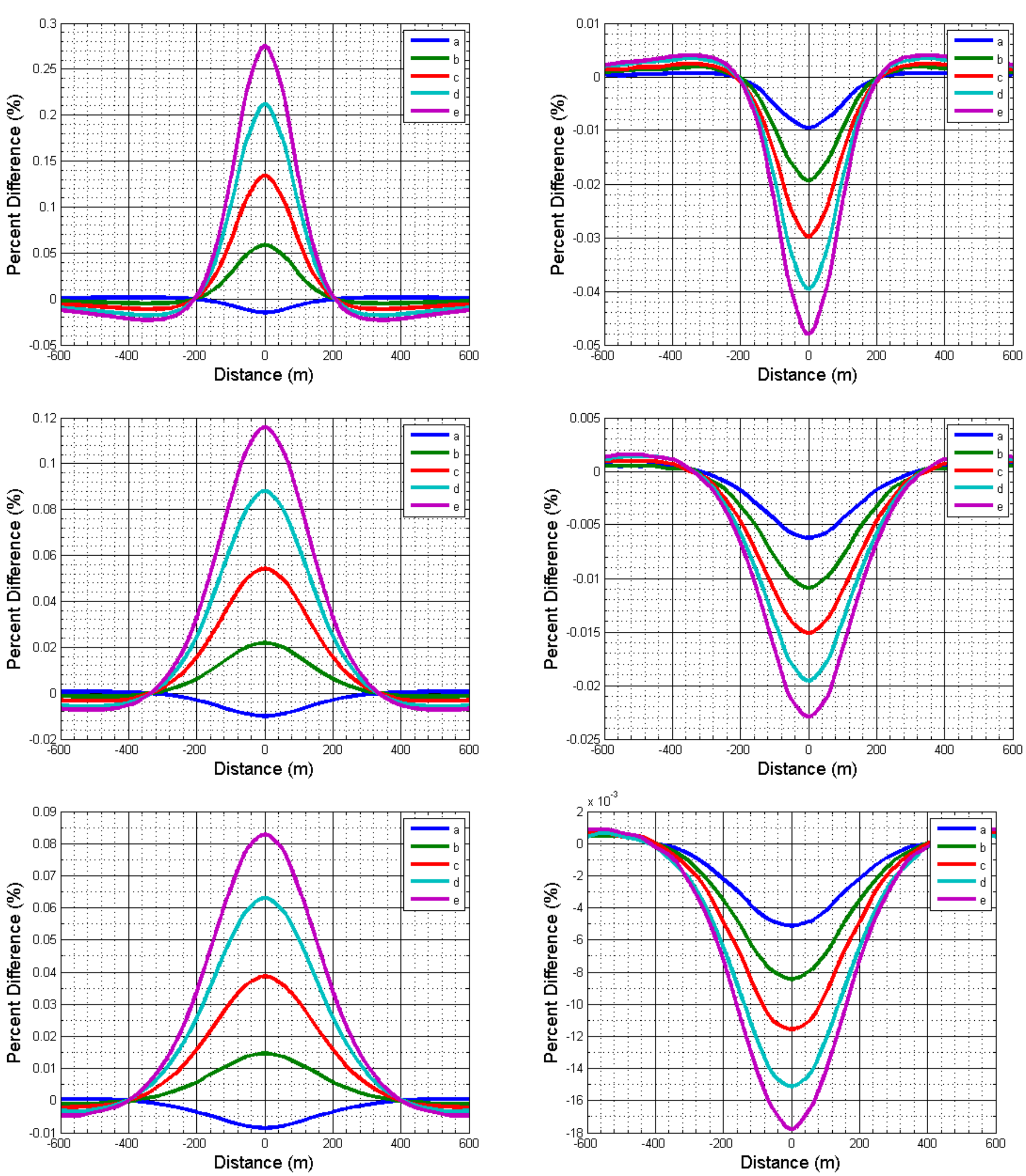

Fig. 19: (Left to Right) Apparent resistivity and phase percent difference between 0.01 Hz and 0.1 Hz. (Top to Bottom) VMS-1 model responses at depths of 100m, 150m and 200m.

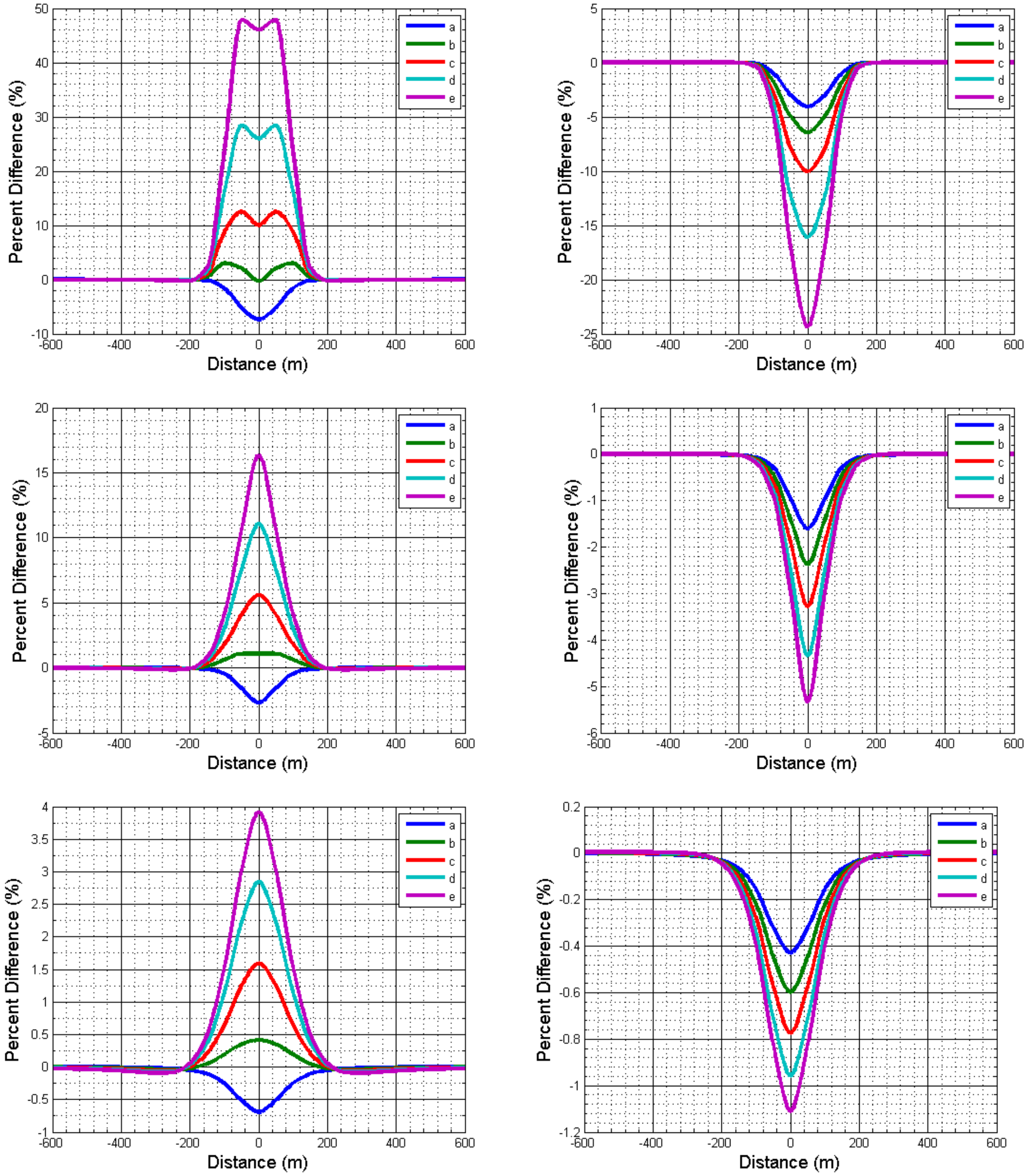

Fig. 20: (Left to Right) Apparent resistivity and phase percent difference between 0.01 Hz and 0.1 Hz. (Top to Bottom) VMS-2 model responses at depths of 30m, 60m and 100m.

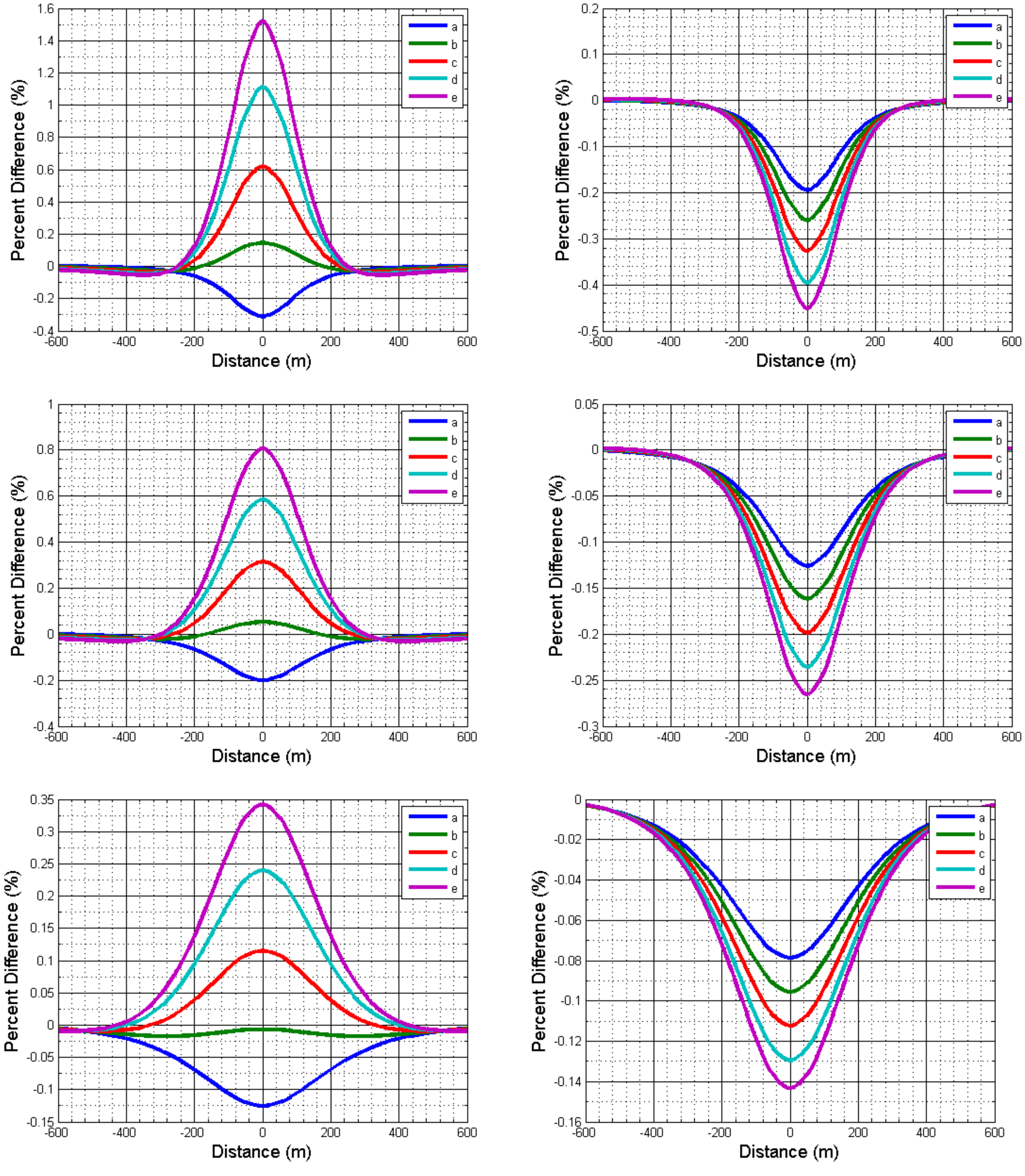

Fig. 21: (Left to Right) Apparent resistivity and phase percent difference between 0.01 Hz and 0.1 Hz. (Top to Bottom) VMS-2 model responses at depths of 100m, 150m and 300m.

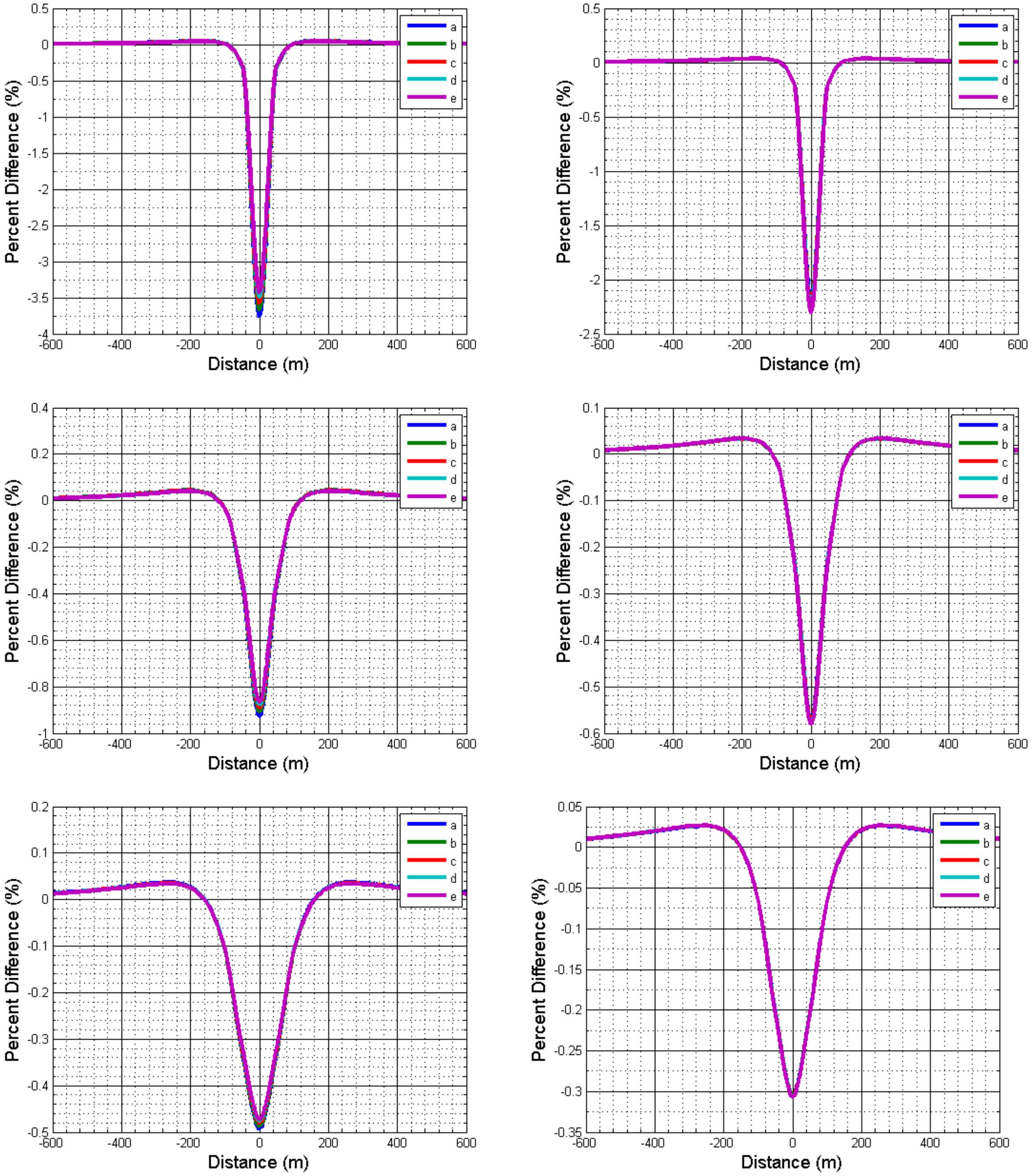

Fig. 22: (Left to Right) Apparent resistivity and phase percent difference between 0.01 Hz and 0.1 Hz. (Top to Bottom) Raglan-1 model response at depths of 30m, 60m and 100m.

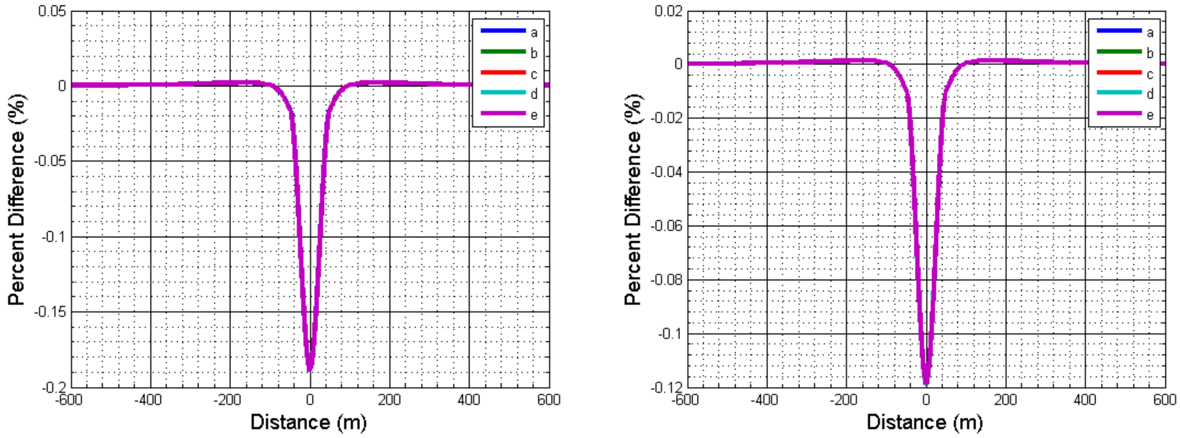

Fig. 23: (Left to Right) Apparent resistivity and phase percent difference between 0.01 Hz and 0.1 Hz. Raglan-2 model response with orebody located at 30m from the surface.

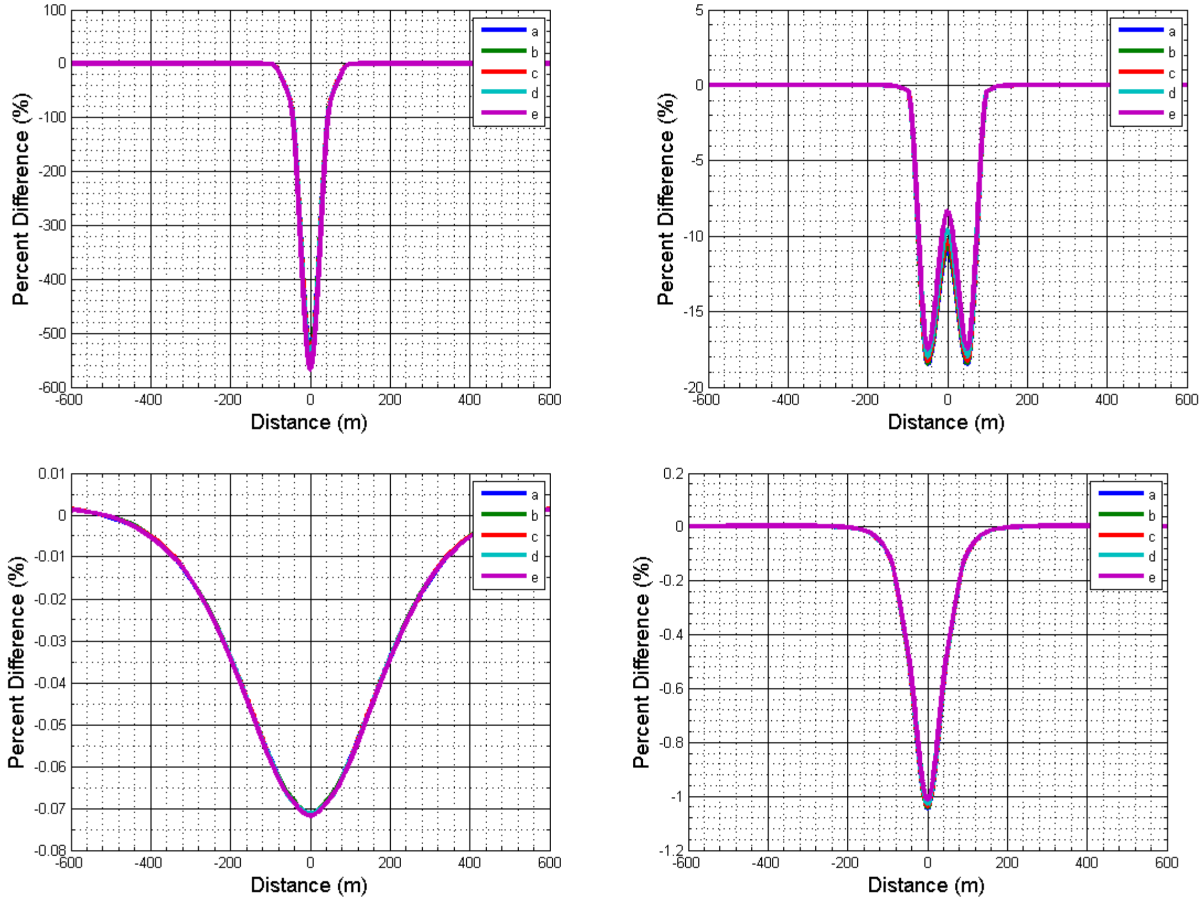

Fig. 24: (Left to Right) Apparent resistivity and phase percent difference between 0.01 Hz and 0.1 Hz. (Top to Bottom) Matagami model responses with orebody located at depths of 30m and 60m from the surface.

APPENDIX C – 2D MT MODELING #1

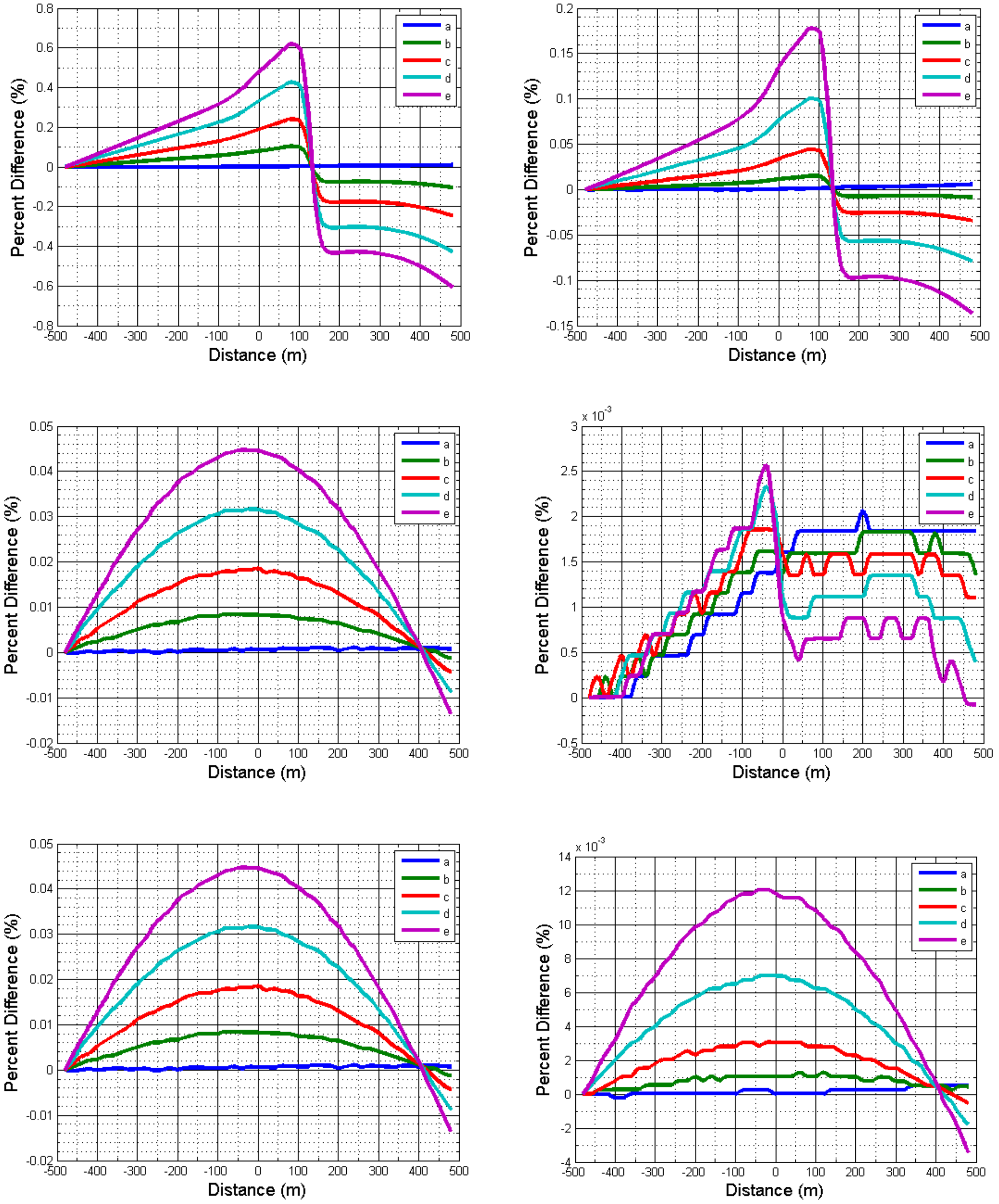

Fig. 25: (Left to Right) Apparent resistivity and phase percent difference between 0.01 Hz and 0.1 Hz for the station located at the center of the model. (Top to Bottom) Bracmac, Mcleoid and Bell Allard MT responses. (Key Tuffite = 1 kΩ·m and massive sulfide = 1 Ω·m)

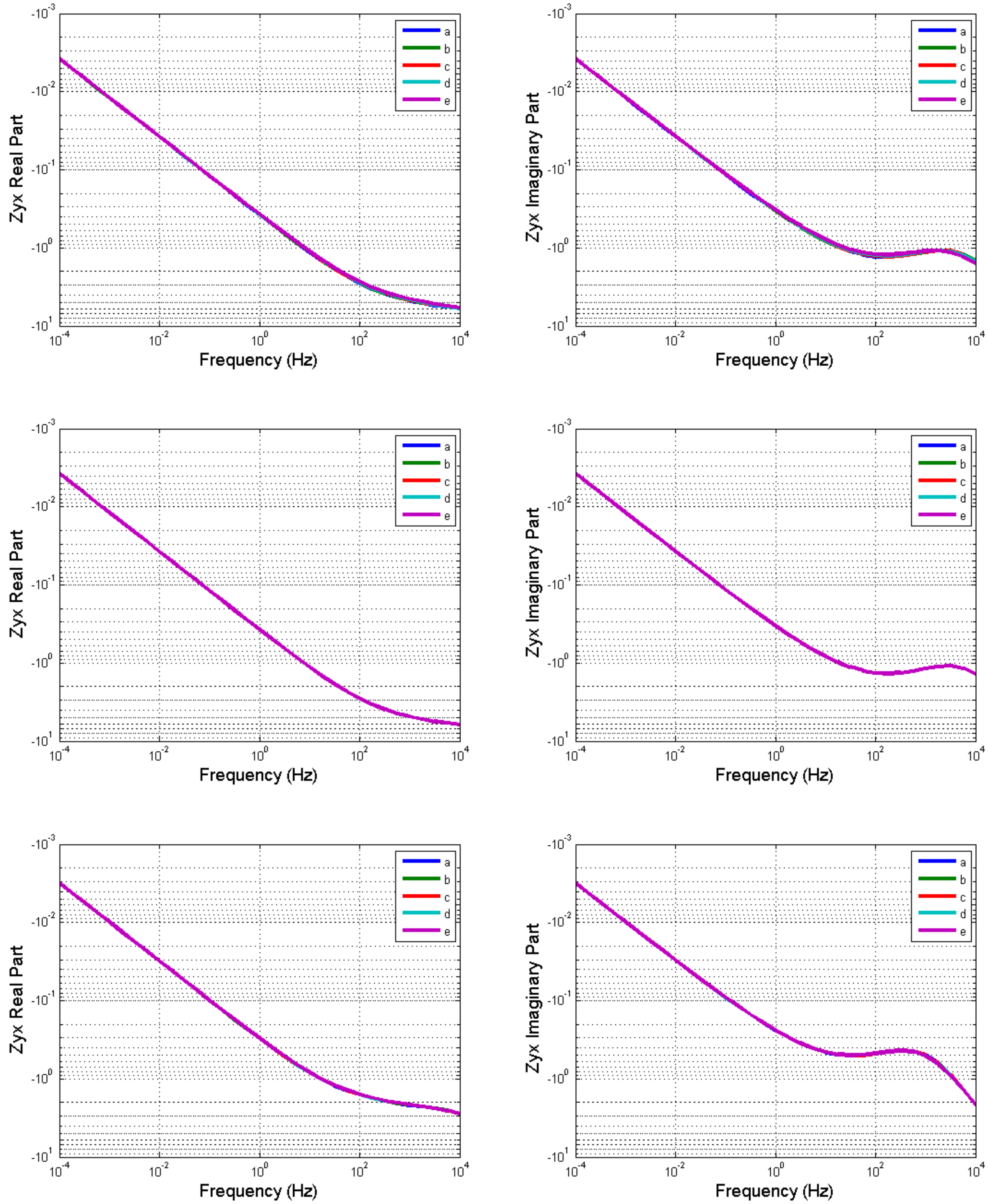

Fig. 26: Real and complex part of the TM impedence for the middle stations. Top: Bracmac. Middle: Mcleoid. Bottom: Bell Allard.

APPENDIX D – 2D MT MODELING #2

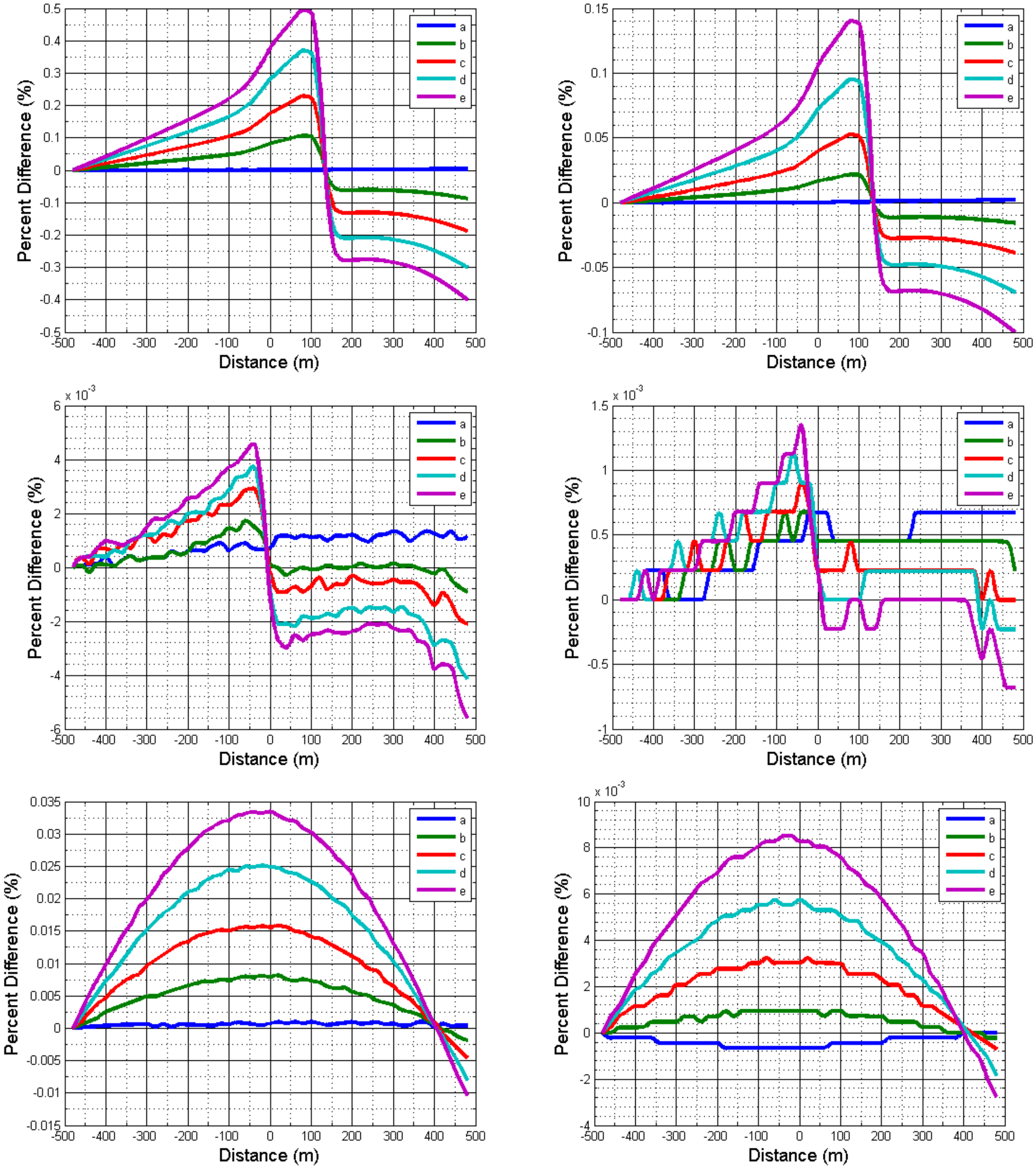

Fig. 27: (Left to Right) Apparent resistivity and phase percent difference between 0.01 Hz and 0.1 Hz for the station located at the center of the model. (Top to Bottom) Bracmac, Mcleoid and Bell Allard MT responses. (Key Tuffite = 533.79 kΩ·m and massive sulfide = 0.1 Ω·m)

APPENDIX E – 2D MT MODELING #3

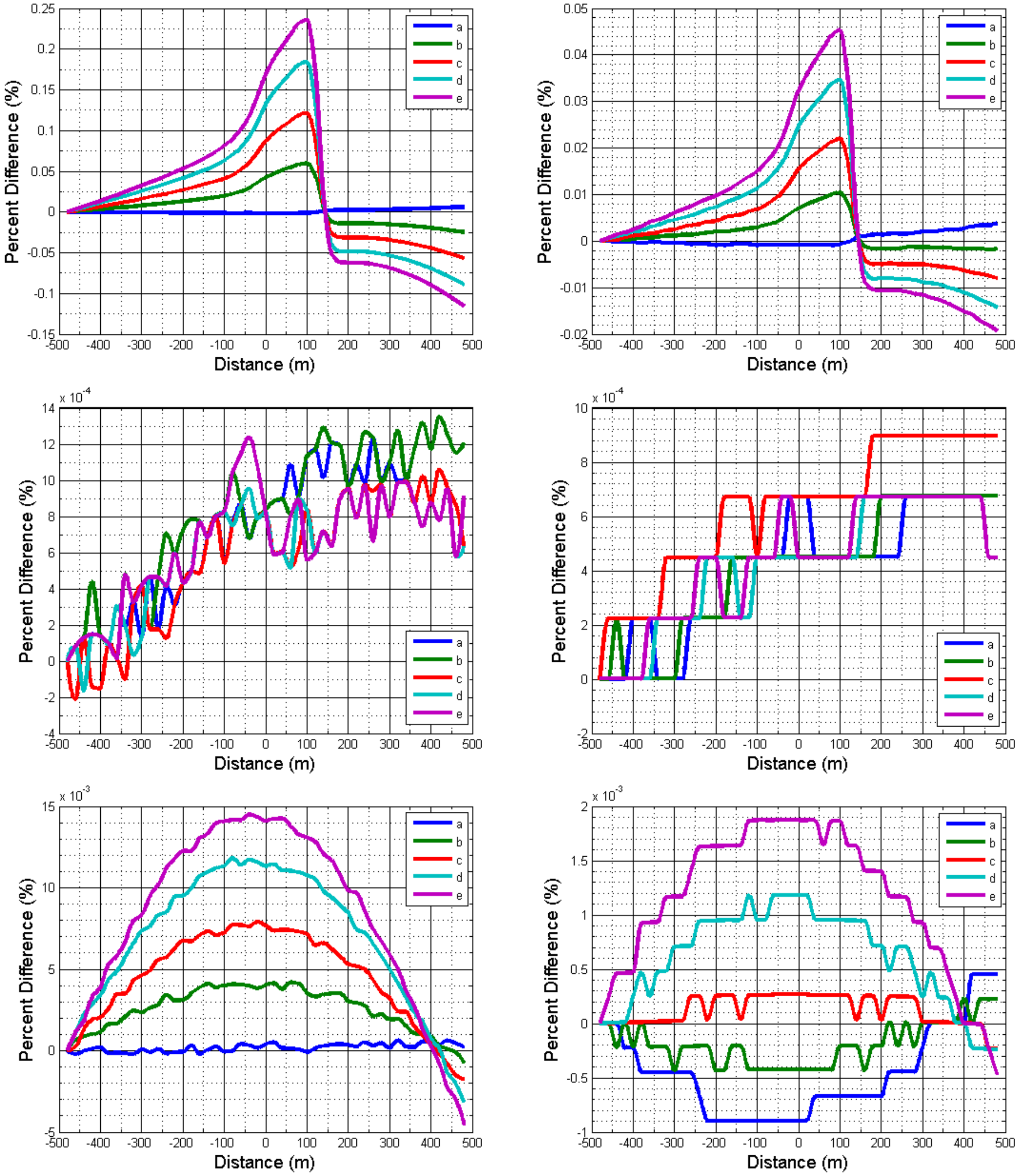

Fig. 28: (Left to Right) Apparent resistivity and phase percent difference between 0.01 Hz and 0.1 Hz for the station located at the center of the model. (Top to Bottom) Bracmac, Mcleoid and Bell Allard MT responses. (Key Tuffite = 29.02 Ω·m and massive sulfide = 0.1 Ω·m)

APPENDIX F – 2D INVERSION RESISTIVITY MAP

Figures in this appendix correspond to the resistivity map generated through the 3D models. The 3D models are constructed by interpolating the 2D inversions models. In this thesis, we have run the 2D inversion through 3 different procedures (See section 6.5).

Recaps:

> **Setting 1.** The first setting was set as follows: Both TE & TM modes and phase were set at 5% error. The interval of frequency was from 0.1 Hz to 10 000 Hz. The initial model contained a homogenous medium of 40 000 Ω·m with a fixed 1D anisotropy model starting below 5 000m. The number of iterations varies between profiles and the number of iterations was limited to 500. Static shift was added and another 100 iterations were done for all profiles.
>
> **Setting 2.** The second setting was set as follows: The TM resistivity and TM & TE phase were set with 5% error while the TE resistivity was set at 50% error. 200 iterations were done for frequencies between 0.1 Hz to 10 000 Hz with static shift. The inversion started with a homogenous model of 40 000 Ω·m without the 1D anisotropy model.
>
> **Setting 3.** The third setting was set as follows: TE resistivity and TE & TM phase are set to 5% error throughout the inversions. The TM resistivity was first set at 50% error with 50 iterations. Afterward, the TM resisitivity error was reduced to 5%, the static shift was added and another 50 iterations were done. The inversion started with a homogenous model of 40 000 Ω·m with frequency ranging from 0.1Hz to 1 000 Hz.

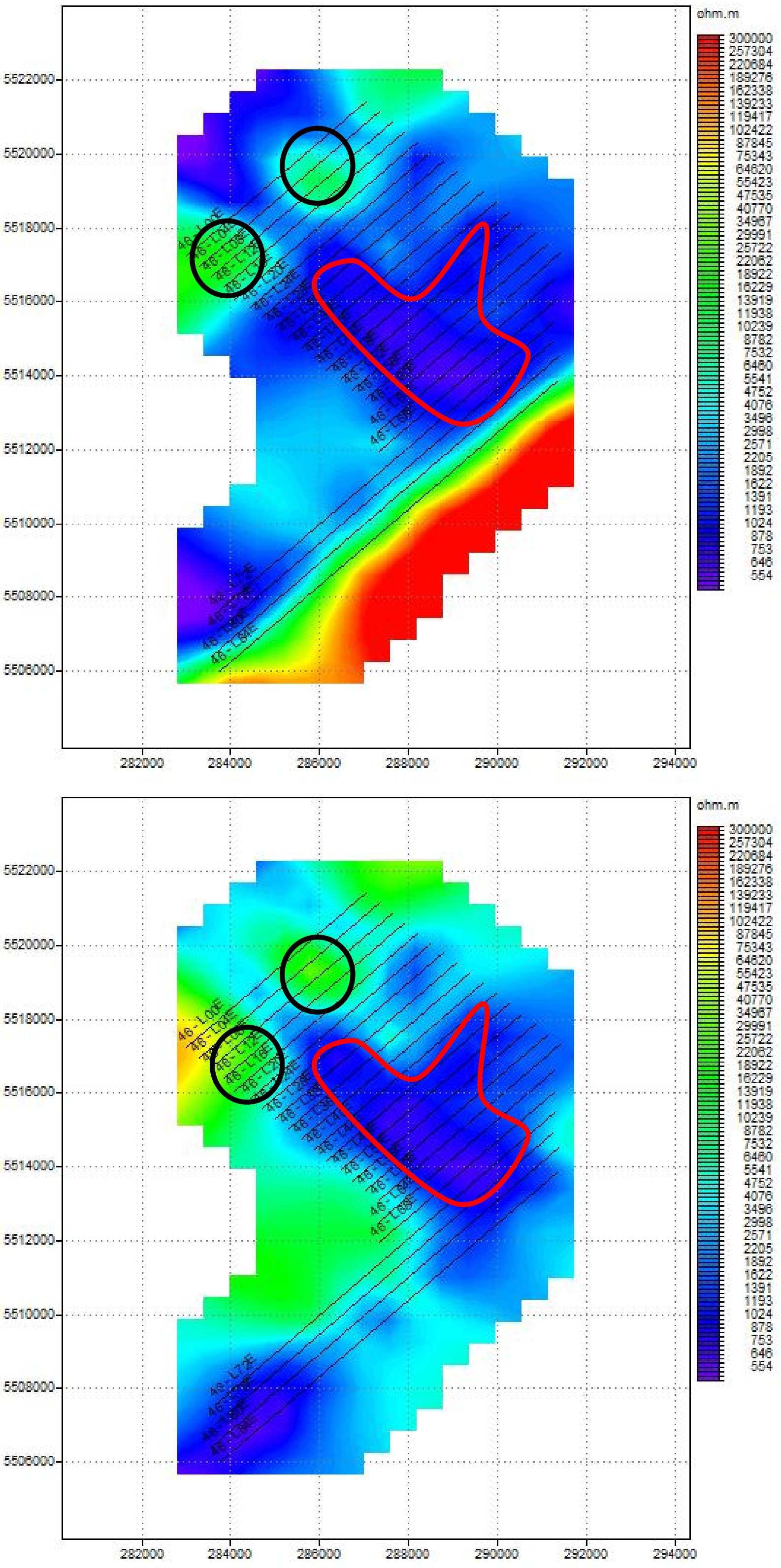

Fig. 29: Resistivity maps at depth of 100m. Top: Setting 2. Bottom: Setting 3.

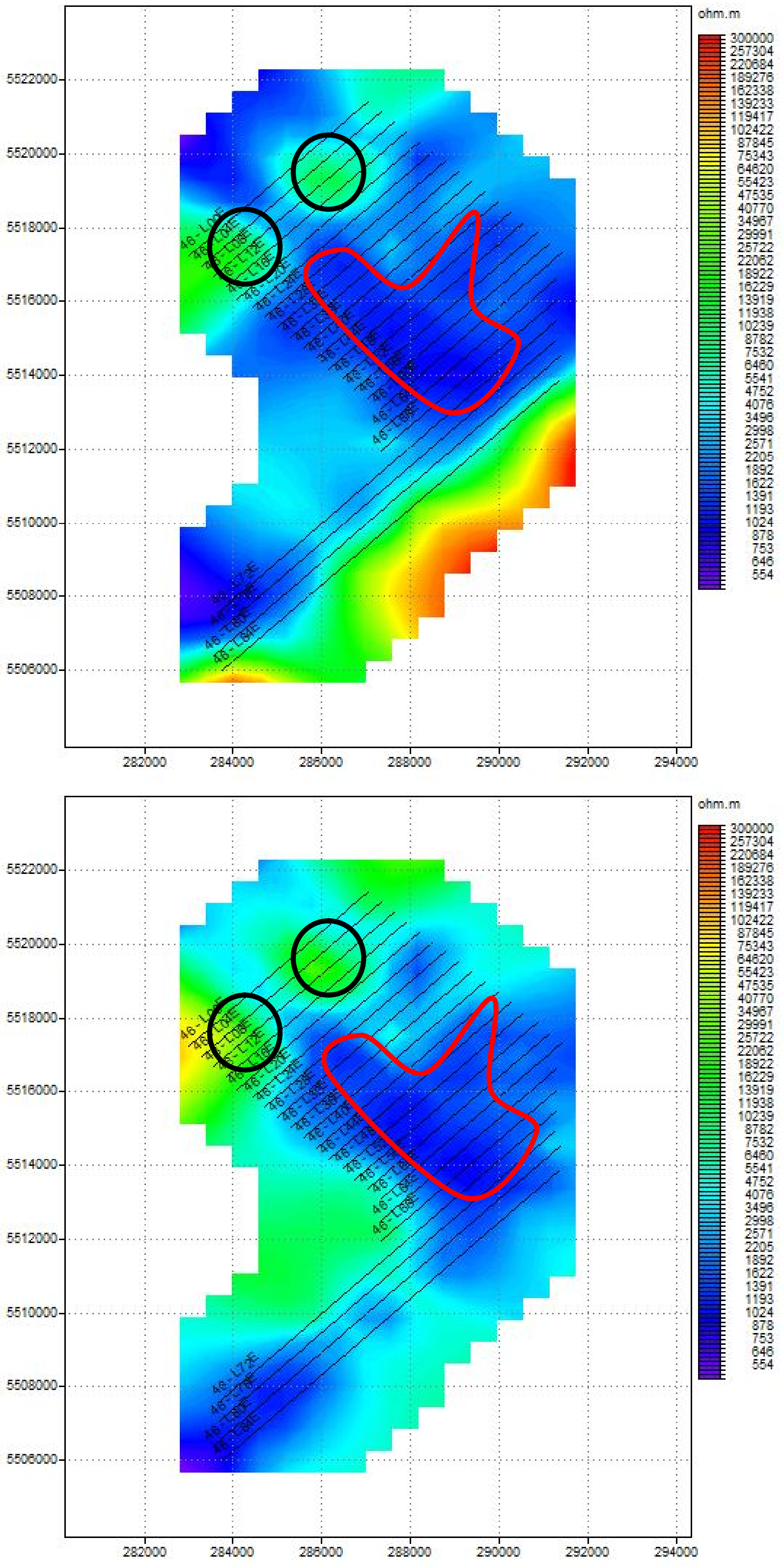

Fig. 30: Resistivity maps at depth of 250m. Top: Setting 2. Bottom: Setting 3.

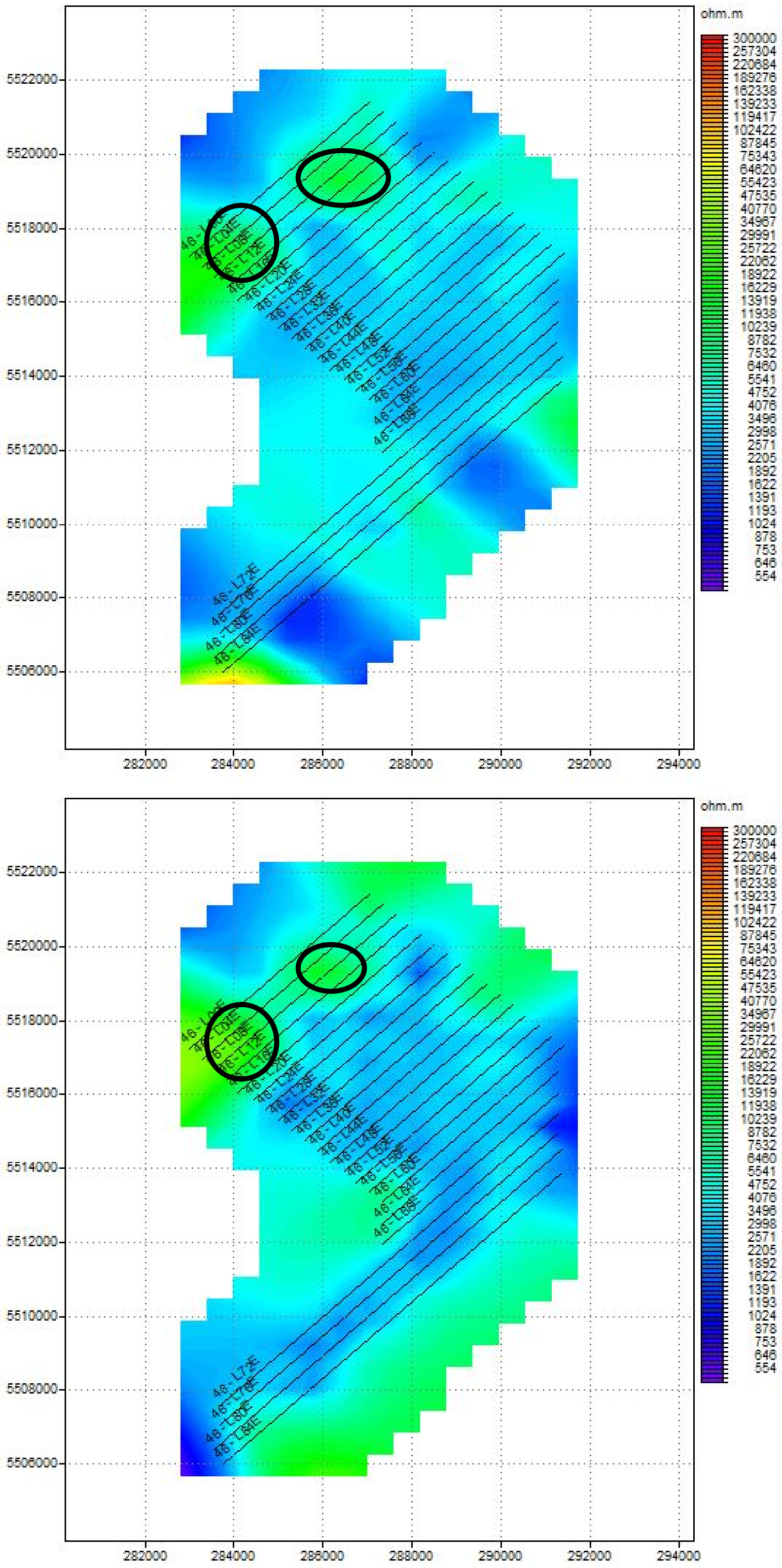

Fig. 31: Resistivity maps at depth of 500m. Top: Setting 2. Bottom: Setting 3.

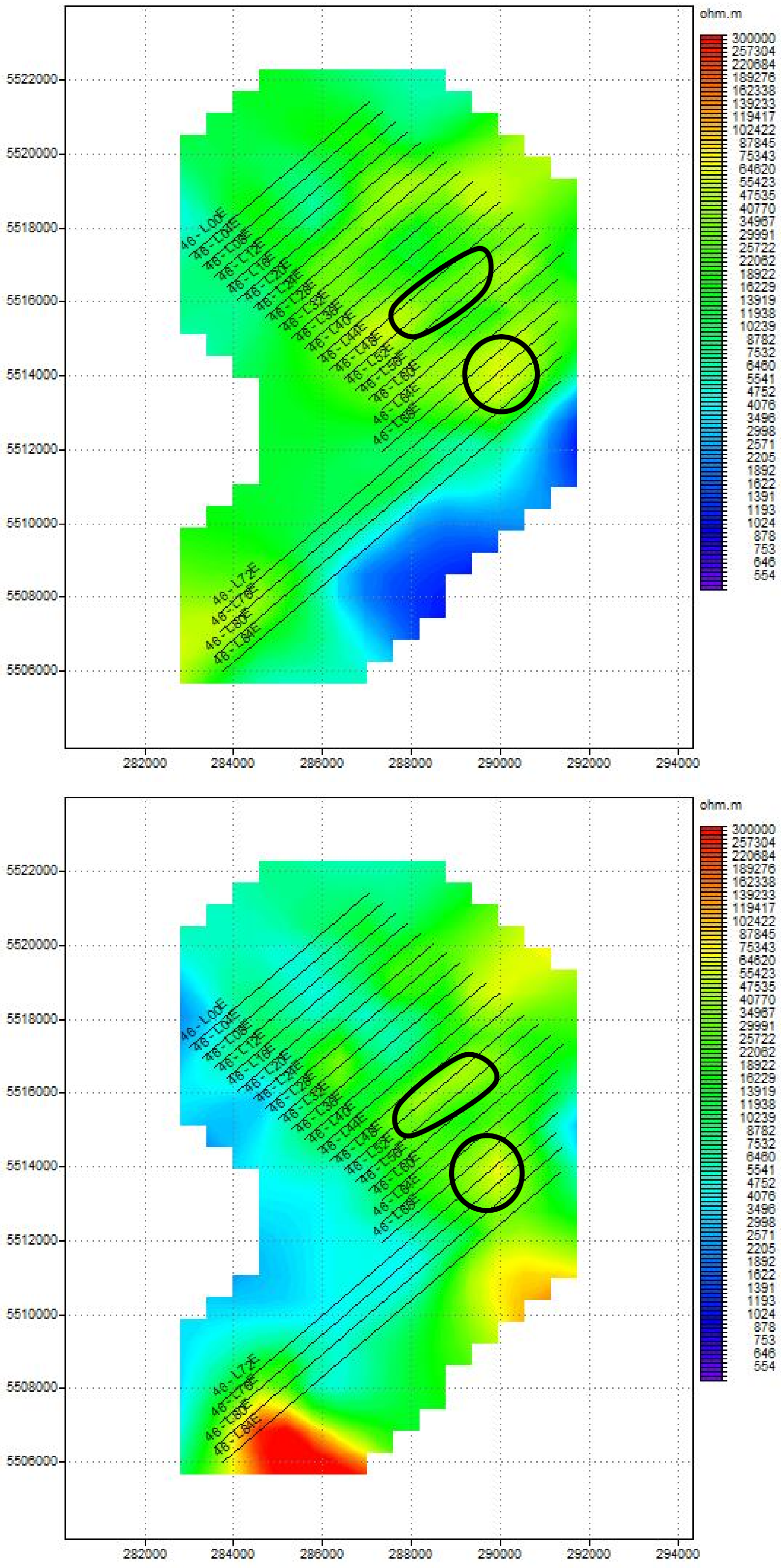

Fig. 32: Resistivity maps at depth of 1000m. Top: Setting 2. Bottom: Setting 3.

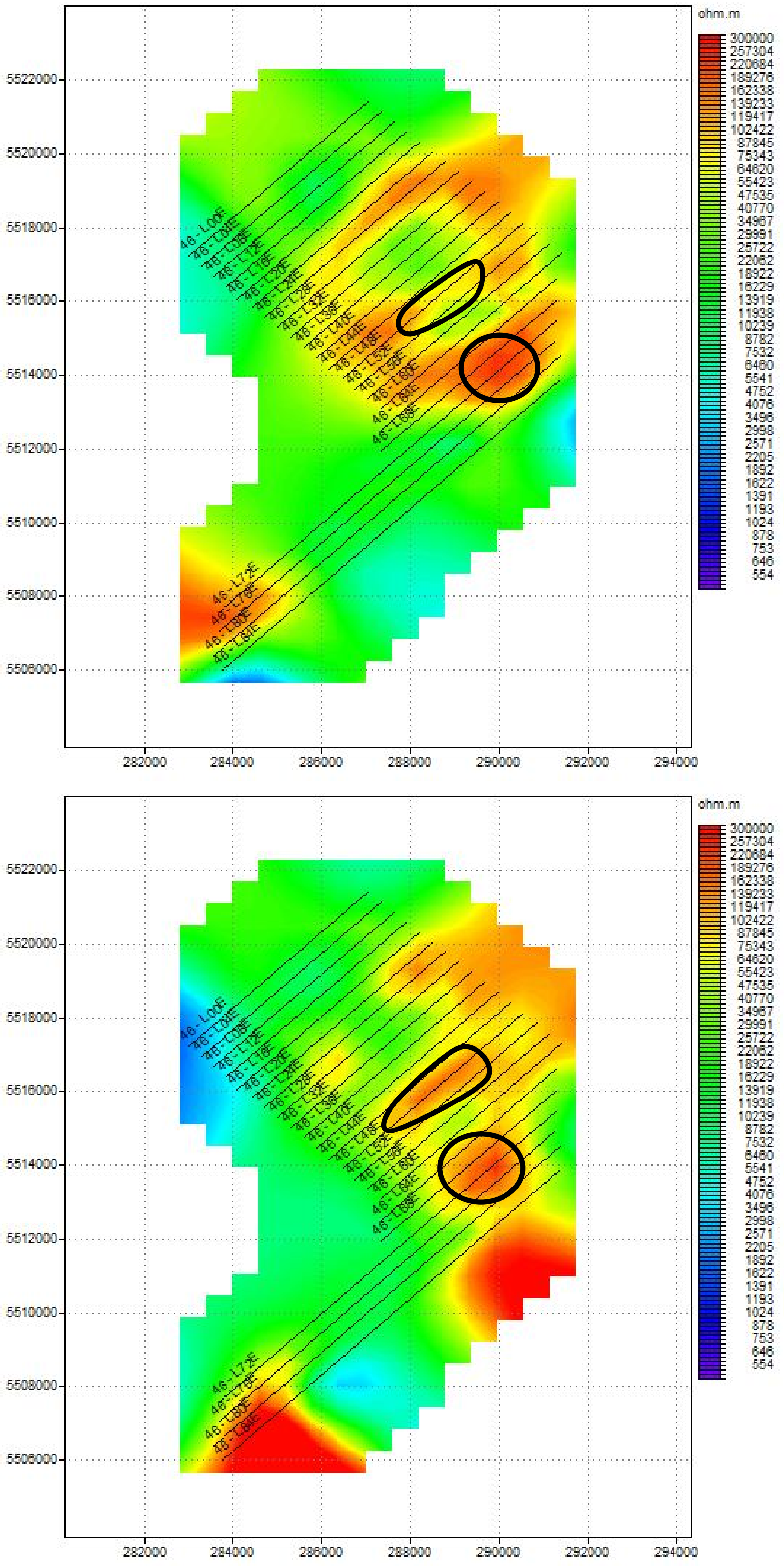

Fig. 33: Resistivity maps at depth of 1500m. Top: Setting 2. Bottom: Setting 3.

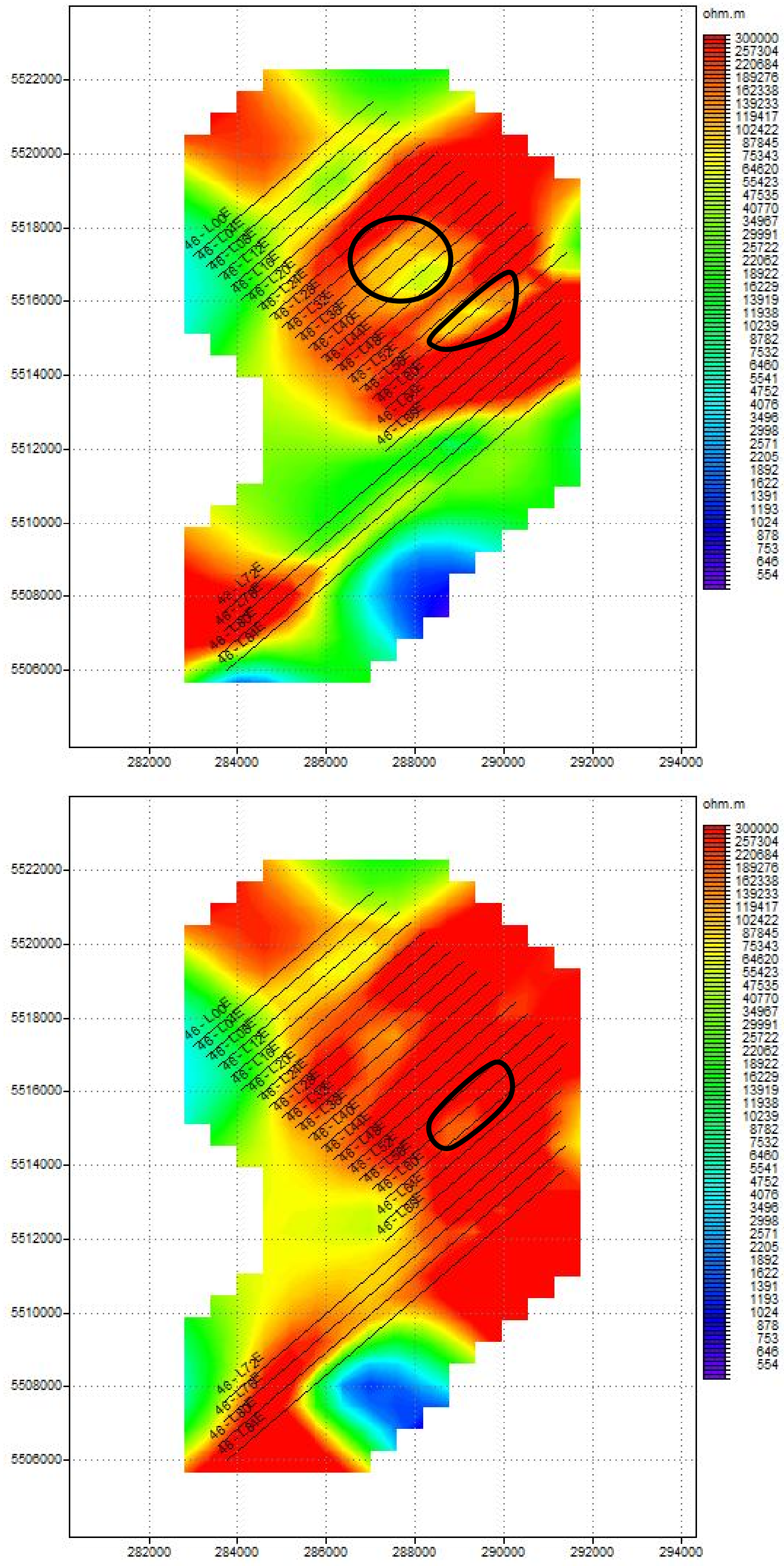

Fig. 34: Resistivity maps at depth of 2000m. Top: Setting 2. Bottom: Setting 3.

APPENDIX G – INTERPOLATED 3D MODELS

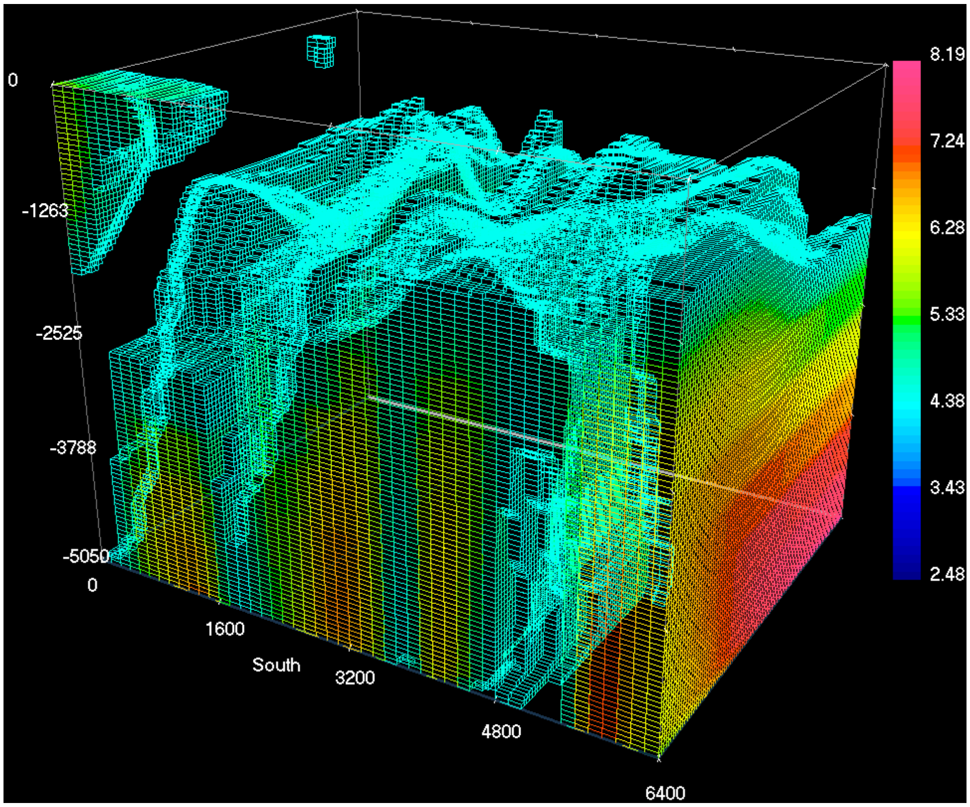

Fig. 35: 2D inversion (setting 1) results interpolated into 3D models with a minimum cut off of 10^4 Ω·m.

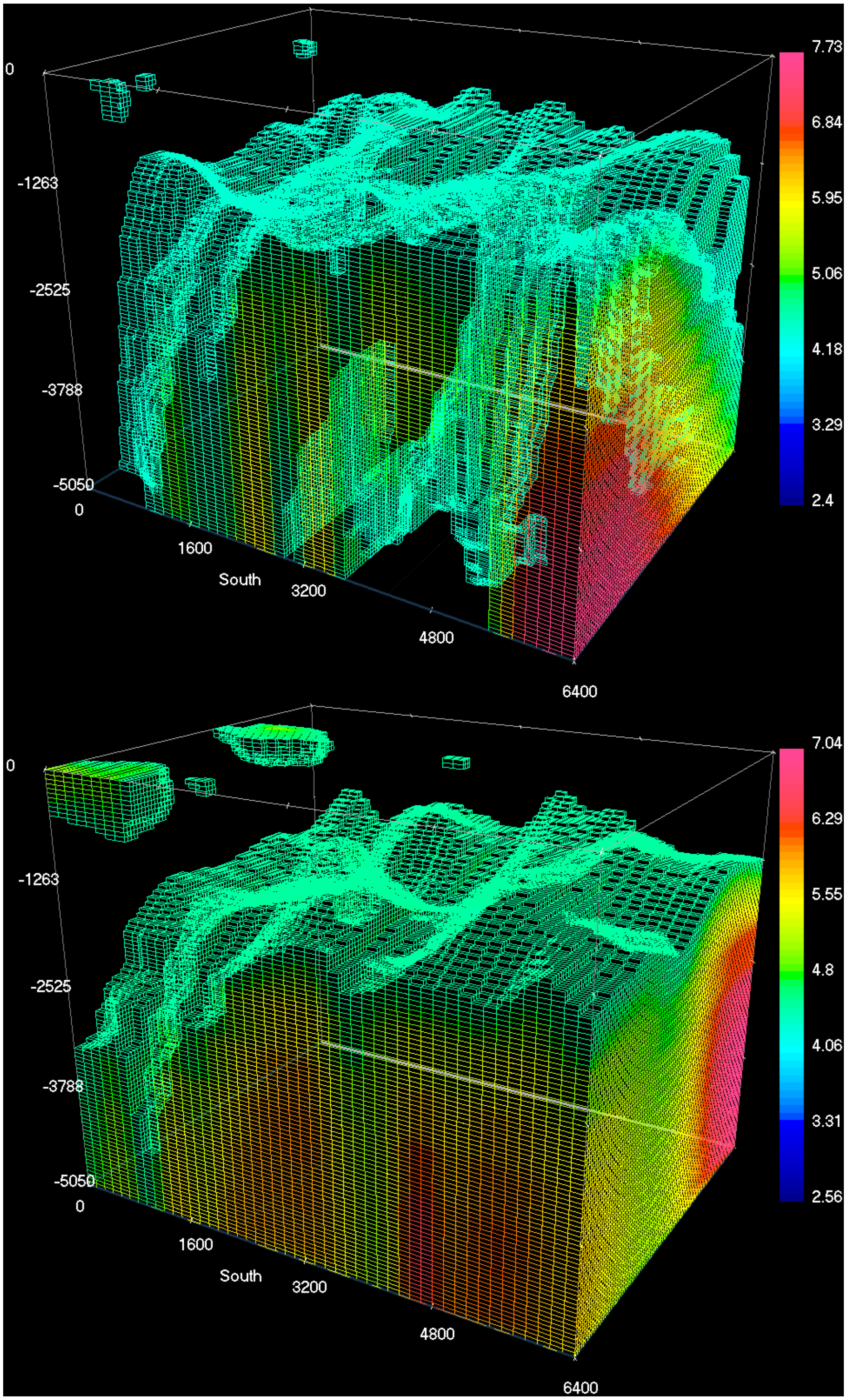

Fig. 36: 2D inversion results interpolated into 3D models with a minimum cut off of 10^4 Ω·m. (Top: setting 2, Bottom: setting 3)

APPENDIX H – 3D MODEL RESPONSES

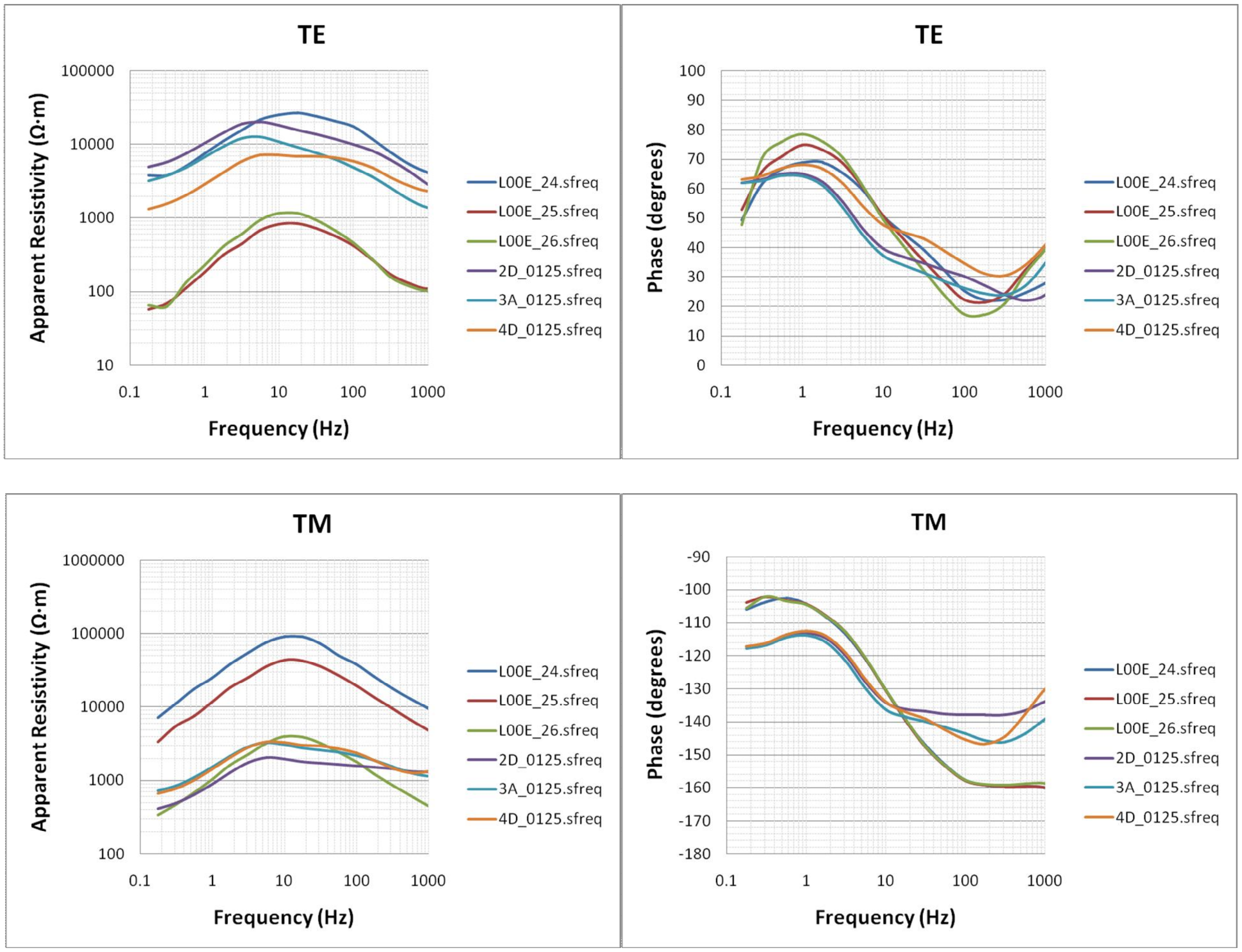

Fig. 37: Comparison of the 3D modeling responses produced by the three 3D models with the MT stations 24, 25 and 26 of MT survey profile L00E.

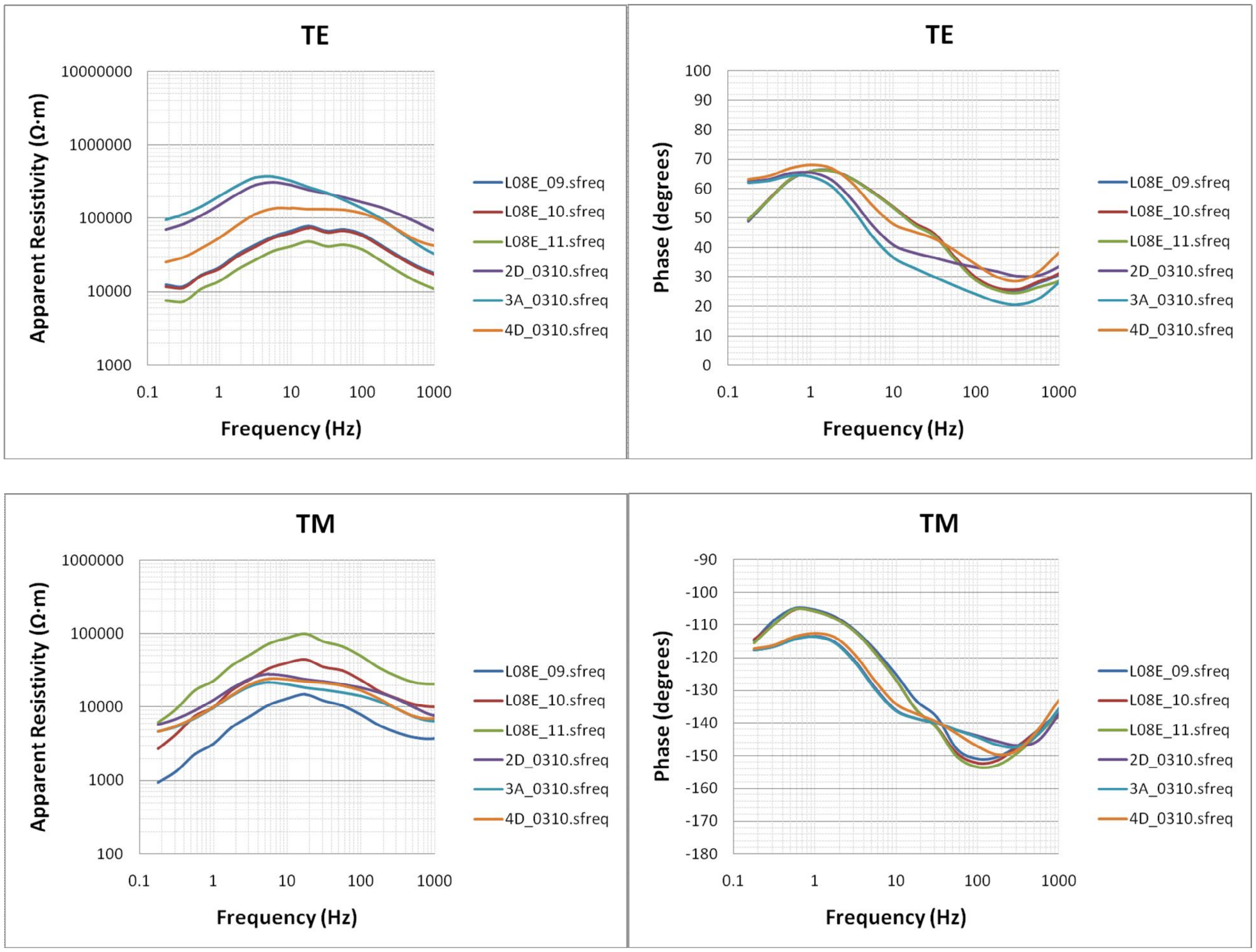

Fig. 38: Comparison of the 3D modeling responses produced by the three 3D models with the MT stations 09, 10 and 11 of MT survey profile L08E.

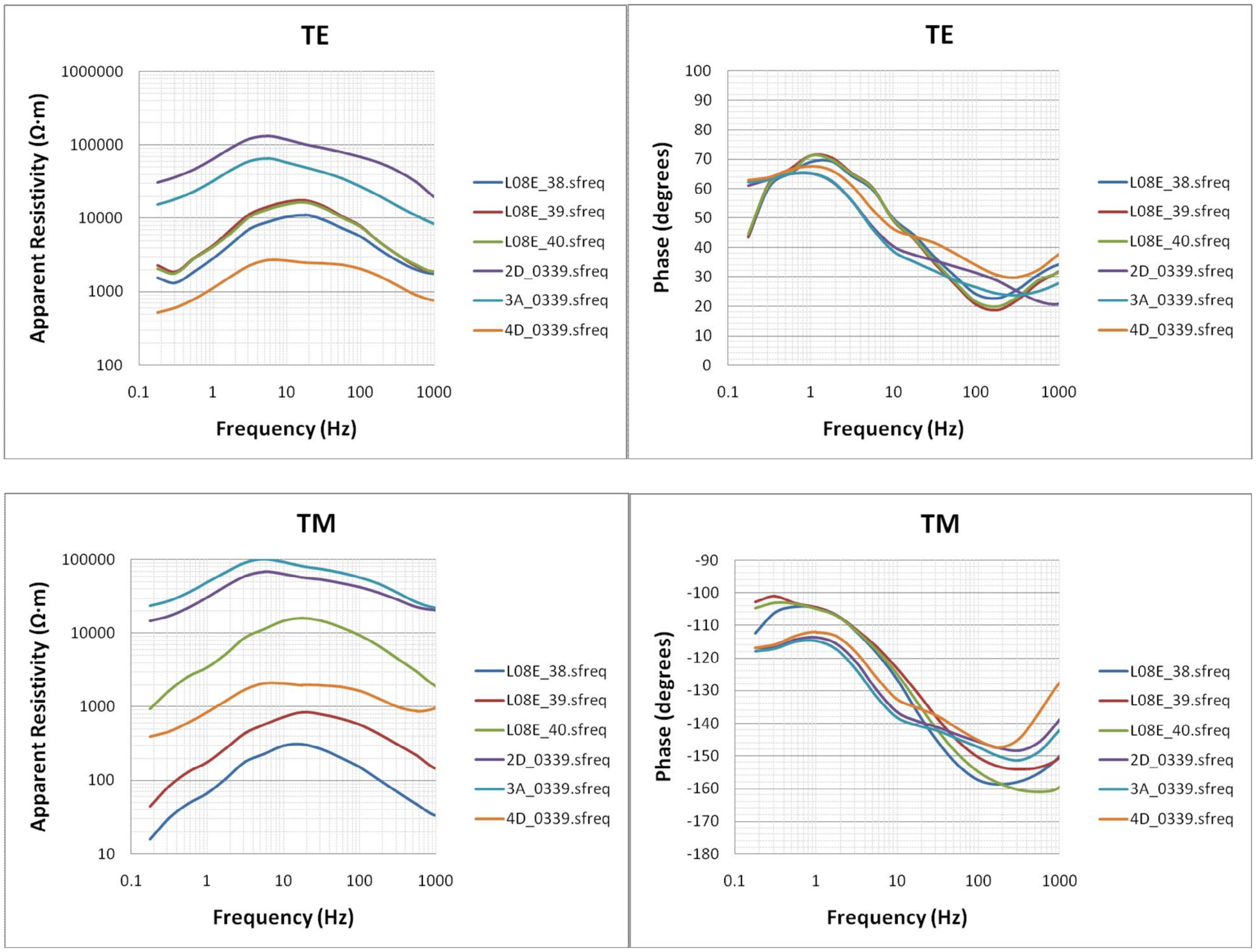

Fig. 39: Comparison of the 3D modeling responses produced by the three 3D models with the MT stations 38, 39 and 40 of MT survey profile L08E.

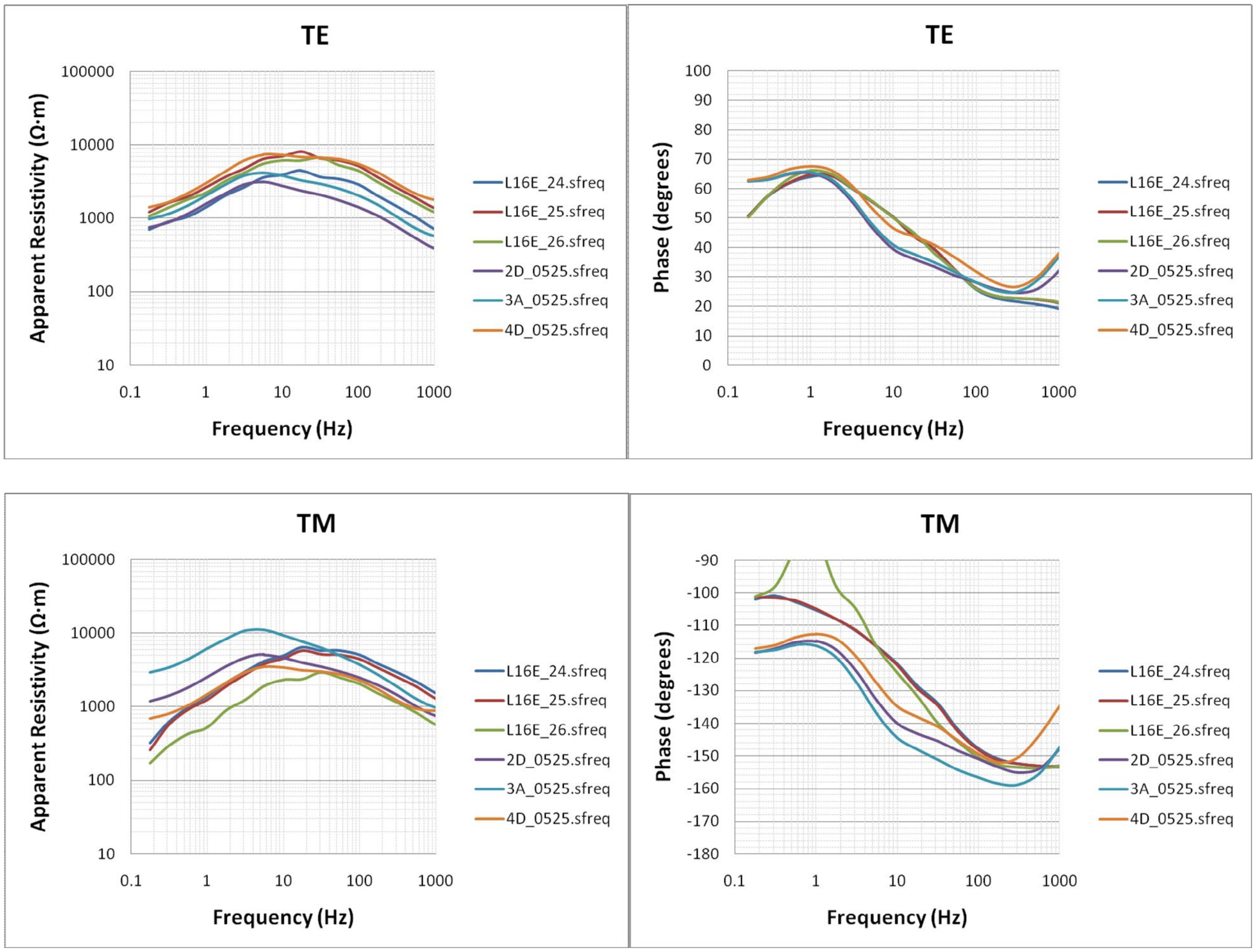

Fig. 40: Comparison of the 3D modeling responses produced by the three 3D models with the MT stations 24, 25 and 26 of MT survey profile L16E.

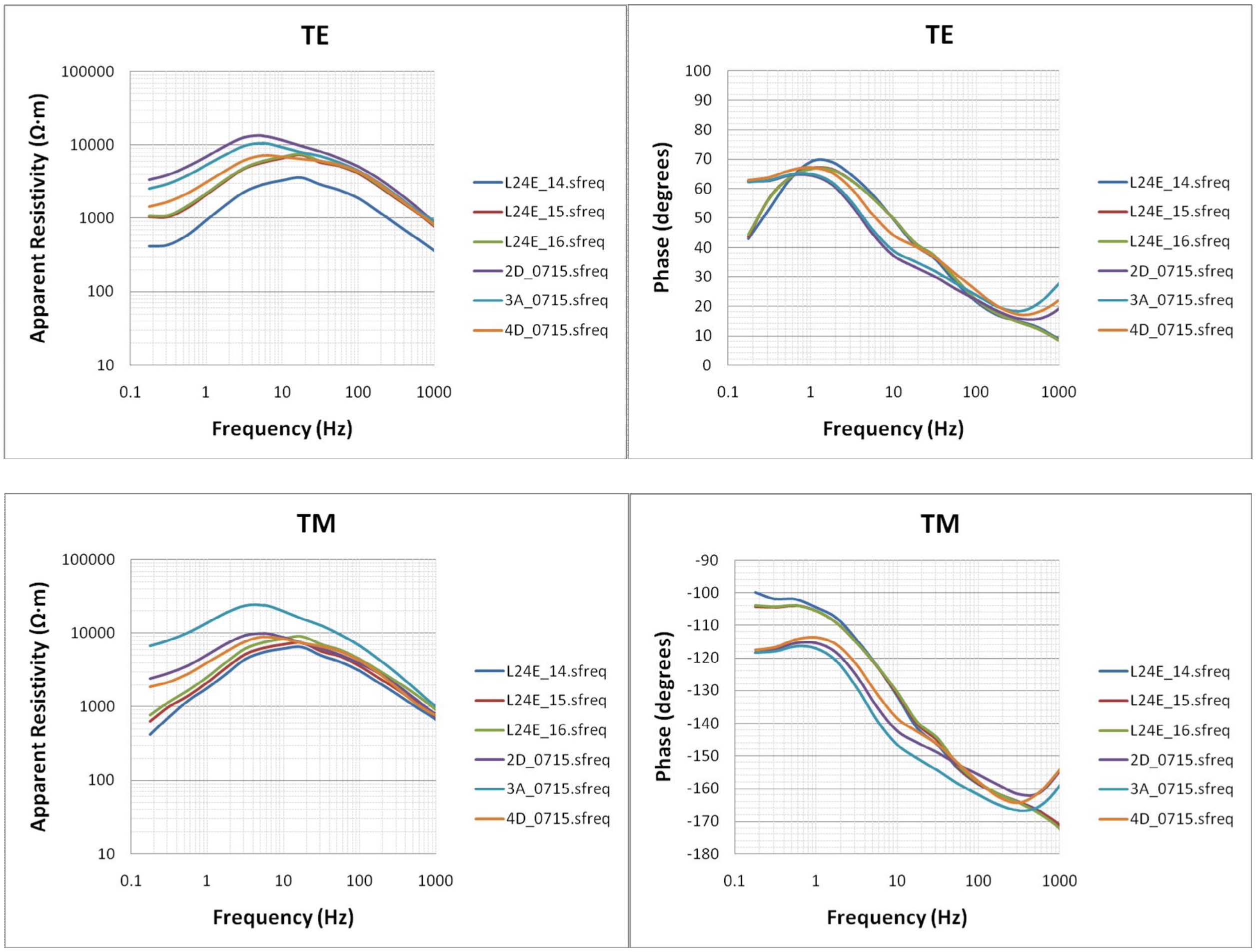

Fig. 41: Comparison of the 3D modeling responses produced by the three 3D models with the MT stations 14, 15 and 16 of MT survey profile L24E.

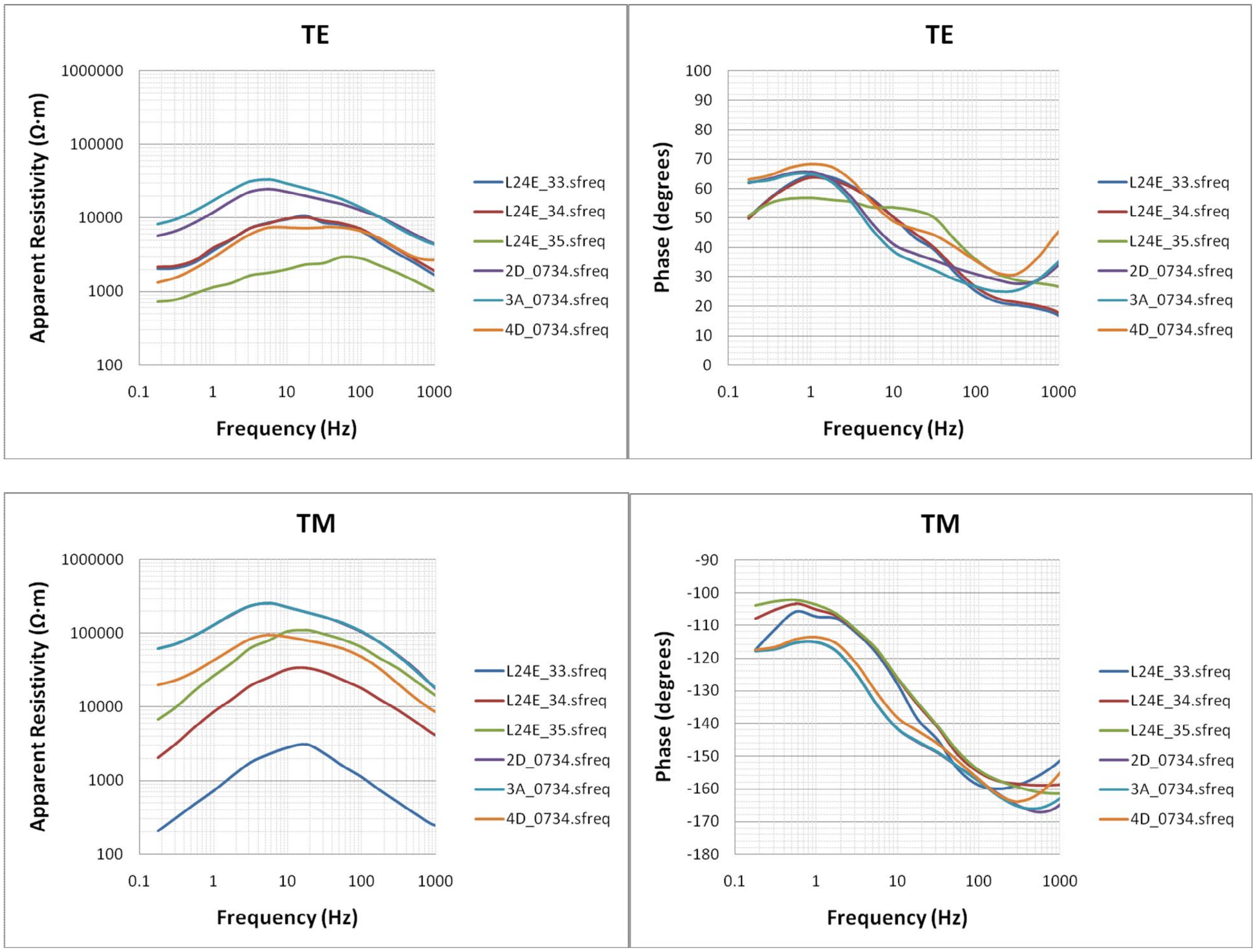

Fig. 42: Comparison of the 3D modeling responses produced by the three 3D models with the MT stations 33, 34 and 35 of MT survey profile L24E.

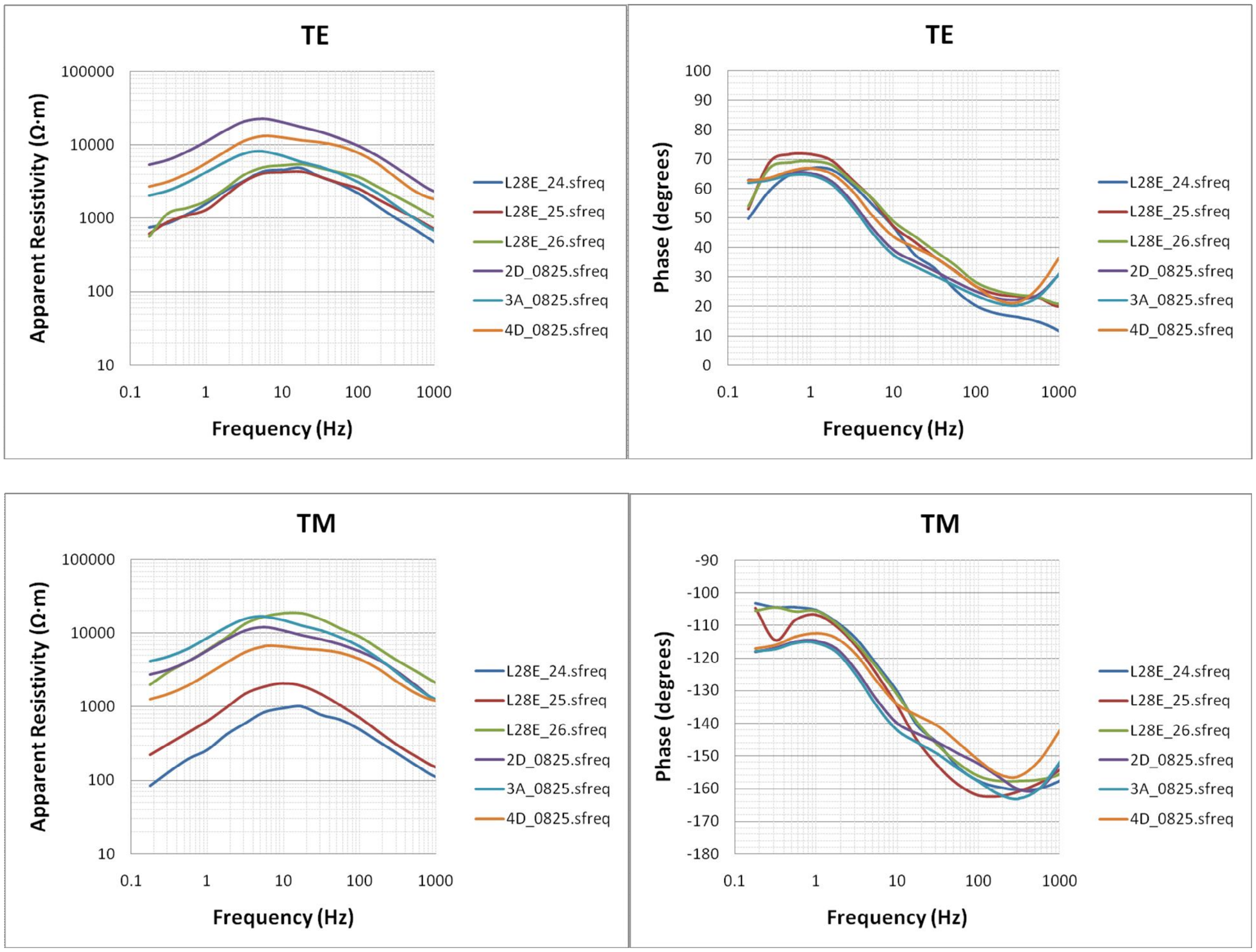

Fig. 43: Comparison of the 3D modeling responses produced by the three 3D models with the MT stations 24, 25 and 26 of MT survey profile L28E.

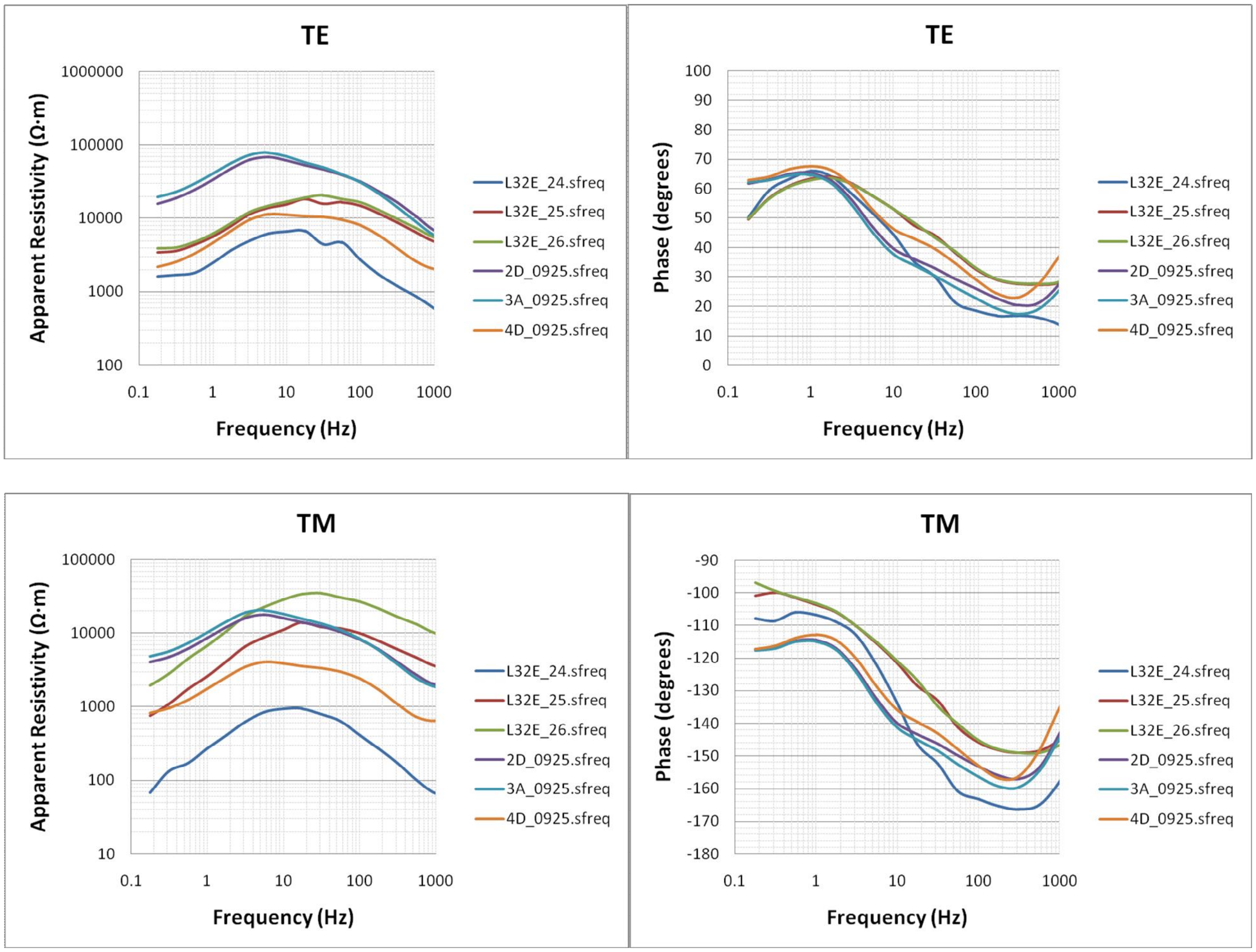

Fig. 44: Comparison of the 3D modeling responses produced by the three 3D models with the MT stations 24, 25 and 26 of MT survey profile L32E.

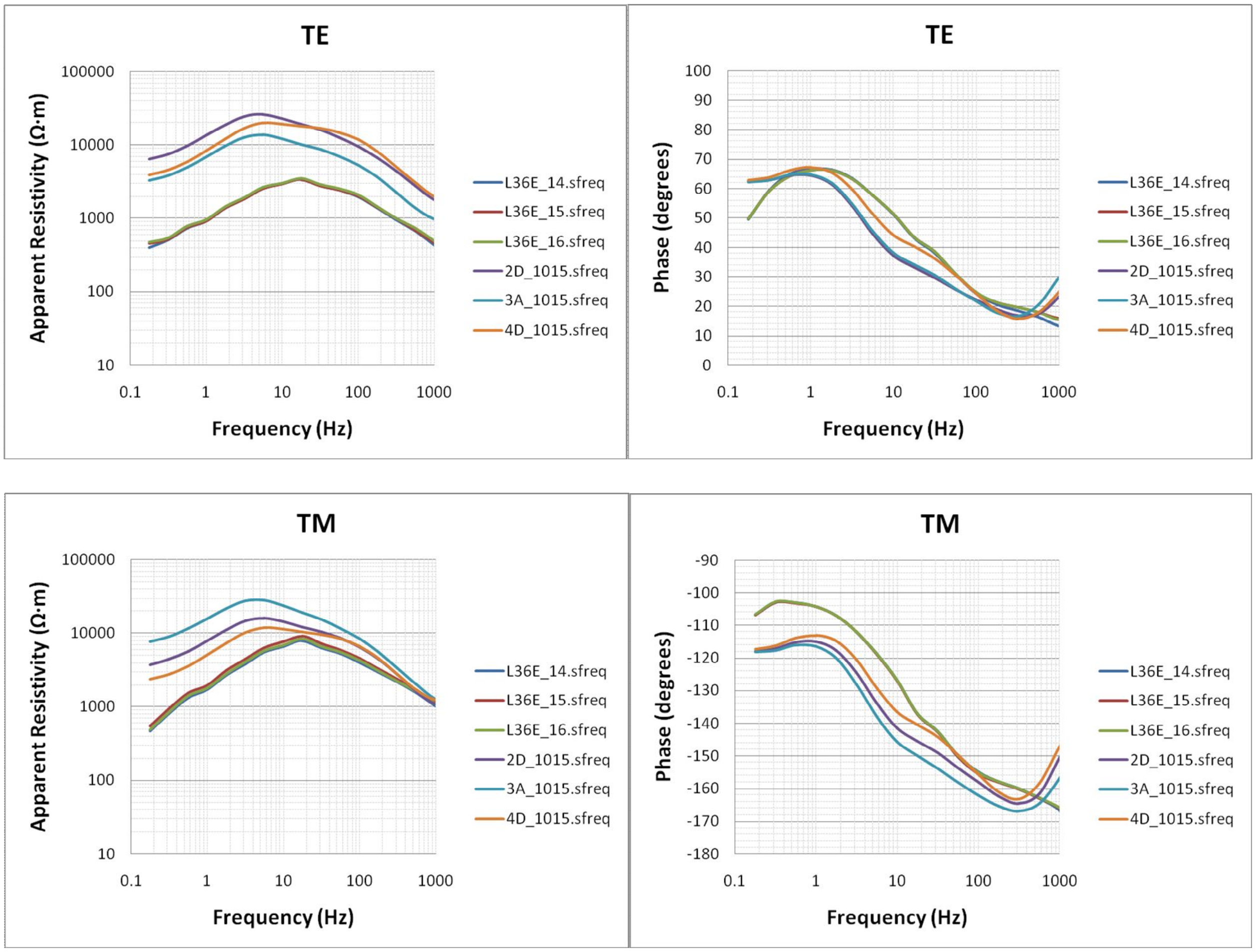

Fig. 45: Comparison of the 3D modeling responses produced by the three 3D models with the MT stations 14, 15 and 16 of MT survey profile L36E.

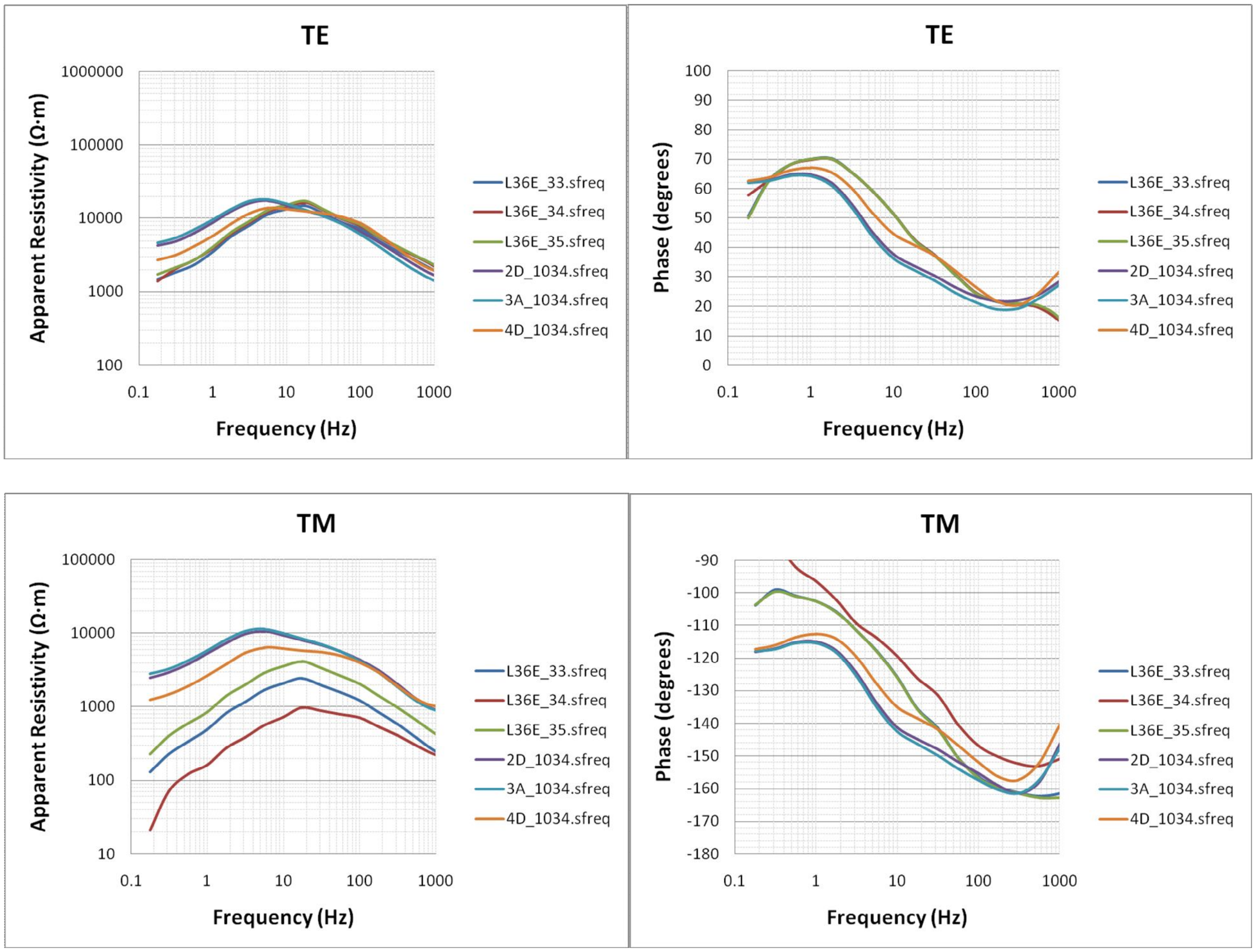

Fig. 46: Comparison of the 3D modeling responses produced by the three 3D models with the MT stations 33, 34 and 35 of MT survey profile L36E.

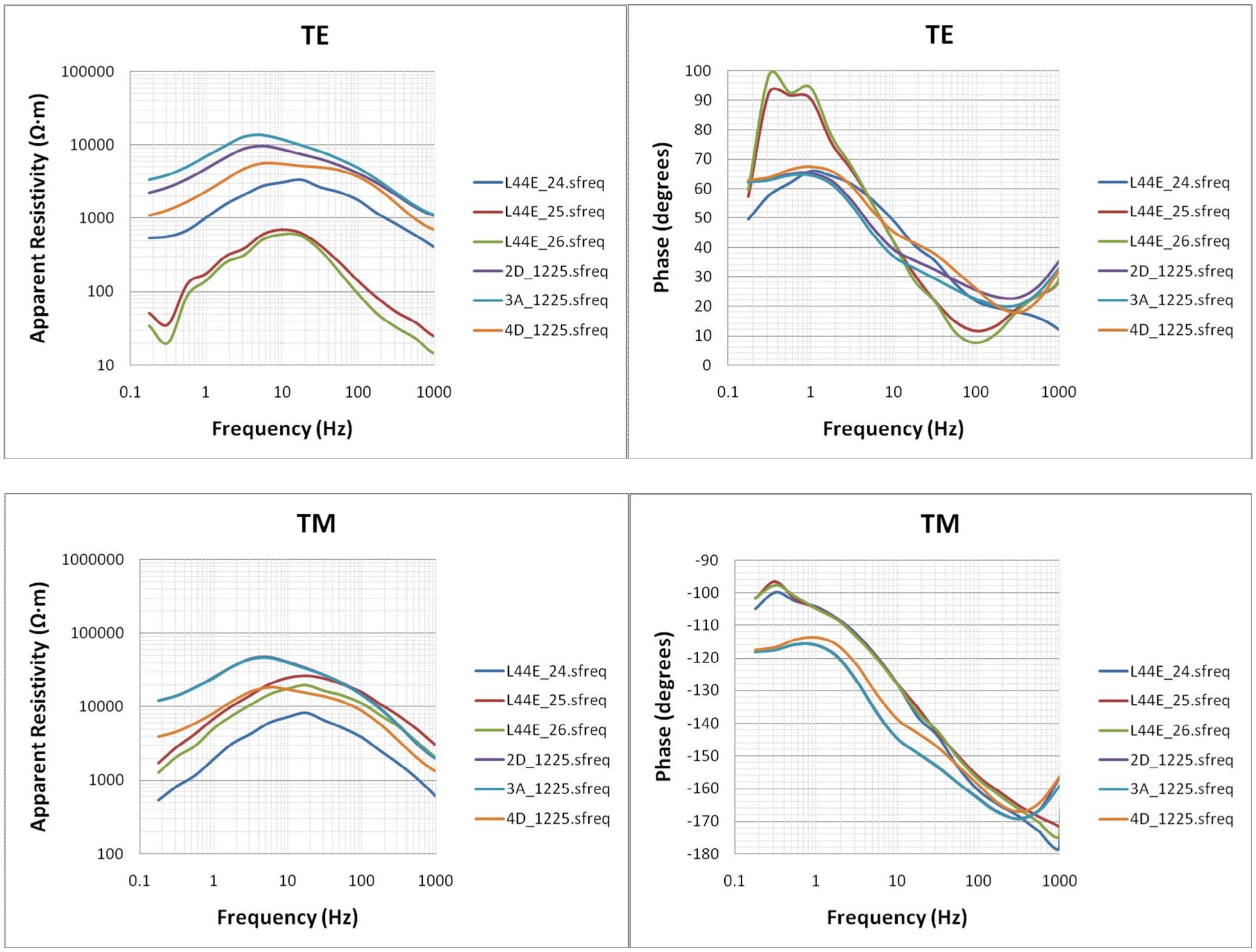

Fig. 47: Comparison of the 3D modeling responses produced by the three 3D models with the MT stations 24, 25 and 26 of MT survey profile L44E.

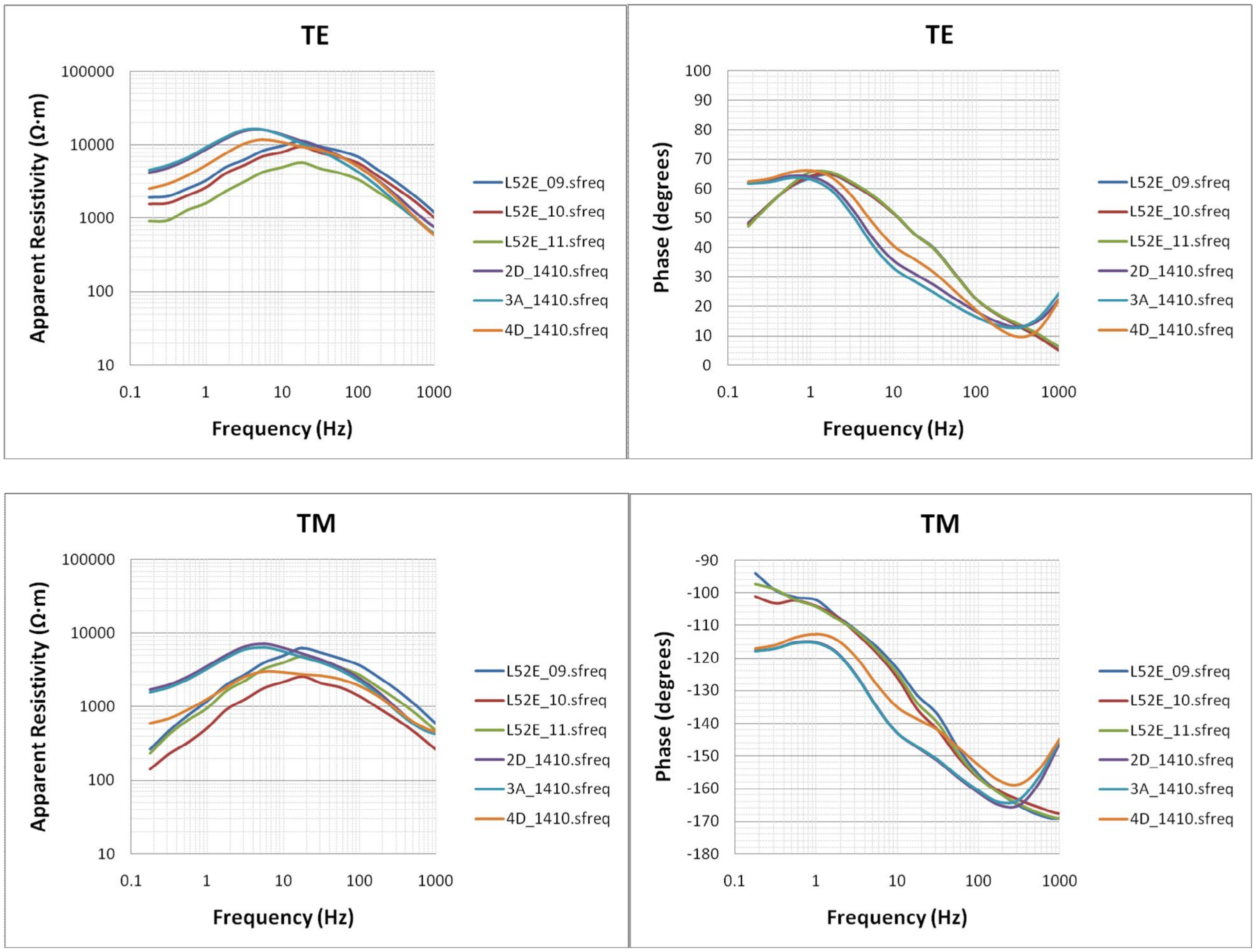

Fig. 48: Comparison of the 3D modeling responses produced by the three 3D models with the MT stations 09, 10 and 11 of MT survey profile L52E.

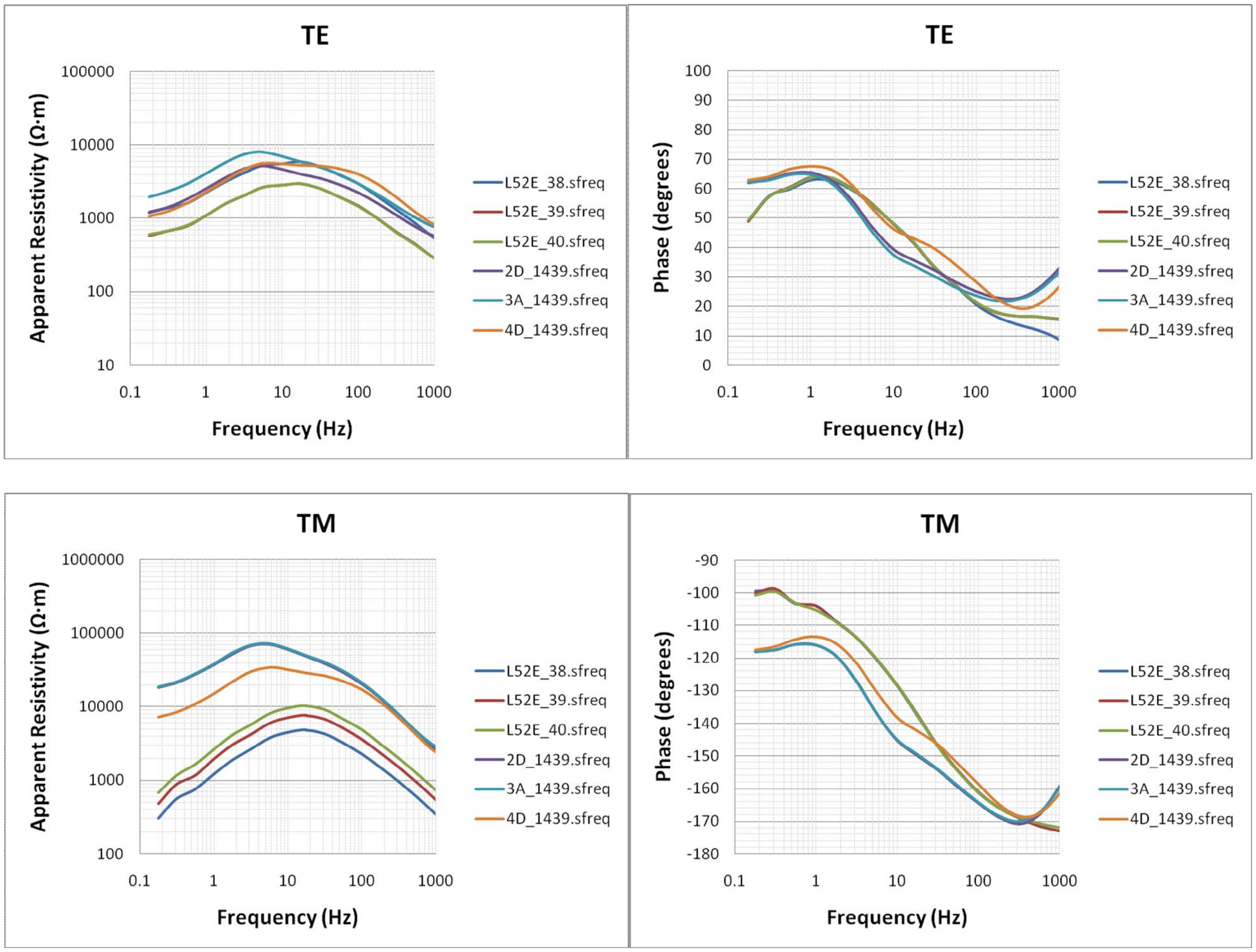

Fig. 49: Comparison of the 3D modeling responses produced by the three 3D models with the MT stations 38, 39 and 40 of MT survey profile L52E.

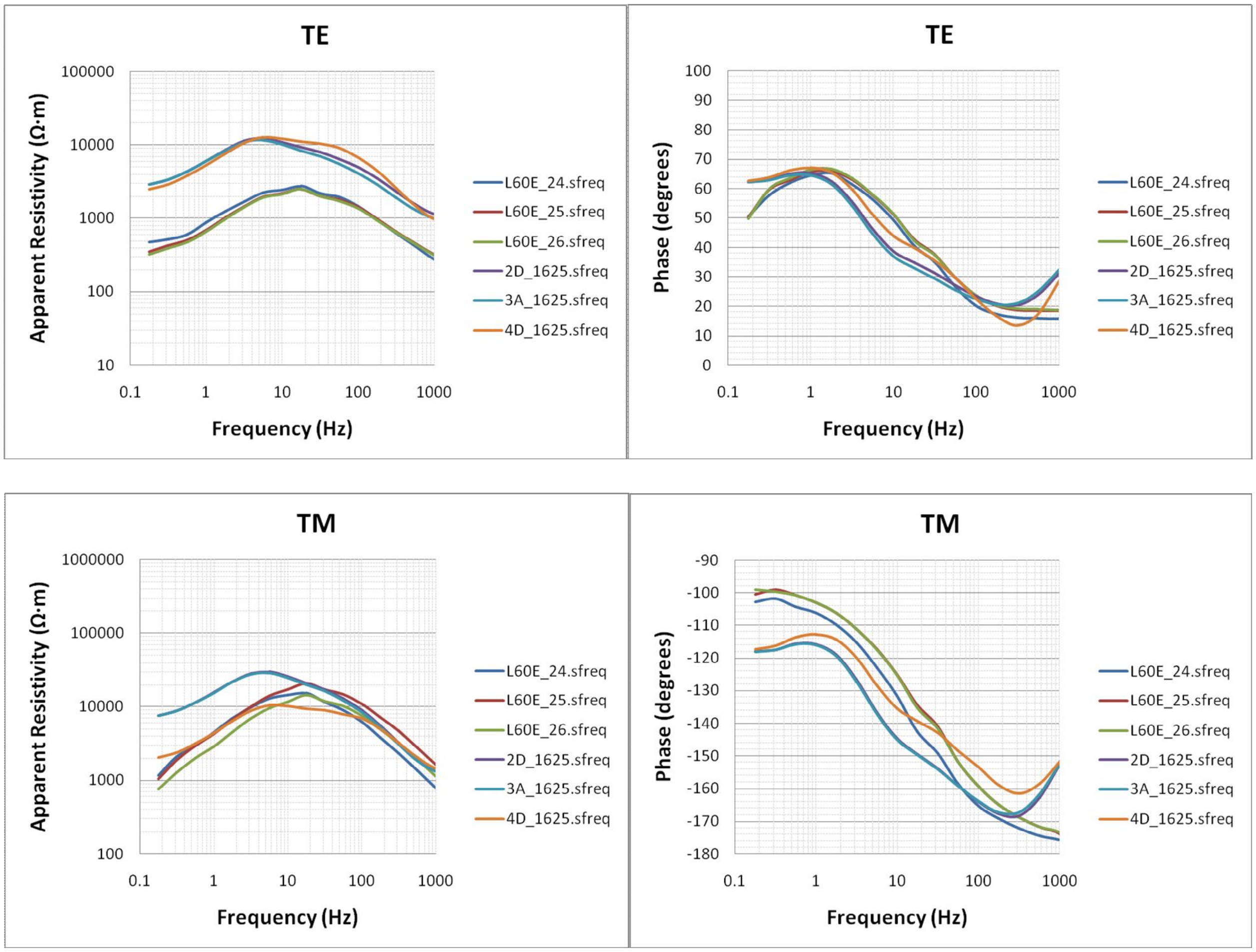

Fig. 50: Comparison of the 3D modeling responses produced by the three 3D models with the MT stations 24, 25 and 26 of MT survey profile L60E.